NANYANG TECHNOLOGICAL UNIVERSITY

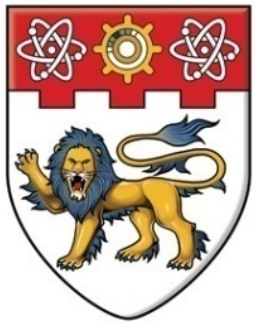

NANYANG TECHNOLOGICAL UNIVERSITY

Synthesis and Electrochemical Performance of Transition Metal Oxide Anodes in Lithium Ion Batteries

A thesis submitted to Nanyang Technological University in fulfillment of the requirement for the degree of Doctor of Philosophy

TEH PEI FEN

School of Materials Science and Engineering

2013

Acknowledgements

The author would like to express her deepest gratitude to:

Assoc. Prof. Madhavi Srinivasan	Dr. Yogesh Sharma
Dr. Stevin Snellius Pramana	Dr. Jordi Jimenze Cabana
Dr. Chunjoong Kim	Dr. Ulrike Boesenberg
Dr. Chuang Cheng-Hao	Assoc. Prof Cheng Zhong
Asst. Lydia Helena Wong	Assoc. Prof Tan Lay Poh
Mrs. Peony Ferguson	Dr. Grace Wee Tsyh Ying
Dr. Cheah Yan Ling	Dr. Mak Wai Fatt
Dr. Wong Chui Ling	Ms. Ko Yah Wen
Mr. Sutanto	Mr. Lee Chee Siang
Mr. Arun Nagasubramanian	Ms. Shubha Nageswaran
Ms. Chen Hanyi	Ms. Li Linlin
Mr. Tan Zixi	Mr. Lee Yong Leng, Benny

Laboratory technicians in FACTS Lab, Inorganic Lab and Consumable Stores (NTU, MSE)

My families and my dearest friends

My classmate since 1999 till now: Ms. Phua Si Lei

I am really grateful and fortunate to know each of you. Thanks for your valuable companionship and understanding whenever I am facing difficulties or being demotivated. I am tremendously appreciative of your constant patience, support, encouragement, guidance, inspiration and insightful comments during the course of this dissertation. It would not have been possible to finish this thesis without you.

Publications

P.F. Teh, S.S. Pramana, C. Kim, C.-M. Chen, C.-H. Chuang, Y. Sharma, J. Cabana and S. Madhavi, Electrochemical Reactivity with Lithium of Spinel-type $ZnFe_{2-y}Cr_yO_4$ ($0 \leq y \leq 2$), *Journal of Physical Chemistry C*, 2013, 117, (46), 24213-24223.

P.F. Teh, S.S. Pramana, Y. Sharma, Y.W. Ko, S. Madhavi, Electrospun $Zn_{1-x}Mn_xFe_2O_4$ Nanofibers As Anodes for Lithium-Ion Batteries and the Impact of Mixed Transition Metallic Oxides on Battery Performance, *ACS Applied Materials & Interfaces*, 2013, 5, (12), 5461-5467.

P.F. Teh, Y. Sharma, Y.W. Ko, S.S. Pramana, S. Madhavi, Tuning the morphology of $ZnMn_2O_4$ lithium ion battery anodes by electrospinning and its effect on electrochemical performance, *RSC Advances*, 2013, 3, (8), 2812-2821.

P. F. Teh, Y. Sharma, S.S. Pramana, S. Madhavi, Nanoweb Anodes composed of One Dimensional, High aspect ratio, Size Tunable Electrospun $ZnFe_2O_4$ Nanofibers for Lithium Ion Batteries, *Journal of Materials Chemistry*, 2011, 21, (38), 14999-15008.

L. Li, S. Peng, Y. L. Cheah, Y.W. Ko, **P. F. Teh**, G. Wee, C. Wong, S. Madhavi, Chemistry - A European Journal, 2013, 19, (44), 14823-14830.

L. Li, Y. L. Cheah, Y.W. Ko, **P. F. Teh**, G. Wee, C. Wong, S. Madhavi, The facile synthesis of hierarchical porous flower-like $NiCo_2O_4$ with superior lithium storage properties, *Journal of Materials Chemistry A*, 2013, 1, (36), 10935-10941.

L. Li, S. Peng, Y. L. Cheah, **P. F. Teh**, J. Wang, G. Wee, Y. Ko, C. Wong, S. Madhavi, Electrospun porous $NiCo_2O_4$ nanotubes as advanced electrodes for electrochemical capacitors, *Chemistry - A European Journal*, 2013, 19, (19), 5892-5898.

L. Li, S. Peng, Y. L. Cheah, J. Wang, **P. F. Teh**, Y. Ko, C. Wong, S. Madhavi, Electrospun eggroll-like $CaSnO_3$ nanotubes with high lithium storage performance, *Nanoscale*, 2013, 5, (1), 134-138.

L. Li, S. Peng, J. Wang, Y.L. Cheah, **P. F. Teh**, Y. Ko, C. Wong, S. Madhavi, Facile approach to prepare porous $CaSnO_3$ nanotubes via a single spinneret electrospinning technique as anodes for lithium ion batteries, *ACS Applied Materials and Interfaces*, 2012, 4, (11), 6005-6012.

S. Saadat, Y. Y. Tay, J. Zhu, **P. F. Teh**, S. Maleksaeedi, M. M. Shahjamali, M. Shakerzadeh, S. Madhavi, B.Y. Tay, H. H. Hng, J. Ma, Q. Yan, Template-free electrochemical deposition of interconnected ZnSb nanoflakes for Li-Ion battery anodes, *Chemistry of Materials*, 2011**,** 23, (4), 1032-1038.

Oral Presentations

P. F. Teh, Y. Sharma, S. Pramana, S. Madhavi, Fundamental Studies of Electrospun Spinel-based Oxides Anodes for Lithium ion Battery Application, MRS Spring, Apr., 2012, San Francisco, United States

P. F. Teh, Y. Sharma, S. Pramana, S. Madhavi, Fundamental Studies of Transition Metallic Oxide Anodes for Lithium ion Batteries, 2012 Joint Symposium on Materials Science and Engineering for the 21st Century, Jun., 2012, Gwangju, Korea. **(Best Oral Award)**

Table of Contents

Acknowledgements ..... **i**

Publications ..... **ii**

Oral Presentations ..... **iii**

Table of Contents ..... **iv**

List of Figures ..... **vii**

List of Schemes ..... **x**

List of Tables ..... **xi**

List of Abbreviations ..... **xii**

Abstract ..... **xiii**

Chapter 1 **Introduction** **1**

1.1. Problem Statement 1

1.2. Motivation 2

1.3. Research Scope and Objectives 3

1.3.1. Investigate the contributions of nanostructured TMOs on battery performance 3

1.3.2. Investigate the reaction mechanism of a variety of spinels towards lithium ions during cycling by comprehensive characterization techniques 4

1.3.3. Investigate the impact of A- and B-site cation substitution within spinel on structural properties and battery performances 4

1.4. Dissertation Overview 5

1.5. Findings and Outcomes 6

Chapter 2 **Literature Review** **7**

2.1. Basic Principles of LIBs 8

2.2. Anode Materials Performed by Different Reaction Mechanisms Towards Lithium 9

2.2.1. Anodes by intercalation 10

2.2.2. Anodes by alloy/dealloy 10
2.2.3. Anodes by conversion reaction 11
2.2.3.1. Co-based binary oxides 14
2.2.3.2. Fe-based binary oxides 15
2.3. Current Issues in Spinel-based Transition Metal Oxides 16
2.3.1. Crystallography information of spinel 17
2.3.2. Cobaltites (ACo_2O_4) 18
2.3.3. Ferrites (AFe_2O_4) 19
2.3.3.1. Reaction mechanism of $ZnFe_2O_4$ as LIB anode 21
2.3.4. Manganites (AMn_2O_4) 22
2.4. Counter ion Effect In Spinel Anodes: Research Gap Analysis 23
2.5. Importance of Material Nanoscaling 25
***Chapter 3* Materials and Methods 27**
3.1. Materials Synthesis 27
3.1.1. High energy ball milling (HEBM) 27
3.1.2. Wet high energy ball milling (HEBM) 28
3.1.3. Colloidal synthesis 28
3.1.4. Hydrothermal synthesis 29
3.1.5. Electrospinning 29
3.1.5.1. Preparation of $ZnMn_2O_4$ nanorods, nanofibers and nanowebs 29
3.1.5.2. Preparation of $ZnFe_2O_4$ nanorods and nanofibers 30
3.1.5.3. Preparation of $ZnCr_2O_4$ and $Zn_{1-x}Mn_xFe_2O_4$ nanofibers 31
3.2. Characterization Methodologies 31
3.2.1. Microscopy methods 31
3.2.1.1. Field emission scanning electron microscope (FESEM) 31
3.2.1.2. Transmission electron microscope (TEM) 32
3.2.2. Diffraction methods 32
3.2.2.1. Powder x-ray diffraction (XRD) 32
3.2.2.2. Thin film x-ray diffraction (XRD) 32
3.2.2.3. Synchrotron x-ray diffraction (XRD) 32
3.2.2.4. Selected area electron diffraction (SAED) 33
3.2.3. Spectroscopy methods 33
3.2.3.1. Fourier transform infrared spectroscopy (FTIR) 33
3.2.3.2. Energy dispersive x-ray spectroscopy (EDS) 33
3.2.3.3. X-ray photoelectron spectroscopy (XPS) 34
3.2.3.4. Electron energy loss spectroscopy (EELS) 34
3.2.3.5. X-ray absorption spectroscopy (XAS) 34
3.2.4. Porosity measurement 35
3.2.5. Viscosity measurement 35
3.2.6. Thermal analysis 35
3.2.6.1. Thermogravimetric analysis (TGA) 35

3.2.6.2. Differential calorimetric studies (DSC) *35*

3.3. Electrochemical Studies 36

3.3.1. 2016 coin cell fabrication 36

3.3.2. Cyclic voltammetry 36

3.3.3. Galvanostatic cycling 36

3.3.4. Impedance spectroscopy 37

3.3.5. *Ex situ* electrode preparation 37

Chapter 4 **Results 38**

4.1. NiO 38

4.1.1. Variation of NiO particle size by using different synthesis methods 39

4.1.2. Impact of particle size on electrochemical performance of NiO 40

4.2. Electrospun TMOs 41

4.2.1. Electrospun $ZnMn_2O_4$ nanorods, nanofibers and nanowebs: Impact of sintering profiles of surface morphology 42

4.2.2. Electrospun $ZnMn_2O_4$ nanorods, nanofibers and nanowebs: Materials characterization 45

4.2.3. Electrospun $ZnMn_2O_4$ nanorods, nanofibers and nanowebs: Comparison of electrochemical performance 48

4.2.4. Electrospun $ZnFe_2O_4$ nanorods and nanofibers: Impact of precursor solution viscosity on surface morphology 51

4.2.5. Electrospun $ZnFe_2O_4$ nanorods and nanofibers: Materials characterization 54

4.2.6. Electrospun $ZnFe_2O_4$ nanorods and nanofibers: Comparison of electrochemical performance 56

4.2.7. Electrospun $ZnCr_2O_4$ nanofibers: Materials characterization 60

4.2.8. Electrospun $ZnCr_2O_4$ nanofibers: Electrochemical measurement 61

4.2.9. Electrospun $Zn_{1-x}Mn_xFe_2O_4$ nanofibers ($0 \leq x \leq 0.7$): Materials characterization 62

4.2.10. Electrospun $Zn_{1-x}Mn_xFe_2O_4$ nanofibers ($0 \leq x \leq 0.7$): Comparison of electrochemical performance 65

4.3. Ball Milled TMOs 66

4.3.1. Ball milled $ZnMn_2O_4$, $ZnFe_2O_4$ and $ZnCr_2O_4$: Materials characterization 67

4.3.2. Ball milled $ZnMn_2O_4$, $ZnFe_2O_4$ and $ZnCr_2O_4$: Comparison of electrochemical performance 69

4.3.3. Ball milled $MgMn_2O_4$, $MgFe_2O_4$ and $MgCr_2O_4$: Materials characterization 71

4.3.4. Ball milled $MgMn_2O_4$, $MgFe_2O_4$ and $MgCr_2O_4$: Comparison of electrochemical performance 74

4.3.5. Ball milled $ZnFe_{2-y}Cr_yO_4$ nanoparticles: Materials characterization 77

4.3.6. Ball milled $ZnFe_{2-y}Cr_yO_4$ nanoparticles: Comparison of electrochemical performance 83

4.4. Application of Ball Milled $ZnMn_2O_4$ and $ZnFe_2O_4$ Particles as Anodes in Full LIB 87

Chapter 5 **Discussions 89**

5.1. Effect of Nanostructuring in Conversion Reaction 89

5.1.1. Effect of Particle Size 89
5.1.2. Effect of mass loading on NiO performance 91
5.1.3. Effect of 1D electronic wiring in electrospun $ZnMn_2O_4$ 93
5.1.4. Effect of 1D electronic wiring in electrospun $ZnFe_2O_4$ 95
5.1.5. Comparison of electrochemical performance between 0D ball milled particles and 1D electrospun nanofibers 96

5.2. Conversion Reaction Mechanism in TMOs 98

5.2.1. Ball milled MgB_2O_4 (B: Mn, Fe or Cr) 98
5.2.2. Ball milled $ZnFe_2O_4$ 100
5.2.3. Electrospun $ZnFe_2O_4$ 101
5.2.4. Electrospun $Zn_{1-x}Mn_xFe_2O_4$ nanofibers 103
5.2.5. Ball milled $ZnFe_{2-y}Cr_yO_4$ 106

5.3. Effect of A site Substitution 110

5.3.1. Electrospun $Zn_{1-x}Mn_xFe_2O_4$ nanofibers 110
5.3.2. Ball milled AMn_2O_4 and AFe_2O_4 (A: Zn and Mg) 111

5.4. Effect of B Site Substitution 112

5.4.1. ZnB_2O_4 (B: Mn, Fe, Cr) and $ZnFe_{2-y}Cr_yO_4$ 113
5.4.2. Ball milled MgB_2O_4 (B: Mn, Fe, Cr) 115

Chapter 6 **Conclusions 117**

6.1. Novel Contributions 119

6.1.1. Scientific contributions 119
6.1.2. Technological significances 120

Chapter 7 **Recommendations for Future Works 121**

7.1. Fundamental Studies on Crystal Chemistry of AB_2O_4 and their Lithium Activity 121

7.2. Investigation of the Voltage Hysteresis 122

7.3. Enhancement of Full Cell Performance 122

References 124

Appendix 134

List of Figures

Figure 2-1 Comparison of LIB with other rechargeable batteries....7
Figure 2-2 Schematic diagram of LIB operating principles....8
Figure 2-3 Theoretical specific capacities of some elements....11
Figure 2-4 Typical first discharge and charge profiles of TMOs-based anode....13
Figure 2-5 Arrangement and packing of atoms in normal spinel....17
Figure 4-1 NiO with different morphologies. 39
Figure 4-2 XRD patterns of NiO samples.....39
Figure 4-3 TGA and DSC of NiO samples 40
Figure 4-4 First and second discharge/charge cycles of NiO samples.....41
Figure 4-5 Cyclability of NiO samples at 0.1C....41
Figure 4-6 FESEM images of high aspect ratio as-spun nanofibers 42
Figure 4-7 TGA of as-spun nanofibers 42
Figure 4-8 Temperature profiles used in sintering of as-spun nanofibers....43
Figure 4-9 FESEM micrographs of nanofibers carbonized at 350 °C 45
Figure 4-10 FTIR analysis in $ZnMn_2O_4$ formation. 46
Figure 4-11 TGA of sintered $ZnMn_2O_4$ 46
Figure 4-12 XRD patterns and Rietveld refinements of ZMO-NR, ZMO-NF and ZMO-NW...46
Figure 4-13 Size distribution of nanocrystals in ZMO-NR, ZMO-NF and ZMO-NW....47
Figure 4-14 Zn and Mn XPS multiplex scans....48
Figure 4-15 CV of ZMO-NR, ZMO-NF and ZMO-NW 49
Figure 4-16 First galvanostatic cycling of (a) ZMO-NR, (b) ZMO-NF and (c) ZMO-NW 50
Figure 4-17 Cycling performance of $ZnMn_2O_4$ 50
Figure 4-18 Nyquist plots for (a) ZMO-NR, (b) ZMO-NF and (c) ZMO-NW.....51
Figure 4-19 Equivalent circuit used to fit the Nyquist plot....51
Figure 4-20 FESEM images of as-spun (a, c) and sintered (b, d) nanofibers. 52
Figure 4-21 TGA of as-spun $ZnFe_2O_4$ nanofibers....52
Figure 4-22 FTIR analysis of $ZnFe_2O_4$ synthesis....54
Figure 4-23 Rietveld refinement to XRD pattern of sintered $ZnFe_2O_4$.....55
Figure 4-24 EDS spectra of (a) ZFO-NR and (b) ZFO-NF.....55
Figure 4-25 Characterization of ZFO-NF by TEM.....56
Figure 4-26 Galvanostatic cycling for $ZnFe_2O_4$ electrode 57
Figure 4-27 CV of ZFO-NF 58
Figure 4-28 Cyclability of $ZnFe_2O_4$. 59
Figure 4-29 Nyquist plots for ZFO-NR and ZFO-NF.....59
Figure 4-30 Equivalent circuit used to fit the Nyquist plot.....59
Figure 4-31 FESEM image of $ZnCr_2O_4$ nanofibers 60
Figure 4-32 Rietveld refinement of $ZnCr_2O_4$ nanofibers 60
Figure 4-33 Electrochemical measurement of ZCO-NF. 61
Figure 4-34 Cyclability of ZCO-NF 61
Figure 4-35 FESEM images of $Zn_{1-x}Mn_xFe_2O_4$ nanofibers....62
Figure 4-36 Materials characterization of $Zn_{1-x}Mn_xFe_2O_4$ nanofibers. 64
Figure 4-37 XRD patterns of MF nanofibers....64
Figure 4-38 Electrochemical results of $Zn_{1-x}Mn_xFe_2O_4$ nanofibers. 65

Figure 4-39 Electrochemical testings of $Zn_{1-x}Mn_xFe_2O_4$ nanofibers after cycling. 66
Figure 4-40 FESEM images of annealed ZnB_2O_4 67
Figure 4-41 Powder XRD results of annealed ZnB_2O_4 68
Figure 4-42 Materials characterization of annealed ZnB_2O_4 68
Figure 4-43 Galvanostatic cycling results of annealed ZnB_2O_4 69
Figure 4-44 Extended galvanostatic cycling of ZnB_2O_4 70
Figure 4-45 Magnified view of first CV cycle of ZCO-NP. 71
Figure 4-46 TGA of citric acid 72
Figure 4-47 XRD patterns of MgB_2O_4 (B: Mn, Cr, Fe) 73
Figure 4-48 FESEM images of MgB_2O_4. 73
Figure 4-49 CV scans of MgB_2O_4. 74
Figure 4-50 Initial discharge/charge behaviors MgB_2O_4. 75
Figure 4-51 Battery performance of commercial MgO 76
Figure 4-52 Cyclability of MgB_2O_4 (B: Mn, Cr and Fe) 76
Figure 4-53 Materials characterization of annealed $ZnFe_{2-y}Cr_yO_4$ ($0 \le y \le 2$). 77
Figure 4-54 FESEM micrographs of annealed $ZnFe_{2-y}Cr_yO_4$ ($0 \le y \le 2$). 78
Figure 4-55 XPS spectra of the annealed $ZnFe_{2-y}Cr_yO_4$ samples. 79
Figure 4-56 FTIR spectra of annealed $ZnFe_{2-y}Cr_yO_4$. 80
Figure 4-57 XAS studies of $ZnFe_{2-y}Cr_yO_4$. 82
Figure 4-58 Galvanostatic cycling data of $ZnFe_{2-y}Cr_yO_4$ 84
Figure 4-59 First discharge/charge behaviors 85
Figure 4-60 Cycling performance of $ZnFe_{2-y}Cr_yO_4$ particles 87
Figure 4-61 CV of full LIB cell. 88
Figure 4-62 Cyclability of full LIB cell. 88
Figure 5-1 First discharge behaviour of TMOs can be categorized into three regions 90
Figure 5-2 First cycling behavior of commercial NiO with different mass loadings 92
Figure 5-3 Phase transition from ZnO and Fe_2O_3 to $ZnFe_2O_4$ 96
Figure 5-4 Cyclability of $ZnFe_2O_4$ prepared by electrospinning HEBM 97
Figure 5-5 *Ex situ* study of reaction mechanisms of MgB_2O_4. 98
Figure 5-6 *In situ* characterization by XRD on ZFO-NP electrode. 101
Figure 5-7 *Ex situ* characterization by XRD on $ZnFe_2O_4$ 102
Figure 5-8 *Ex situ* SAED of charged ZFO-NF 102
Figure 5-9 *Ex situ* characterization of cycled electrodes. 104
Figure 5-10 *Ex situ* XRD pattern 107
Figure 5-11 SAED and simulated diffraction rings of (top) pristine $ZnFe_{2-y}Cr_yO_4$ powders and (bottom) *ex situ* electrodes after 1st discharge. 108
Figure 5-12 Impact of A-site substitution on battery performance 111
Figure 5-13 Impact of B-site substitution on battery performance. 114

List of Schemes

Scheme 2-1 Schematic illustration of conversion reaction 12
Scheme 3-1 Schematic illustration of nanofibers on copper current collector. 29
Scheme 3-2 Schematic illustration of electrospinning set up 30
Scheme 4-1 Schematic representation of formation mechanism of $ZnMn_2O_4$. 44
Scheme 4-2 Schematic illustration of $ZnFe_2O_4$ formation mechanism. 53

List of Tables

Table 2-1 Electrochemical performance of Co-based binary oxides as anode in LIB. 14
Table 2-2 Experimental values of working potential and capacity of α-Fe_2O_3 15
Table 2-3 Electrochemical performance of several cobaltites 18
Table 2-4 Experimental data of ferrites with different morphologies and counter ion A. 20
Table 2-5 Electrochemical performance of some manganites 22
Table 2-6 Gibbs free energy of formation (ΔG^0), theoretical working voltage (E) and experimental values of some binary oxides 24
Table 3-1 TMOs used in this thesis were prepared by the following synthesis methods 27
Table 4-1 Lattice parameters and crystallite sizes of $ZnMn_2O_4$ 47
Table 4-2 Site occupancies of Zn, Mn and Fe cations at A or B sites 64
Table 4-3 Results of Rietveld refinement of annealed $ZnFe_{2-y}Cr_yO_4$ 79
Table 4-4 Summary of battery performance of $ZnFe_{2-y}Cr_yO_4$ particles 85
Table 5-1 Participation of lithium ions in each region 91
Table 5-2 Lithium participation of NiO with different mass loadings 92
Table 5-3 Summary of the electrospun ZMO-NR, ZMO-NF and ZMO-NW 93
Table 5-4 Impedance values of electrospun $ZnMn_2O_4$ 94
Table 5-5 Summary of the electrospun ZFO-NR and ZFO-NF 95
Table 5-6 Impedance of electrospun $ZnFe_2O_4$ 96
Table 5-7 d-spacing and possible Miller indices observed in SAED pattern. 103
Table 5-8 d-spacings and possible Miller indices observed in *ex situ* SAED 105
Table 5-9 Mn $L_{2,3}$ ELNES data measured by EELS analysis 106
Table 5-10 Comparison of electrochemical performance between some manganites and ferrites after A-site substitution. 112
Table 5-11 Summary of electrochemical performance of ZnB_2O_4 with different morphologies prepared by electrospinning or HEBM. 113
Table 5-12 Performance of MgB_2O_4 anodes 116

List of Abbreviations

BET	Brunauer-Emmett-Teller
CFSE	Crystal Field Stabilization Energy
CV	Cyclic Voltammetry
DSC	Differential Calorimetric Studies
EDS	Energy Dispersive X-ray Spectroscopy
EELS	Electron Energy Loss Spectroscopy
EIS	Electrochemical Impedance Spectroscopy
ELNES	Electron-Energy Loss Near-Edge Structure
EVs	Electric Vehicles
FESEM	Field Emission Scanning Electron Microscope
FFT	Fast Fourier Transform
FTIR	Fourier Transformed Infra Red
HEBM	High Energy Ball Milling
HEVs	Hybrid Electric Vehicles
HRTEM	High Resolution Transmission Electron Microscope
IC	Internal Combustion
LIB	Lithium Ion Battery
NiCd	Nickel Cadmium
NiMH	Nickel Metal Hydride
PVP	Poly(vinylpyrolidone)
SAED	Selected Area Electron Diffraction
SEI	Solid Electrolyte Interface
TEM	Transmission Electron Microscope
TGA	Thermogravimetric Analysis
TMOs	Transition Metal Oxides
XAS	X-Ray Absorption Spectroscopy
XPS	X-Ray Photoelectron Spectroscopy
XRD	X-Ray Diffraction
0D	0-Dimension
1D	1-Dimension
2D	2-Dimension

Abstract

To answer the intensive quest for enhanced lithium ion battery equipped to future automobiles and other advanced applications, new generation anode with good storage properties, great safety and low production cost is currently extensively explored. Transition metal oxides are one of the mostly studied candidates, which are able to uptake/release lithium ions through a new operating concept, 'conversion reaction'. However, several factors currently handicap the conversion reaction-based anodes from commercialization. Hence, scientific research and breakthroughs to meet the application requirements are still an imperious need.

A series of transition metal oxides crystallizing in spinel structure (AB_2O_4) prepared by different synthesis techniques is presented in this thesis, and their electrochemical performance as lithium ion battery anode is discussed in depth. This thesis mainly aims to access the common issues encountered in conversion reaction from three different perspectives, *i.e.* practicality of nanomaterials in enhancing the battery performance, comprehensive characterization of the reaction mechanism between spinel-based anodes and lithium ions, as well as the impact of counter ion substitution (either A- or B-sites in AB_2O_4 spinel) on the electrochemical properties.

Based on the results of systematic cation substitution in spinels with different nanostructures, the battery performance of transition metal oxides is found to be highly contingent upon the morphology of host materials. The mixed transition metal oxides demonstrate the possibility to achieve better storage properties and greater energy density by selecting the best counter ion pairs. As a result, $ZnMn_2O_4$ and $ZnFe_2O_4$ anodes are observed to possess better lithium storage characteristics than other combination of mixed oxides, indicating their promising potential to replace currently used commercial graphite. To account for their excellent battery behaviors, detailed characterizations on cycled electrodes are conducted, especially on $ZnFe_2O_4$.

Chapter 1 Introduction

1.1. Problem Statement

In response to surging oil prices and growing concern over global warming caused by excessive emission of gaseous by-products, electrical storage systems coupled with renewable energy sources are anticipated as plausible solution to limit CO_2 emission, as well as to reduce our dependency on fossil fuels, diesels and gasoline.[1] Among various electrical energy storage solutions, lithium ion battery (LIB) has been particularly popularized as it is a better option than other rechargeable batteries (*e.g.* lead-acid, nickel cadmium (NiCd), nickel metal hydride (NiMH)).[2] As a result, LIB has been extensively employed in versatile mobile electronic devices, such as laptops, cellular phones, camera, as well as in bioengineering devices and implants, including cardiac pacemakers, defibrillators, left ventricular assist devices and total artificial heart.[3, 4]

Conventional internal combustion (IC) engine powered by non-renewable resources is expected to be complemented or replaced by electric motor powered by rechargeable energy storage devices in near future. Plug-in hybrid vehicles (PHEVs) and hybrid electric vehicles (HEVs) with the combination of electric motor and IC engine for vehicular propulsion have been introduced to the commercial market, for instance Toyota Prius ride on NiMH battery was realized in 2005,[5] whereas it was substituted by LIB in Toyota RAV4 in 2012.[6] Generally, PHEVs require a battery with large capacity (5-15 kWh) because the electric motor and stored energy are used to power up the vehicles when travelling for short distances, while IC engine is used after the battery energy is depleted. On the contrary, HEVs are designed to store energy captured during braking and convert this energy to accelerate the vehicles, so battery in HEVs requires only little amount of energy (~1-2 kWh), instead excellent power density is favorable.[7] Consequently, the development of lithium ion technology is now being stimulated towards the high power and energy density, in order to replace long relied IC engine and eventually leading to pure electric vehicles (EVs, require>40 kWh).[7]

Specialty graphite has been widely used as anode since first commercial LIB by Sony Corporation in 1990,[2, 8] as it is cheap and non-toxic. However, the theoretical specific

capacity of graphite (~372 mAh g^{-1}) is much lower than the requirements for future automobiles.[8] In addition, safety issues with extended use of graphite anode are critical as there is likelihood of lithium dendrites formation especially when discharging and charging at high C rate.[9] It leads to the possibility of explosion due to the puncturing of separator and short circuiting, eventually causing in thermal runaway.[10, 11] There were a few newspaper reports about LIBs in cellular phones or notebook computers catching fire or evolving smoke during charging or discharging operation.[12] These drawbacks have directed research community to explore alternatives to graphite to realize safer LIBs with higher power/energy density.[3, 13-15]

Although extensive research has been conducted world widely for the last 15 years, merely one alternative anode, Sn-Co-C composite was successfully commercialized by Sony Corporation in 2005.[3, 16] Each mole of Sn reacts with maximum 4.4 moles of lithium ions by forming intermetallic alloy, while conductive carbon and electrochemically inactive Co serve as buffer matrix to retain the cyclability.[17] A reversible and stable capacity of ~350−450 mAh g^{-1} can be obtained but this material may not be the ultimate solution. Therefore, a continuation of efforts is necessary in exploring new classification of materials for future LIB applications.

1.2. Motivation

Lithium ion reacts reversibly with graphite anode by intercalation mechanism, *i.e.* lithium ion occupies the interstitial sites within carbon layers without destructing the primary structure. The shortcoming lies as the intrinsic available intercalation hosts is limited with LiC_6 as end compound after deep discharge *versus* Li/Li^+, leading to low storage capacity.[18] Poizot *et al.* reported a new charging/discharging mechanism in 2000,[19] briefly a large number of lithium ions can be stored in per unit formula of transition metal oxides (TMOs, for instance, CoO, Co_3O_4, Cu_2O, FeO, NiO) by 'conversion' reaction, associated with higher theoretical capacity (~400–1000 mAh g^{-1}) than graphite anodes.[15, 20] However, the drawbacks of conversion reaction must be taken care before realizing it as the next-generation anodes. The delivery of high capacity inevitably causes drastic volumetric expansion/contraction on the electrode, resulting in the pulverization of active material from the current collector after prolonged cycling. Their high operating voltage *versus* Li/Li^+ compensates the overall energy density of LIB.[20-24]

Particularly interesting, preliminary results by research society show that some oxide systems with two transition metals are able to provide some competitive advantages than simple binary oxides. In a mixed transition compound, it offers the flexibility to select the best "inter-beneficial" counter ion to achieve high and stable specific capacity, as well as providing the possibility to tune the working voltage with respect to Li/Li^+ reference.[20] For instance, the combination of Zn with Co_3O_4 and Fe_2O_3 to construct ternary $ZnCo_2O_4$[25] and $ZnFe_2O_4$,[9, 26, 27] crystallizing in spinel structure has shown excellent capacity values on cycling. Although these results are inspiring, this field has yet to be adequately researched and there is currently no available theory to verify the effect of counter ion on lithium absorption/extraction behaviors in spinel-based anode.[20, 25] Hence, this thesis aims to contribute more understanding in this direction.

1.3. Research Scope and Objectives

To address the gaps in the literature, the research scope of this thesis is to investigate oxide systems with two transition metals crystallizing in a AB_2O_4 spinels (A: divalent transition metal, B: trivalent transition metal) as an alternative anode for LIB with higher capacity and better safety than graphite. The sub-objectives are proposed below:

1.3.1. Investigate the contributions of nanostructured TMOs on battery performance

Many research efforts have been devoted to develop a new candidate or to enhance the quality of LIB anode. Nanostructuring has become one of the most overwhelming direction since the lithium storage characteristic of TMOs is highly dependent on its size, morphology and structure.[14, 28] Nanomaterials with higher surface area allow high amount of interfacial contact with the organic electrolyte and permit facile lithium ion flux,[14] thus manifestly enhancing the kinetics. As compared to their micro-sized counterparts, higher power and energy density are obtained by nanostructured anodes.[21-23] However, nanomaterials have great tendency to form agglomerates due to their high specific surface area and excessive surface energy.[14, 22, 23]

For this purpose, TMOs with 0-dimension (0D), 1-dimention (1D) and 2-dimension (2D) shape are fabricated through several versatile and simple synthesis routes in this thesis, in

order to study the effect of morphology on the electrochemical performance. A crucial concern when employing nanomaterials is the reduction of electrode volumetric density, as mass loading per electrode may vary significantly between bulk- and nano-electrode. So, optimum loading per electrode will be discussed to standardize a fair comparison throughout this thesis.

1.3.2. Investigate the reaction mechanism of a variety of spinels towards lithium ions during cycling by comprehensive characterization techniques

Materials characterization of cycled TMOs at different level of cutoff voltages is always more intricate than expected, as the TMOs are amorphized during conversion reaction to metallic nanograins with size smaller than x-ray diffraction (XRD) coherence length. So far, there are many reports using *ex situ* high resolution transmission electron microscope (HRTEM) and selected area electron diffraction (SAED) to verify the phase formation within the electrode after prolonged cycling,[29-31] however this technique always involves some ambiguous speculation. The further understanding of real time reaction between lithium ions and TMOs was still restricted by *ex situ* study of electrodes. So, it is important to investigate the reaction mechanism of TMOs by other more sophisticated characterization techniques. Owing to it, electron-energy loss near-edge structure (ELNES) spectrum and *in situ* XRD will be discussed in this thesis, aiming to gain a more reliable analysis than *ex situ* TEM. Furthermore, the reaction mechanisms of several unreported TMOs anodes are established.

1.3.3. Investigate the impact of A- and B-site cation substitution within spinel on structural properties and battery performances

As previously mentioned, distinguishable capacity and working voltage of anodes are generally observed by changing the counter ion in AB_2O_4 spinel structure. For instance, nanocrystalline $CoFe_2O_4$, $NiFe_2O_4$, $ZnFe_2O_4$ and $CuFe_2O_4$ thin film showed working voltage/capacity retention (at 100^{th} cycles) of 1.7 V/365 mAh g^{-1}, 1.7 V/355 mAh g^{-1}, 1.6 V/432 mAh g^{-1} and 1 V/340 mAh g^{-1}, respectively.[32]

As of yet, there is no systematic study to provide information about the effect of counter ion within spinels and their reactivity towards lithium ions during discharging/charging. Owing to it, A-site and B-site substitutions in spinel structure will be focused in this thesis. Studies are conducted based on full stoichiometric replacement at A and B-sites, as well as solid solution series of mixed TMOs. The structural information will be provided and the reaction mechanism of mixed TMOs will be proposed to contribute a better insight of mixed TMOs as new anodes.

1.4. Dissertation Overview

The thesis is organized as follows.

The Introduction (Chapter 1) provides the research justification and establishes the working scope and objectives. This thesis aims to further investigate and enhance the battery performance of spinel-based TMOs as LIB anodes to outperform commercially available graphite.

Chapter 2 briefly reviews the state-of-art LIB, the construction and operating principles. Anodes currently under research are classified into different categories based on their activities with lithium ion, the advantages and disadvantages will be evaluated. A detailed review about binary and spinel-based TMOs anodes is provided. The role of nanomaterials in excelling the TMOs-anodes performance is also introduced.

Chapter 3 introduces the various synthesis methods to obtain anodes with different morphologies and sizes. The material analysis is conducted by a suite of characterization techniques, while the procedures of device fabrication and electrochemical characterization are also discussed.

Chapter 4 details the experimental results followed by its discussion in Chapter 5. Finally, the impact of nanomaterials on LIB anode performance is experimentally investigated. The lithium storage characteristic of a variety of spinels-based TMOs is proposed on the basis of careful materials characterization. Tailoring the counter ion within the spinels structure is presented and the consequences on electrochemical properties are highlighted.

Chapter 6 concludes the whole project and Chapter 7 proposes some recommendations of future works that help to further understand the spinel anodes. Suggestions are made to

elucidate these new concepts through addressing correlations of crystal chemistry, lithium ion migration mechanisms and device fabrication.

1.5. Findings and Outcomes

This thesis leads to several outcomes:

- Demonstrating simple and cost effective methods to prepare nanomaterials.
- Suggesting an optimum of range of particle size and mass loading per electrode required to establish a fair comparison among TMOs anodes with different nanostructures.
- Proposing reaction mechanisms for a few new spinel-based anodes.
- Formulating the impact of counter ion in spinels on battery performance.

Chapter 2 Literature Review

Although rechargeable batteries require higher initial manufacturing cost than primary batteries (non-rechargeable), they are more environmentally benign than disposable batteries and allow to be reused cheaply. The first rechargeable battery was invented in 1859 by combining Pb and PbO_2 electrodes to construct lead acid battery, which is still applicable in automobiles until now.[2] Over the last century, a few different combinations of chemicals has been gradually brought into the commercial market, such as NiCd, NiMH and LIB.[8] LIB technology is more popular than other electrical energy storage solutions because it offers higher energy density of 250-400 Wh kg^{-1} for ~1200 cycle and lighter weight (Figure 2-1).[33] Besides, a single cell of LIB has a higher operating voltage (~3.7 V) than NiCd or NiMH (typically 1.2 V) with lower self discharge rate.[2, 3]

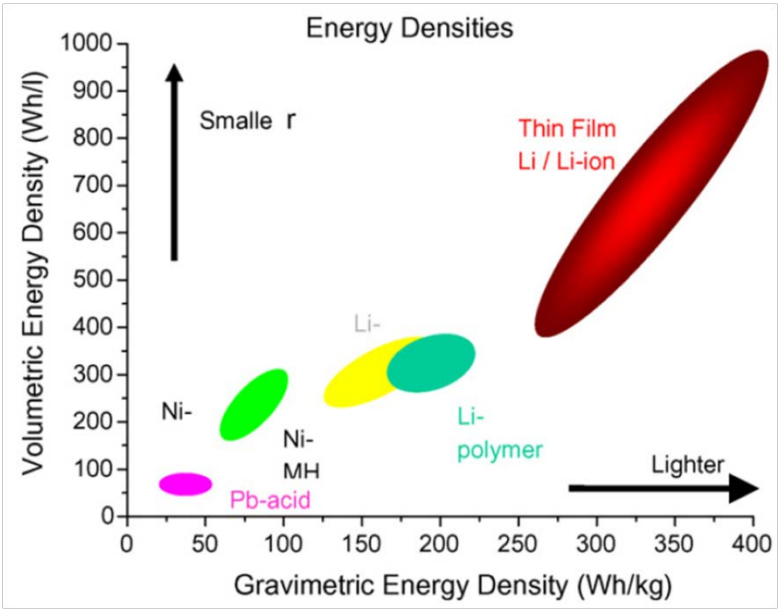

Figure 2-1 Comparison of LIB with other rechargeable batteries based on the volumetric (energy density, expressed in Wh L^{-1}) and gravimetric energy density (specific energy, expressed in Wh kg^{-1}).[33] (Reprinted with permission from Elsevier)

This chapter discusses the basic operating principles of commercial LIB with $LiCoO_2$ and graphite as cathode and anode, respectively. To answer the explosive demand of future LIB with higher energy/power density, this thesis particularly focuses on the development of potential LIB anode to replace commercial graphite. To deepen our knowledge,

published reports regarding alternative anode candidates are categorized according to their unique reaction mechanisms with lithium ion. Moreover, material synthesis strategies in enhancing the electrode materials are also summarized and discussed.

2.1. Basic Principles of LIBs

Looking at the development history of LIB, Goodenough *et al.* reported the usage of lithium cobalt oxide ($LiCoO_2$) as cathode in 1980s,[34] while Yazami *et al.* revealed the likelihood of reversible lithium intercalation into graphite anode using a solid organic electrolyte in 1980.[18] Later on, first LIB prototype by combining these electrodes were built by Asahi Chemical in 1985[35] and Sony Corporation commercialized it into consumer market in 1990. Since its introduction, it has earned numerous attentions in versatile applications, such as portable electronic gadgets, cellular phones and laptops.

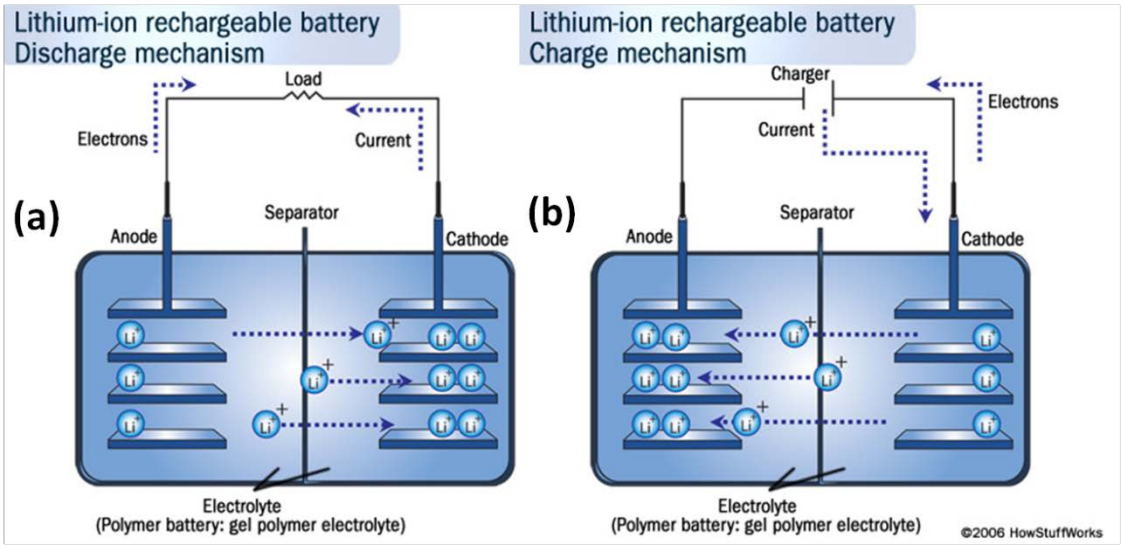

Figure 2-2 Schematic diagram of LIB operating principles during (a) discharge and (b) charge.[36]

Figure 2-2 shows a typical LIB comprising a positive electrode (cathode, such as $LiCoO_2$, $LiMn_2O_4$, $LiFePO_4$), a lithium-conducting organic electrolyte and a negative electrode (anode, such as graphite). Polyvinylidene diflouride (PVDF) binder is incorporated into both electrodes to improve adhesion between active materials and current collector (either Al or Cu), as well as to alleviate volume change during operation. When the battery is discharged (Figure 2-2(a)), lithium ions are driven by the external voltage and extracted from the anode, passing through the organic electrolyte and intercalated into cathode. On charging (Figure 2-2(b)), lithium ions are released by cathode and intercalated into anode.

Half cell reaction of positive electrode ($LiCoO_2$) during charging (forward reaction) can be summarised as following:[34]

Equation 2-1 $LiCoO_2 \leftrightarrow Li_{1-x}CoO_2 + xLi^+ + xe^-$

On the contrary, half cell reaction of negative electrode (graphite) during charging (forward reaction):

Equation 2-2 $6C + xLi^+ + xe^- \leftrightarrow Li_xC_6$

Hence, the overall reaction of a LIB is summarised in Equation 2-3. Lithium ions are transported to and from the cathode or anode by reducing Co^{4+} to Co^{3+} upon discharging, or oxidising cobalt (Co) in Li_xCoO_2 from Co^{3+} to Co^{4+} during charging. To maintain the charge balance, lithium flows in the conductive organic electrolyte while electrons move along the external circuit.

Equation 2-3 $LiCoO_2 + 6C \leftrightarrow Li_{1-x}CoO_2 + Li_xC_6$

Typically, it is advised to operate the battery in the temperature range of 15 °C to 60 °C. Below 15 °C, the kinetics of the battery is affected thus resulting in lower capacity, while the electrode and electrolyte experience slow degradation if the battery is operated above 60 °C.[3] LIBs are usually charged and discharged at ~0.2 − 1C (C: C rate, discharging/charging rate of a battery to full capacity), representing the charge/discharge process is completed within ~5−1 h.

2.2. Anode Materials Performed by Different Reaction Mechanisms Towards Lithium

As previously discussed, commercially used graphite anode has a theoretical capacity of only 372 mAh g^{-1}, accompanied with possible safety hazards related to the lithium plating and explosion.[10, 11] As a consequence, attention in exploiting alternative anode to substitute graphite anodes has surged to a new high. The new anode is expected to be a material with high specific capacity, good cyclability, environmentally friendly, cheap and preferably possess lower working voltage *versus* lithium to increase the total energy density output of a LIB. Although undeniable obstacles ahead, noteworthy efforts have been invested by research organizations and companies to investigate the next possible commercial LIB anode.

Generally, anodes can be categorized based on their reaction mechanisms in absorbing/releasing lithium during cycling: intercalation, alloy-dealloy or conversion reaction. This section briefly introduces the distinct differences between these three reactions and their advantages and drawbacks.

2.2.1. Anodes by intercalation

Both $LiCoO_2$ and graphite electrodes contain intercalation hosts for migrating lithium ion to electrochemically insert or de-insert into/out from their layered structures. Since no major structural change is caused on the host materials, reversibility of intercalation based electrodes are always pleased. This transfer mechanism was first proposed by Armand and Scrosati *et al.* who labeled them as a 'rocking chair' battery.[37]

Other than graphite, various intercalation materials have also been investigated as new anodes for LIB, such as oxides and chalcogenides.[37] Among all, spinel $Li_4Ti_5O_{12}$ was the most promising candidate due to their excellent reversibility with zero mechanical strain upon cycling. It is safer choice than graphite anodes, however maximum capacity delivered is capped at 175 mAh g^{-1}.[38] So, a common issue encountered by intercalation anodes is their poor storage properties due to limited interstitial sites.[37]

2.2.2. Anodes by alloy/dealloy

Other than intercalation mechanism, Dey *et al.* demonstrated a range of metallic or semi-metallic elements that can achieve larger capacity by forming alloy or intermetallics with lithium during discharging (Li_xM, M = Sn, Si, In).[39] On charging, lithium can be de-alloyed and left behind the nanocrystalline M.[38]

Speculated from the phase diagrams of lithium with other elements, some elements convey extremely high theoretical capacities, such as $Li_{4.4}Si$ and Li_3Mg (Figure 2-3). Among all, Mg and Al are always covered by a layer of native oxide which compensates their lithium kinetics, so they have gained less focus as compared to Si and Sn. Alloy formation of $Li_{4.4}Si$ and $Li_{4.4}Sn$ contributes maximum capacities of ~4200 mAh g^{-1} and ~960 mAh g^{-1}, respectively. In spite of their higher capacities than graphite, alloy/dealloy anodes were extensively reported to have poor capacity retention due to the excessive volumetric change during extended cycling, for instance $Li_{4.4}Si$ experiences a 400% lattice expansion after being alloyed.[40, 41] The huge variation of the electrode volume

creates high mechanical stresses or cracks in the host materials, which is detrimental to long cycling. This drawback hinders alloy/dealloy-based anodes from commercialization. So, considerably intense progress has been made to enhance their performance, mainly to limit the volumetric changes. These remedies inevitably involved high production expenses and sophisticated preparation technique, such as nanoscaling with specialized nanostructures[42] or incorporation of conductive carbon.[43] Nevertheless, the efforts invested by research community were not in vain as Sony developed Nexelion commercial LIB that uses Sn-Co-C as new anode in 2005 with a reversible capacity of 500 mAh g^{-1}.[17] The good cyclability can be attributed by the presence of Co_xSb particles of ~5 nm in the composites to alleviate the stress.[38, 44] Nevertheless, it is necessary to replace Co eventually due to its high cost and toxicity.[45, 46]

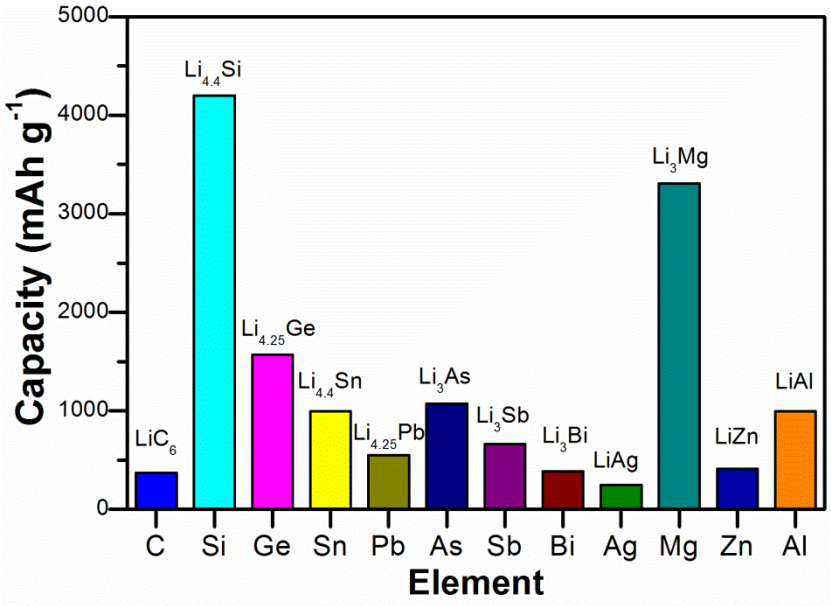

Figure 2-3 Theoretical specific capacities of some elements in forming alloys or intermetallics with lithium.[38, 47]

2.2.3. Anodes by conversion reaction

Nowadays, transition metal oxides (TMOs) have received concerted research efforts as they are regarded as high-capacity anodes (~400-1000 mAh g^{-1}), in accordance with their ability to reversibly react with more than one lithium ions through 'conversion reaction'.[19] Although this reaction mechanism have also been observed in some transition metal fluorides, sulphides, nitrides and phosphides, this thesis only concentrates on the performance of oxides, as TMOs exhibit better reversibility and stability as LIB anode than the remaining candidates.[20, 46]

Lithium storage in TMOs was always perceived to be irreversible at room temperature due to the formation of inactive Li_2O before the inspiring finding given by P. Poizot *et al.*[19]. CoO is a rocksalt structure with no interstitial sites for lithium intercalation and de-intercalation. Poizot *et al*. successfully demonstrated the reduction of nanosized CoO to Co/Li_2O during first discharge, while nanocrystalline CoO was reversibly formed upon subsequent lithium ion extraction. It is worth noting that nanoscaling of TMOs is very crucial to realize this 'conversion reaction',[14, 48] as nanomaterials provide a higher surface area to volume ratio and a shorter diffusion pathway for lithium ions and electrons transportation to remarkably improve the battery kinetics than their bulk counterparts.[23]

Since then, many reports have been published to employ nanosized TMO as anodes by conversion reaction.[20, 22, 49] Overall lithiation and delithiation process of a binary transition metal oxide can be written as

Equation 2-4 $M_xO_n + 2n\ Li \leftrightarrow x\ M + n\ Li_2O$

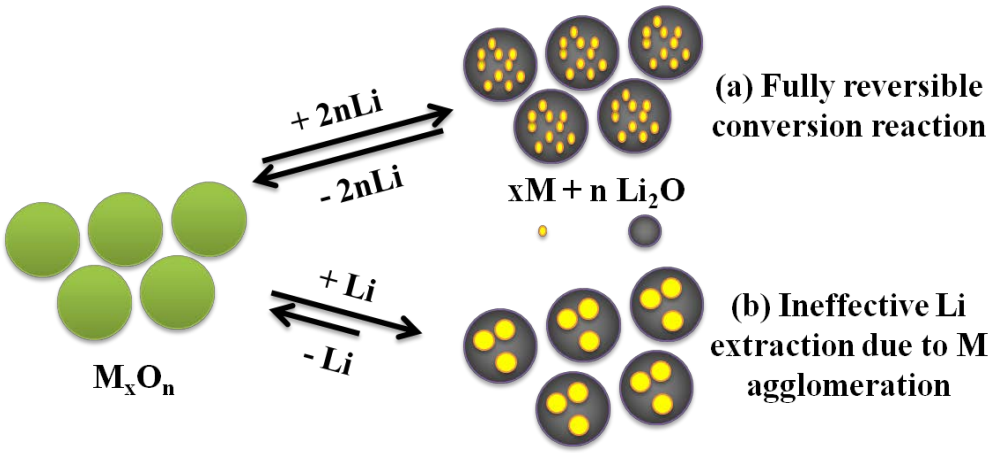

Scheme 2-1 Schematic illustration of conversion reaction according to Equation 2-4. Forward reaction represents the reduction of M_xO_n anode during discharge, while backward reaction indicates re-oxidation upon subsequent charging. (a) Fully reversible conversion reaction based on theoretical assumption; however capacity fading is always encountered due to ineffective lithium extraction during cycling as illustrated in (b).

At the first discharge, M_xO_n (M: transition metal, such as Co, Fe, Zn, Cu) absorbs 2n mole of lithium ion per formula unit and reduces to form M/Li_2O nanocomposite, in which 2-5 nm of metallic nanograins (M) are uniformly embedded in an amorphous Li_2O matrix (Scheme 2-1(a)).[8] Due to the nature of the products, XRD failed to identify the phase formed after the first discharge, as the nanocrystalline particles has size smaller than XRD coherence length.[20] Surface area of metallic nanograins are hence greatly maximized after this irreversible amorphization process, forming an intimate contact with

Li_2O matrix and leading to higher electrochemical reactivity during the following cycles.[49] After the deep discharge, a thin polymeric layer appears around metallic nanograins due to electrolyte decomposition catalyzed by the existence of nanoparticles,[25, 50, 51] serving as the envelope to retain the contact of metallic nanograins.[51] It was found to be decomposable in the subsequent charging process. Metallic nanograins are actively re-oxidized and Li_2O is decomposed during the following charge cycles according to Equation 2-4 due to the large amount of interfacial surface with different bonding environment (ionic and metallic), however the initial crystallinity of the TMOs cannot be resumed.

The capacity delivered by TMOs based on Equation 2-4 can be speculated by Faraday's law, *i.e.* capacity (Q, A-hr) = It = 2nFN (I: current, t: duration, F: Faraday's constant (96500 sA mol^{-1}), N: number of mole of reacting species and 2n: lithium ion transferred). After some simple mathematics, theoretical specific capacity of a TMO can be derived using Equation 2-5 (MW: molecular weight of host materials).[52]

Equation 2-5 $Specific\ Capacity\ (mAh\ g^{-1}) = \frac{26800 \times 2n}{MW(TMO)}$

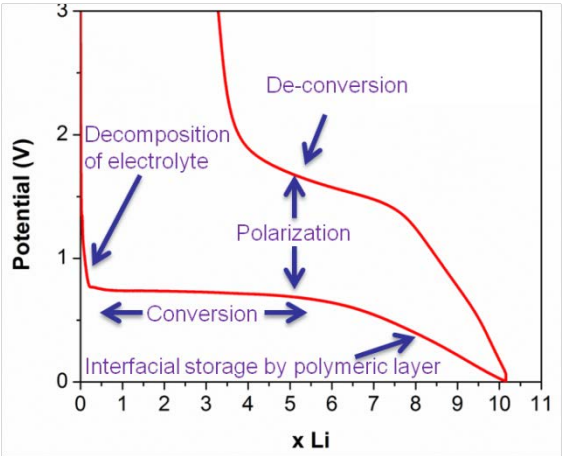

Figure 2-4 Typical first discharge and charge profiles of TMOs-based anode with lithium ions *via* conversion reaction (potential *versus* lithium insertion/extraction), the lithium metal acts as counter and reference electrode.

TMOs were widely reported to have high irreversible coulombic efficiency of less than 75% at first cycle, although the efficiency can be enhanced to ~100 % at the following cycles. This occurs due to the irreversible electrolyte decomposition to form solid electrolyte interface (SEI) layer at 0.7-0.9 V during first discharge (Figure 2-4). SEI is an organic-like layer comprised by ethylene-oxide-based oligomers, Li_2CO_3, LiF and lithium alkylcarbonate ($ROCO_2Li$).[53, 54] The discharge profile is then followed by a

characteristic long plateau to represent conversion reaction, while the plateau length is equivalent to number of mole of lithium ion required to fully reduce the TMOs (expressed as 2n in Equation 2-4). Subsequently, highly reversible interfacial storage by the formation of polymer layer around the metallic nanograins is characterized by the sloping curve till deep discharge.[20, 55] Gradual capacity depletion was observed in some TMOs, this phenomenon may be explained by the agglomeration of tiny metallic nanograins after prolonged cycling with ineffective lithium extraction/absorption, causing the presence of inaccessible region (Scheme 2-1(b)). Besides, structural re-organization experienced by the TMOs electrode to accommodate the chemical modifications during discharging/charging causes volumetric expansion/contraction and probably leads to pulverization of active material from current collector.[56]

Based on the nature of conversion reaction, strong covalent M-O bond yields high reaction potential above 1.0 V and induces a large overpotential between the discharge and charge profiles or difference between practical working voltage and theoretical thermodynamics equilibrium voltage.[49] By comparing with graphite anode which intercalates/deintercalates at 0.1 V, TMO has a narrower voltage window if preserving $LiCoO_2$ as cathode in LIB. Low voltage battery inevitably reduces the gravimetric and volumetric energy density. As a consequence, research committees are working together to overcome all these shortcomings before introducing TMO as next-generation anode.

2.2.3.1. Co-based binary oxides

Table 2-1 Electrochemical performance of Co-based binary oxides as anode in LIB.

Chemical Formula	Working voltage at extended cycle (V)		Reversible capacity/N^{th} cycle (mAh g^{-1})	Current density used for cycling
	Discharge	Charge		
CoO [57]	1.4	2.1	750/100^{th}	600 mA g^{-1}
CoO [58]	0.8	2.2	1050/20^{th}	71.5 mA g^{-1}
Co_3O_4 [59]	1.3	2.0	700/100^{th}	890 mA g^{-1}
Co_3O_4 [60]	1.2	2.0	1000/30^{th}	50 mA g^{-1}

Among TMOs, cobalt oxides were the first and most extensively investigated conversion anodes in last decade, for instance Co_3O_4 [56, 59, 61] and CoO [19] which exhibit excellent electrochemical performance of about 700-1000 mAh g^{-1} with good cyclability (Table 2-1). However, cobalt based TMO is not an ideal alternative anode to graphite because of its high working voltage (~2.1 V *versus* lithium),[25, 56, 59, 61] high cost and toxicity.[45]

2.2.3.2. Fe-based binary oxides

Other than Co-based binary oxides, Fe oxides that are chemically stable, cheap, abundant and safe have become a new focus of researchers. Theoretically, each mole of Fe_2O_3 uptakes/releases 6 moles of lithium ions during discharging/charging, contributing a theoretical capacity of 1007 mAh g^{-1} (Equation 2-6).

Equation 2-6 $Fe_2O_3 + 6\,Li^+ + 6\,e^- \leftrightarrow 2\,Fe + 3\,Li_2O$

Table 2-2 Experimental values of working potential and capacity of α-Fe_2O_3 nanostructured anodes. The morphology of materials has a direct impact on the battery performance.

Morphology	Working voltage at extended cycle (V)		1st discharge capacity (mAh g^{-1})	Reversible capacity/Nth cycle (mAh g^{-1})	Current density used for cycling
	Discharge	Charge			
commercial sample [62]	~0.8	~1.6	~1000	~50/100th	127 μA cm^{-2}
nanoflakes [50]	1.2	2.1	1235	680/80th	65 mA g^{-1}
nanospheres [63]	~1.0	~1.5	1398	414/60th	101 mA g^{-1}
nanorods [64]	0.8/0.95	1.65/1.9	1281	603/30th	101 mA g^{-1}
nanotubes [65]	~1.0	1.6	~1500	450/150th	134 mA g^{-1}
submicron flower [66]	0.7	1.85	906	325/50th	100 mA g^{-1}
submicron spheres [67]	0.7	1.8	1248	586/30th	20 mA g^{-1}
porous nanoflowers [68]	~1.0	~1.5	974	548/30th	0.2 mA cm^{-2}

Table 2-2 summarizes the electrochemical performance of hematite α-Fe_2O_3 reported by a few research groups. The first discharge capacities were found to be higher than their long term capacity retentions, as the volumetric expansion, SEI formation or agglomeration of metallic nanograins may cause the mechanical instability and capacity fading. Moreover, it is worth noting that the size and surface morphology of the host material has significant impact on storage properties. Commercial Fe_2O_3 purchased from Aldrich has worse performance than other nanostructured materials,[62] whereas nanoflakes and nanorods presented ~2 times of graphite capacity.[50, 64] Consequently, it is critically important to design a nanostructured electrode with suitable morphology and size.

As compared to α-Fe_2O_3, spinel Fe_3O_4 received lesser attention in the past. Although Fe_3O_4 theoretically reacts with 8 moles of lithium ions during lithiation/delithiation (Equation 2-7), the gravimetric capacity is lesser (926 mAh g^{-1}) due to its higher active mass per formula unit.

Equation 2-7 $Fe_3O_4 + 8\,Li^+ + 8\,e^- \leftrightarrow 3\,Fe + 4\,Li_2O$

Moreover, the reversibility of Fe_3O_4 is very poor, Liu *et al.* observed the capacity of Fe_3O_4/carbon fades from initial high capacity of 1126 mAh g^{-1} to 394 mAh g^{-1} after cycling for 100 cycles at 100 mA g^{-1}.[69] The low reversible capacity occurs possibly due to the incomplete re-oxidation to Fe^{3+} (initial valence state of Fe^{3+} is not fully recovered) upon cycling and contradictorily Fe^{2+} was observed.[50, 70]

To enhance the efficiency of Fe_3O_4, conductive agents such as graphene[71] or carbon coating[69] can be utilized to construct a facile diffusion pathway and provide a buffer zone to against excessive volumetric expansion during cycling. Consequently, remarkably high capacity of 900-1000 mAh g^{-1} has been observed. Another approach to improve the performance of Fe_3O_4 is by replacing the Fe^{2+} atoms by other transition metals which have a better reversibility with lithium ions (see Section 2.3.3).

2.3. Current Issues in Spinel-based Transition Metal Oxides

As discussed earlier, cobalt is highly toxic and expensive despite their excellent storage properties and reversibility, so considerable effort has been made to partially replace cobalt in Co_3O_4 by other transition elements to form a ternary cobaltite. Besides, Fe^{2+} in Fe_3O_4 was proposed to be replaced by other elements in order to boost up their battery performance. After the cation substitution to form ternary ACo_2O_4 and AFe_2O_4 (A: bivalent cation, such as Zn, Mn, Cu), they are still isostructural to their binary oxides (spinel structure).

Spinel oxides with high storage capacity, safe and long cyclability provide competitive advantages than commercial graphite, especially in the aspect of high volume electrochemical energy storage applications.[20] While their applicability is still hampered by severe fundamental issues as discussed in Section 2.2.3,[20] so there is a growing research interest in exploring their viability as commercial anodes.[22, 23] The electrochemical performance of reported cobaltities, ferrites and manganites anodes is reviewed in this section.

2.3.1. Crystallography information of spinel

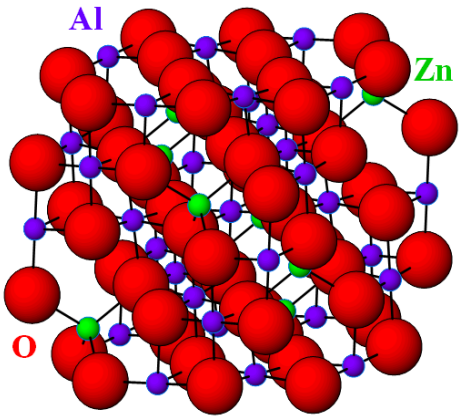

Figure 2-5 Arrangement and packing of atoms in normal spinel unit cell ($ZnAl_2O_4$,[72] generated by ATOMS) with projection of (111) plane.

Ternary transition metal oxides with the spinel structure (ideally AB_2O_4, space group $Fd\bar{3}m$ (227)) are of wide interest in solid state chemistry due to their rich variety of crystallographic arrangements, as well as their physical and chemical properties, which render them applicable as magnetic materials, catalysts, semiconductors and pigments.[72-74] A and B may be either elements from d- or f-blocks; group IA, IIA, IIIA or IVA, generally forming $A^{2+}B_2^{3+}O_4$ (*e.g.* $ZnAl_2O_4$).[75] Other species such as $A^{4+}B_2^{2+}O_4$ (*e.g.* Zn_2SnO_4)[76] and $A^{+}B_2^{3.5+}O_4$ (*e.g.* $LiMn_2O_4$)[77] were also known. If the unit cell origin is taken at a center of symmetry $\bar{4}3m$, one-eighth of the tetrahedral sites (8a, 0, 0, 0, $\bar{4}3m$) are filled by A cations, while B cations occupy one-half of the all octahedral sites (16d, $^5/_8$, $^5/_8$, $^5/_8$, . $\bar{3}m$) in a cubic close packed arrays of oxygen atoms (32e, u, u, u, . $3m$) to form a normal spinel.[75] If half of B cations occupy the tetrahedral sites, this ordered configuration experiences a transition from normal to inverse spinel (retains in $Fd\bar{3}m$ structure).[78] The degree of inversion significantly affects the chemical and physical properties of spinel-based materials.[72, 75] It can usually be tailored by controlling temperature and pressure during synthesis.

Intercalation ternary spinels have received considerable interest as cathodes in LIB before conversion reaction was established. Improved battery performance (capacity and cyclability) and tunable discharge/charge voltage plateaus of spinel-based cathodes were widely observed after doping or cation substitution by other transition metals, for instance doped-$LiMn_2O_4$ with iso- or aliovalent cations to construct $LiM_xMn_{2-x}O_4$ (M: Ni, Al, Co,

Mg, Fe) developed interesting electrochemical enhancement.[77, 79] Hence, this strategy can also be employed in spinel-based anodes to develop spinel as viable anode with enhanced capacity retention and lower working voltage, with the purpose to increase the energy density output of a LIB with respect to $LiCoO_2$ as cathode material.

2.3.2. Cobaltites (ACo_2O_4)

Table 2-3 Electrochemical performance of several cobaltites (working voltages and capacity retention) were tabulated.

Chemical Formula	Morphology	Working Voltage at extended cycle (V)		Reversible capacity/N^{th} cycle (mAh g^{-1})	Current density used for cycling
		Discharge	Charge		
Co_3O_4 [59]	powder	1.3	2.0	700/100^{th}	890 mA g^{-1}
Co_3O_4 [60]	nanotubes	1.2	2.0	1000/30^{th}	50 mA g^{-1}
$NiCo_2O_4$/C [80]	nanocomposites	0.8	1.7/2.2	716/50^{th}	40 mA g^{-1}
$ZnCo_2O_4$ [81]	particles	1.0	1.5/2.2	500/50^{th}	100 mA g^{-1}
$ZnCo_2O_4$ [25]	nanoparticles	1.1	1.6/2.0	900/60^{th}	60 mA g^{-1}
$FeCo_2O_4$ [30]	nanoparticles	1.1/1.2	1.8/2.1	747/50^{th}	60 mA g^{-1}
$CuCo_2O_4$ [82]	nanoparticles	1.2	2.1	900/6^{th}	60 mA g^{-1}
$MnCo_2O_4$ [83]	hollow spheres	0.9	1.6/2.1	755/25^{th}	200 mA g^{-1}

A summary of some cobaltites (ACo_2O_4, A: divalent element) was shown in Table 2-3, all remain in spinel structure. Although it does not include all the research related to cobaltite-anodes, it is sufficient to imply that the partial substitution of Co^{2+} by other elements substantially influences the working voltage and capacity.

According to the comparison in Table 2-3, all cobaltites exhibited greater capacity than graphite with excellent cyclability. $ZnCo_2O_4$ by Sharma *et al.*[25] offers the highest capacity retention of ~900 mAh g^{-1} at 60^{th} cycle other than Co_3O_4.[60] All listed ACo_2O_4 anodes exhibited an average discharge voltage of ~0.8-1.3 V, similar to binary Co_3O_4. The charge voltage in the range of ~2.0-2.2 V can be attributed to the re-oxidation of Co metallic to Co^{2+} or further oxidation to Co^{3+}.[82] Some cases demonstrated another charge voltage below 2 V may be related to the re-oxidation of cation A.

To this end, since toxic and expensive cobaltites cannot hold the promise to fully replace conventional graphite as alternative anode despite their excellent storage properties, researchers have diverged to other transition metal oxides which are cheaper and environmental friendlier. Nevertheless, the understanding obtained from cobaltites can be universally applied to comprehend other spinel oxides.

2.3.3. Ferrites (AFe_2O_4)

Spinel ferrites (AFe_2O_4) were widely used in technological applications due to their excellent physical properties. They have been implemented in the magnetic recording, high frequency transformers, antennae and other microelectronic devices.[84] Since versatile techniques are available to synthesize nanostructured ferrites, and inspired by the interesting studies of cobaltites, a renewed interest is now emerging to utilize ferrites as LIB anodes. Table 2-4 summarizes the electrochemical performance of reported AFe_2O_4. Obviously, the working voltages and capacity are disturbed by changing the counter ion A^{2+} toward Fe^{3+}. Although the overall electrochemical performance of ferrites is still lagging behind cobaltities in terms of capacity and retention, ferrites are always a superior choice from the consideration of cost and toxicity. Thus, more notorious effort has to be devoted to ameliorate their electrochemical properties in LIB.

Among all the ferrites, $ZnFe_2O_4$ has been the object of several studies, as it is environmentally benign and exhibits a high and stable reversible capacity of ~600-1100 mAh g^{-1}.[9, 26, 27] Similar to α-Fe_2O_3 (Section 2.2.3.2), battery performance of $ZnFe_2O_4$ is also highly contingent upon the nanostructures. NuLi *et al.* published $ZnFe_2O_4$ thin film with reversible capacity of 432 mAh g^{-1},[26] an improved lithium uptake of urea-combustion synthesized 100-300 nm particles (615 mAh g^{-1}) was then reported by Sharma *et al.* in 2008.[9] The performance was further enhanced by either nanostructuring strategies to form hierarchically hollow microspheres (~900 mAh g^{-1}),[85] nanoparticles (818 mAh g^{-1})[86] or by the incorporation of conductive carbon framework to construct $ZnFe_2O_4$/C hollow spheres (841 mAh g^{-1})[87] and carbon coated $ZnFe_2O_4$ nanoparticles (1100 mAh g^{-1}).[88] Higher capacity and better retention are generated by $ZnFe_2O_4$ as compared to other ferrites, probably due to the feasibility of Zn to additionally alloy/dealloy with lithium ion reversibly other than undergoing conversion reaction. Detailed reaction mechanism will be discussed in Section 2.3.3.1. By comparing $ZnCo_2O_4$ nanoparticles [25] and $ZnFe_2O_4$ nanoparticles [9] by Sharma *et al.*, it is obvious that the electrochemical performance is not only decided by substituting cation A, but also cation B. To sum up, TMOs with two transition elements (both A and B – site in AB_2O_4 systems) provide feasibility to tune the energy density and working voltages by varying the transition metal content. Hence, this thesis will study $ZnFe_2O_4$ in depth and further understand the impact of counter ion in LIB anode application.

Table 2-4 Experimental data of ferrites with different morphologies and counter ion A.

Chemical formula	Morphology	Working voltage at extended cycle (V)		1st charge capacity (mAh g^{-1})	Reversible capacity/Nth cycle (mAh g^{-1})	Current density used for cycling	Reference
		Discharge	Charge				
$CoFe_2O_4$	thin film	0.48	1.85	~900	610/100th	114 mA g^{-1}	[89]
$NiFe_2O_4$	nanoparticles	0.77	1.7	~750	709/3rd	0.2 mA cm^{-2}	[90]
$MgFe_2O_4$	nanosized grain	-	~1.5	~900	~300/10th	0.2 mA cm^{-2}	[91]
$CoFe_2O_4$	nano-crystalline thin film	~0.5	1.7	460	365/100th	10 μA cm^{-2}	[32]
$CuFe_2O_4$		~0.5	1.0	452	340/100th		
$NiFe_2O_4$		~0.5	1.7	460	355/100th		
$ZnFe_2O_4$		0.5	1.75	~556	432/100th		[26]
$ZnFe_2O_4$	nanoparticles	1.0	1.5	810	615/50th	60 mA g^{-1}	[9]
$ZnFe_2O_4$	hollow spheres	1.0	1.4	770	900/50th	65 mA g^{-1}	[85]
$ZnFe_2O_4$/C	hollow spheres	1.3/0.95	1.5/1.75	910	841/30th	65 mA g^{-1}	[87]
$ZnFe_2O_4$	nanoparticles	0.8	1.7	958	818/50th	116 mA g^{-1}	[86]
$ZnFe_2O_4$/C	nanoparticles	0.95	1.5	1050	1100/60th	100 mA g^{-1}	[88]

2.3.3.1. Reaction mechanism of $ZnFe_2O_4$ as LIB anode

On the basis of *ex situ* characterization of cycled electrodes, the reaction mechanism of $ZnFe_2O_4$ with lithium was proposed as follows:

Equation 2-8 $ZnFe_2O_4 + 8Li^+ + 8e^- \rightarrow Zn + 2\,Fe + 4\,Li_2O$ (only during first discharge) [9, 27, 85, 86]

Equation 2-9 $Zn + x\,Li^+ + x\,e^- \leftrightarrow Li_xZn$ $(x \leq 1)$ [26, 27, 85]

Equation 2-10 $Zn + Li_2O \leftrightarrow ZnO + 2\,Li^+ + 2\,e^-$(first charge onwards) [9, 27, 85, 92]

Equation 2-11 $Fe + Li_2O \leftrightarrow Fe^{(II)}O + 2\,Li^+ + 2\,e^-$(first charge onwards) [9, 26, 27]

Equation 2-12 $2Fe + 3\,Li_2O \leftrightarrow Fe_2^{(III)}O_3 + 6\,Li^+ + 6\,e^-$(first charge onwards) [85]

During the first discharge, theoretically 8 moles of lithium reacts with $ZnFe_2O_4$ in accordance to Equation 2-8.[9, 27, 85, 86] The reduction reaction is mostly accompanied by irreversible electrode amorphization,[9, 27, 85] resulting in Zn and Fe metallic nanograins of 2-5 nm uniformly embedded in an amorphous Li_2O matrix.[19] This process can be well recognized by a single discharge plateau instead of two that would initially be assumed due to different working voltage of ZnO and Fe_2O_3,[49] indicating the state mixing at Fermi levels takes place.[20] It is worth noting that, Sharma *et al.* proposed a small amount of lithium was found to intercalate into $ZnFe_2O_4$ prior conversion reaction,[9, 27, 85] although this was not seen after the destruction of spinel.[9] This phenomenon was supported by the work done by Chen *et al.*, which proposed that intercalated lithium occupies vacant 16c sites in AB_2O_4 spinels.[93] The possibility to obtain intercalated $ZnFe_2O_4$ highly relies on the particle size and shape of the host materials, so hollow microspheres and nanoparticles were found to accommodate ~2 moles of lithium,[85, 86] but it was absent in $ZnFe_2O_4$/C hollow spheres.[87] In the following discharge/charge cycles, Zn can further reversibly alloy/dealloy with maximum 1 mole of lithium (Equation 2-9). This lithiation process was experimentally observed by Guo *et al.*[85] and NuLi *et al.*[26] in discharged state of formally $ZnFe_2O_4$ anodes by *ex situ* HRTEM/SAED and x-ray photoelectron spectroscopy (XPS), respectively.

From first charge onwards, reversible lithiation/delithiation behaviors are expressed by Equation 2-9-Equation 2-12. Theoretically, maximum 9 lithium ions can be reversibly

released/absorbed by Zn/Fe/Li_2O nanocomposites. However, dealloying reaction between Li and Zn is not highly reversible,[9, 27] while incomplete re-oxidation of Fe resulting in $Fe^{(II)}O$ or a mixture with $Fe_2^{(III)}O_3$.[9, 26, 27] Sharma *et al.*[9] reported the observation of $Fe^{(II)}O$ during charged state after 50 cycles by *ex situ* HRTEM and SAED, these are analogue to the investigation done by NuLi *et al.* using *ex situ* XPS.[26] Guo *et al.* instead reported the reversible formation of only $Fe_2^{(III)}O_3$ by *ex situ* HRTEM and SAED. So, Equation 2-11 and Equation 2-12 may be coexistent at the subsequent cycling, similar to the previous discussion about partial re-oxidation of Fe in Fe_3O_4 (Section 2.2.3.2). This may be the reason to cause capacity fading on $ZnFe_2O_4$ anodes at long term cycling.

2.3.4. Manganites (AMn_2O_4)

Table 2-5 Electrochemical performance of some manganites , $ZnMn_2O_4$ is the main focus in this thesis due to their better storage behaviors.

Chemical formula	Morphology	Working voltage at extended cycle (V)		1st charge capacity (mAh g^{-1})	Capacity at extended cycle (mAh g^{-1})	Current density used for cycling
		Discharge	Charge			
$CoMn_2O_4$ [94]	nanoparticles	~0.7	1.3	~520	330/50th	100 mA g^{-1}
$NiMn_2O_4$ [94]		~1.1/0.6	1.3/1.9	~830	210/20th	
$ZnMn_2O_4$ [94]		0.5	1.3/1.6	~800	490/25th	
$ZnMn_2O_4$ [53]	nanocrystalline	0.4	1.2/1.5	766	569/50th	100 mA g^{-1}
$ZnMn_2O_4$ [95]	nanoparticles	0.6	1.2/1.6	680	430/100th	100 mA g^{-1}
$ZnMn_2O_4$ [54]	flower-like superstructure	0.4	1.2/1.5	763	626/50th	100 mA g^{-1}
$ZnMn_2O_4$ [96]	flake-shaped particles	0.5	1.2/1.5	680	640/50th	100 mA g^{-1}
$ZnMn_2O_4$ [97]	nanowires	0.4	1.2/1.5	~830	650/40th	100 mA g^{-1}
$ZnMn_2O_4$ [98]	hollow microspheres	0.4/0.3	1.3/1.55	742	607/100th	100 mA g^{-1}
$ZnMn_2O_4$ [99]	hollow submicron spheres	0.5	1.2/1.5	835	599/40th	100 mA g^{-1}

Since $ZnFe_2O_4$ received numerous attention, a simple substitution to form $ZnMn_2O_4$ have emerged as another possible candidate to replace graphite anodes (Table 2-5). As compared to $CoMn_2O_4$ and $NiMn_2O_4$, $ZnMn_2O_4$ nanoparticles maintain higher capacity reversibility at ~490 mAh g^{-1}.[94] Generally speaking, $ZnMn_2O_4$ demonstrated consistent cyclability of 550 – 650 mAh g^{-1} after nanostructuring, which is almost two times of graphite anode. This may be again contributed by alloy/dealloy mechanism performed by Zn with addition of their capability to go through conversion reaction. The average

discharge voltage of 0.4-0.6 V may be attributed to the sequential reduction of ZnO and Mn_2O_3, only one peak was observed as these two materials have adjacent reduction voltages at ~0.5 V and 0.4 V.[100, 101] On the other hand, their corresponding oxidation peaks were widely reported at ~1.5 V and 1.2 V for ZnO and Mn_2O_3, respectively.[100, 101] In simplicity, reaction mechanism of $ZnMn_2O_4$ was observed to be very identical with $ZnFe_2O_4$, although the working voltages are different due to nature of thermodynamics parameters.

2.4. Counter ion Effect In Spinel Anodes: Research Gap Analysis

By mixing two TMOs, it is possibly to consolidate their competitive advantages, such as the flexibility to alter theoretical capacity and control the working voltages.[20] So far, the reduction/oxidation potentials of binary TMOs are estimated by referring to their thermodynamic values reported in the literature.[49, 102] Based on the reaction pathway described in Equation 2-4, the theoretical working voltage (electromotive force, E) of a binary oxide (M_xO_n) can be calculated by the Nernst equation:

Equation 2-13 $$\Delta G = n\Delta G^0(Li_2O) - \Delta G^0(M_xO_n) = -2nEF$$

2n represents to the number of the charge transferred during the reaction per mole of M_xO_n and F is the Faraday constant (96500 sA mol^{-1}). These theoretical working voltages are exclusively suitable for highly crystalline and bulk samples, however conversion reaction involves *in situ* formed nanoscale products (amorphous Li_2O and metallic nanograins) with excessive interfacial surface area and lower crystallinity. Unlike intercalation-based anode, a well defined and long discharge/charge plateau was seldom spotted in conversion reaction (refer to Figure 2-4), instead a sloping curve was noticed with substantial voltage hysteresis due to the sequential reduction/oxidation of TMOs (*eg.* $Co^0 \rightarrow Co^{2+} \rightarrow Co^{3+}$ has different equilibrium potentials) and large surface area induced during amorphozation. As a consequence, large deviations were always observed between the experimental data and theoretical expectation. Some examples of binary oxides were presented in Table 2-6, the theoretical capacity is presumed based on Equation 2-5.

Table 2-6 Gibbs free energy of formation (ΔG^0), theoretical working voltage (E) and experimental values of some binary oxides .[49]

Oxide	ΔG^0 (kJ mol^{-1})	Theoretical E (V)	Experimental Voltage (discharge/charge)	Theoretical Capacity (mAh g^{-1})	Experimental Capacity/N^{th} cycle (mAh g^{-1})	Morphology
Li_2O	-562	-	-	-	-	-
CoO	-214	1.802	0.8/2.2	715	~320/20th	particles [58]
Fe_2O_3	-742	1.631	1.2/2.1	1007	680/80th	nanoflakes [50]
			0.9/1.7		~350/150th	nanotubes [65]
MnO	-363	1.032	0.6/1.2	756	~472/25th	thin film [103]
Mn_2O_3	-881	1.431	0.4/1.2	1007	~680/20th	porous nanorods [100]
Mn_2O_3			0.5/1.2		524/200th	microspheres [104]
Cr_2O_3	-1058	1.085	0.2/1.2	1058	~650/20th	ball milled powder with carbon [105]
Cr_2O_3			0.1/1.2		~380/80th	mesoporous [106]
ZnO	-320	1.252	0.7/1.5	659	~250/20th	nanorods [101]
ZnO			0.5/1.5		~380/15th	nanorods [107]

As of now, there are no systematic and conclusive studies about the influence of counter ion in tuning the voltage profiles of a spinel-based anode. Although NuLi *et al.* reported AFe_2O_4 by varying A to be either Co, Cu, Ni, and Zn (refer to Table 2-4), there was no obvious impact on their working voltages (all discharge and charge potentials maintained at ~0.5 V and ~1.7 V) and no further investigation has been accounted for the replacement of counter ion.[26, 32] Another study on $NiMn_{2-x}Fe_xO_4$ by Lavela *et al.* suggested that first discharge voltage is irrespective of the transition metal content, while lowest reduction voltage at second cycle was exhibited by $NiMn_2O_4$ (x=0) at 0.6 V, as opposed to the higher reduction voltage of $NiFe_2O_4$ at 1.06 V.[108] By cross comparing $NiFe_2O_4$ results by NuLi and Lavela, there is an obvious discrepancy between of their reported second discharge voltage (Δ = ~0.56 V). On the other hand, ACo_2O_4 series (A: Zn, Fe, Cu, Table 2-3) and AMn_2O_4 series (A: Co, Ni, Zn, Table 2-5) prepared under similar conditions demonstrated disparate electrochemical results in both working voltages and capacities after cation substitution.

So far, there are plenty of open questions required to be addressed to further understanding the impact of counter ion replacement in spinel. Since the guidelines based on the thermodynamics parameters cannot fully suggest the possible working voltages of AB_2O_4 anodes, systematic studies by either solid solution or systematic cation

substitution are urged to gather understanding in depth, thus this part will be focused in this thesis. Undeniably, the strategy by having mixed transition metal oxides in AB_2O_4 spinels have established a new possible approach to discover better conversion anode with desirable properties qualified for future LIB applications.

2.5. Importance of Material Nanoscaling

TMOs typically encountered a massive structural reorganization which may lead to huge volumetric expansion and contraction during prolonged cycling, the electrode might be pulverized from the current collector in the worst scenario due to the induced mechanical fatigue.[20, 46] There were many reports suggesting this drawback can be circumvented by engineering the electrode, *i.e.* nanoscaling or nanostructuring of the active materials.[14, 48] By employing nanomaterials as LIB anode, kinetics of lithium ion are appreciably increased due to excessive surface area and shortened diffusion pathway, thus leading to higher power and energy densities in LIB application.[22, 23] Besides, nanostructured TMOs show enhanced cyclability as their smaller grain sizes and larger portion of surface atoms help in relieving the volume expansion and contraction encountered during cycling.[13, 22, 24] However, the application of nanomaterials is still complicated by several limitations including difficulty in synthesis, poor reproducibility, inhomogeneity of their final morphologies and prohibitively high fabrication costs due to sophisticated fabrication techniques. Furthermore, nanomaterials have great tendency to form agglomerates due to their high specific surface area and excessive surface energy.[14, 22, 23] Therefore, it is important to acquire further knowledge in this direction before nanomaterials become a commercial reality in future.

Some practical comparison among ferrites (Table 2-4) indicates the lithium storage characteristic of a material is highly dependent on its size and morphology,[14, 22] thereby $ZnFe_2O_4$ with different surface morphologies behaved differently in terms of their capacity retention. Nanocrystalline thin film of $ZnFe_2O_4$ provided lowest reversible capacity of ~432 mAh g^{-1},[26] whereas hierarchically constructed hollow spheres sustained at ~900 mAh g^{-1} after 50^{th} cycle,[85] which is close to its theoretical capacity (1000 mAh g^{-1} by considering 9 mole of lithium absorption). By incorporating carbon coating around the nanoparticles, an enhanced cyclability of 1100 mAh g^{-1} that surpassed the pure nanoparticles can be obtained.[88] Similar observation in $ZnMn_2O_4$ (Table 2-5),

nanocrystalline $ZnMn_2O_4$ by polymer pyrolysis method[53] and nanoparticles by hydrothermal synthesis[95] have shown lower capacity retention of 569 mAh g^{-1} and 430 mAh g^{-1} after prolonged cycling than other nanostructures. This may be explained by the greater tendency of nanoparticles to agglomerate due to their high specific surface area and excessive surface energy, in turn inhibiting their electrochemical performance.[22, 23] To prevent the existence of inactive regions by agglomeration and retain the extraordinary properties brought by nanomaterials, extensive study about the engineering of nanomaterials has been reported.[14, 48] The nano/micro hierarchical electrode materials combine the competitive advantages of both micro and nanomaterials,[23, 109] wherein the synthesis method is tailored to fabricate a self-assembled parent micro-sized structure that is made up of numerous building blocks at nanodimensions. For example, the formation of $ZnFe_2O_4$ and $ZnMn_2O_4$ hollow microspheres by their respective nanosized building blocks were demonstrated.[85, 98] Each building block of $ZnFe_2O_4$ or $ZnMn_2O_4$ provides the benefits of nanometer-sized materials during prolonged cycling, while the micro-sized assembly ensures better structural stability and cyclability as LIB anodes.[23]

In summary, the common approaches conducted by the researchers to restrain pulverization and improve the capacity retention include:

- Reduction of particle size to nanoscales [14, 48]
- Incorporating the active material with a buffer zone to cushion the expansion, such as carbon coating [110, 111]
- Confining the active materials by inactive nanomaterials to restrain the volume fluctuation, such as CaO matrix helps in maintaining the superior storage properties of SnO_2 [31]
- Design a 3D hierarchical nanostructures,[112] such as nano/micro-assembly [109]

In this thesis, a few synthesis methods will be touched on to produce materials with different nanostructured architectures, so the specialty of each technique and their impact on the battery performance will also be discussed.

Chapter 3 Materials and Methods

This chapter summarizes the experimental procedures employed in the materials synthesis, characterization methodologies and device fabrication of nanostructured TMOs for LIB anode application.

3.1. Materials Synthesis

Several methods were used to prepare TMOs, it can be broadly classified as solid state and wet chemical synthesis. The latter includes hydrothermal, electrospinning and colloidal methods. For detailed crystallographic analyses and mechanistic study of TMOs in lithium ion activity, highly crystalline materials were synthesized by solid state high energy ball milling. More information will be discussed in Chapter 4 and Chapter 5. Table 3-1 summarises various TMOs and their preparation techniques employed in this thesis. Details of experimental procedures are provided in the following section.

Table 3-1 TMOs used in this thesis were prepared by the following synthesis methods.

Samples	**Synthesis Methods**				
	HEBM	**Wet HEBM**	**Colloidal Synthesis**	**Hydrothermal Synthesis**	**Electrospinning**
NiO			√	√	
$ZnMn_2O_4$	√				√
$ZnFe_2O_4$	√				√
$ZnCr_2O_4$	√				√
$MgMn_2O_4$		√			
$MgFe_2O_4$		√			
$MgCr_2O_4$		√			
$Zn_{1-x}Mn_xFe_2O_4$					√
$ZnFe_{2-y}Cr_yO_4$	√				

3.1.1. High energy ball milling (HEBM)

High energy mechanical milling is a solid state top down approach to prepare 0D fine particles. It is a cheap and facile method to mechanically break down the starting materials, and heat energy applied during annealing process promotes the atomic diffusion to form new material. However, severe agglomeration and wide distribution of

particle size are the common drawbacks of this technique. Besides, elevated temperature is required to initialize the phase formation.[70, 113]

AB_2O_4 samples were prepared by mixing analytical purity ZnO (BDH, AnalaR®) and B_2O_3 (such as, Fe_2O_3 (GCE), Cr_2O_3 (Merck), Mn_2O_3 (Sigma)) at desired stoichiometric ratio as starting materials. High energy ball milling (Spex Sample Preparation Mixer) was conducted in stainless steel vials with stainless steel balls (~5 mm in diameter) for 3 h, ball to powder weight ratio was 4:1. Subsequently, as-milled powder was annealed at 1000 °C for 3 h at ambient conditions to form spinel phase.

3.1.2. Wet high energy ball milling (HEBM)

$MgFe_2O_4$ was prepared by mixing magnesium nitrate ($Mg(NO_3)_2 \cdot 6H_2O$, GCE Laboratory Chemicals), iron nitrate ($Fe(NO_3)_3 \cdot 9H_2O$, Sigma Aldrich) and citric acid monohydrate ($C_6H_8O_7 \cdot H_2O$, GCE Laboratory Chemicals) in 1:2:1 stoichiometric molar ratio. The mixtures were synthesized using HEBM in stainless steel vials with stainless steel balls (~5 mm in diameter) for 30 min, ball to powder weight ratio was 4:1. Resulting ball milled mixture was annealed at 800 °C for 5 h at ambient conditions to form $MgFe_2O_4$ spinels. $MgMn_2O_4$ was synthesized following same steps by using manganese acetate ($Mn(CH_3COO)_3 \cdot 2H_2O$, Sigma Aldrich). As-milled product was heated at 500 °C for 3 h to obtain $MgMn_2O_4$. When $Cr(NO_3)_3 \cdot 9H_2O$ (chromium nitrate nonahydrate, Acros) was used, $MgCr_2O_4$ was obtained after the annealing at 700 °C for 3 h.

3.1.3. Colloidal synthesis

0.5 g of $Ni(C_5H_7O_2)_2$ (nickel acetylacetonate, Sigma Aldrich) was added to 0.5 ml of oleyamine (Sigma), and pre-heated to 200 °C. Subsequently, the solution was placed into the oil bath and further heated for another 2 h to obtain a homogenous and clear solution. This solution was centrifuged in 10 ml of ethanol for 10 min at the rate of 8000 rpm to remove the supernatant liquid. Later on, as-synthesized product was dissolved in 3 ml of hexane and 6 ml of of ethanol, in order to wash off the excessive oleyamine. Centrifugation was conducted at 8000 rpm for 10 min, and these washing steps were repeated for 3 times. NiO colloids were obtained after being dried at 60 °C for overnight. To convert the residual oleyamine into carbon coating, as-prepared NiO colloids were heated at 250 °C for 30 min in air, the heating rate used was 5 °C min^{-1}.

3.1.4. Hydrothermal synthesis

3.6 g of $NiCl_2 \cdot 6H_2O$ (nickel chloride hexahydrate, Sigma Aldrich) was dissolved in 40 ml sodium hydroxide solvent (NaOH, 5M) till a clear solution was obtained. The solution was heated at 180 °C for 12 h inside a 45 ml Teflon-lined autoclave. Subsequently, the products were washed by deionised water for three times and retrieved via centrifugation. After post-annealing at 500 °C for 2 h, NiO plates were produced.

3.1.5. Electrospinning

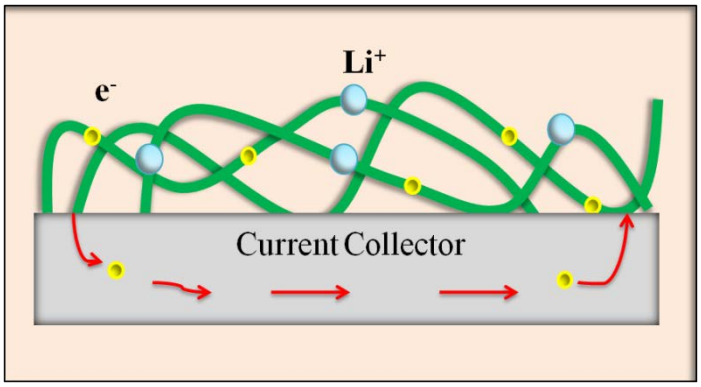

Scheme 3-1 Schematic illustration of nanofibers on copper current collector. Continuous networks provided by 1D nanofibers serve as the diffusion pathway for lithium ions and electrons.

Electrospinning is a relatively simple and cost effective strategy to produce high aspect ratio 1D fibers. Electrospinning technique performs unique ability to produce diverse fibrous arrays with noticeable properties, for instance long lengths, tunable diameters at nano- or meso-levels, high surface area and controllable textures by simply varying the electrospinning parameters such as the applied potential, viscosity and flow rate of the precursor solution.[114] Electrospinning is able to develop disordered network composing of 1D functional nanofibers for LIB application. A facile diffusion pathway and higher surface area are provided by nanofibers for better kinetic.[114] There is also some open pores between the interwoven nanofibers which can effectively buffers the stress associated with any volume change, as well as allow deeper penetration of electrolyte to enhance electrode/electrolyte contact area (Scheme 3-1).[112]

3.1.5.1. Preparation of $ZnMn_2O_4$ nanorods, nanofibers and nanowebs

The $ZnMn_2O_4$ nanorods (ZMO-NR), nanofibers (ZMO-NF) and nanowebs (ZMO-NW) were prepared by electrospinning. Stoichiometric amounts of $Zn(C_5H_7O_2)_2 \cdot xH_2O$ (zinc

acetylacetonate hydrate, Sigma Aldrich) and $Mn(C_5H_7O_2)_3$ (manganese acetylacetonate, Sigma Aldrich) were mixed in 3 ml of acetic acid (Tedia) with vigorous stirring. Poly(vinylpyrolidone) (PVP; Fluka) (molecular weight of 360, 000) was dissolved in absolute ethanol (Sigma Aldrich) to form a 9.5 wt% solution. Subsequently, PVP/ethanol solution was added to metallic precursor/acetic acid solution and vigorously stirred to obtain a homogenous solution.

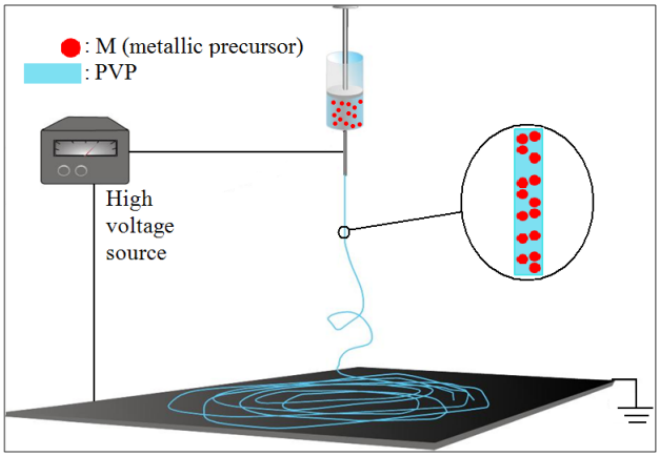

Scheme 3-2 Schematic illustration of electrospinning set up, inset shows magnified details of the as-spun fibers which consist of PVP as the polymer agent and dispersed metallic precursors.

During electrospinning, the precursor solution was connected to a high voltage power supply (Gamma High Voltage Research DC Power Supply) as shown in Scheme 3-2. A positive voltage of 12 kV was applied between the needle tip and grounded aluminium foil collector with a distance of 12 cm. The solution was ejected at a constant flow rate of 1 ml hr^{-1} by computer-controlled syringe pump (Kd Scientific). The as-spun fibers were heated in ambient atmosphere at different sintering temperature profiles (ramp rate, duration and maximum temperature) to acquire $ZnMn_2O_4$ with different morphologies. $ZnMn_2O_4$ nanorods (ZMO-NR) were obtained when the as-spun fibers were heated directly to 400 °C for 2 h with ramp rate of 0.5 °C min^{-1}. $ZnMn_2O_4$ nanofibers (ZMO-NF) were prepared by heating the as-spun fibers to 350 °C at 1 °C min^{-1} and dwelled for 3 h, subsequently ramped up again to 400°C at 0.5 °C min^{-1}, with a dwelling time of 15 min before cooling down to room temperature at 1 °C min^{-1}. When the dwell duration at 350 °C was increased from 3 h to 4 h, $ZnMn_2O_4$ nanowebs (ZMO-NW) were formed.

3.1.5.2. Preparation of $ZnFe_2O_4$ nanorods and nanofibers

Firstly, poly(vinylpyrolidone) (PVP; Fluka) of molecular weight 360, 000 was dissolved in absolute ethanol (Sigma Aldrich) to form a 15 wt% solution. Stoichiometric amounts

of $Zn(CH_3COO)_2 \cdot 2H_2O$ (Sigma Aldrich) and $Fe(NO_3)_3 \cdot 9H_2O$ (Sigma Aldrich) were mixed in 2 ml of deionised water and 0.5 ml of acetic acid (Tedia) with vigorous stirring. After the mixture was stirred for 0.5 h, appropriate amount of PVP/ethanol solution was added and vigorously stirred for 24 h at room temperature to obtain a homogenous solution. Two different precursor solutions were prepared with varying weight ratio of PVP versus metallic precursor (denoted as M) to study the effects of viscosity on the fibrous morphology. To have a fair comparison, weight of metallic precursors were kept constant. Samples were denoted as ZFO-NF ($ZnFe_2O_4$ nanofibers) with PVP:M = 3.93:1 and ZFO-NR ($ZnFe_2O_4$ nanorods) with PVP:M = 5.04:1.

The electrospinning set up was similar to the previous section (Section 3.1.5.1), except a positive voltage of 18 kV was applied and the distance between needle tip and collector was changed to 14 cm. The as-spun fibers were then heated in ambient atmosphere at 450 °C for 2 h. The ramp rate was maintained at 0.5 °C min^{-1}.

3.1.5.3. Preparation of $ZnCr_2O_4$ and $Zn_{1-x}Mn_xFe_2O_4$ nanofibers

Similar experimental procedures were used to prepare $ZnCr_2O_4$ nanofibers (ZCO-NF), simply replacing the $Fe(NO_3)_3 \cdot 9H_2O$ (Sigma Aldrich) by $Cr(NO_3)_3 \cdot 9H_2O$ (Sigma Aldrich).

Similarly, $Zn_{1-x}Mn_xFe_2O_4$ nanofibers ($0 \leq x \leq 1$) were prepared through substituting $Zn(CH_3COO)_2 \cdot 2H_2O$ (Sigma Aldrich) by $Mn(CH_3COO)_2 \cdot 4H_2O$ (Sigma Aldrich). Based on the stoichiometric ratio, the samples were labeled as ZF (x=0), Z7M3 (x=0.3), Z5M5 (x=0.5), Z3M7 (x=0.7) and MF (x=1) accordingly. In order to remove PVP backbone and promote the oxide crystallization, as-spun ZF, Z7M3, Z5M5 and Z3M7 nanofibers were sintered at 450 °C. whereas fully replaced as-spun MF was sintered at 400 °C.

3.2. Characterization Methodologies

3.2.1. Microscopy methods

3.2.1.1. Field emission scanning electron microscope (FESEM)

The surface morphology of the samples was examined by FESEM (JEOL 7600F), with working distance of 6 cm and accelerating voltage of 5 kV. Prior to imaging, the samples were stabilized by carbon tapes on the aluminum sample holder and coated with ~10-15 nm of platinum using a sputtering coater (JEOL JFC-1600).

3.2.1.2. Transmission electron microscope (TEM)

To understand the nanostructured features of synthesized samples, characterization was conducted using JEOL 2100F TEM microscope to exploit the morphological and crystallographic information. Since TEM was operated at 200 kV, shorter wavelength of electron beam than FESEM enables HRTEM images to be captured by interfering with the thin crystals within the samples and resulting in an electron interference patterns at an appropriate defect-of-focus, which can be directly interpreted as projected potential of the crystal structure. This can be useful for structure determination, atomic regularities investigation at atomic scale.[115]

3.2.2. Diffraction methods

3.2.2.1. Powder x-ray diffraction (XRD)

The structural information was characterized by powder XRD (Bruker D8 Advance, Cu Kα radiation, λ = 1.54 Å) with a step size of 0.05°. XRD machine was collimated with a 2.5° soller, 1° divergence and 0.3 mm receiving slits with a scintillation counter and a secondary graphite monochromator. Rietveld refinement was performed using fundamental parameters peak shape profile[116] implemented in TOPAS.[117] A five-coefficient Chebychev polynomial background, a zero error, sample displacement, unit cell parameters, scale factor and crystallite sizes were sequentially refined.

3.2.2.2. Thin film x-ray diffraction (XRD)

The structural information of electrode materials was exploited by thin film XRD (Bruker D8 Discover, Cu Kα radiation, λ = 1.54 Å) with a step size of 0.05°. This XRD machine is collimated 1 mm divergence slit and no receiving slit was used, while a secondary graphite monochromator and a scintillation counter were employed.

3.2.2.3. Synchrotron x-ray diffraction (XRD)

Detailed analysis about crystal structures was also characterized by transmitted XRD at beamline 11-3 in Stanford Synchrotron Radiation Laboratory (SSRL, USA). Diffraction patterns were collected using a MAR345 imaging plate of 345 mm diameter with the exposure time of 30 s at 12.735 keV with the spot size of 200 μm × 200 μm. The obtained data was processed by Area Diffraction Machine Version 1.0.5.

3.2.2.4. Selected area electron diffraction (SAED)

SAED was conducted inside TEM column (Section 3.2.1.2). The principle of electron diffraction in this technique is similar with XRD by adhering to Bragg's law. Due to the extremely short wavelength of highly coherent electron beam in TEM chamber (0.0251 Å), the wave-like electron passes through the lattice plane within the crystal which serve as diffraction grating, eventually resulting in diffraction. This technique provides information of crystal orientation relationships between grains, and it is able to identify the lattice metrics of the crystals.[118]

Samples for SAED were prepared by grinding under ethanol and drops of the resulting suspension deposited on holey-carbon coated copper-grids, and fitted with a low-background Gatan double tilt holder. Simulated images were calculated by the multislice method implemented in *JEMS*[119] and the structure model obtained by Rietveld refinement was used as the input file.

3.2.3. Spectroscopy methods

3.2.3.1. Fourier transform infrared spectroscopy (FTIR)

FTIR spectroscopy detects the molecular absorption and transmission characteristics of a material when exposed to infrared (IR) radiation. Hence, this technique was utilized on the electrospun products to understand the transformation of functional groups before and after sintering at different conditions.[120] For ball milled samples, FTIR was used to investigate the vibration bands of metallic ions in the crystal lattices. Basically, FTIR was carried out on the samples in KBr translucent pellets using Perkin Elmer Spectrum GX in the range of 4000 - 400 cm^{-1} at a resolution of 2 cm^{-1} and scan number of 16.

3.2.3.2. Energy dispersive x-ray spectroscopy (EDS)

Elemental compositions of the samples were analyzed by EDS equipped to FESEM (Section 3.2.1.1) or TEM (Section 3.2.1.2). For EDS-FESEM, working distance of 15 cm and accelerating voltage of 20 kV were selected and scanned on an area of ~50 μm x 50 μm for 10 min to obtain the spectrum. After irradiated by a focused electron beam, ground state electrons in energy level bounded to nucleus absorb the incident energy and escape away from the orbital, leaving behind empty holes. An electron from higher energy shell subsequently fills up the hole and releases the energy difference between

these two discrete shells in the form of a characteristic x-ray. Hence, energy-dispersive spectrometer analyzes the amount and energy values of characteristic x-ray and reveals the elemental composition of a sample.[121]

3.2.3.3. X-ray photoelectron spectroscopy (XPS)

By irradiating the samples with x-ray beam at known energy values, the electrons within the samples absorb energy and escape from the top surface (~10 nm). By measuring the kinetic energy of escaped electrons, the characteristic binding energy values of each element on the top surface layer can be identified. This characteristic binding energy peaks can be correlated to the specific orbitals in the atoms, for instance 1s, 2s, 2p. Hence, XPS provides useful information of elemental composition, chemical states of element, and quantitative amount of each element.[122]

Herein, the chemical states of samples were analysed by using a Kratos AXIS Ultra spectrometer equipped with Al Kα monochromatic radiation. Survey scans were conducted between 0 and 1200 keV calibrated against adventitious carbon at 284.8 eV. Deconvolution and peak fitting were performed with Vision Processing Software using a Voigt function with 30% Lorentzian character and a Shirley background.

3.2.3.4. Electron energy loss spectroscopy (EELS)

EELS was conducted inside TEM chamber. When the samples were exposed to a focused electron beam (200 kV in TEM), a portion of the electron loses their energy due to the inelastic interaction with the atoms within the samples, resulting in randomly deflected beam. By analyzing the amount of energy loss using electron spectrometer, valuable information such as quantitative analysis of valence states, coordination and site symmetry of the atoms experiencing excitation can be obtained.[123]

Currently, Gatan Imaging Filter (GIF) Quantum Spectrometer with an energy resolution of ~1.2 eV was used. The spectra were routinely obtained using a collection half angle of β = 4 mrad collected with an energy dispersion of 0.25 eV per channel under scanning TEM mode.

3.2.3.5. X-ray absorption spectroscopy (XAS)

Above mentioned diffraction techniques characterises the materials from a macroscopic perspective, *i.e.* average structural information concerning whole specimen. On the other hand, XAS provides reliable information of a localised site within materials. Gathering the oscillations aroused from the interference of an ejected photoelectron wave and backscattered wave from the neighboring absorbing atom, the corresponding energy edges and relative intensities can be analyzed to understand the metal site symmetry, valence state and the local coordination environment.[124-126]

XAS measurement was performed at beamline 20A at the National Synchrotron Radiation Research Center in Taiwan. The spherical grating monochromator provides the range from 60 eV to 1250 eV with the average resolving power of 5000. The highly dense TMO powder was pressed onto indium foil to improve the electrical contact and subsequently transferred into the chamber at high vacuum condition (pressure = ~5 $\times$ 10^{-9} torr). All XAS spectra were collected by the total electron yield (TEY) treatment and normalized against the background intensity at the post-edge range to be unity.

3.2.4. Porosity measurement

The Brunauer-Emmett-Teller (BET) surface area of the samples were recorded using Micromeritics, ASAP 2020 by N_2 adsorption-desorption isotherms at 77 K. Before to the measurement, the samples were degassed at 393 K under nitrogen flow for 6-12 h.

3.2.5. Viscosity measurement

The viscosity of electrospinning precursor solution was measured by using a rotational automated rheometer (Anton Paar, Physical MCR 501) at 298 K, for shear rate between 2 and 100 s^{-1}. Rotating plates with a diameter of 49.914 mm (CP50-1/TG) was used.

3.2.6. Thermal analysis

3.2.6.1. Thermogravimetric analysis (TGA)

TGA was performed by using TA Instrument Q500 by heating the samples (~30-50 mg) from room temperature to target temperature under air at a ramp rate of 10 °C min^{-1}, with 40% air as sample gas and 60% nitrogen as balance gas.

3.2.6.2. Differential calorimetric studies (DSC)

Thermal analysis was also performed by DSC using Research Instrucment DSC Q10 under nitrogen atmosphere at the heating rate of 10°C min^{-1}

3.3. Electrochemical Studies

3.3.1. 2016 coin cell fabrication

The electrochemical performances of TMOs were evaluated in a 2016-coin cell. The electrodes were prepared by mixing 60 wt% of active materials, 20 wt% of binder (Kynar) and 20 wt% of Super P (Timcal) in solvent, N-methyl-pyrrolidinone (NMP, Sigma Aldrich) to form a homogenous slurry. The slurry was coated on etched copper foil by doctor blade technique (thickness ~ 25-40 µm) and dried at 80 °C in vacuum oven for 12 h. Subsequently, the coating was pressed between twin rollers to improve the adhesion between copper foil and active materials. The electrodes were cut into circular disks with the diameter of 16 mm, each disk contains ~3-5 mg of active materials. The electrodes were assembled in an argon filled glovebox (MBraun, Germany) with oxygen and water content less than 1 ppm. Lithium metal served as a counter electrode, Celgard 2400 as the separator and 1 M solution of $LiPF_6$ dissolved in ethylene carbonate/diethylene carbonate (EC:DEC = 1:1 by volume, Charslton Technologies Pte Ltd.) was used as electrolyte.

3.3.2. Cyclic voltammetry

The cyclic voltammetry (CV) measurements were conducted using CHI Model 1000A or Solartron 1470E in the voltage window of 0.005 - 3.0 V at room temperature with a constant scanning rate of either 0.05 mV s^{-1} or 0.1 mV s^{-1}, depends on the respective purposes. In this context, cathodic peaks indicate the presence of reduction reaction (lithium insertion) with lithium metal as reference electrode, whereas anodic peaks can be designated as oxidation reaction (lithium extraction process).

3.3.3. Galvanostatic cycling

Based on the convention in LIB research aspect, all the potential/working voltages mentioned in this thesis uses lithium metal as counter and reference electrode (Li^+/Li_0, E^0 with respect to H^+/H_0 (SHE) = -3.04 V). The lithium storage properties of samples were

examined by galvanostatic cycling (Multichannel Battery Tester, Neware Technology Limited) in the voltage window of 0.005 - 3.0 V at room temperature, under a current density of 60 mA g^{-1}. In this context, discharge curve represents the lithium insertion process, whereas lithium extraction behavior is expressed by charge curve.

3.3.4. Impedance spectroscopy

Electrochemical impedance spectroscopy (EIS) can derive the electrical and ionic resistance of a sample by changing applied frequency of altering current (AC).[127]

In current study, EIS was carried out on both of the bare electrodes and cycled electrodes. Prior the EIS measurement, the cells were also galvanostatically discharged/charged at 60 mA g^{-1} to a specific cutoff voltage and applied potentiostat for 2 h. Subsequently, EIS was measured in the range of 100 MHz–0.1 Hz by using the bias voltage of 10 mV. The data was shown in the form of Nyquist plots (Z′ vs –Z″, where Z′ and Z″ are the real and imaginary parts of complex impedance) and an equivalent circuit to describe the electrochemical behaviour was suggested in the discussion.

3.3.5. *Ex situ* electrode preparation

For *ex situ* characterization using XRD (Section 3.2.2.2 and 3.2.2.3), electrodes were retrieved by disassembling the coin cells and rinsed them with sufficient DEC to remove the organic electrolyte. The electrodes were kept dry in glovebox for at least 3 days before the characterization and sealed in an air tight container while transportation.

For *ex situ* characterization using TEM, SAED or EELS, active material was peeled off from the current collector and rinsed with DEC in glovebox. It was ground into finer particles and ultrasonicated until homogenous solution was achieved before dipping onto the TEM grids. EDS analysis (Section 3.2.1.2) was also conducted (equipped to TEM JEOL-2100F) on a respective region to confirm that the observation is on the active material, instead of Super P before collecting the SAED (Section 3.2.2.4) or EELS (Section 3.2.3.4) results.

Chapter 4 Results

This chapter presents results of all the experiments conducted in this thesis. Both characterization and electrochemical data were detailed. First of all, NiO with different sizes and morphologies was explored to verify the feasibility in implementing nanomaterials as commercial LIB anode. Subsequently, several TMOs ($ZnMn_2O_4$, $ZnFe_2O_4$, $ZnCr_2O_4$) nanofibers, nanorods or nanowebs prepared by electrospinning technique are shown. Nanofibers exhibited highest capacity retention, and thus a solid solution of $Zn_{1-x}Mn_xFe_2O_4$ to investigate the impact of counter ion toward Fe^{3+}.

To continue the effort in understanding the influence of cation substitution in spinel-based anodes, highly crystalline TMOs were also synthesized by HEBM to acquire better quality of structural information and correlate with their electrochemical properties.

4.1. NiO

Despite the various positive contributions given by nanomaterials (Section 2.5), excessive surface area may significantly increase the interfacial layer between the organic electrolyte and electrodes. It may catalyze the electrolyte decomposition to gain the chemical equilibrium between the interfaces, inevitably creating greater amount of side reactions (thick SEI formation and electrolyte decomposition) and causing poor reversibility during cycling.[22] In addition, nanomaterials have lower volume density and thus bringing down the mass loading of active materials per electrode as compared to the micro-sized TMOs with fixed electrode thickness.

This section aims to study the optimum particle size and mass loading to be beneficial in LIB anode application. Hence, NiO with different particle sizes were prepared by two synthesis methods, while commercial NiO was used as reference material. NiO was chosen because its commercial powder is widely available in commercial market, unlike AB_2O_4 spinels-based TMOs. However, the data obtained here can be universally applied on any TMOs anode.

4.1.1. Variation of NiO particle size by using different synthesis methods

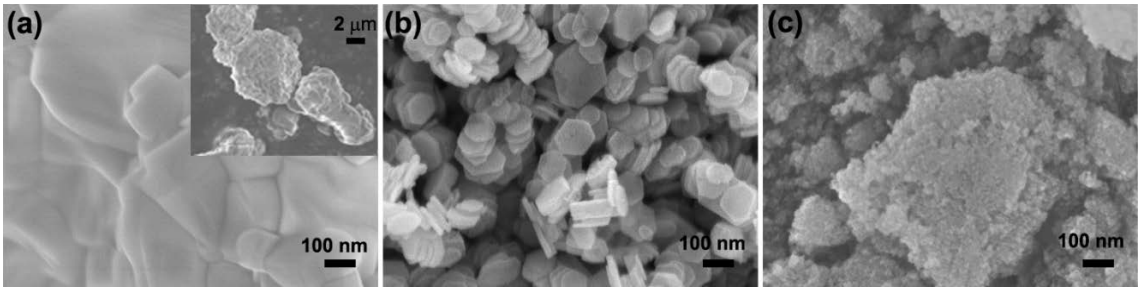

Figure 4-1 NiO with different morphologies. (a) The commercial NiO (Alfa Aesar) was used as reference material. NiO samples prepared by (b) hydrothermal method (denoted as NiO plates) and (c) colloidal synthesis (denoted as NiO colloids), respectively.

NiO samples synthesized by different methods show diversified morphology and particle size (Figure 4-1). NiO plates prepared by hydrothermal method formed the nanoplates with ~100 nm diameter. On the other hand, NiO colloids in the range of 10-20 nm were prepared by colloidal synthesis with oleylamine as stabilizer in the synthesis to control the size and shape of nanoparticles. Briefly, the presence of excess oleylamine in the hexane environment formed weaker bonds on the nanoparticles surface, thus restricting the nucleation and growth direction to form spherical nanocolloids.[4, 12] The commercial NiO powders purchased from Alfa Aesar were found to be larger than 2 μm. XRD was undertaken to confirm the single phase NiO formation (space group: $Fd\bar{3}m$) in three samples without any impurities. The peak broadening was observed in NiO plates and colloids, implying the existence of fine nanocrystals.

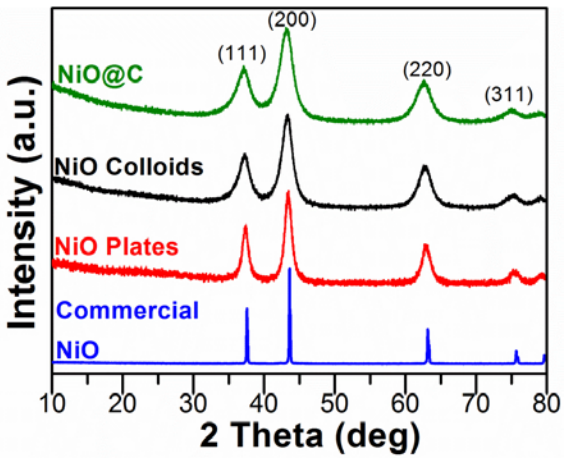

Figure 4-2 XRD patterns of NiO samples. NiO plates and colloids were proven to have same phases as commercial NiO (Alfa Aesar). NiO@C was annealed in air atmosphere to obtain carbon coating, however the NiO phase reserved after the heat treatment.

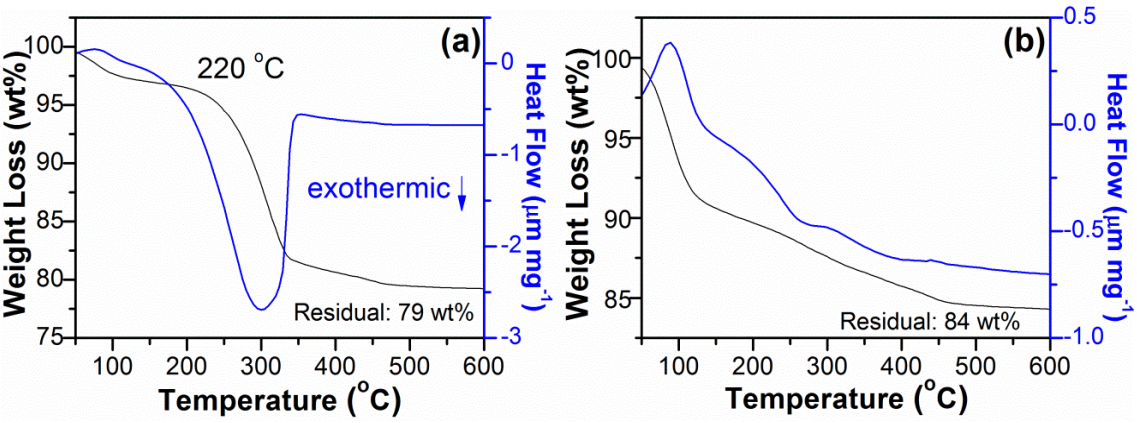

Figure 4-3 TGA and DSC of NiO samples: (a) as-prepared NiO colloids and (b) NiO@C obtained after heat treated NiO colloids in air atmosphere for 30 min.

TGA and DSC were conducted on as-prepared NiO colloids to understand the removal process of oleylamine. The weight loss below 100 °C was assigned as the evaporation process of trapped moisture on the nanocolloids with excessive surface area (Figure 4-3(a)). There is an exothermic process occurred at ~220 °C associated with a weight loss of ~18 wt%, which can be ascribed to the removal of residual oleylamine. This residual was then utilized as the source to form carbon coating by heating as-prepared NiO colloids at 250 °C in air atmosphere for 30 min (heating rate = 5 K min^{-1}). A colour transition from dark green to dark brown was observed. TGA and DSC were again recorded and no exothermic peak was noticed (Figure 4-3(b)), indicating the residual oleylamine was fully converted to the carbon coating. This sample was denoted as NiO@C and the XRD pattern depicts the preservation of single phase NiO.

4.1.2. Impact of particle size on electrochemical performance of NiO

Cycling of NiO samples at 0.05C and 0.1C (C rate: discharging/charging rate of a battery, 0.1C or 0.05C means discharge/charge to full capacity in 10 h or 20 h, respectively) was shown in Figure 4-4. NiO achieved better capacity at a lower C rate or when particle size was reduced. NiO@C exhibits highest capacity as carbon coating has been widely reported as a conductive pathway for lithium ions to enhance the battery efficiency.[43] Figure 4-5 displays the long term cycling performance of all NiO samples at 0.1C to elucidate the cyclability. Surprisingly, commercial NiO with largest particle size maintained highest reversible capacity after 30 cycles, despite its lowest initial capacity. After 5^{th} cycle, other NiO samples suffered from severe capacity depletion to less than 150 mAh g^{-1}. The explanation of these circumstances will be done in Section 5.1.

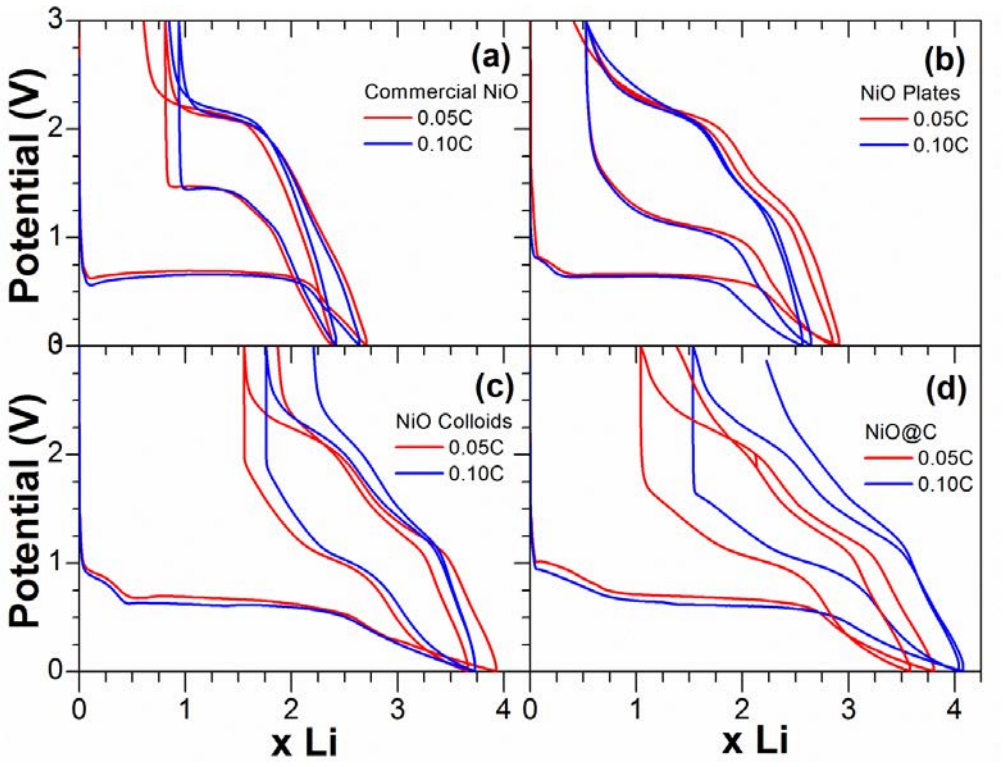

Figure 4-4 First and second discharge/charge cycles of NiO samples. (a) Commercial NiO, (b) NiO plates, (c) NiO colloids and (d) NiO@C at C rates of 0.05C and 0.1C respectively.

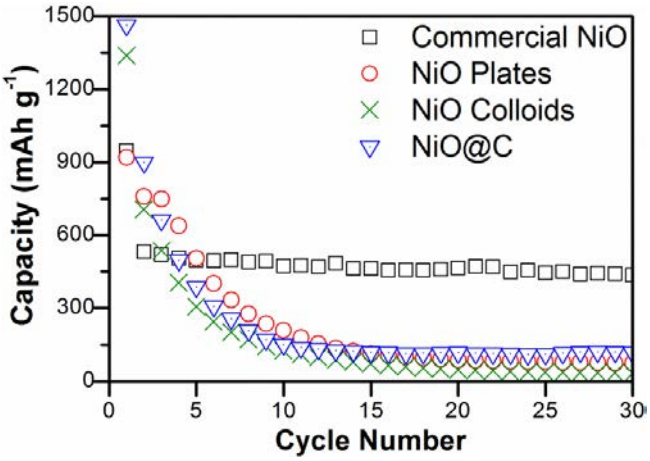

Figure 4-5 Cyclability of NiO samples at 0.1C.

4.2. Electrospun TMOs

By altering the experimental conditions (heat treatment profile, viscosity of precursor solution), electrospinning is able to produce different nanostructured architectures. Therefore, results of electrospun $ZnMn_2O_4$, $ZnFe_2O_4$ and $ZnCr_2O_4$ spinels with different morphologies (nanofibers, nanorods and nanowebs) are shown in this section. $ZnFe_2O_4$ delivers promising battery performance and subsequently a solid solution of Zn_{1-}

$_xMn_xFe_2O_4$ was prepared, with the purpose to investigate the impact of A-site substitution in AB_2O_4 spinels on structural aspect.

4.2.1. Electrospun $ZnMn_2O_4$ nanorods, nanofibers and nanowebs: Impact of sintering profiles of surface morphology[1]

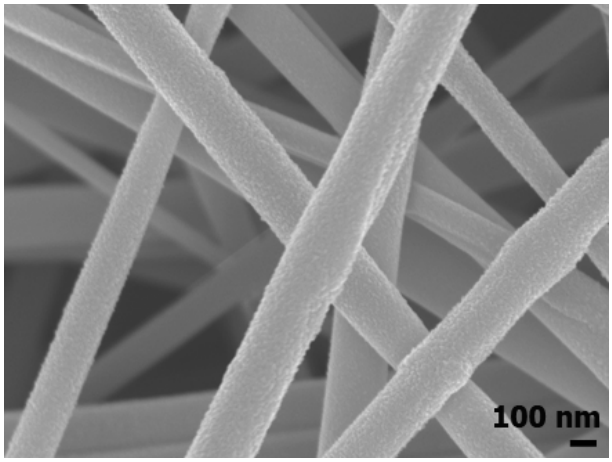

Figure 4-6 FESEM images of high aspect ratio as-spun nanofibers with diameters of 150-220 nm. (Reproduced by permission of The Royal Society of Chemistry)

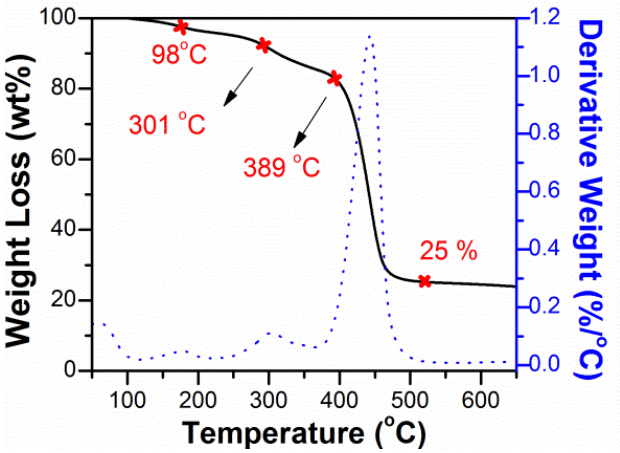

Figure 4-7 TGA of as-spun nanofibers conducted in air from room temperature to 650 °C. (Reproduced by permission of The Royal Society of Chemistry)

As-spun nanofibers made up by PVP, metallic precursor and some volatile solvent are in high aspect ratio with uniform diameter of ~150-220 nm (Figure 4-6). A post heat treatment is required to remove PVP, as well as to convert the metallic precursor into their respective oxides. As a result, TGA was conducted on as-spun nanofibers to interpret its decomposition behavior as a function of temperature (Figure 4-7). The weight

[1] Reproduced by permission of The Royal Society of Chemistry.

loss of 2 % below 100 °C belongs to the evaporation of volatile species, such as acetic acid, trapped moisture or residual ethanol. The second peak starting at 301 °C corresponds to the decomposition of metallic precursors, namely manganese acetylacetonate and zinc acetylacetonate. The prominent weight loss at 389 °C indicates the onset of PVP backbone removal, which is the main constituent in the as-spun nanofibers. The weight stabilizes at ~25 % after ~460 °C, indicating the completion of chemical reactions. TGA provides an important guideline to design the sintering temperature profile, so 400 °C was chosen as maximum sintering temperature.

Three different sintering conditions (Figure 4-8(a)-(c)) were employed to tune the mechanical integrity of sintered products leading to the formation of $ZnMn_2O_4$ nanorods (ZMO-NR), nanofibers (ZMO-NF) and nanowebs (ZMO-NW) (Figure 4-8(d)-(f)).

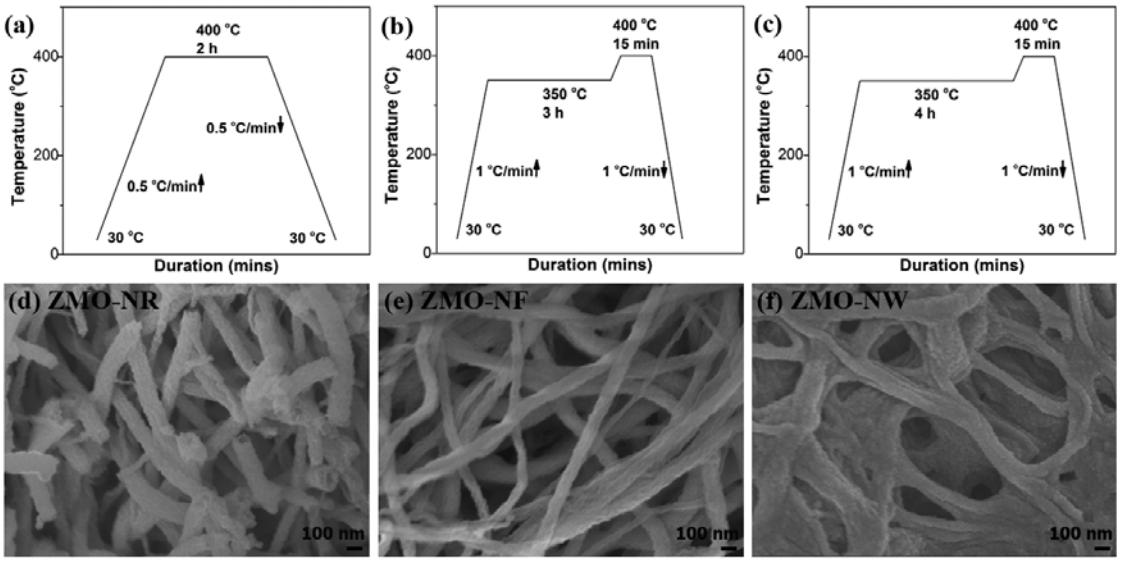

Figure 4-8 Temperature profiles used in sintering of as-spun nanofibers are illustrated in (a), (b) and (c). 1-step sintering (a) resulted in the formation of (d) ZMO-NR, 2-step sintering formed (e) ZMO-NF. Excessive carbonization step caused the formation of (f) ZMO-NW. (Reproduced by permission of The Royal Society of Chemistry)

1-step sintering (Figure 4-8(a)) was commonly employed as post heat treatment after electrospinning,[128] but it often led to rupturing of the fibrous morphology after PVP backbone disappeared, thence breaking down into some irregular shapes.[114, 129] A critically low heating/cooling rate was required to prevent this destruction, at the expense of extra energy and time costs.[114, 129] This circumstance was also noticed in the formation of nanorods (ZMO-NR, Figure 4-8(d)) after a direct sintering at 400 °C for 2 h.

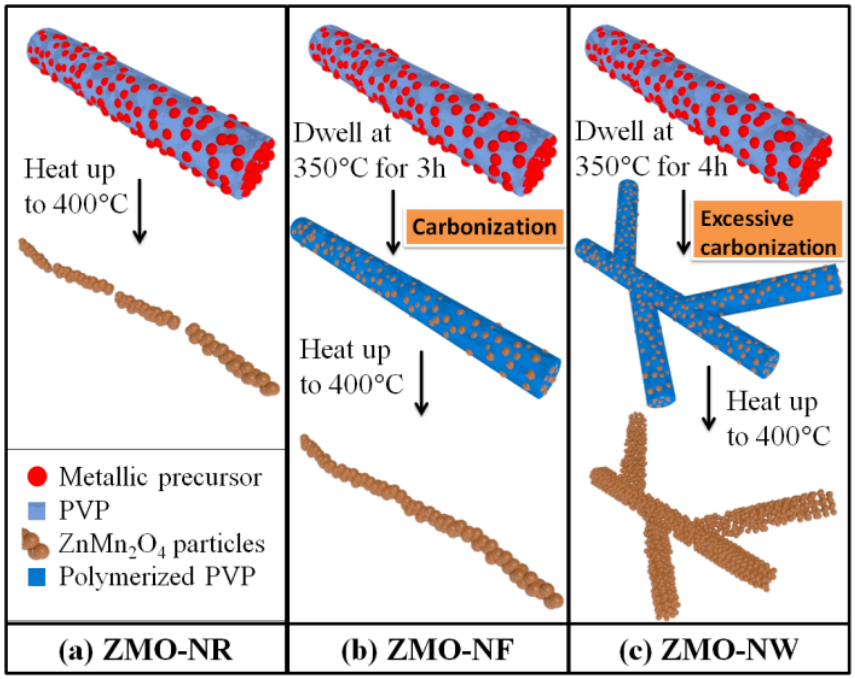

Scheme 4-1 Schematic representation of formation mechanism of $ZnMn_2O_4$. (a) 1-step sintering to produce ZMO-NR, (b) 2-steps sintering with the addition of carbonization at 350 °C to yield ZMO-NF, and (c) ZMO-NW formed after longer carbonization process of 4 h. (Reproduced by permission of The Royal Society of Chemistry)

Scheme 4-1(a) schematically explains that as-spun nanofibers are unable to accommodate the sudden volumetric change upon the removal of polymer backbone and disassembling into nanorods. Herein, a 2-step sintering was introduced (Figure 4-8(b)) by firstly heating the as-spun nanofibers at 350 °C for 3 h to allow PVP carbonization process. 350 °C was chosen as it is lower than the PVP decomposition temperature at 389 °C, so carbonization step causes the gradual shrinkage of fiber diameter to ~100-150 nm (Figure 4-9) that brings the metallic precursors closer within the fibers (Scheme 4-1(b)). Hence, the nanofibers posses better mechanical integrity during PVP removal process at 400 °C and formed ZMO-NF (Figure 4-8(e)). It is worth noting that the heating rate applied on ZMO-NF (1 °C min^{-1}) is two times that used for ZMO-NR (0.5 °C min^{-1}), despite the fibrous morphology was retained and energy cost was reduced. The diameters of sintered ZMO-NF are thinner (80-130 nm) than as-spun fiber (Figure 4-6) after the disappearance of organic component. Individual nanofibers are interwoven to form a network with open pores, which could not be observed in relatively short ZMO-NR. By prolonging the duration of carbonization to 4 h, merging of as-spun fibers into interlinked nanostructures (Scheme 4-1(c)) was greatly promoted, forming nanowebs (ZMO-NW) (Figure 4-8(f)). ZMO-NW has relatively lesser open pores than ZMO-NF due to the coalescence. So, nanostructures of electrospun products can be tuned by altering the sintering conditions.

Further increasing the sintering temperature or extending the carbonization duration causes the breakage of nanofibers and/or diminishment of open pores.

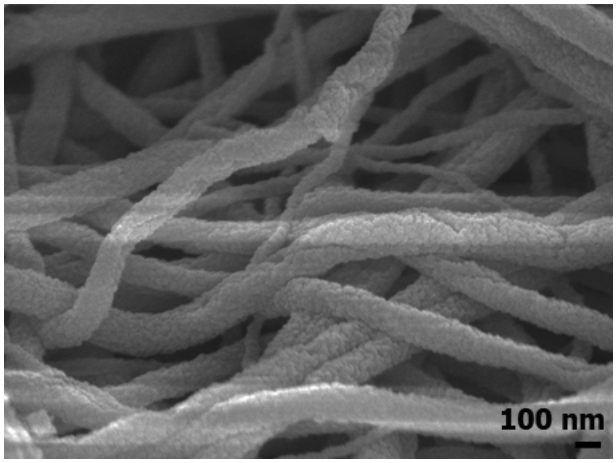

Figure 4-9 FESEM micrographs of nanofibers carbonized at 350 °C, the diameter of nanofibers (~100-150 nm) is relatively smaller than as-spun fibers. (Reproduced by permission of The Royal Society of Chemistry)

4.2.2. Electrospun $ZnMn_2O_4$ nanorods, nanofibers and nanowebs: Materials characterization[2]

Transformation of functional groups by sintering at different heating conditions was investigated by FTIR spectroscopy (Figure 4-10). PVP and as-spun nanofibers have remarkably identical vibration bands, as the main component of as-spun fibers is the PVP backbone.[27] Broad band at ~3439 cm^{-1} suggests the existence of O-H stretching vibration from adsorbed water molecules or moisture. Two neighboring peaks at ~2959 cm^{-1} and ~2874 cm^{-1} represent asymmetric stretching of CH_2 and C-H stretching from PVP. Vibration band at 1663 cm^{-1} correlates to either C=O or C–N functional groups, while CH_2 scissoring and wagging were noted at 1452 cm^{-1} and 1267 cm^{-1}, respectively. All these PVP functional groups disappeared after carbonization, in addition, a new vibration band was found at 1629 cm^{-1} that repeatedly appeared in ZMO-NR, ZMO-NF and ZMO-NW (Figure 4-10(c)-(e)). This peak was almost negligible when as-spun nanofibers were heated up to 650 °C (Figure 4-10(f)), so it may be the organic ligands converted from carbonized PVP, *eg.* C=C or carbonyl derivative (x-C=O-y) with specific coordination environment (x and y: different functional groups).[120, 130] Another peak at ~1130 cm^{-1} can be interpreted as C-O stretching presented in all sintered samples.[120]

[2] Reproduced by permission of The Royal Society of Chemistry.

Vibration bands at ~630 cm^{-1} and ~516 cm^{-1} indicates metal-oxygen stretching bond with increasing intensity at 650 °C, so this proves the formation of $ZnMn_2O_4$ oxide.

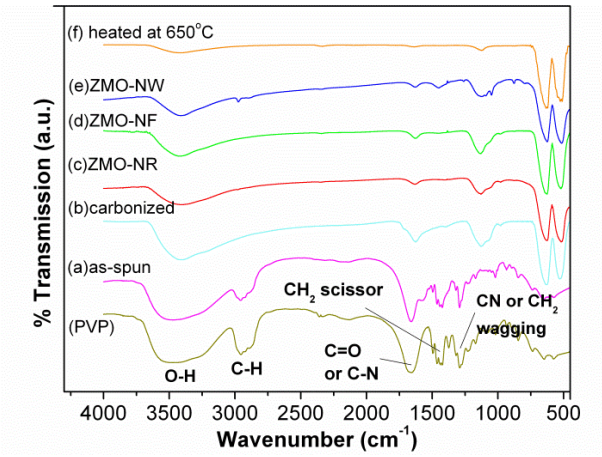

Figure 4-10 FTIR analysis in $ZnMn_2O_4$ formation. (a) As-spun, (b) carbonized nanofibers heated at 350 °C, (c) ZMO-NR, (d) ZMO-NF, (e) ZMO-NW and (f) nanofibers heated to 650 °C. FTIR of PVP was also included. (Reproduced by permission of The Royal Society of Chemistry)

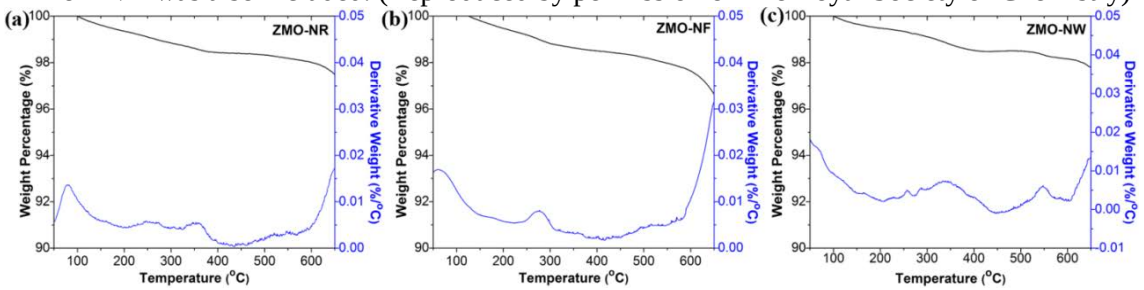

Figure 4-11 TGA of sintered $ZnMn_2O_4$ to measure PVP residual content by re-heating all samples to 650 °C at ambient condition. (a) ZMO-NR, (b) ZMO-NF and (c) ZMO-NW. (Reproduced by permission of The Royal Society of Chemistry)

Maximum sintering temperature (400 °C) is not sufficient to fully decompose PVP, TGA quantifies the weight percentage of carbonaceous residuals to be less than 4 wt% in all cases (Figure 4-11). Such a tiny amount has negligible influence on battery performance.

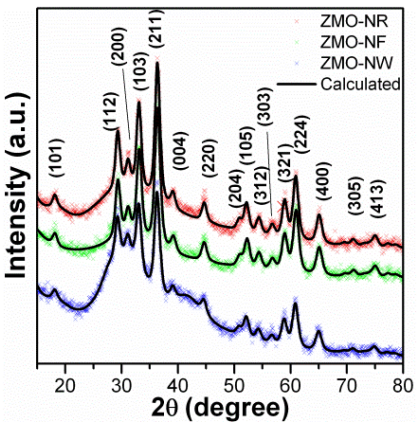

Figure 4-12 XRD patterns and Rietveld refinements of ZMO-NR, ZMO-NF and ZMO-NW.

XRD patterns (Figure 4-12) ensure the formation of tetragonal phase $ZnMn_2O_4$ spinel with space group of $I4_1/amd$ (identical with ICSD code 15305), since Mn^{3+} is a Jahn Teller ions.[131] The structural information of $ZnMn_2O_4$, including lattice parameters and crystallite sizes were refined by Rietveld method and tabulated in Table 4-1. A slight variation on lattice parameters may due to different sintering conditions (Section 4.2.1). Due to the fact that spinel crystal structure is destroyed and amorphized after first discharge conversion reaction, initial lattice parameters of spinel may be assumed to have least impact on long term cycling. Besides, three samples have comparable crystallite size as being confirmed by Rietveld refinement (Table 4-1), as well as the size distribution plots obtained by manual measurement of nanocrystals in HRTEM image (Figure 4-13).

Table 4-1 Lattice parameters and crystallite sizes of $ZnMn_2O_4$ computed by Rietveld refinement and the actual nanocrystals size measured by HRTEM.

Sample	Lattice parameters		Crystallite size (nm)	Nanocrystal Size (nm)
	a (Å)	c (Å)		
ZMO-NR	5.719(2)	9.171(5)	6.7(1)	9(2)
ZMO-NF	5.726(2)	9.186(3)	6.5(1)	9(2)
ZMO-NW	5.733(2)	9.193(4)	6.5(1)	9(1)

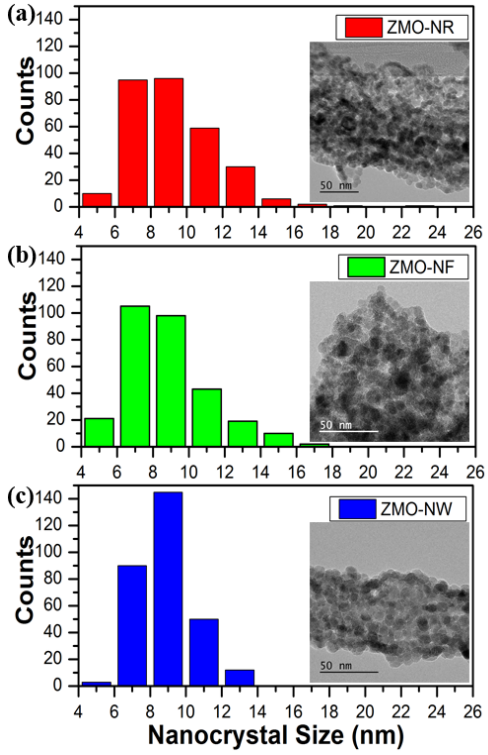

Figure 4-13 Size distribution of nanocrystals in ZMO-NR, ZMO-NF and ZMO-NW compiled by measuring 300 nanocrystals in HRTEM images (inset in the histograms) of different regions within the samples, the numeric results were tabulated in Table 4-1. (Reproduced by permission of The Royal Society of Chemistry)

The chemical state analysis of all pristine powders were recorded by XPS. The spectra of Zn (Figure 4-14(a)) comprises two peaks at ~1043.2 eV and ~1020.2 eV, corresponding $2p_{1/2}$ and $2p_{3/2}$.[132] Besides, Mn $2p_{1/2}$ and $2p_{3/2}$ were observed at ~652.7 eV and ~641.3 eV, respectively.[133] These values were found to be identical to the previous reports, so XPS analysis depicts the oxidation states in three samples to be Zn^{2+} and Mn^{3+}.

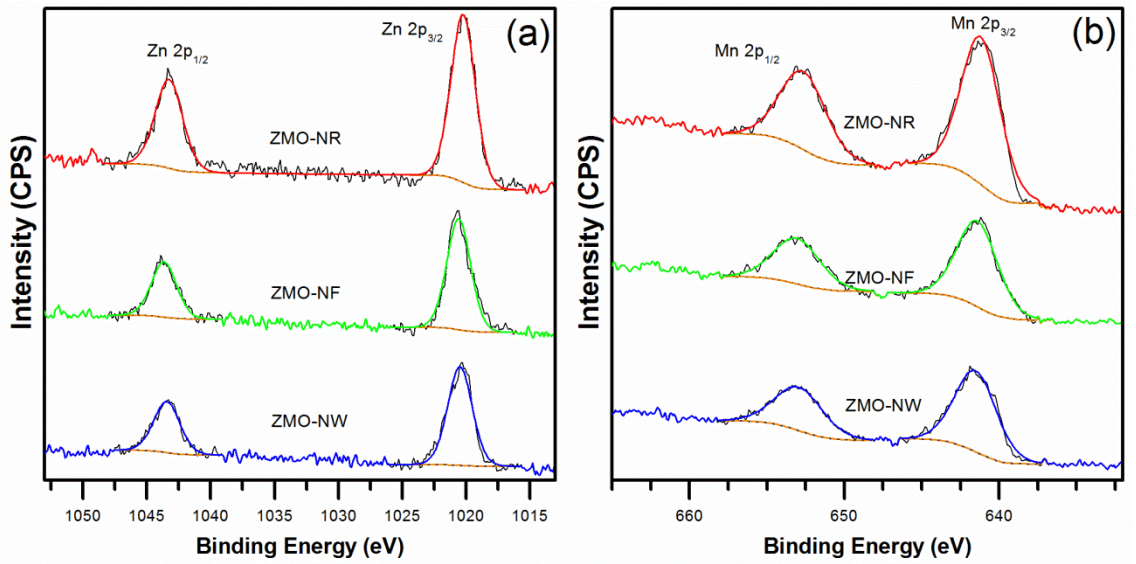

Figure 4-14 Zn and Mn XPS multiplex scans of ZMO-NR, ZMO-NF and ZMO-NW. (Reproduced by permission of The Royal Society of Chemistry)

4.2.3. Electrospun $ZnMn_2O_4$ nanorods, nanofibers and nanowebs: Comparison of electrochemical performance[3]

Reduction (lithium insertion) and oxidation (lithium extraction) peaks of CV of $ZnMn_2O_4$ samples were apparently identical regardless of the morphology. The first cathodic scan (Figure 4-15(a)) shows an extremely mild reduction peak at ~1.4 V and this peak was absent in 2nd and 5th cycles, which may be ascribed to the intercalation of lithium ions into spinel structure which was also observed in $ZnFe_2O_4$,[9, 85] however, this is the first time being reported in $ZnMn_2O_4$ spinel. Another small hump at ~0.7 V correlates to the irreversible decomposition of electrolyte to form SEI layer. Most intense peak at ~0.25 V represents the conversion reaction of $ZnMn_2O_4$ spinel into Zn and Mn metallic nanograins dispersed in Li_2O matrix.[53, 96] So, $ZnMn_2O_4$ spinel was thoroughly amorphized and hence the first CV curve was evidently distinguishable from the remaining cycles. In the

[3] Reproduced by permission of The Royal Society of Chemistry.

reverse anodic sweep, two oxidation peaks were observed at ~1.2 V and ~1.6 V respectively, corresponding to re-oxidation of Mn to MnO and Zn to ZnO.[53, 54, 97]

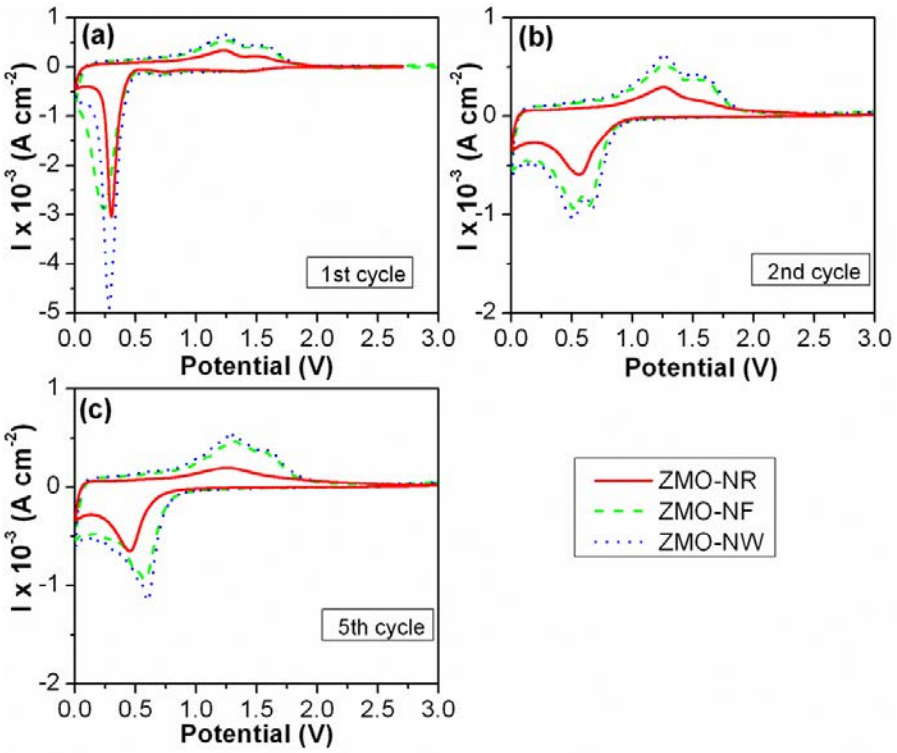

Figure 4-15 CV of ZMO-NR, ZMO-NF and ZMO-NW at 0.1 mV s^{-1}, (a) 1st cycle, (b) 2nd cycle and (c) 5th cycle.

At second cycle (Figure 4-15(b)), two coupled redox peaks were observed as reduction/oxidation of ZnO and MnO at ~0.65/1.6 V and ~0.5/1.3 V for ZMO-NF and ZMO-NW, respectively.[49] However, it was not recognizable in ZMO-NR, as there was only a single redox pair at ~0.6 V and ~1.3 V. At 5th CV cycle of ZMO-NF and ZMO-NW, reduction peaks of ZnO and MnO merged and appeared as a single peak at ~0.6 V, but their oxidation peaks were still resolvable.

The galvanostatic discharging/charging curves of 1st cycle were displayed for comparison (Figure 4-16). The first discharge (lithium insertion) capacity of ZMO-NF and ZMO-NW were similar, *i.e.* 1469 mAh g^{-1} and 1526 mAh g^{-1} respectively, corresponding to ~13 mole of lithium ions per unit formula of $ZnMn_2O_4$. Among three morphologies, ZMO-NR has lowest first discharge capacity of 1257 mAh g^{-1} (~11 mole of lithium ions). However, it was found that all three samples express similar discharge behavior when looking closely into the first discharge curve, especially in the capacity range of 0-200 mAh g^{-1} (~1.8 mole of lithium ions). A short plateau at ~1.4 V was considered as lithium intercalation into spinels, whereas electrolyte decomposed at ~0.75 V. Subsequently,

conversion reaction occurred at ~0.49 V and represented by a long characteristic plateau. ZMO-NF and ZMO-NW surpassed ZMO-NR by taking in extra ~2 mole lithium ions during conversion reaction, indicating that the battery efficiency depends on the morphology of host materials. Above observation matches well with their CV scans (Figure 4-15). At the first charge (lithium extraction), capacities of ZMO-NR, ZMO-NF and ZMO-NW rapidly leveled off to ~680 mAh g^{-1}, ~716 mAh g^{-1} and 891 mAh g^{-1} mainly explained by the irreversible SEI formation [25, 27] and the conversion of spinel ($ZnMn_2O_4$) into binary oxides (ZnO , MnO and Mn_2O_3).[53, 54, 95, 98]

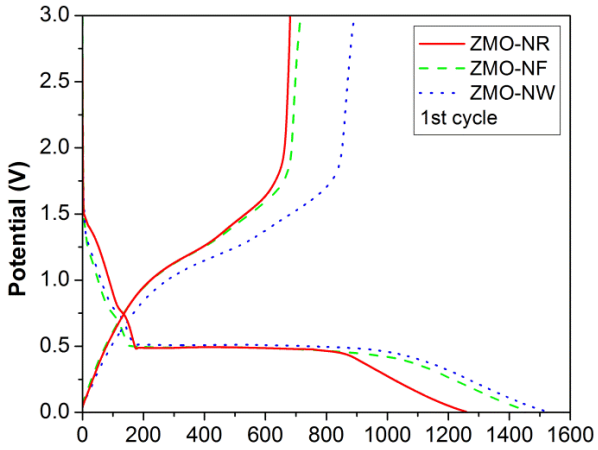

Figure 4-16 First galvanostatic cycling of (a) ZMO-NR, (b) ZMO-NF and (c) ZMO-NW at 60 mA g^{-1}. (Reproduced by permission of The Royal Society of Chemistry)

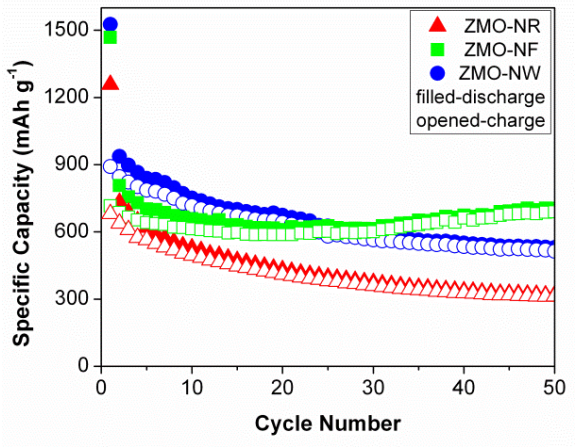

Figure 4-17 Cycling performance of $ZnMn_2O_4$ with different morphologies at 60 mA g^{-1}. (Reproduced by permission of The Royal Society of Chemistry)

At 50th cycles, ZMO-NR exhibited worst storage ability of ~318 mAh g^{-1} (~2.8 mole of lithium ions) (Figure 4-17). The cyclability of ZMO-NW was greater than ZMO-NF during initial 25 cycles, however the capacity declined to ~530 mAh g^{-1} (~4.7 mole of lithium ions) at 50th cycles. ZMO-NF demonstrated the best performance among three morphologies by maintaining at ~705 mAh g^{-1} (~6.3 mole of lithium ions).

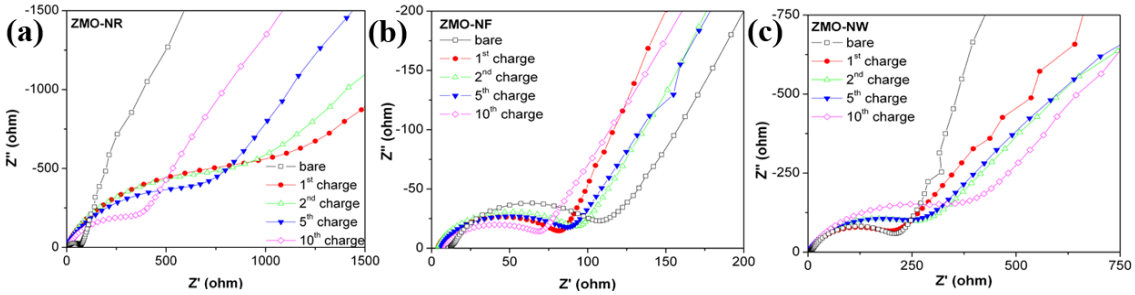

Figure 4-18 Nyquist plots for (a) ZMO-NR, (b) ZMO-NF and (c) ZMO-NW. (Reproduced by permission of The Royal Society of Chemistry)

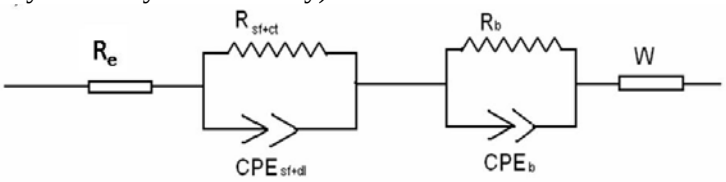

Figure 4-19 Equivalent circuit used to fit the Nyquist plot (Figure 4-18). The circuit elements are denoted as electrolyte resistance (R_e), impedance of inseparable surface film and charge transfer ($R_{(sf+ct)}$), constant phase elements ($CPE_{(sf+dl)}$, dl: double layer), bulk impedance (R_b) and the Warburg impedance (W). (Reproduced by permission of The Royal Society of Chemistry)

Figure 4-18 shows the EIS of bare electrodes, as well as the charged electrodes at 2nd, 5th and 10th cycles. Experimental data was analyzed by fitting with an equivalent electrical circuit in Figure 4-19, similar to the model employed in other literatures.[30, 134, 135]

All bare electrodes under OCV comprised a depressed semi-circle at high frequencies in their Nyquist plots (Figure 4-18). So, the spectra was firstly fitted to a single semicircle attributed by charge transfer and surface film formation ($R_{(sf+ct)}$ and $CPE_{(sf+dl)}$). CPEs were used instead of pure capacitors due to the existence of depressed semi-circles which suggested the deviation from ideal behavior of a capacitor. Warburg-type behaviour was noticed at low frequency region and expressed by symbol W in the equivalent circuit. The fitted values were tabulated in Table 5-4 (Section 5.1.3).

4.2.4. Electrospun $ZnFe_2O_4$ nanorods and nanofibers: Impact of precursor solution viscosity on surface morphology[4]

Since Section 4.2.1 presented the impact of sintering conditions on electrospun $ZnMn_2O_4$ nanostructures. This section will further investigate the relationship between viscosity of precursor solution and obtained morphologies of $ZnFe_2O_4$ samples.

[4] Reproduced by permission of The Royal Society of Chemistry.

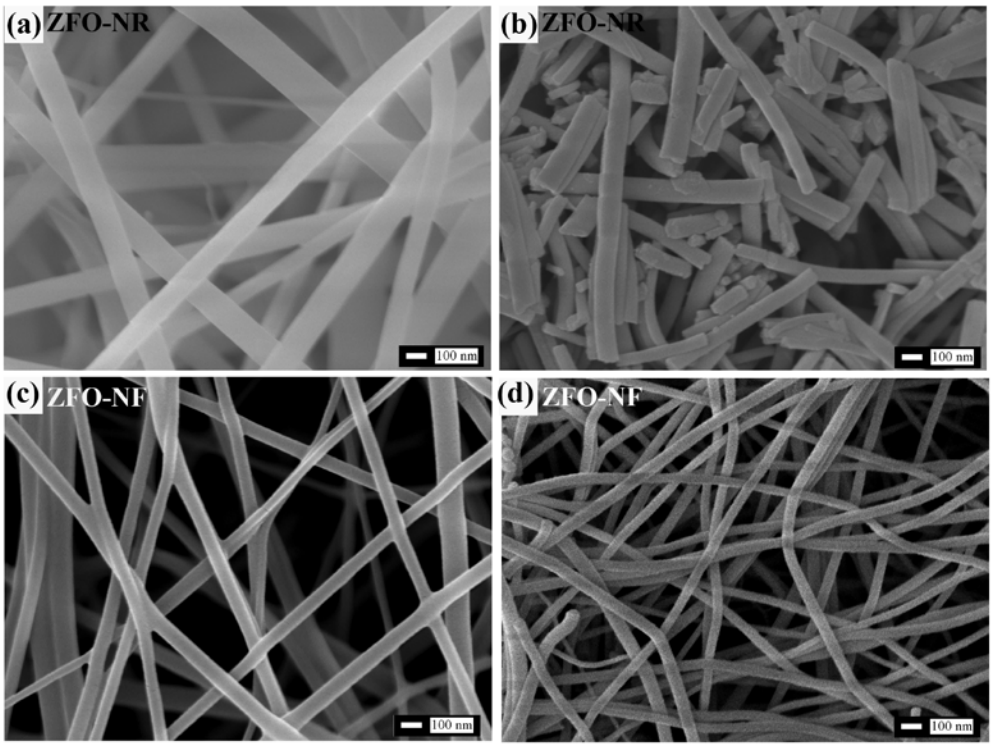

Figure 4-20 FESEM images of as-spun (a, c) and sintered (b, d) nanofibers. By using PVP:M ratio from (a, b) 5.04 : 1 (ZFO-NR) to (c, d) 3.93 : 1 (ZFO-NF), the diameters of the as-spun fibers shrunk significantly, as well as the length of these sintered products retained longer. (Reproduced by permission of The Royal Society of Chemistry)

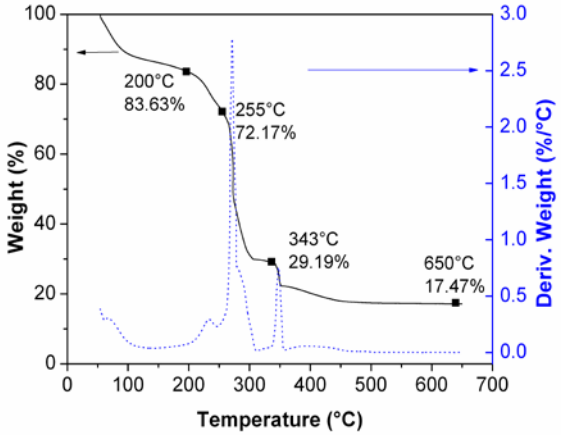

Figure 4-21 TGA of as-spun $ZnFe_2O_4$ nanofibers. (Reproduced by permission of The Royal Society of Chemistry)

Two different precursor solutions were prepared with different viscosity by changing the weight ratio of PVP polymer:metallic precursor (PVP:M, experimental details provided in Section 3.1.5.2). Figure 4-20(a) and (c) demonstrates the fibrous morphology of as-spun nanofibers with smooth surface and uniform diameter. TGA was conducted (Figure 4-21) on as-spun nanofibers to decide the sintering temperature. A weight loss of ~17 wt% was noticed below 200 °C and it may be contributed by the evaporation of volatile species,

similar to aforementioned observation in as-spun $ZnMn_2O_4$ (see Section 4.2.1). The intense peak at 255 °C corresponded to the decomposition of metal precursors (iron nitrate and zinc acetates), while a sudden depletion at 343 °C indicated the removal of PVP. Negligible weight loss was found at temperature higher than 500 °C, implying the complete removal of PVP backbone and hence maximum sintering temperature was selected to be 450 °C. FESEM images of sintered products were shown in Figure 4-20(c) and (d) and apparently there is a diverse change in morphologies by altering the viscosity level of electrospinning precursor solution.

By reducing PVP:M ratio from 5.04:1 (ZFO-NR) to 3.93:1 (ZFO-NF), a steady decrement of viscosity from 125(3) cP to 101 (3) cP was observed. Most interestingly, fibrous structure of as-spun nanofibers with higher viscosity (PVP:M=5.04:1) collapsed after sintering, forming nanorods (ZFO-NR). On the contrary, nanofibrous morphology was retained (ZFO-NF) for precursor solution with lower PVP:M ratio. Previously, Macías *et al.* reported that longer and thinner electrospun metallic oxide fibers could be obtained by increasing the viscosity of precursor solution.[136] Noteworthy, a contradict phenomenon was revealed in present investigation, *i.e. l*onger and more consistent nanofibers can be obtained by reducing the viscosity of precursor solution, *vice versa* for nanorods. Diameter of as-spun nanofibers evidently shrunk from 168(40) nm to 90(20) nm after sintering, while BET surface area was found to be 40 – 60 $m^2 g^{-1}$ in both cases.

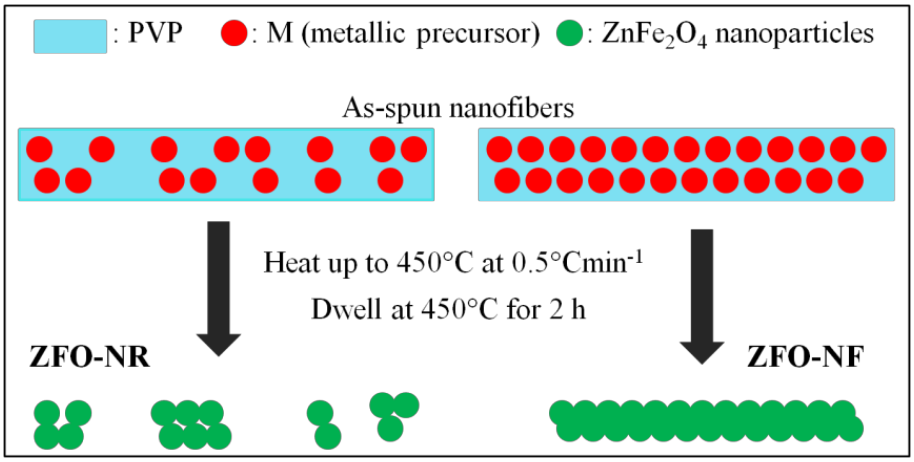

Scheme 4-2 Schematic illustration of $ZnFe_2O_4$ formation mechanism. If the viscosity of the solution is higher (PVP:M = 5.04:1), it carries lesser $ZnFe_2O_4$ nanoparticles, so the as-spun fibers are broken and become nanorod (ZFO-NR) after the PVP removal. On the contrary, when PVP:M is reduced to 3.93:1, higher amounts of $ZnFe_2O_4$ nanoparticles are encapsulated so continuously long nanofibers are obtained after the thermal treatment (ZFO-NF). (Reproduced by permission of The Royal Society of Chemistry)

Sintering process not only removed the polymeric PVP precursor backbone, but also crystallized $ZnFe_2O_4$ oxides. Owing to it, formation mechanism of electrospun ZFO-NR and ZFO-NF are hereby proposed. Upon sintering, individual $ZnFe_2O_4$ crystals serve as the building blocks that self-assemble and grow into a continuous fibrous morphology. If the PVP:M ratio is higher (higher viscosity), $ZnFe_2O_4$ building blocks are further apart within the PVP backbone and so fibrous morphology break into several segments of shorter nanorods (ZFO-NR) due to the drastic structural changes upon PVP removal at 450 °C (Scheme 4-2). On the other hand, decrement of PVP:M ratio (lower viscosity) leads to denser dispersion of individual $ZnFe_2O_4$ crystals that tend to construct long ZFO-NF with coherent diameter in nanodimension after sintering. When electrospinning duration is increased, continuous nanofibers gradually overlay to form interlocking mats with open pores existing in between the nanofibers. Stacking of nanofibers is essential in LIB application to provide mechanical integrity during lithiation/delithiation.

4.2.5. Electrospun $ZnFe_2O_4$ nanorods and nanofibers: Materials characterization[5]

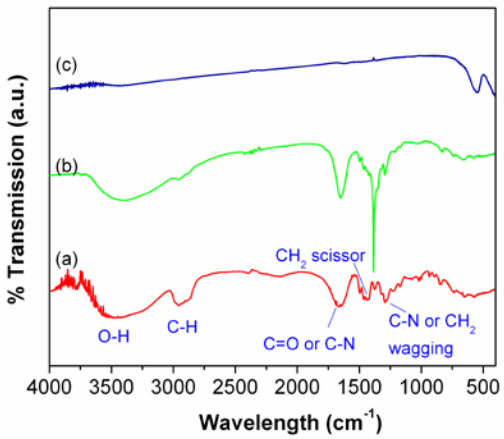

Figure 4-22 FTIR analysis of $ZnFe_2O_4$ synthesis. Spectra of (a) PVP and (b) as-spun nanofibers and (c) sintered $ZnFe_2O_4$ nanofibers (ZFO-NF). (Reproduced by permission of The Royal Society of Chemistry)

Similar to the study in $ZnMn_2O_4$ (refer to Section 4.2.2), FTIR spectra analysis was employed to prove the absence of PVP in sintered ZFO-NF (Figure 4-22). Identical molecular vibration modes alike to PVP were observed in as-spun fibers, although peaks

[5] Reproduced by permission of The Royal Society of Chemistry.

were weaker. An intense band at 1385 cm^{-1} in as-spun fibers indicated the existence of trapped ethanol solvent.[120] After sintering at 450 °C, all the peaks assigned to PVP and ethanol solvent disappeared, whereas an indvidual peak located at high frequency bands (546 cm^{-1}) formed. This may be due to the stretching vibrations between oxygen atoms and cation in either octahedral or tetrahedral positions,[137] so 450 °C is sufficient for simultaneous removal of PVP and crystallization of $ZnFe_2O_4$ nanocrystals.

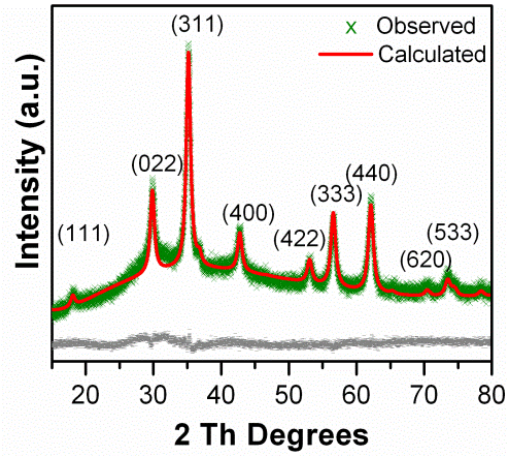

Figure 4-23 Rietveld refinement to XRD pattern of sintered $ZnFe_2O_4$.(Reproduced by permission of The Royal Society of Chemistry)

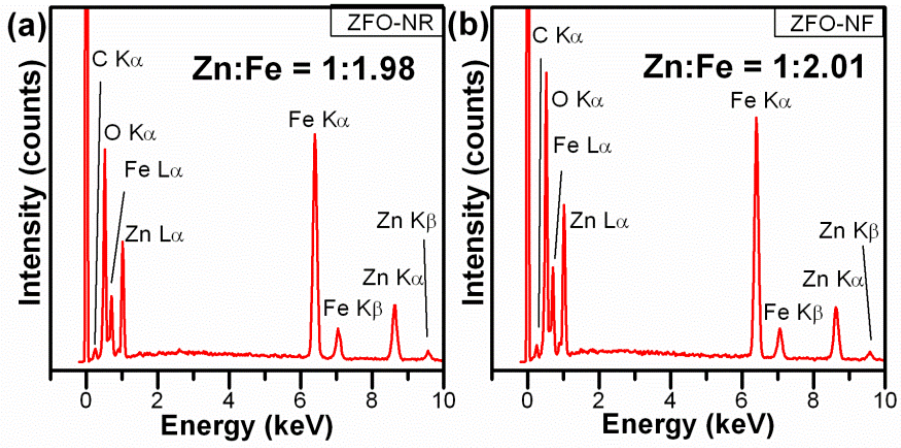

Figure 4-24 EDS spectra of (a) ZFO-NR and (b) ZFO-NF. (Reproduced by permission of The Royal Society of Chemistry)

XRD pattern confirms the formation of single-phase cubic spinel structure (space group: $Fd\bar{3}m$) of $ZnFe_2O_4$ (Figure 4-23). Lattice parameter of $ZnFe_2O_4$ obtained by Rietveld method was 8.442(1) Å, in good agreement with 8.431(5) Å (ICSD code 91829). The crystallite size was refined as 8.3(1) nm. Elemental composition analysis of ZFO-NF and ZFO-NR were analyzed by EDS (Figure 4-24), correct stoichiometric atomic ratios between Zn and Fe were found in both samples. Besides, HRTEM micrographs and SAED patterns were taken with the purpose to evaluate the nanostructure of sintered

ZFO-NF. Bright field TEM image (Figure 4-25(a)) reveals the secondary microstructure of sintered nanofibers, it is primarily composed of nanocrystals with crystallite size of 11(3) nm, which is coherent with the observation in Rietveld refinement. This observation supported our previous hypothesis about $ZnFe_2O_4$ building blocks in formation mechanism (Scheme 4-2). ZFO-NF is polycrystalline with d-spacing consistent with XRD results (Figure 4-25(b)). HRTEM micrograph was taken along [101] zone axis with d_{200} (0.42 nm) and $d_{1\bar{1}\bar{1}}$ (0.49 nm) (Figure 4-25(c)), while corresponding fast Fourier transform (FFT) was shown as inset. Simulated HRTEM pattern (Figure 4-25(d)) depicts the thickness of $ZnFe_2O_4$ nanocrystals to be ~5 nm.

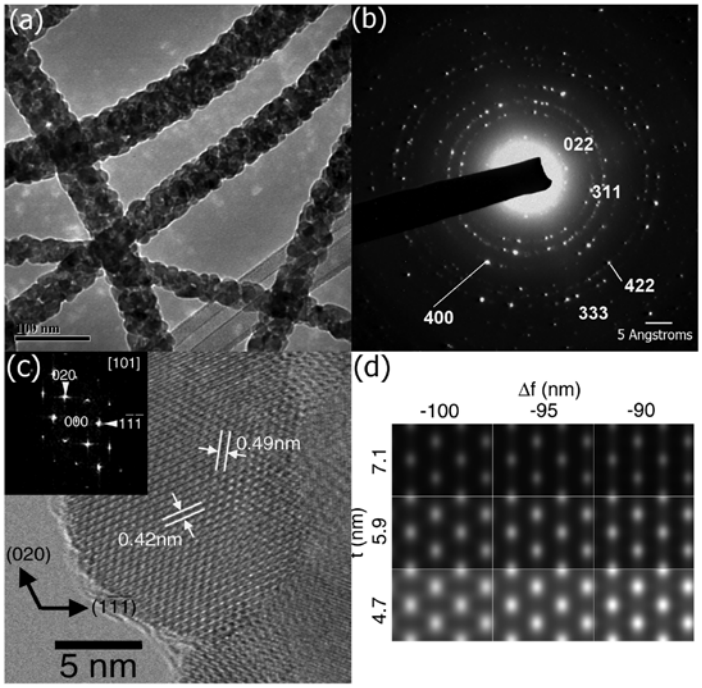

Figure 4-25 Characterization of ZFO-NF by TEM.(a) TEM micrograph and (b) corresponding SAED pattern. (c) HRTEM image taken along [101] zone axis, inset image is the corresponding FFT. (d) Simulated HRTEM patterns indicate the thickness of crystal to be ~5 nm. (Reproduced by permission of The Royal Society of Chemistry)

Electrospun $ZnFe_2O_4$ nanorods and nanofibers: Comparison of electrochemical performance[6]

First discharge of both ZFO-NR and ZFO-NF commenced from OCV at ~2.5 V to a deep discharge at 0.005 V. In the beginning of first discharge of ZFO-NF, two small plateaus were noticed at ~1.4 V and ~0.95 V (Figure 4-26(b)), which were contemplated by its CV

[6] Reproduced by permission of The Royal Society of Chemistry.

scan (Figure 4-27). Their corresponding capacities of 22 mAh g^{-1} and ~170 mAh g^{-1} were equivalent to the consumption of ~0.2 and ~1.5 mole of lithium ions per formula unit of $ZnFe_2O_4$, respectively. Interestingly, these two plateaus may represent lithium intercalation, but it was reported neither in micro-level thin film [26] nor nanoparticles of 100–300 nm.[9] They were also evidently absent in ZFO-NR (Figure 4-26(d)), suggesting that lithium reactivity and storage behavior are highly selective on the properties of host materials, such as particle size, morphology and structure architecture.[14, 28]

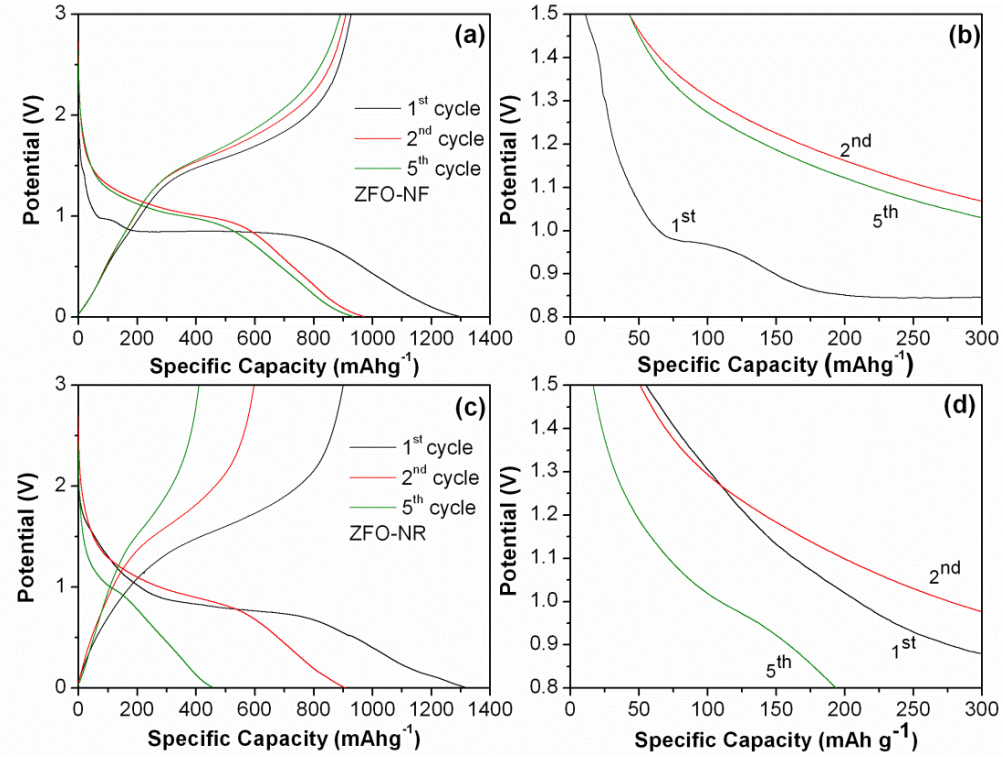

Figure 4-26 Galvanostatic cycling for $ZnFe_2O_4$ electrode (a) ZFO-NF and (c) ZFO-NR at first, second and fifth cycles at current density of 60 mA g^{-1}. Magnified discharge/charge patterns between 0.8 – 1.5 V of (b) ZFO-NF and (d) ZFO-NR. (Reproduced by permission of The Royal Society of Chemistry)

A vivid cathodic peak at 0.8 V was seen in first CV scan (Figure 4-27) and a large plateau at 0.8 V was simultaneously noted in galvanostatic cycling (Figure 4-26). This potential inferred the occurrence of crystal structure amorphization by conversion reaction, and thus the first discharge trend was distinguishable from subsequent discharge curves due to the reduction of $ZnFe_2O_4$ into Li_2O, Fe and Zn.[9] Afterwards, a very shallow peak at ~0.4 V was detected in CV as the reduction of $Zn^{(II)}$ to $Zn^{(0)}$,[138] followed by another cathodic peak at very low potential, ~0.1 V, which was previously reported as the formation of LiZn alloy.[92] The first charge curve started by a smooth increasing curve till ~1.35 V and subsequently a plateau at ~1.5 V corresponding to re-oxidation of $Zn^{(0)}$

and $Fe^{(III)}$. CV curve also exhibited a similar oxidation peak at ~1.5 V. By comparing the galvanostatic behavior of ZFO-NF and ZFO-NR (Figure 4-26), coherent discharge/charge plateaus were recognized in both samples, despite ZFO-NR demonstrated a shorter and steeper gradient than ZFO-NF, possibly due to its poorer kinetics in lithium diffusion.

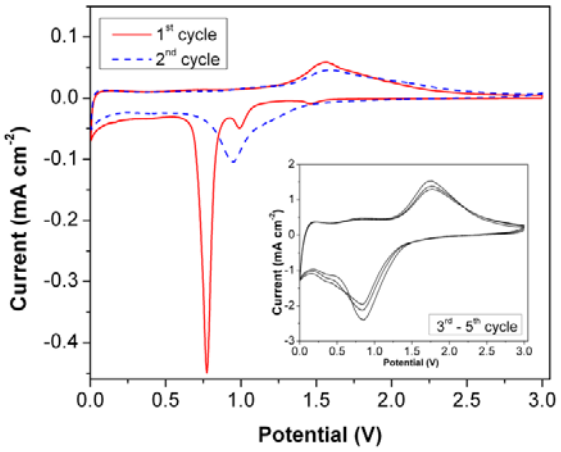

Figure 4-27 CV of ZFO-NF at 0.01 mV s^{-1} for first two cycles. (Inset) Scan rate of 0.1 mV s^{-1} was used from 3rd to 5th cycles. (Reproduced by permission of The Royal Society of Chemistry)

Overall, first discharge capacities of ~1292 mAg h^{-1} (~11.6 moles of lithium ions) and ~1316 mAh g^{-1} (~11.8 moles of lithium ions) were delivered by ZFO-NF and ZFO-NR (Figure 4-26), these are well above than the theoretical capacity (1000.5 mAh g^{-1} or 9 moles of lithium ions per unit formula of $ZnFe_2O_4$). Extra capacities were contributed by SEI formation and interfacial polymeric layer around $Zn^{(0)}$ and $Fe^{(0)}$ nanograins.[25, 70] During first charge, ZFO-NF and ZFO-NR disclosed reversible capacities of ~925 mAh g^{-1} (~8.3 moles of lithium ions) and ~900 mAh g^{-1} (~8.1 moles of lithium ions), respectively. ZFO-NR has poorer capacity retention than ZFO-NF at 2nd and 5th cycles.

Although capacity fading is inevitable in all previous studies on Fe-based oxides (Table 2-2 and Table 2-4), ZFO-NF effectively reduced the capacity loss and outperformed ZFO-NR (Figure 4-28).[26, 80, 139] The observed capacity in ZFO-NF depleted slowly for the first few cycles and eventually retained at ~733 mAh g^{-1} up to 30 cycles, which is almost two times higher than commercial graphite.[18] Coulombic efficiency remained higher than 95 % and even slightly increased as the cycling prolonged. Although capacities of ZFO-NR were comparable with ZFO-NF at initial cycles, its retention was extremely poor with only ~200 mAh g^{-1} capacities left after 30 cycles. Furthermore, rate capability of ZFO-NF was also examined by galvanostatic cycling at different current densities (Figure 4-28(c)). A high capacity of ~400 mAh g^{-1} was noticed even at 800 mA g^{-1} (~1C).

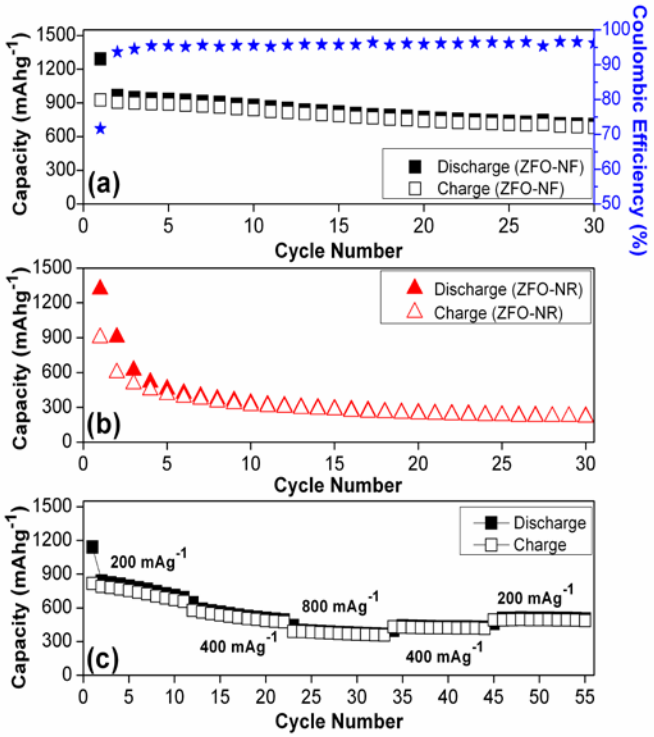

Figure 4-28 Cyclability of $ZnFe_2O_4$. (a) Capacity and coulombic efficiency *versus* cycle number of the electrospun ZFO-NF (current density = 60 mA g^{-1}). (b) Cycling performance of ZFO-NR at 60 mA g^{-1}. (c) Capacity *versus* cycle number of ZFO-NF at different current densities. (Reproduced by permission of The Royal Society of Chemistry)

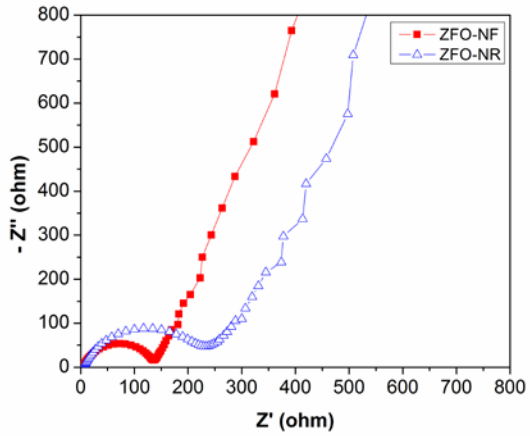

Figure 4-29 Nyquist plots for ZFO-NR and ZFO-NF. (Reproduced by permission of The Royal Society of Chemistry)

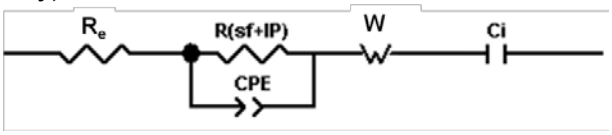

Figure 4-30 Equivalent circuit used to fit the Nyquist plot. (R_e: electrolyte resistance, IP: inter-particle resistance, CPE: constant phase elements, W: Warburg impedance, C_i: intercalation capacitance). (Reproduced by permission of The Royal Society of Chemistry)

To correlate the morphology (especially length) of $ZnFe_2O_4$ with cycling performance, EIS study was carried out. The impedance spectra (Figure 4-29) consisting of a semicircle in the high to medium frequency region (100 kHz-10 Hz), and an inclined line in the low frequency range (10 Hz-0.1 Hz). To quantify the experimental impedance values, an equivalent circuit made up by electrolyte resistance, capacitance, Warburg impedance was suggested (Figure 4-30), while the fitted values were listed in Table 5-6.

4.2.7. Electrospun $ZnCr_2O_4$ nanofibers: Materials characterization

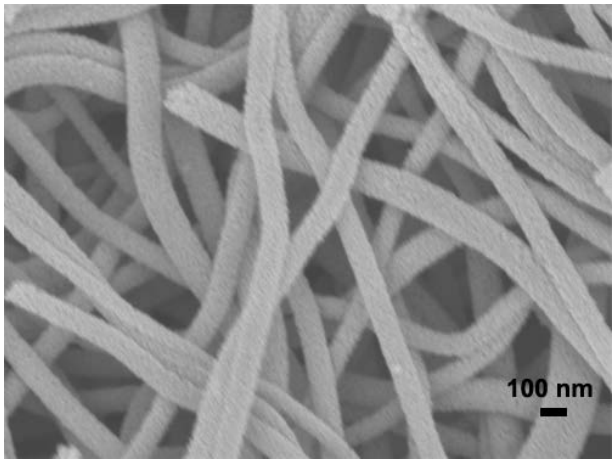

Figure 4-31 FESEM image of $ZnCr_2O_4$ nanofibers (ZCO-NF) after sintering.

Since electrospun $ZnFe_2O_4$ nanofibers (ZFO-NF in Section 4.2.6) rendered promising electrochemical results as LIB anodes, a simple substitution of Fe element by Cr at B-sites was performed to construct $ZnCr_2O_4$ nanofibers (denoted as ZCO-NF). FESEM micrographs (Figure 4-31) reveals the uniform and long sintered nanofibers with diameter of ~100-120 nm and length of several micrometer.

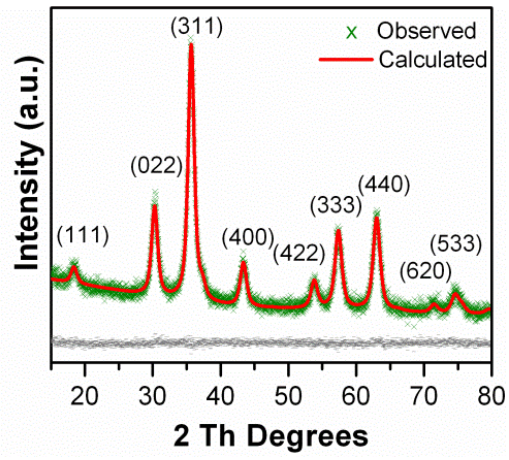

Figure 4-32 Rietveld refinement of $ZnCr_2O_4$ nanofibers (ZCO-NF).

XRD pattern depicts that $ZnCr_2O_4$ is isostructural with previously discussed $ZnFe_2O_4$ spinels (space group: $Fd\bar{3}m$, Figure 4-32). The lattice parameter and crystallite size were found to be 8.343(1) Å and 6.2 (1) nm by Rietveld refinement. These values are alike with ZFO-NF in Section 4.2.5.

4.2.8. Electrospun $ZnCr_2O_4$ nanofibers: Electrochemical measurement

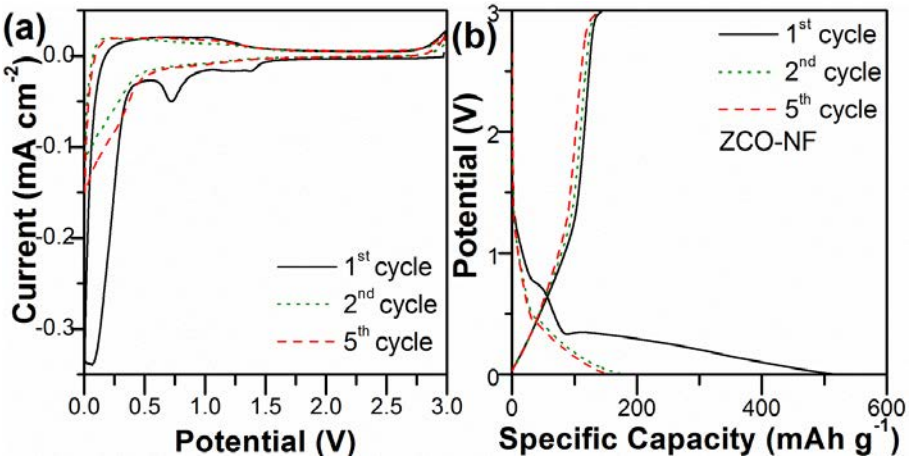

Figure 4-33 Electrochemical measurement of ZCO-NF. (a) CV at 0.1 mV s^{-1}; (b) corresponding galvanostatic discharge/charge bahaviour at 60 mA g^{-1}.

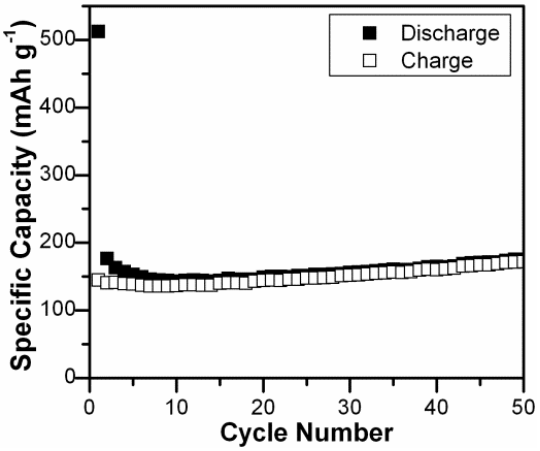

Figure 4-34 Cyclability of ZCO-NF at 60 mA g^{-1}.

Area underneath the CV curve of ZCO-NF was very narrow (Figure 4-33(a)), notably the recorded current was 10 times lower than ZFO-NF (inset of Figure 4-27), although both samples were prepared by exactly similar method. Looking into its galvanostatic performance (Figure 4-33(b)), ZCO-NF delivered ~513 mAh g^{-1} at first discharge and a reversible charge capacity of merely ~145 mAh g^{-1}. Theoretically, 9 moles of lithium ions

can be acquired upon the conversion reaction by reducing Zn and Cr into their metallic states, associated with capacity of ~1033 mAh g^{-1}. By excluding the lithium ions consumption by electrolyte decomposition (witnessed by a reduction peak at ~ 0.73 V in CV),[20] $ZnCr_2O_4$ is presumed to have negligible reaction with lithium. The possible hidden reason will be provided in Chapter 5.

4.2.9. Electrospun $Zn_{1-x}Mn_xFe_2O_4$ nanofibers ($0 \leq x \leq 0.7$): Materials characterization[7]

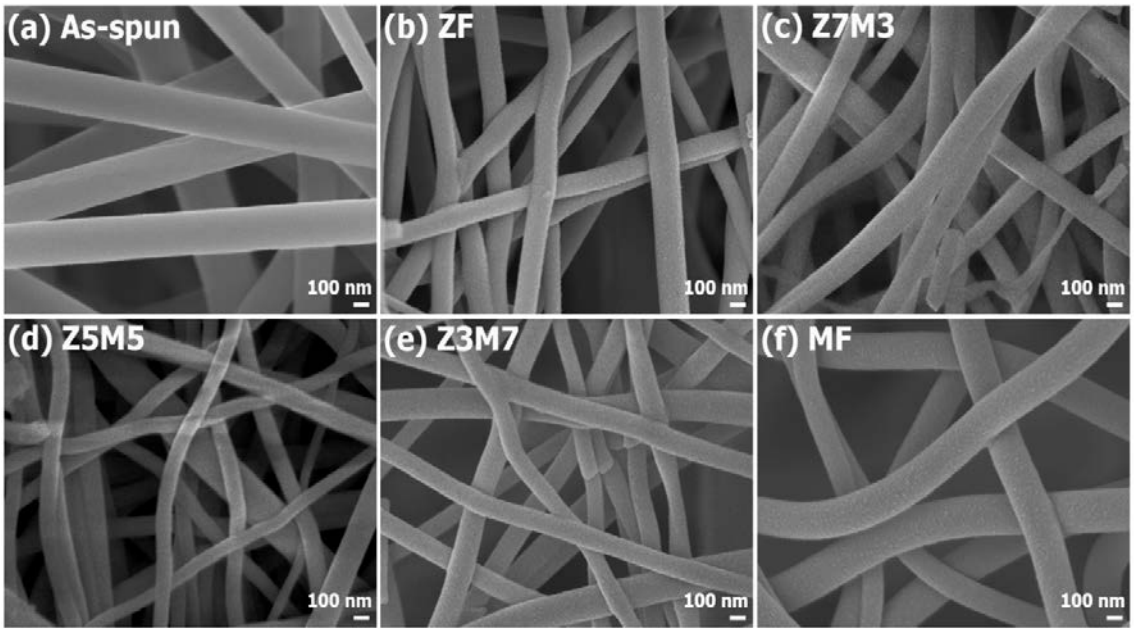

Figure 4-35 FESEM images of $Zn_{1-x}Mn_xFe_2O_4$ nanofibers. (a) As-spun, sintered (b) ZF, (c) Z7M3, (d) Z5M5, (e) Z3M7 and (f) MF nanofibers. (Reprinted with permission from [140], Copyright 2013 American Chemical Society.)

Electrospun $ZnCr_2O_4$ nanofibers (ZCO-NF in Section 4.2.8) did not show promising electrochemical performance after B-site substitution in AB_2O_4 structures as compared to previously studied electrospun $ZnMn_2O_4$ (ZMO-NF, Section 4.2.3) and $ZnFe_2O_4$ (ZFO-NF, Section 4.2.6) nanofibers. As a result, A-site substitution by using the same synthesis procedures are demonstrated in this section to construct electrospun $Zn_{1-x}Mn_xFe_2O_4$

[7] Reprinted with permission from [140] Teh, *et al.*, *Electrospun $Zn_{1-x}Mn_xFe_2O_4$ Nanofibers as Anodes for Lithium-Ion Batteries and the Impact of Mixed Transition Metallic Oxides on Battery Performance.* ACS Applied Materials & Interfaces, 2013. **5**(12): p. 5461-5467. Copyright 2013 American Chemical Society.

nanofibers (experimental details in Section 3.1.5.3). Electrochemical impact of systematic replacement of Zn by Mn in AFe_2O_4 spinels-based anodes was investigated. MnO was chosen to substitute ZnO as it has a lower working voltage and higher theoretical capacity (Table 2-6). Practically, MnO thin film [103] exhibited higher reversible capacity of 650 mAh g^{-1} than ZnO particles (~400 mAh g^{-1}), which was caused by low electronic conductivity and large volume change in ZnO during cycling.[101] Based on the stoichiometric ratio, samples were labelled as ZF (x=0), Z7M3 (x=0.3), Z5M5 (x=0.5), Z3M7 (x=0.7) and MF (x=1) accordingly.

Figure 4-35 illustrates the morphology of as-spun and sintered $Zn_{1-x}Mn_xFe_2O_4$ nanofibers. The as-spun nanofibers fell into range of 200-280 nm in diameter (Figure 4-35(a)), while ZF (x=0), Z7M3 (x=0.3), Z5M5 (x=0.5) and Z3M7 (x=0.3) shrunk obviously to around 140-200 nm after sintering (Figure 4-35(b)-(e)). This is analogous to our previous studies on ZFO-NF (Section 4.2.4) and ZCO-NF (Section 4.2.7), *i.e.* sintering process at 450 ^oC caused the removal of PVP and reduction of nanofibers diameter.[27] MF (x=1) (Figure 4-35(f)) has a larger diameter range of ~150-220 nm as it was sintered at 400 °C to preserve their crystal structure. Overall, all sintered nanofibers have smooth surface and uniform diameter despite Mn substitution. No trace of agglomeration was observed and a connective framework with open pores was formed that is favorable for lithium kinetics.

XRD patterns provide structural information of sintered $Zn_{1-x}Mn_xFe_2O_4$ nanofibers(Figure 4-36(a)). After Rietveld refinement, XRD result of ZF ensured the formation of a single phase spinel structure (space group: $Fd\bar{3}m$), in good agreement with ICSD code 91829. Identical XRD patterns were also observed in Z7M3, Z5M5 and Z3M7. MF was excluded here because high amount of Fe_2O_3 impurities was identified after being sintered at 450 °C. By raising the sintering temperature to 500 °C, $MnFe_2O_4$ structure totally disintegrated into a combination of Mn_2O_3 and Fe_2O_3 composites (Figure 4-37). When heating as-spun MF nanofibers at 400 °C to prevent the decomposition of spinel structure into binary oxides, XRD pattern with very low signal to noise ratio was obtained, since 400 °C is too low to remove PVP thoroughly. Multiple phases were obtained either sintered at 400 °C, 450 °C or 500 °C and thus MF was excluded from the comparison.

Table 4-2 summarizes A and B-sites occupancies by Zn, Mn or Fe using sequential Rietveld refinements. However, due to the fact that number of electrons of these three cations is very similar with indistinguishable scattering factors, therefore the values presented here might not be precise. Besides, broadened XRD peaks due to the presence

of numerous nanocrystals in nanofibers also complicated the structural analysis. Thus, a series of highly crystalline samples is preferred for such study.

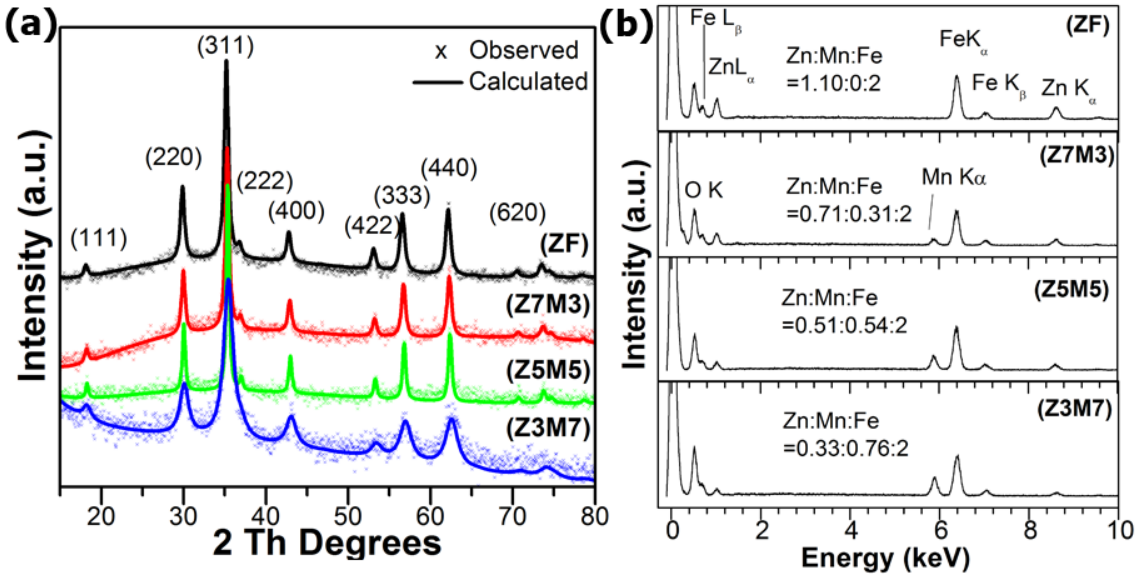

Figure 4-36 Materials characterization of $Zn_{1-x}Mn_xFe_2O_4$ nanofibers. (a) XRD Rietveld refined patterns with the observed data (b) EDS analysis of sintered ZF, Z7M3, Z5M5 and Z3M7 nanofibers. (Reprinted with permission from [140], Copyright 2013 American Chemical Society.)

Table 4-2 Site occupancies of Zn, Mn and Fe cations at A or B sites when crystallizing in spinel structures, generated by Rietveld refiment method. (Reprinted with permission from [140], Copyright 2013 American Chemical Society.)

Sample Name	A site			B site		
	Zn	Fe	Mn	Zn	Fe	Mn
ZF	0.99	0	0	0.01	1	0
Z7M3	0.64	0.10	0.27	0.03	0.95	0.01
Z5M5	0.43	0.14	0.48	0.04	0.93	0.01
Z3M7	0.19	0.48	0.42	0.06	0.78	0.14

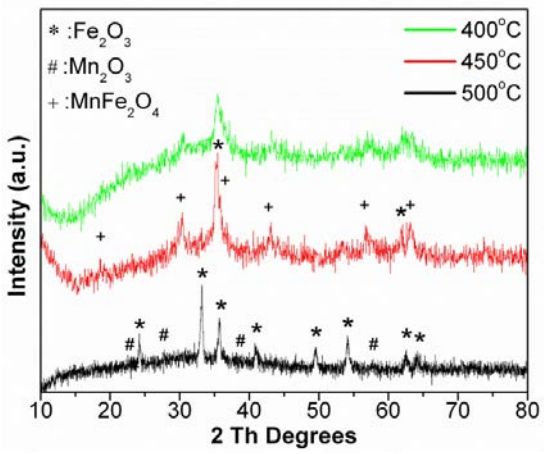

Figure 4-37 XRD patterns of MF nanofibers sintered at 400 °C, 450 °C and 500 °C. (Reprinted with permission from [140], Copyright 2013 American Chemical Society.)

To quantify the ratio of Zn and Mn ions towards Fe ions, EDS was conducted on sintered ZF, Z7M3, Z5M5 and Z3M7 (Figure 4-36(b)). The atomic ratio was normalized by taking Fe as 2 moles. The analysis shows a substantial decrement of Zn L_α and K_α peaks as Mn content increases, whereas Mn K_α peak gets more and more intense, so all samples were successfully prepared based on their presumed stoichiometric ratio and were applied as LIB anodes to understand the impact of Mn substitution on battery performance.

4.2.10. Electrospun $Zn_{1-x}Mn_xFe_2O_4$ nanofibers ($0 \leq x \leq 0.7$): Comparison of electrochemical performance[8]

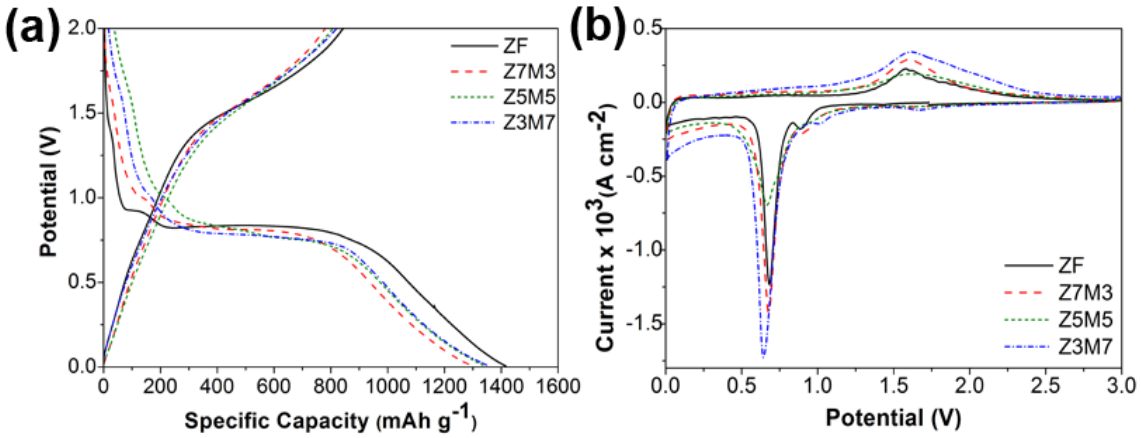

Figure 4-38 Electrochemical results of $Zn_{1-x}Mn_xFe_2O_4$ nanofibers. (a) First galvanostatic cycle (rate = 60 mA g^{-1}), and (b) first CV (rate = 0.05 mV s^{-1}) of ZF, Z7M3, Z5M5 and Z3M7. (Reprinted with permission from [140], Copyright 2013 American Chemical Society.)

ZF reacts with lithium ions in a similar mechanism as our previous discussion on electrospun ZFO-NF (Section 4.2.6), in which two short plateaus were observed at ~1.4 V and ~0.9 V due to lithium intercalation into spinel layered structure (Figure 4-38(a)).[9, 27] Similarly, these two short plateaus were consistently noticed in both CV and galvanostatic cycling of Z7M3, Z5M5 and Z3M7 (Figure 4-38(b)), *i.e.* two irreversible shallow peaks at ~1.66 V and ~0.92 V to represent lithium intercalation. Likewise, ZF demonstrated a flat conversion plateau at ~0.83 V (Figure 4-38(a)) which was identical to previously discussed ZFO-NF, whereas this characteristic plateau was observed to be

[8] Reprinted with permission from [140]. Copyright 2013 American Chemical Society.

slightly lower in Z7M3 (~0.81 V), Z5M5 (~0.8 V) and Z3M7 (~0.76 V). Simultaneously, CV detected the working voltage of this characteristic amorphization process as ~0.69 V in ZF, whereas lower peaks of ~0.68 V, 0.67 V and ~0.64 V were shown by Z7M3, Z5M5 and Z3M7, respectively (Figure 4-38(b)).

From the perspective of lithium ions storage properties, first discharge/charge capacities achieved by ZF, Z7M3, Z5M5 and Z3M7 were 1417/1025 mAh g^{-1}, 1302/948 mAh g^{-1}, 1344/972 mAh g^{-1}, 1358/1015 mAh g^{-1}, respectively with coulombic efficiencies of 72-75 % (Figure 4-39(a)). Slight variation of the capacities may be due to different degree of electrolyte decomposition or SEI formation on the electrodes.[13, 50] After 50 cycles, Z3M7 showed highest reversible capacity of ~612 mAh g^{-1} as compared to Z5M5 with capacity of ~521 mAh g^{-1}, Z7M3 of ~426 mAh g^{-1} and ZF of ~532 mAh g^{-1}. Reversible capacity of Z3M7 is ~2 times higher than commercial graphite.[10] Besides, CV scan was also conducted on the cycled electrodes and shown in Figure 4-39(b). Z3M7 presented highest current in CV scans, so Mn replacement helps in enhancing the cyclability.

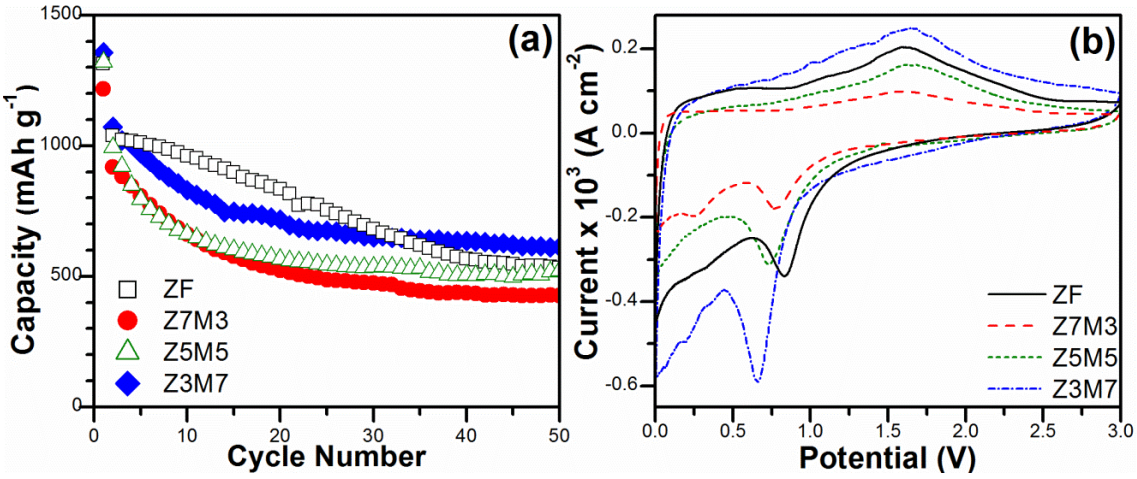

Figure 4-39 Electrochemical testings of $Zn_{1-x}Mn_xFe_2O_4$ nanofibers after cycling. (a) Cyclability at 60 mA g^{-1} and (b) their corresponding CV scan at 0.1 mV s^{-1}) after cycled for 50 times. (Reprinted with permission from [140], Copyright 2013 American Chemical Society.)

4.3. Ball Milled TMOs

Electrospun AB_2O_4 has shown interesting electrochemical performances and the reversible capacities higher than the commercial graphite anode.[10] As previously discussed in the solid solution series of electrospun $Zn_{1-x}Mn_xFe_2O_4$ nanofibers (Section 4.2.9), broadening of XRD peaks due to the nature of nanostructured products has inevitably compensated the accuracy when characterizing the structural information. To

address this issue, highly crystalline samples will be favourable in order to obtain high quality crystallography information and investigate its impact on the battery performance. Hence, HEBM was employed in this section to produce $ZnMn_2O_4$, $ZnFe_2O_4$ and $ZnCr_2O_4$, as well as a solid solution series of $ZnFe_{2-y}Cr_yO_4$.

4.3.1. Ball milled $ZnMn_2O_4$, $ZnFe_2O_4$ and $ZnCr_2O_4$: Materials characterization

Aforementioned electrospun $ZnMn_2O_4$ (Section 4.2.3), $ZnFe_2O_4$ (Section 4.2.6) and $ZnCr_2O_4$ (Section 4.2.8) nanofibers demonstrated distinctly different capacity/working voltage after the replacement of cation B in AB_2O_4 spinels, thus giving a clear insight that electrochemical reaction towards lithium ions is influenced by B-site substitution. As a result, ZnB_2O_4 (B = Fe, Cr or Mn) were synthesized by HEBM method in this framework of investigations to reliably characterize the structural information and correlate to their battery performances. Detailed experimental procedures were presented in Section 3.1.1.

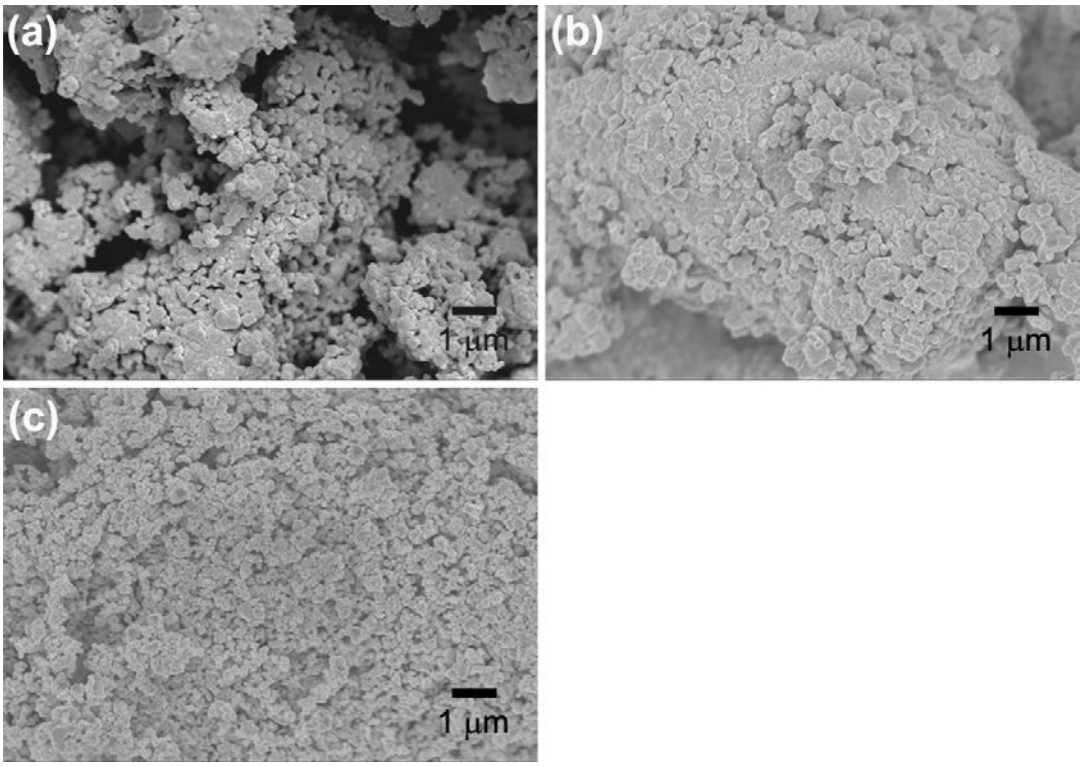

Figure 4-40 FESEM images of annealed ZnB_2O_4 indicate the uniform distribution of particle size in (a) $ZnMn_2O_4$ (ZMO-NP), (b) $ZnFe_2O_4$ (ZFO-NP) and (c) $ZnCr_2O_4$ (ZCO-NP).

FESEM images of annealed $ZnMn_2O_4$, $ZnFe_2O_4$ and $ZnCr_2O_4$ (named as ZMO-NP, ZFO-NP, ZCO-NP, respectively) reveal consistent distribution of particle size between 200-

400 nm (Figure 4-40). Crystal information was retrieved from XRD data and Rietveld refinement (Figure 4-41). ZFO-NP and ZCO-NP were confirmed to crystallize in phase pure cubic spinel (symmetry: $Fd\bar{3}m$) with lattice parameters of 8.444 (1) Å and 8.327(1) Å, which are similar to ICSD code 180748 and 91829, respectively. The shrinkage of lattice parameter is due to the shorter ionic radius of Cr^{3+} (0.62 Å) than Fe^{3+} (0.645 Å).[141] Jahn Teller ions, Mn^{3+} causes ZMO-NP to have tetragonal structure (symmetry: $I4_1/amd$) with lattice parameters of 5.716(1) Å and 9.251(1) Å. Subsequently, EDS analysis was conducted and the result proved correct stoichiometric atomic ratio between Zn and B (either Mn, Cr or Fe) after annealing (Figure 4-42(a)).

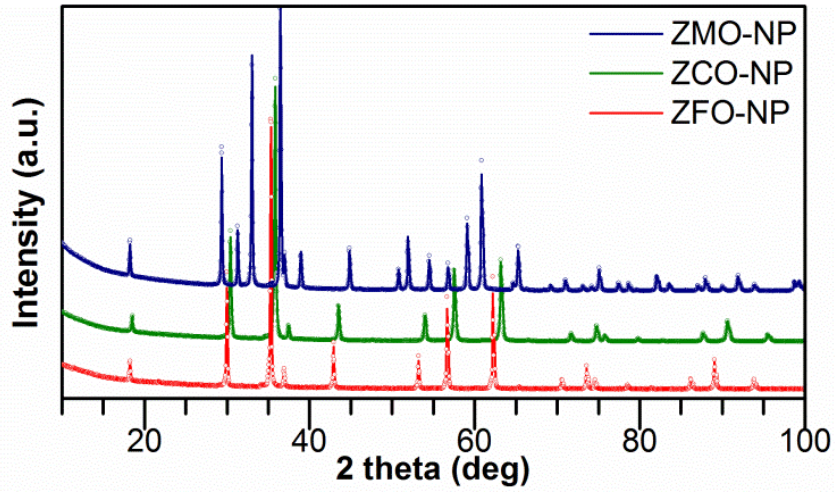

Figure 4-41 Powder XRD results of annealed ZnB_2O_4 , experimental (dots) and calculated (solid lines) patterns were shown.

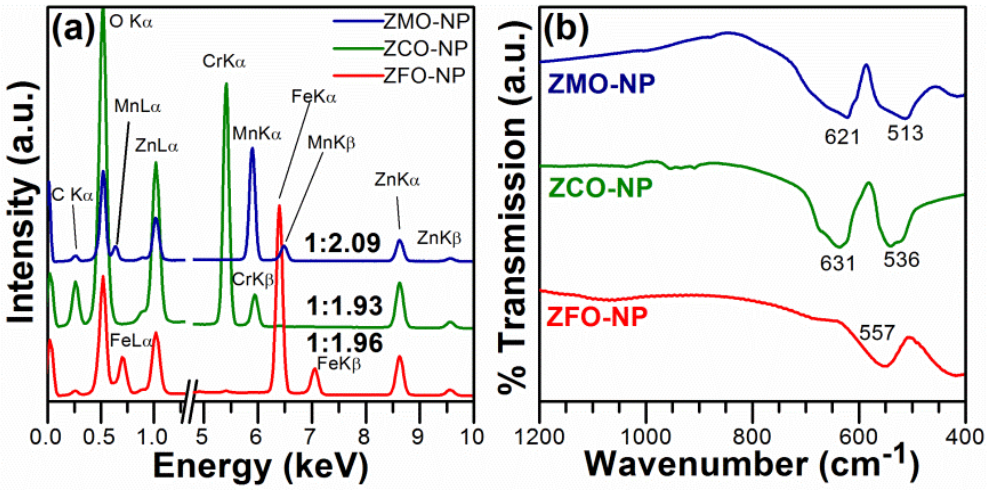

Figure 4-42 Materials characterization of annealed ZnB_2O_4 by (a) EDS analysis and the stoichiometric atomic ratio of Zn:B was stated. (b) FTIR analysis.

FTIR characterization was adopted to determine the vibration bands of metallic ions in crystal lattice of annealed ZnB_2O_4 powders (Figure 4-42(b)). In the case of ZMO-NP,

peaks at ~621 cm^{-1} and ~513 cm^{-1} can be attributed by Mn^{3+}-O^{2-} stretching bonds, well aligned with our previous observation in electrospun ZMO-NF (Figure 4-10).[142] Besides, vibration peaks of Cr^{3+}-O^{2-} in ZCO-NP was found to be similar with published Cr_2O_3 data,[143] whereas ZFO-NP showed qualitative resemblance with reported Fe^{3+}-O^{2-} in Fe_2O_3.[144] So, ZnB_2O_4 with B-site cation variation was successfully formed. According to Dunitz *et al.*,[131] ZnB_2O_4 (B=Mn, Cr and Fe) crystallizes in normal spinel configuration, so cation B replacement preferentially occurs only on octahedral sites.

4.3.2. Ball milled $ZnMn_2O_4$, $ZnFe_2O_4$ and $ZnCr_2O_4$: Comparison of electrochemical performance

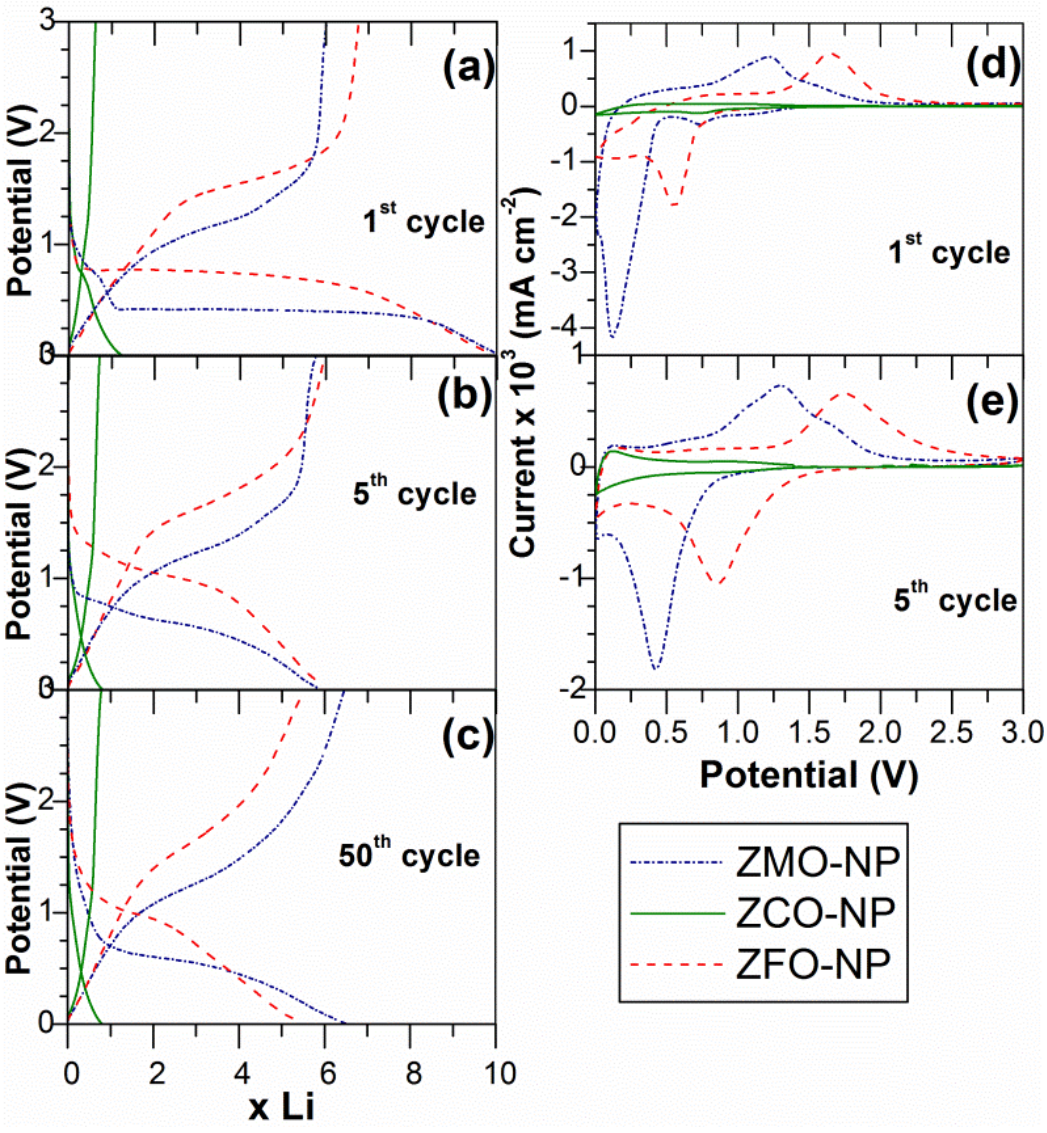

Figure 4-43 Galvanostatic cycling results of annealed ZnB_2O_4 at current density of 60 mA g^{-1}: (a) 1st cycle, (b) 5th cycle, (c) 50th cycle. Corresponding CV data of (d) 1st cycle and (e) 5th cycle at scan rate of 0.1 mV s^{-1}.

Basically, battery performance of ball milled ZnB_2O_4 was similar to electrospun ZnB_2O_4 (Figure 4-43). First discharge behavior of ZMO-NP and ZFO-NP initially started by an abrupt decrease of cell potential, followed by conversion plateaus at ~0.42 V and ~0.77 V, respectively.[27, 142] The subsequent sloping region until 5 mV was caused by the formation of organic polymeric layer surrounding the reduced metallic nanograins.[20, 22] Then, greatly polarized (plateaus found at ~1.2 V and ~1.6 V for ZMO-NP and ZFO-NP respectively) and partially irreversible charging curves were observed. During charging, the spinel structure was not recovered so the discharge/charge curves at 5th and 50th cycle were distinctly different from their first cycle due to the modified environments around the metallic nanograins. CV scans were well aligned with the galvanostatic cycling with a better indication of discharge/charge working voltages. At 5th cycle onwards, the discharge and charge voltages of ZMO-NP were ~0.42 V and ~1.31 V, respectively. On the other hand, the discharge and charge voltages of ZFO-NP were ~0.8 V and ~1.7 V. In overall, ZMO-NP has a lower working voltage and higher capacity of ~730 mAh g^{-1} (equivalent to ~6.52 moles of lithium ions) than ZFO-NP (~615 mAh g^{-1}, ~5.54 moles of lithium ions) at 50th cycle (Figure 4-44).

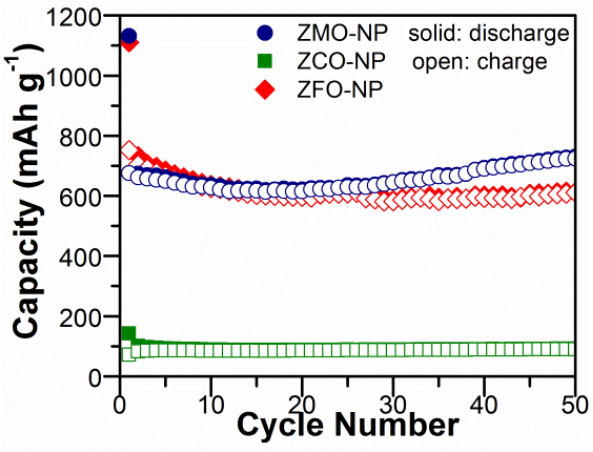

Figure 4-44 Extended galvanostatic cycling of ZnB_2O_4 at 60 mA g^{-1}.

Our previous studies indicated the presence of an additional intercalation plateau before the spinel amorphization,[9, 27, 142] such as ZMO-NF (Section 4.2.3) and ZFO-NF (Section 4.2.6). However, this was less obvious in this section. Moreover, it is worth noting that ZCO-NP expressed extremely low storage behavior than ZMO-NP and ZFO-NP (Figure 4-44), similar to electrospun ZCO-NF in Section 4.2.8. Its magnified view of CV result (Figure 4-45) did not contain any deep discharge/charge peak, but the shallow discharge peaks at ~1.4 V and ~0.7 V can be assigned as the lithium insertion and the

decomposition of organic electrolyte.[2, 20, 22] Along 50 discharge/charge cycles, ZCO-NP retained a low capacity at ~91 mAh g^{-1} (equivalent to ~0.8 moles of lithium ions), which might be solely consumed by side reaction and conductive carbon. Therefore, poor electrochemical properties of $ZnCr_2O_4$ regardless of nanostructure (ZCO-NP and ZCO-NF) are still an unsolved doubt. More discussion will be made in Section 5.2.5 to tackle this issue. In summary, this section gives a clue that it is possible to alter the battery performance of spinel-anodes by changing the counter ion.

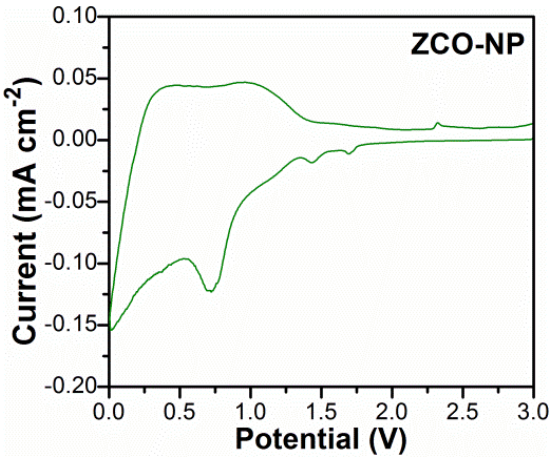

Figure 4-45 Magnified view of first CV cycle of ZCO-NP.

4.3.3. Ball milled $MgMn_2O_4$, $MgFe_2O_4$ and $MgCr_2O_4$: Materials characterization

As mentioned in Section 2.5, incorporation of inactive component with electrode material helps in promoting better cyclability. As a result, electrochemically inactive MgO was utilized as coating layer on cathode materials (such as $LiCoO_2$, $LiMn_2O_4$) to improve the structural stability and reduce the side reactions after having interfacial contact with polymer electrolyte.[145] In the perspective of anode, Wang *et al.* proved that MgO serves as a buffer matrix to prevent excessive volumetric expansion/contraction of NiO anode.[146] Besides, it is beneficial in reducing the voltage polarization and increase the capacity retention.[146] Sivakumar *et al.* combined Fe_2O_3 and MgO to form $MgFe_2O_4$ anode with capacity retention of ~300 mAh g^{-1} at 10^{th} cycle.[91] Later on, the capacity was enhanced to 744 mAh g^{-1} by adding a carbon coating layer.[147]

In previous section, ZnB_2O_4 (B: Mn, Cr and Fe) was studied systematically to identify the effect of counter ion B in ZnB_2O_4 spinel structure. Hence, a similar approach was conducted in this section, since Mg is another divalent cation to replace Zn perfectly in

the spinel to form MgB_2O_4 (B: Mn, Cr and Fe). Instead of the conventional HEBM applied in last section, a modified HEBM incorporated citric acid was introduced. The presence of citric acid creates a wet milling condition which helps in facilitating size reduction and decreasing required milling duration and annealing temperature. Besides, steric effect of citric acid is anticipated to effectively suppress the aggregation of fine ball milled particles. Detailed procedures were included in Section 3.1.2.

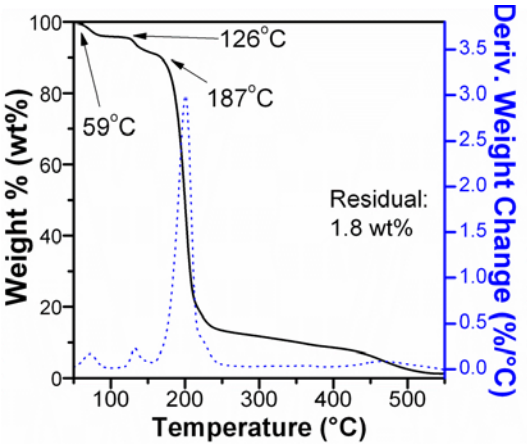

Figure 4-46 TGA of citric acid heated from room temperature to 550 °C in air atmosphere.

In order to decide the annealing temperature for as-milled metallic citrate solution, TGA of citric acid was conducted (Figure 4-46). The initial decomposition below 100 °C may be assigned to the desolvation of water molecules and the dehydration process occurred at ~126 °C. Then, 187 °C represents the onset decomposition of citric acid, which encounters an abrupt weight loss of ~90 wt% till ~450 °C.[148] Beyond 450 °C, very minor weight loss was observed with residual maintaining at ~1.8 wt%, this indicates the thorough removal of citric acid and thus 500 °C, 700 °C and 800 °C were chosen as annealing temperatures to produce $MgMn_2O_4$, $MgCr_2O_4$ and $MgFe_2O_4$, respectively.

After annealing, dry powders were obtained and XRD patterns in Figure 4-47 confirmed the formation of single phase spinel structure. $MgFe_2O_4$ (MFO-NP) and $MgCr_2O_4$ (MCO-NP) crystallized in cubic spinel structure (symmetry: $Fd\bar{3}m$) with lattice parameter of 8.395(2) Å and 8.335(1) Å, which are identical to reported data in ICSD code 240848 and 171106. As previously discussed, Jahn-Teller ion Mn^{3+} elongates the octahedral coordination and caused the formation of tetragonal $MgMn_2O_4$ (MMO-NP) with $I4_1/amd$ symmetry.[131] Lattice parameters were also refined by Rietveld method to be 5.734(2) Å and 9.264(4) Å (ICSD code 167399). MMO-NP exhibited peak broadening effect as compared to highly crystalline MCO-NP and MFO-NP because of being heated at lower

temperature (500 °C). Minor impurity of Mn_2O_3 impurities were noticed if annealing temperature exceeded 500 °C. Average crystallite sizes of MMO-NP, MCO-NP and MFO-NP were refined to be ~9(1) nm, ~23(1) nm and ~28(1) nm, respectively.

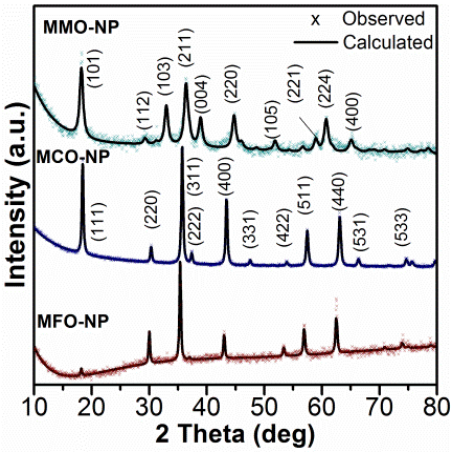

Figure 4-47 XRD patterns of MgB_2O_4 (B: Mn, Cr, Fe) , the structural information was derived by Rietveld refinement method.

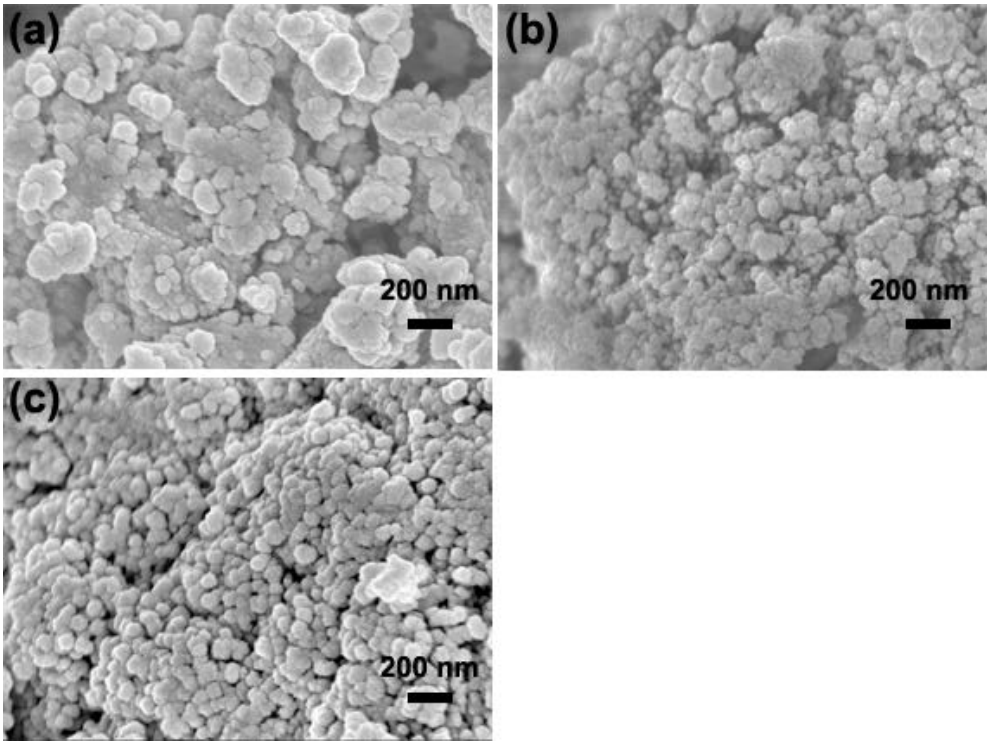

Figure 4-48 FESEM images of MgB_2O_4. (a) MMO-NP, (b) MCO-NP and (c) MFO-NP.

Surface morphology of annealed MgB_2O_4 was studied by FESEM (Figure 4-48). The micrographs clearly indicate the formation of dense and uniform particles in the range of 100-300 nm. Hence, HEBM with the citric acid as a reagent is able to obtain good quality particles and this technique is time and cost effective than other sophisticated chemical related procedures.[27, 67]

4.3.4. Ball milled $MgMn_2O_4$, $MgFe_2O_4$ and $MgCr_2O_4$: Comparison of electrochemical performance

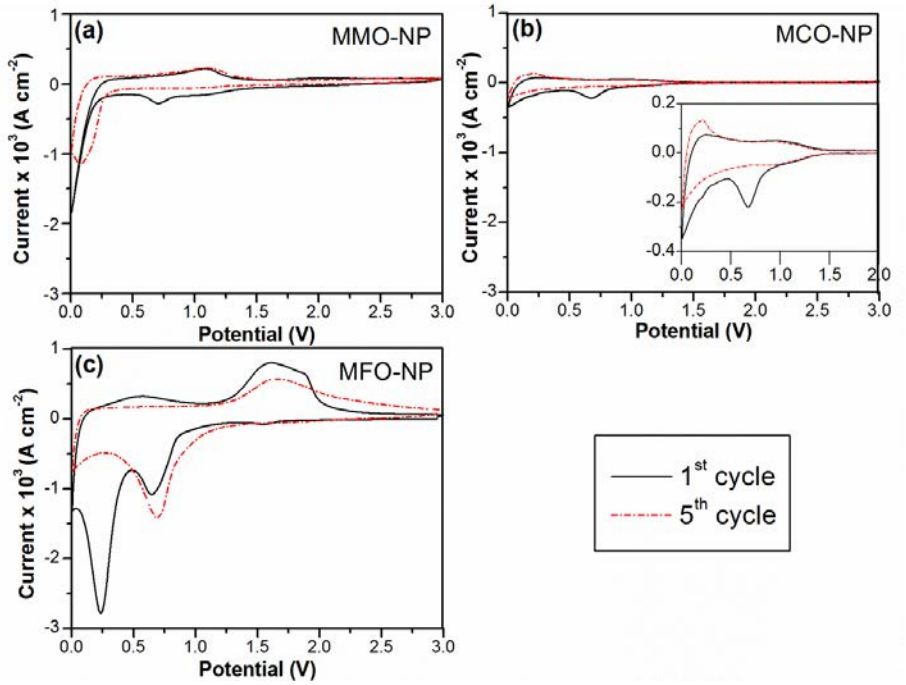

Figure 4-49 CV scans of MgB_2O_4. (a) MMO-NP, (b) MCO-NP and (c) MFO-NP at scan rate of 0.1 mV s^{-1}. The inset in (b) represents the magnified view of MCO-NP.

As shown in CV (Figure 4-49), reaction mechanism of annealed MMO-NP, MCO-NP and MFO-NP were distinctly different, suggesting the great impact of counter ion (Mn, Cr or Fe) on the battery performance. In all cases, the first reduction peak was seen at ~0.65 V, which can be assigned to the SEI formation or the lithium intercalation into the spinel structures which was also previously mentioned. MFO-NP (Figure 4-49(c)) illustrated the largest area underneath CV curves with an intense cathodic peak at ~0.23 V, implying some irreversible reactions as there was no corresponding oxidation peak in the following charging process. This may belong to the characteristic discharge plateau in conversion reaction, *i.e.* complete reduction of Fe^{3+} to Fe metallic nanograins dispersed in amorphous Li_2O matrix.[91] The second cycle of CV exhibited only a pair of coupled peaks at ~0.64 V and ~1.69 V, representing the reversible redox reaction of Fe^{3+} and Fe^0. First CV scan of MMO-NP (Figure 4-49(a)) demonstrated an intense reduction peak started at ~0.25 V and continued to approximate 0.005 V. This can be identified as the reduction of MMO-NP to their metallic states. In subsequent cycle, the reduction and oxidation reaction of MgO/Mn_2O_3 took place at ~0.1 V and ~1.1 V. Similar to the observation in Section 4.3.2, CV curve of MCO-NP displays no noticeable reduction/oxidation peak (Figure 4-49(b)),

other than the peak relevant to electrolyte decomposition at ~0.7 V. Similarly, their galvanostatic discharge/charge in Figure 4-50(b) depicted an extremely low volume of lithium absorption and extraction. Albeit, first discharge capacity of MCO-NP was found to be ~175 mAh g^{-1} and reverse charge capacity was merely ~82 mAh g^{-1}, which may be contributed by conductive carbon. Thus, electrochemically inactive behavior of MCO-NP was consistent with the observation in electrospun ZCO-NF and ball milled ZCO-NP, regardless of morphology, A-site counter ion or synthesis methods. Since $ZnFe_2O_4$ performed as a promising anodic material, a solid solution series of ball milled $ZnFe_{2-y}Cr_yO_4$ ($0 \leq y \leq 2.0$) will be presented in Section 4.3.5 to elucidate a possible explanation.

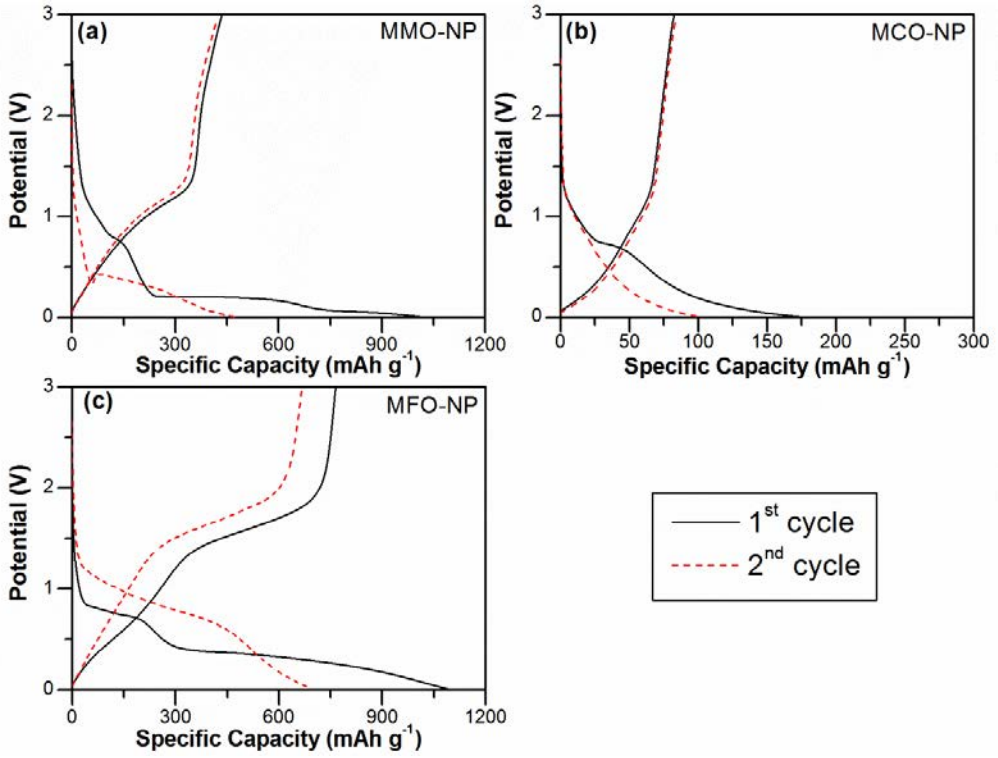

Figure 4-50 Initial discharge/charge behaviors MgB_2O_4. (a) MMO-NP, (b) MCO-NP and MFO-NP tested at current density of 60 mA g^{-1}.

In galvanostatic cycling of MFO-NP (Figure 4-50(c)), two discharge plateaus were observed at ~0.76 V and ~0.38 V which were in analogue with the observation in earlier CV scan. The initial discharge capacity was found to be ~1096 mAh g^{-1} (equivalent to ~8.2 moles of lithium ions). This value is higher than the theoretical capacity of ~804 mAh g^{-1} (6 moles of lithium ions) due to the presence of inevitable side reactions commonly occurred in conversion reaction.[20, 51] First charge plateau observed at ~1.4 V can be assigned as the re-oxidation of $Fe^{(0)}$ to either Fe^{2+} or Fe^{3+} which involving ~5.7 moles of lithium ions (~765 mAh g^{-1}). These were close to theoretical capacity, whereas

first discharge curve of MMO-NP (Figure 4-50(a)) exhibited two plateaus at ~0.76 V and ~0.21 V due to organic electrolyte decomposition and onset of conversion reaction. This discharge curve was similar to MFO-NP, but the plateaus were relatively shorter than corresponding plateaus in MFO-NP, possibly due to larger cell volume of $MgFe_2O_4$ that provides more interstitial sites for lithium ions. First discharge and charge capacities were ~1021 mAh g^{-1} (7.6 moles of lithium ions) and ~435 mAh g^{-1} (3.2 moles of lithium ions).

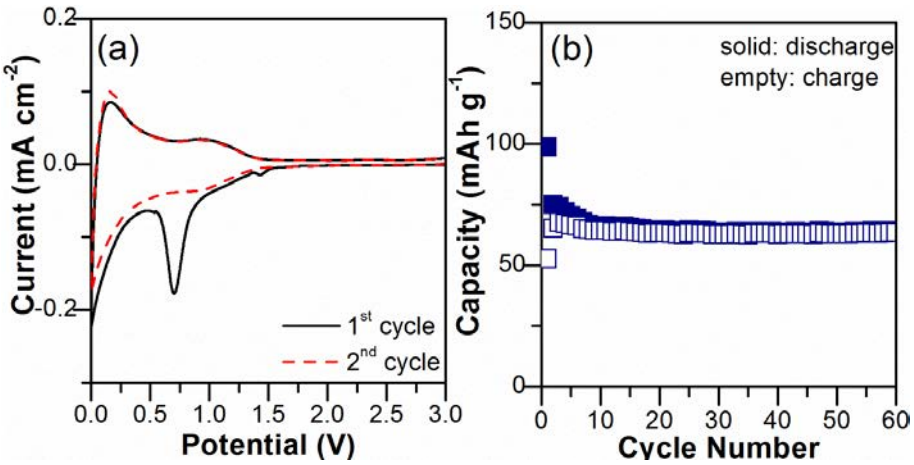

Figure 4-51 Battery performance of commercial MgO powder (Sigma Aldrich). (a) CV scan at 0.1 mV s^{-1}, (b) cyclability at 60 mA g^{-1}.

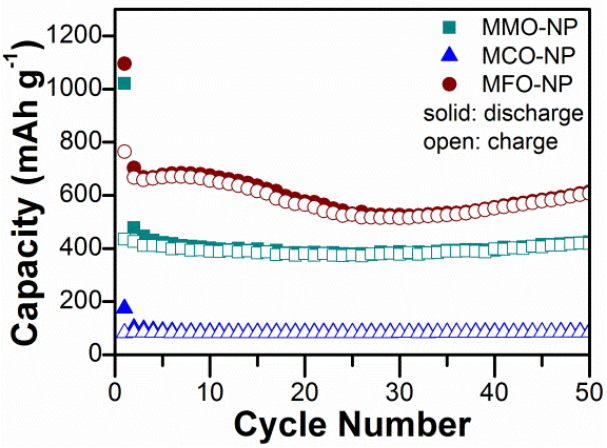

Figure 4-52 Cyclability of MgB_2O_4 (B: Mn, Cr and Fe) at current density of 60 mA g^{-1}.

Due to the fact that MgO is thermodynamically stable with large negative enthalpy of formation (ΔH_f), so the reduction of Mg^{2+} to Mg^0 is impossible.[149] Therefore, MgO remains as a buffer matrix surrounding the transition metal nanograins to alleviate drastic volumetric changes and prevent their agglomeration upon cycling.[146, 150] Figure 4-51 demonstrates CV and cyclability of MgO commercial powders to support our hypothesis. The results clearly showed that MgO does not involve any reaction with lithium ions. So Fe is a better counter ion than Mn and Cr to serve highest and stable capacity in MgB_2O_4

series (Figure 4-52), although MMO-NP and MFO-NP also constantly delivered stable capacity due to the presence MgO buffer matrix.[146, 150]

4.3.5. Ball milled $ZnFe_{2-y}Cr_yO_4$ nanoparticles: Materials characterization[9]

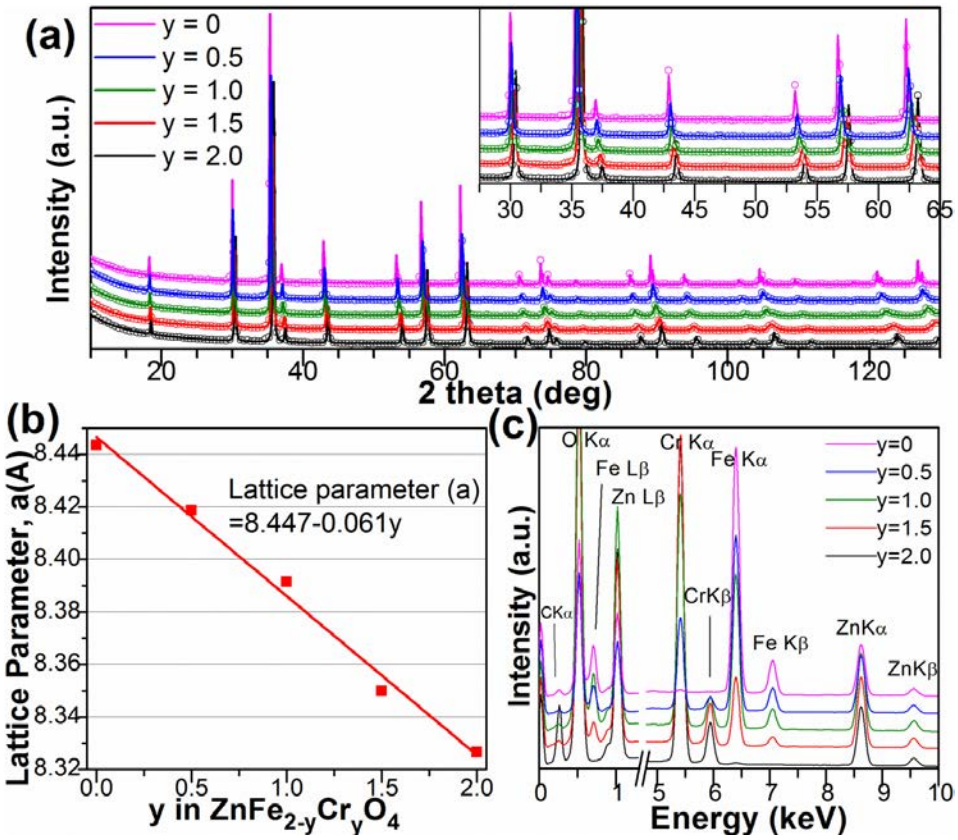

Figure 4-53 Materials characterization of annealed $ZnFe_{2-y}Cr_yO_4$ ($0 \leq y \leq 2$). (a) Experimental (dots) and calculated (full line) powder XRD patterns, the inset graph magnifies the 2θ region from 25° to 65°. (b) Cell edge (Å) of spinel as a function of Cr substitution obeys Vegard's law. (c) EDS analysis (data tabulated in Table 4-3). (Reprinted with permission from [151], Copyright 2013 American Chemical Society.)

Initially, chromium (Cr) was chosen to substitute iron (Fe) in ZnB_2O_4 spinel as $ZnCr_2O_4$ was reported to be more electrically conductive, which is a desirable property in LIB application.[73] Moreover, Cr_2O_3 disclosed a lower working voltage of ~1.058 V than Fe_2O_3 (~1.5 V).[49] As a deduction, comparably good capacity retention but lower working voltage was hypothesized after substituting Fe by Cr in the spinel structure.

[9] Reprinted with permission from[151] Teh, *et al.*, *Electrochemical Reactivity with Lithium of Spinel-type $ZnFe_{2-y}Cr_yO_4$ ($0 \leq y \leq 2$).* The Journal of Physical Chemistry C. **117**(46): p. 24213-24223. Copyright 2013 American Chemical Society.

Contradictorily, ACr_2O_4 (A: Zn and Mg) synthesized by both electrospinning (Section 4.2.8) and HEBM methods (Section 4.3.2 and Section 4.3.4) delivered an extremely low capacity which may merely contributed by conductive carbon. As of yet, the underlying reason of inactive ACr_2O_4 in electrochemical measurements is not justified in literature. Since $ZnFe_2O_4$ was witnessed to be promising LIB anode, a systematic study of $ZnFe_{2-y}Cr_yO_4$ ($0 \leq y \leq 2$) solid solution series is revealed in this section to understand the impact of counter ion within spinels on their electrochemical reactivity towards lithium ion.

XRD patterns (Figure 4-53(a)) show that $ZnF_{e2-y}Cr_yO_4$ are highly crystalline and phase-pure, crystallizing in a cubic spinel structure ($Fd\bar{3}m$ space group). The lattice parameters, bond lengths and coordinate of oxygen (u) were extracted from Rietveld refinements (Table 4-3). The unit cell dimensions decreased with Fe/Cr ratio, as expressed by the shift of XRD peaks to higher 2θ. These results are in good agreement with the smaller ionic radius of Cr^{3+} (0.62 Å) than Fe^{3+} (0.645 Å),[141] and with previously reported data.[72, 73, 78, 152] Figure 4-53(b) plots the change of lattice parameters as a function of Cr substitution; the trend followsd Vegard's law.[153] Lower Fe/Cr ratio also reduced the B-O distance, but the A-O distance remained rather invariable at ~1.97-1.98 Å (Table 4-3), indicating that Cr replaced Fe on the B-site and the oxides remained as normal spinels regardless of Cr (y) content. EDS analysis revealed stoichoimetric ratios of Zn, Cr and Fe that agreed with the initial starting ratio during sample preparation (Figure 4-53(c) and Table 4-3). The microstructure of the annealed $ZnF_{e2-y}Cr_yO_4$ was shown in Figure 4-54; they were all composed of fine and uniform particles of 200-400 nm size.

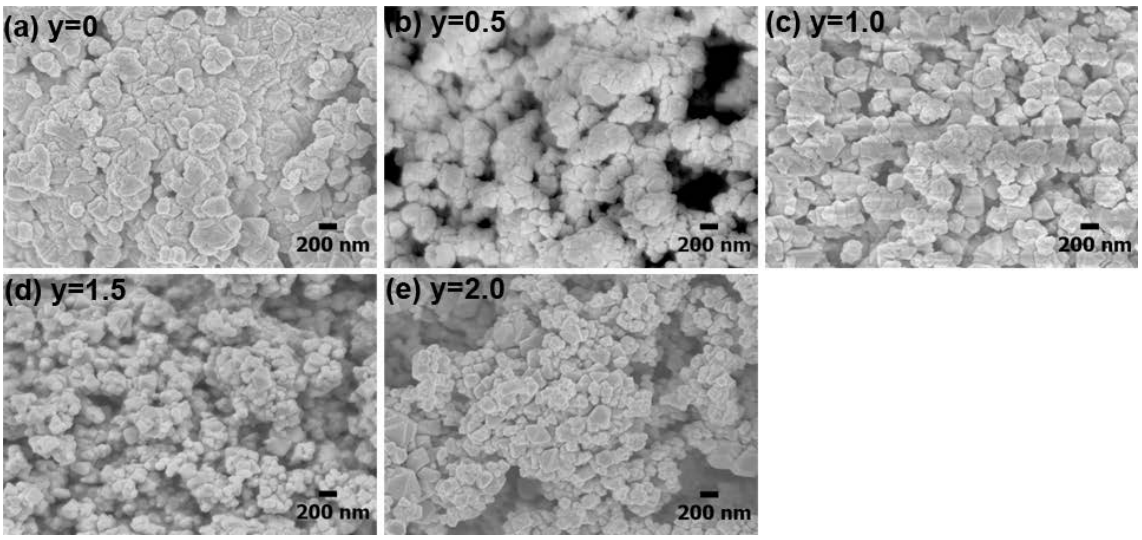

Figure 4-54 FESEM micrographs of annealed $ZnFe_{2-y}Cr_yO_4$ ($0 \leq y \leq 2$). (Reprinted with permission from [151], Copyright 2013 American Chemical Society.)

Table 4-3 Results of Rietveld refinement of annealed $ZnFe_{2-y}Cr_yO_4$ solid solution series: lattice parameter (Å), coordinate of oxygen (u), bond distance of A-O and B-O, R_B and R_{wp} were tabulated. $R_{wp} = sqrt[\sum |I_o - I_c|^2 w]$, w = weighting factor, $R_B = sqrt[\frac{\sum |F_o^2 - F_c^2|}{\sum F_o^2}]/100$. (Reprinted with permission from [151], Copyright 2013 American Chemical Society.)

y	Lattice parameter	Calculated distance between A-O	Calculated distance between B-O	u (O)	R-Bragg (R_B)	R-weighted pattern (R_{wp})	Ratio of Zn:Fe:Cr from EDS
	Å	Å	Å				at%
0	8.4436(1)	1.974(6)	2.030(3)	0.3850(4)	0.86	3.62	1:1.96:0.02
0.5	8.4186(4)	1.980(4)	2.018(2)	0.3858(3)	0.62	3.25	1:1.43:0.54
1.0	8.3915(2)	1.980(6)	2.008(3)	0.3863(4)	0.67	3.10	1:0.95:1.04
1.5	8.3498(2)	1.971(3)	2.000(2)	0.3864(2)	0.55	3.47	1:0.47:1.54
2.0	8.3266(4)	1.972(4)	1.989(2)	0.3867(3)	0.83	4.44	1:0.01:1.93

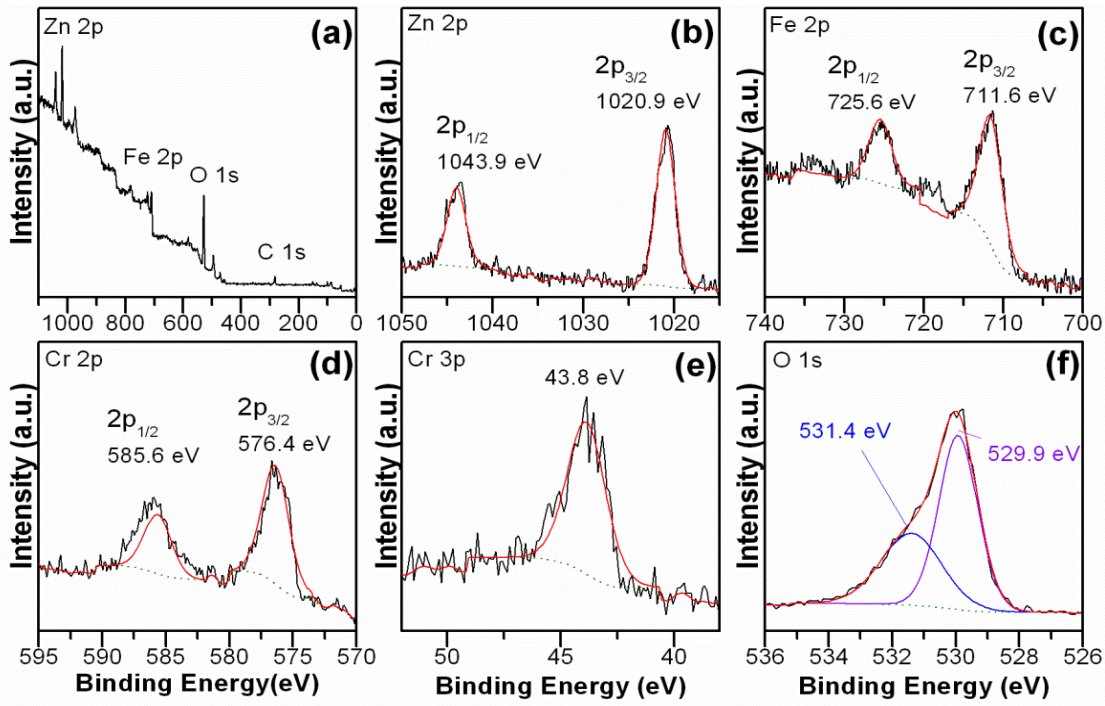

Figure 4-55 XPS spectra of the annealed $ZnFe_{2-y}Cr_yO_4$ samples. (a) The survey scan of $ZnFe_2O_4$ (y=0), and its (b) Zn 2p, (c) Fe 2p core levels. (d) Cr 2p, (e) Cr 3p and (f) O 1s are the core level regions captured from $ZnCr_2O_4$ (y=2.0) samples. (Reprinted with permission from [151], Copyright 2013 American Chemical Society.)

XPS was conducted to investigate the oxidation states of annealed $ZnFe_{2-y}Cr_yO_4$ samples. Figure 4-55(a) shows the survey scan of annealed $ZnFe_2O_4$ (y=0), which revealed the presence of Zn, Fe, O and adventitious carbon. The Zn 2p spectrum showed two peaks at ~1043.9 eV and ~1020.9 eV (Figure 4-55(b)), corresponding to Zn $2p_{1/2}$ and Zn $2p_{3/2}$ levels, respectively.[132] In Figure 4-55(c), Fe $2p_{1/2}$ and Fe $2p_{3/2}$ levels was appeared at

~725.6 eV and ~711.6 eV respectively with a shakeup satellite at ~718.6 eV, these values are also coherent with the published data of Fe^{3+} in Fe_2O_3.[154] Valence states of Zn^{2+} and Fe^{3+} was proposed based on these data. The analysis of Cr 2p peaks was complicated by interference with Zn LMM Auger lines (Figure 4-55(d)).[155] Thus, Cr 3p lines were measured (Figure 4-55(e)). Both Cr $2p_{3/2}$ and Cr 3p binding energies (~577.4 eV and ~43.8 eV) were in agreement with previous reports of Cr^{3+} with no evidence of mixed valence states.[155] XPS spectrum of O 1s of $ZnCr_2O_4$ (Figure 4-55(f)) is deconvoluted into two distinct peaks at ~529.9 eV and ~531.4 eV. Intense peak at ~529.9 eV may be related to the metal-OH bonding or adsorbed moisture on the surface, whereas the latter peak can be attributed to the oxygen atoms in the spinel lattice.[155] Full XPS analysis of $ZnFe_{2-y}Cr_yO_4$ series were provided in Appendix. In summary, all samples contained single oxidation peaks of Zn^{2+}, Fe^{3+}, Cr^{3+} and O^{2-}.

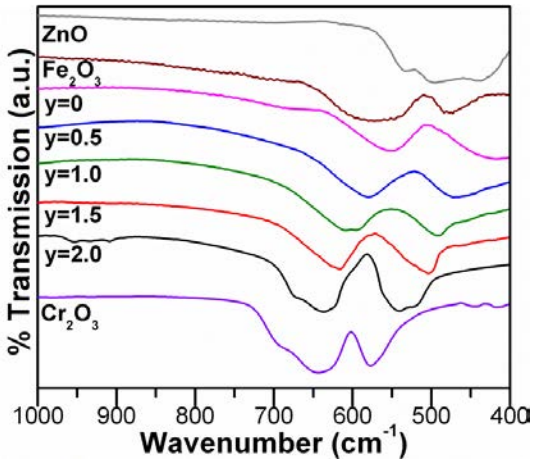

Figure 4-56 FTIR spectra of annealed $ZnFe_{2-y}Cr_yO_4$. ZnO, Fe_2O_3 and Cr_2O_3 were taken. (Reprinted with permission from [151], Copyright 2013 American Chemical Society.)

FTIR spectra were recorded from 1000 cm^{-1} to 400 cm^{-1} (Figure 4-56), as signals in this range are generally attributed to the vibration bands of metallic ions in the crystal lattice. ZnO, Fe_2O_3 and Cr_2O_3 were also analyzed as references. The spectrum of ZnO shows characteristic absorptions by Zn^{2+}-O^{2-} bonds at ~537 cm^{-1} and 438 cm^{-1}.[156] Fe^{3+}-O^{2-} vibration peaks were found at ~570 cm^{-1} and ~480 cm^{-1} for Fe_2O_3, whereas Cr_2O_3 also exhibited Cr^{3+}-O^{2-} bands at ~574 and 643 cm^{-1}, which were consistent with literature reports.[144, 157] Two intense peaks were observed between ~650 cm^{-1} and 400 cm^{-1} for each $ZnFe_{2-y}Cr_yO_4$ sample, the specific shift depending on Cr substitution (y). The peaks within this range are due to different modes of concerted vibration of the bonds around both sites in the spinel structure.[158] $ZnCr_2O_4$ (y=2.0) exhibits absorption at ~640 cm^{-1} and ~530 cm^{-1}, these peaks show qualitative resemblance to the earlier analysis by Yoon

et al.[157] A red shift of the whole spectra was noticed upon introduction of Fe; vibration modes were observed at ~550 cm^{-1} and ~430 cm^{-1} when y=0 ($ZnFe_2O_4$). This behaviour suggests bonding in the structure is affected by the ratio between Fe and Cr,[73] presumably reflecting changes in covalence in the compound.

XAS was conducted on $ZnFe_{2-y}Cr_yO_4$ to determine the local unoccupied electronic structure after transition metal cation substitution. The spectra can be found in Figure 4-57(a)-(d). O *K*-edge spectra of FeO, Fe_3O_4, Fe_2O_3, Cr_2O_3 and ZnO were also collected. The signals between 526 eV and 532 eV (marked in Figure 4-57(a)) are assigned to the unoccupied O 2p orbitals hybridized to either Fe or Cr 3d states with t_{2g} and e_g symmetry, whereas the broader feature at higher energy range can be ascribed as bonding to Fe or Cr 4s/4p states.[125] The former states provide an indication about the position of the Fermi level with respect to the continuum. In $ZnFe_2O_4$ (y=0) and $ZnCr_2O_4$ (y=2), these spectral features are reminiscent of those of Fe_2O_3 and Cr_2O_3, respectively, suggesting that Fe and Cr within the spinel structure exhibit similar structural symmetry and valence to these binary oxides. The O 2p-Fe t_{2g} states in $ZnFe_{2-y}Cr_yO_4$ appeared at 527.5 eV when y≤1.5; yet the second peak of the doublet is forward-shifted from 528.9 eV to 529.7 eV by increasing Cr ratio, a phenomenon that is taken as indication of 3d electron transfer from Fe-e_g state (d^5) to Cr-t_{2g} state (d^3), which lie at higher energy energy (see Fe_2O_3 *versus* Cr_2O_3). The splitting between t_{2g} and e_g states (Δd) was measured to be ~ 1.4 eV in y=0, which is identical th the value found in Fe_2O_3. It became larger with increasing Cr^{3+} ratio: ~1.5 eV in y= 0.5, ~1.7 eV in y=1.0, ~2.1 eV in y=1.5 and ~3.2 eV in y=2.0. It is worth noting that these t_{2g}/e_g states appeared at higher energy for $ZnCr_2O_4$ than for Cr_2O_3, indicating stronger hybridization and thus higher covalence in the ternary oxide. The O 2p states bonded with Zn 4s in ZnO resulted in a broad band starting at ~532.5 eV,[124] whereas the sharp peak at ~540 eV was assigned to non-dispersive O $2p_z$ and $2p_{x+y}$ states.[159] Thus, the O 2p unoccupied states hybridized with Zn^{2+} appear at higher energy range than Fe^{3+} and Cr^{3+} because the 3d orbitals are fully occupied in Zn^{2+} (d^{10}) ions. Finally, two additional peaks at ~533.1 eV and 535.9 eV were consistently noticed in $ZnFe_{2-y}Cr_yO_4$. They are proposed to result from O 2p-Fe/Cr 3d and O 2p-Zn 4s intra-hybridization based on a previous study of (Zn, Cr)O films.[159]

Figure 4-57(b) shows the Zn *L*-edge of $ZnFe_{2-y}Cr_yO_4$ and ZnO. The peak at 1029.9 eV is ascribed to the Zn 2p → 4s transition in ZnO, which was consistently observed in the whole series of $ZnFe_{2-y}Cr_yO_4$. A new peak visible at 1026.5 eV emerged in spinel samples

and this feature was also reported in $Zn_xFe_{3-x}O_4$.[160] As presented in the inset of Figure 4-57(b), peak intensity increased with Cr^{3+} (d^3) content, indicating the alternation of the FeO_6 octahetra by Cr^{3+} replacement also affects the chemical environment of Zn^{2+}, in agreement with the FTIR analysis **(**Figure 4-56). The higher binding strength (shorter B-O distance, refer to Table 4-3) of Cr^{3+}-O^{2-} compared to Fe^{3+}-O+ bonds leads to more significant O 2p electron hybridization, and thus covalence in $ZnCr_2O_4$.

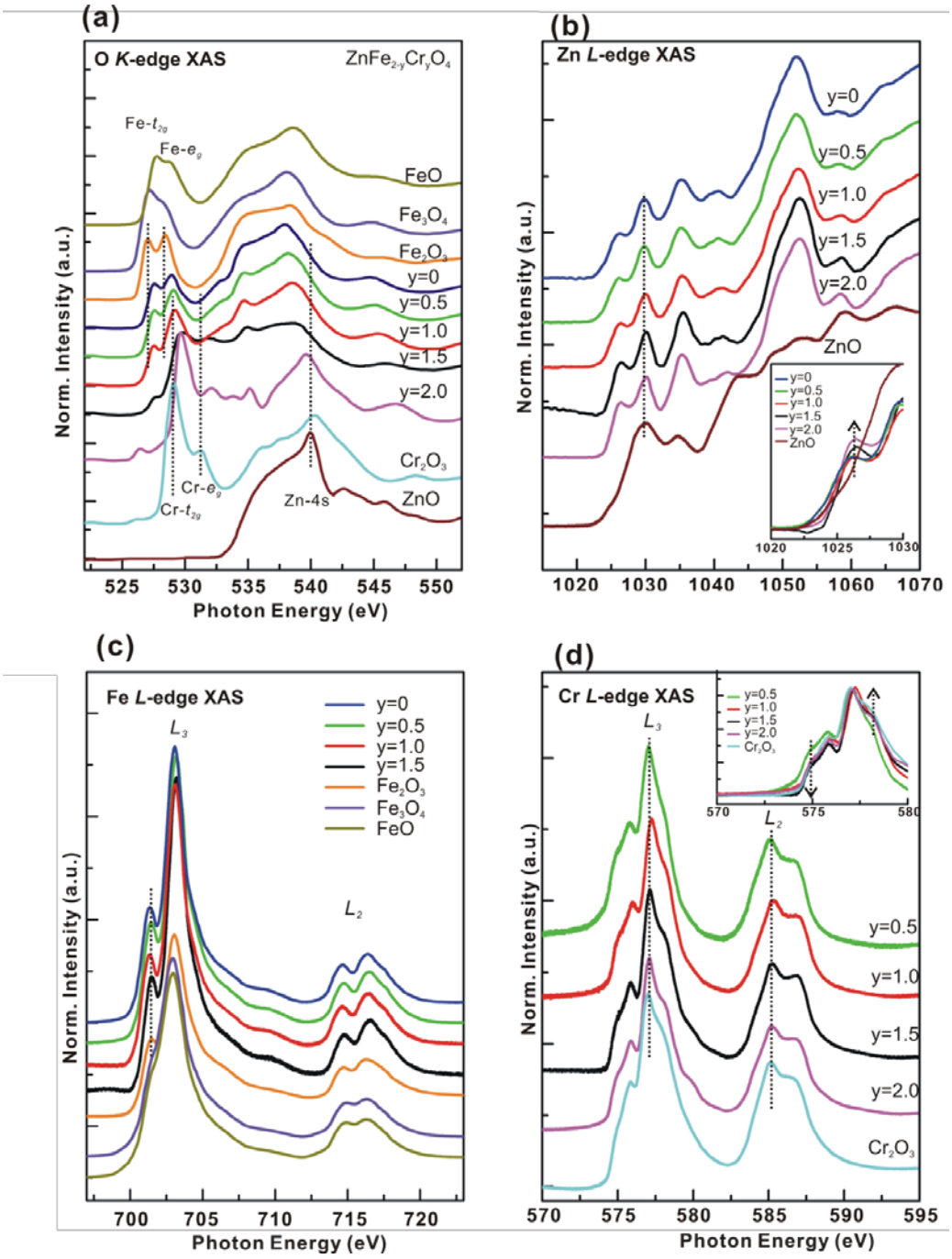

Figure 4-57 XAS studies of $ZnFe_{2-y}Cr_yO_4$. (a) O *K*-edge (b) Zn *L*-edge (c) Fe *L*-edge (d) Cr *L*-edge spectra, standard samples (FeO, Fe_3O_4, Fe_2O_3, ZnO, and Cr_2O_3) were used for quantitative comparison. (Reprinted with permission from [151], Copyright 2013 American Chemical Society.)

4.3.6. Ball milled $ZnFe_{2-y}Cr_yO_4$ nanoparticles: Comparison of electrochemical performance[10]

The voltage *versus* specific capacity curves in the 1st, 10th and 100th cycle of $ZnFe_{2-y}Cr_yO_4$ in cells against Li metal are plotted in Figure 4-58(a), (b) and (c), respectively. The first galvanostatic discharge curve of $ZnFe_2O_4$ was characterized by a long plateau, followed by a sloping region until the low cut off voltage (5 mV). The voltage of the first discharge plateau decreased steadily with Cr content, the same features and trends were also observed by CV (Figure 4-58(d) and summary in Table 4-4), with the exception of a small peak at ~0.2 V in y=0, which was not resolvable in the galvanostatic curves. This feature, which was assigned to the alloying reaction between Li and Zn,[107] was buried by the main reduction peak as the Cr content increased. In general, the theoretical voltage of an electrode process is related to the Gibbs free energy involved in the redox reaction of the transition metal oxides.[49, 102] However, significant deviations were reported in conversion reaction due to factors that remain to be fully uncovered.[20] Nonetheless, as expected, there is a direct impact on battery working voltage when the B cations in ZnB_2O_4 are substituted in our system of study. The gradual decrease in discharge/charge voltages is due to the increasing amount of Cr^{3+} over Fe^{3+}, since Cr_2O_3 gets reduced at a lower voltage (~0.2 V) than Fe_2O_3 (~0.8 V) (Table 2-6). All in all, the analysis of the electrochemical profiles reveals the possibility of tuning the working voltage of a conversion electrode by selecting a combination of transition metals in spinel structure.

The Fe *L*-edge XAS spectra of $ZnFe_{2-y}Cr_yO_4$ together with FeO, Fe_3O_4, and Fe_2O_3 are shown in Figure 4-57(c). The spectra contain L_3 and L_2 edges centered at ~703.0 eV and ~715.5 eV, respectively, which are a result of spin-orbit coupling. These states are split by crystal field, leading to multiplet.[126] Fe^{3+} in octahedral site of Fe_2O_3 shows a feature at ~701.3 eV adjacent to the main L_3 peak, which is absent in octahedral symmetry of FeO (Fe^{2+}) and both tetrahedral and octahedral symmetry of Fe_3O_4 (Fe^{2+} and Fe^{3+}). The spectra of $ZnFe_{2-y}Cr_yO_4$ (y=0-1.5) exhibited similar shoulder, consistent with Fe^{3+} in an octahedral symmetry in the spinel structure. The rest of the spectral features in the ternary phases also ressemble Fe_2O_3. Finally, Cr *L*-edge XAS spectra of $ZnFe_{2-y}Cr_yO_4$ and Cr_2O_3 can be found in Figure 4-57(d). The significant similarities between all spectra imply a

[10] Reprinted with permission from[151]. Copyright 2013 American Chemical Society.

similar chemical environment as well as valence state.[126] Upon close inspection, it was found that the additional features around the main L_3 peak have relatively lower intensity at 575.0 eV and higher intensity at 578.0 eV upon increasing the Cr content (see inset of Figure 4-57(d)). At higher y, the Cr spectra of $ZnFe_{2-y}Cr_yO_4$ were found to be remarkably similar with Cr_2O_3. In conclusion, Cr^{3+} ions substitute Fe^{3+} and preserve the octahedral symmetry, whereas Zn^{2+} ions remain in a tetrahedral environment. However, Cr substitution affects their chemical environment by increasing O 2p hybridization.

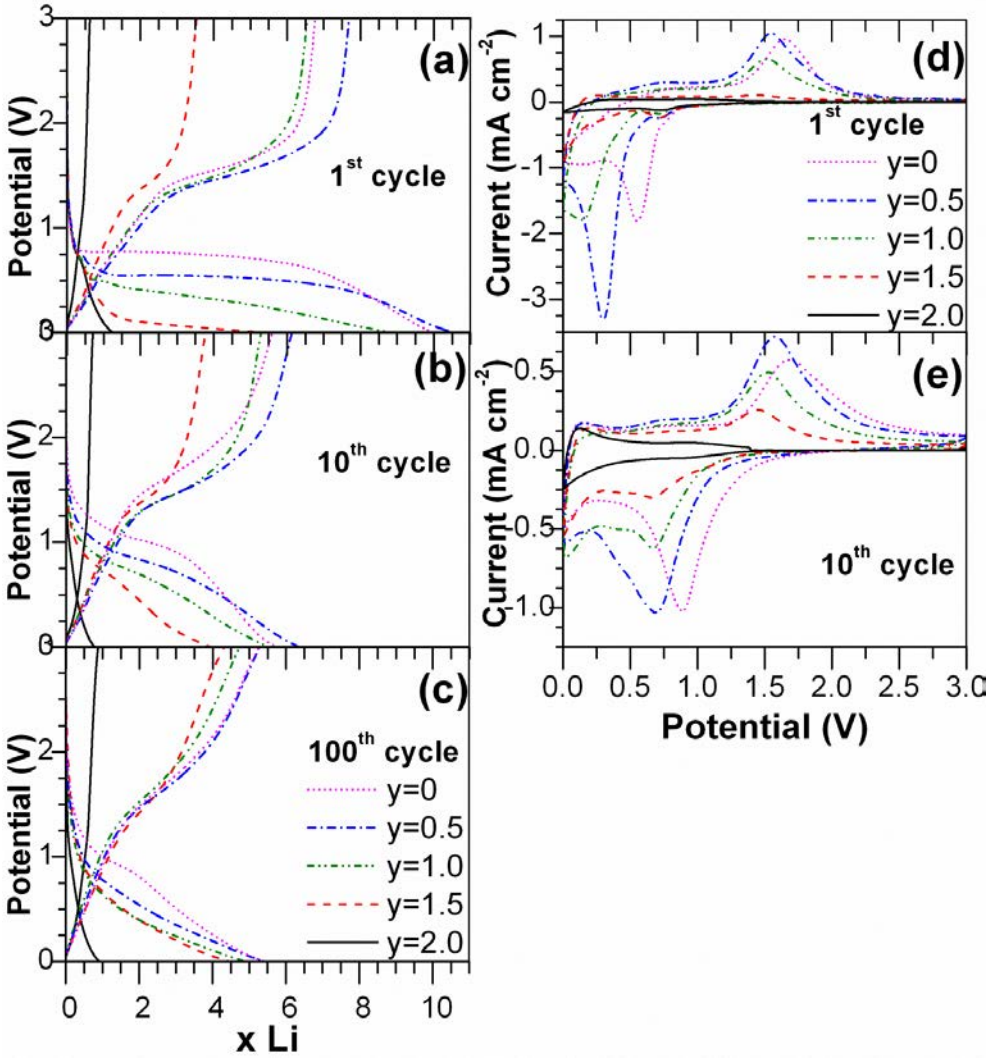

Figure 4-58 Galvanostatic cycling data of $ZnFe_{2-y}Cr_yO_4$ at current density of 60 mA g^{-1} at (a) 1st cycle, (b) 10th cycle and (c) 100th cycle, the capacities of spinels declines significantly with Cr ratio. CV of $ZnFe_{2-y}Cr_yO_4$ at scan rate of 0.1 mV s^{-1}: (d) 1st cycle and (e) 10th cycle. (Reprinted with permission from [151], Copyright 2013 American Chemical Society.)

The charge profile showed a certain degree of symmetry as discharge, with a sloping region followed by a long pseudo-plateau above 1 V. This plateau also shifted to lower voltages with Cr substitution, albeit in a much less pronounced manner than on discharge

(Table 4-4). Close inspection of the CVs again revealed an extra oxidation peak at ~0.15 V, especially for y=0, which was assigned to the dealloying reaction in LiZn.[107]

Table 4-4 Summary of battery performance of $ZnFe_{2-y}Cr_yO_4$ particles at first cycle of galvanostatic discharging/charging and first CV scan. (Reprinted with permission from [151], Copyright 2013 American Chemical Society.)

y	x Li				Working voltage (V)			
	1st discharge	1st charge	10th discharge	10th charge	1st discharge	1st charge	10th discharge	10th charge
0	10.00	6.77	5.73	5.63	0.55	1.67	0.88	1.69
0.5	10.54	7.70	6.34	6.16	0.30	1.55	0.69	1.58
1.0	8.82	6.55	5.50	5.32	0.15	1.52	0.67	1.53
1.5	5.34	3.53	3.92	3.81	n.a.	1.45	0.67	1.45
2.0	1.24	0.62	0.77	0.74	n.a.	n.a.	n.a.	n.a.

'n.a': the plateau/redox peaks cannot be identified unambiguously.

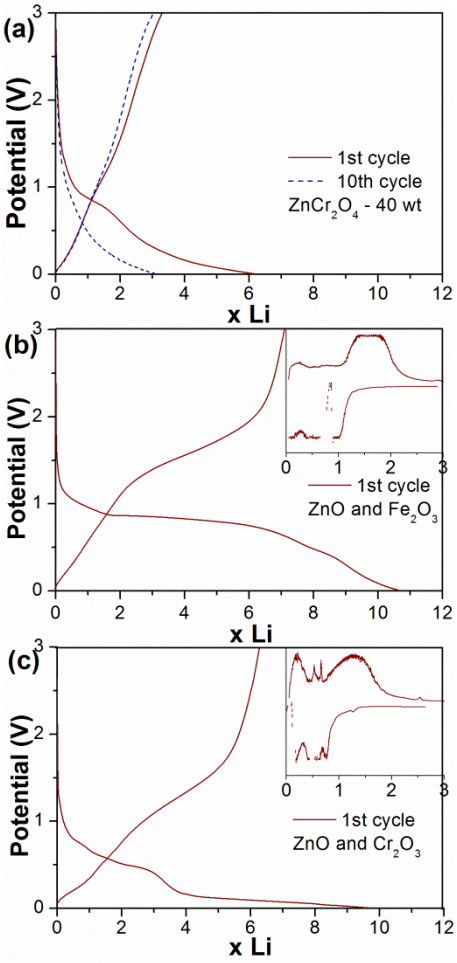

Figure 4-59 First discharge/charge behaviors of (a) $ZnCr_2O_4$ with different weight ratio of conductive carbon (either 20 wt% or 40 wt% of the overall electrode mass). First cycle of (b) ZnO and Fe_2O_3 and (c) ZnO and Cr_2O_3 composites. All measurements were conducted at current density of 60 mA g^{-1}. Inset depicts the corresponding dq/dV (mAh g^{-1} V^{-1}) *versus* voltage curves to derive the discharge/charge working voltages. (Reprinted with permission from [151], Copyright 2013 American Chemical Society.)

Both the discharge and charge capacity of the electrodes were largely unaffected up to $y \leq 1.0$, yet decreased significantly at high Cr content. Indeed, the $ZnCr_2O_4$ electrode reacted with merely ~1.24 moles of Li ion equivalents per unit formula during the first reduction, instead of the 9 moles predicted based on the experience on $ZnFe_2O_4$ electrode. The corresponding CV scan (Figure 4-58(d)) only showed an extremely shallow peak at ~0.8 V with no other reduction peak could be unambiguously identified. The ratio of carbon in the electrode was doubled from 20 to 40 wt% to ensure electronic conductivity was not driving the poor performance. The result was an increase in capacity during the plateau at ~0.8 V (Figure 4-59(a)), but this capacity was extremely irreversible. Highly irreversible processes at these voltages are commonly associated with the decomposition of the organic electrolyte on the surface of the electrode, especially the carbon additive.[20, 161] Thus, the increase in capacity was simply ascribed to an enhanced electrolyte reaction caused by the increment of carbon content in the electrode. It would appear that $ZnCr_2O_4$ is largely inactive in these conditions.

In order to better understand the activity of $ZnFe_2O_4$ and $ZnCr_2O_4$, it was compared to electrodes made of physically mixed ZnO and M_2O_3 (M=Fe or Cr) at 1:1 molar ratio (*i.e.*, the same Zn/M ratio as in the spinel phase). As shown in Figure 4-59(b), ZnO and Fe_2O_3 delivered comparable capacities to $ZnFe_2O_4$. The discharge and charge profiles were also very similar with all the processes taking place at almost same voltages. It is interesting to note that only one broad process was found centered at ~1.5 V in the first charge, which suggests that both Zn and Fe oxidize at adjacent potentials. On the other hand, ZnO and Cr_2O_3 electrodes showed a very high activity, in stark contrast to $ZnCr_2O_4$ (Figure 4-59 (c)). The initial discharge capacity was ~1115 mAh g^{-1} (~9.7 moles of Li), which is close to the theoretical value of 1034 mAh g^{-1} (9 moles of Li) for full conversion with subsequent Li-Zn alloying; a lower capacity of ~724 mAh g^{-1} (~6.3 moles of Li) was obtained on charge. Two discharge plateaus at ~0.48 V and ~0.11 V were observed during first reduction, which can be assigned to the sequential reaction of ZnO and Cr_2O_3.[101, 106] Upon oxidation, dealloying process of LiZn was identified by an anodic peak at ~0.2 V in the derivative curve of both mixtures. Additional oxidation peaks at ~0.54 V and ~0.64 V were proposed to be part of a multistep dealloying process.[107] A very broad peak centered at ~1.29 V can be attributed again to the smearing of Zn and Cr re-oxidation voltages. None of these peaks were found in $ZnCr_2O_4$, suggesting binary oxide composite reacts with lithium differently.

The trends in voltage *versus* capacity profiles of $ZnFe_{2-y}Cr_yO_4$ at 10th and 100th cycles are in agreement with the first cycle (Figure 4-58(b) and (c)), yet even lower capacities were observed. Furthermore, the charge voltages in the 1st and 10th cycle were similar, but the reduction potentials were found to be higher in the 10th than during the 1st discharge. This displacement is also common in conversion electrodes.[20] The cycling performance for all samples was plotted in Figure 4-60. All $ZnFe_{2-y}Cr_yO_4$ (y = 0, 0.5, 1.0 and 1.5) exhibited comparable specific capacity retention after 50th cycles with the values stabilizing at ~612 mAh g^{-1}, ~637 mAh g^{-1}, ~553 mAh g^{-1} and ~504 mAh g^{-1}, respectively. When y = 2.0, a very low capacity of ~91 mAh g^{-1} was observed throughout the 50 cycles. Hence, it would strongly appear that $ZnCr_2O_4$ is inherently inactive, supported by comprehensive *ex situ* characterization in Section 5.2.5.

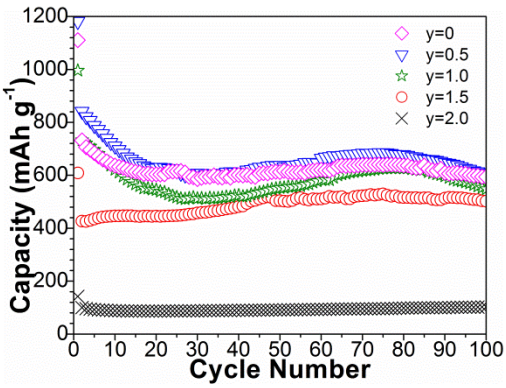

Figure 4-60 Cycling performance of $ZnFe_{2-y}Cr_yO_4$ particles at 60 mA g^{-1}. (Reprinted with permission from [151], Copyright 2013 American Chemical Society.)

4.4. Application of Ball Milled $ZnMn_2O_4$ and $ZnFe_2O_4$ Particles as Anodes in Full LIB

To validate the applicability of the spinel-based anode in LIB, ball milled $ZnMn_2O_4$ (ZMO-NP) and $ZnFe_2O_4$ (ZFO-NP) were assembled *versus* $LiFePO_4$ cathode as LIB full cell. As the first discharge of conversion-based anodes experienced structural reorganization and SEI formation which consumes much higher lithium than its first charge, so ZMO-NP and ZFO-NP were first discharged in half cell configuration *versus* lithium metal and recovered to be assembled together with $LiFePO_4$ at a mass ratio of 1:3, with $LiFePO_4$ as limiting active materials. CV of $LiFePO_4$/ZMO-NP exhibited main oxidation and reduction peaks at ~3.6 V and 3.3 V, respectively. Another pair of broader

redox peaks was centered at ~2.9 V and 2.3 V (Figure 4-61(a)). $LiFePO_4$/ZFO-NP also encountered similar redox process, since their half cells demonstrated alike cycling behaviours (Figure 4-61(b)). Subsequently, no indicative changes can be verified from CV, implying the reactions are highly reversible.

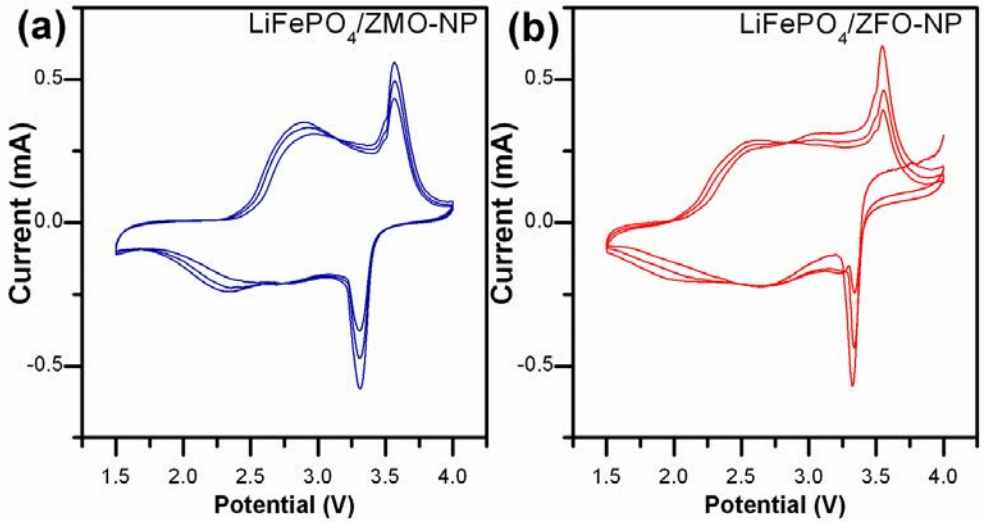

Figure 4-61 CV of full LIB cell. (a) $LiFePO_4$/ZMO-NP and (b) $LiFePO_4$/ZFO-NP atscan rate of 0.1 mV s^{-1}.

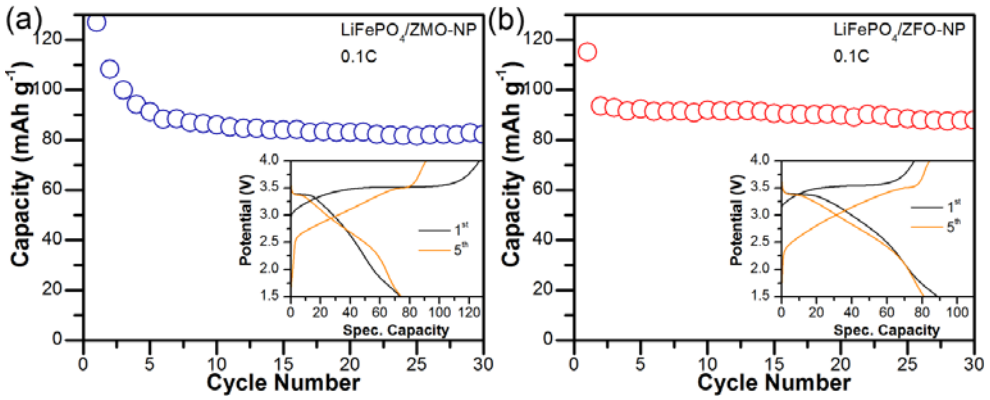

Figure 4-62 Cyclability of full LIB cell. (a) $LiFePO_4$/ZMO-NP and (b) $LiFePO_4$/ZFO-NP at 0.1C. (Inset) Corresponding first and fifth charge/discharge behaviors.

Reversible capacities of $LiFePO_4$/ZMO-NP and $LiFePO_4$/ZFO-NP were found to be comparable with $LiFePO_4$/ZFO-NP achieved ~10 mAh g^{-1} higher than $LiFePO_4$/ZMO-NP. After 30 cycles, $LiFePO_4$/ZMO-NP revealed ~65% of initial cycle, whereas $LiFePO_4$/ZFO-NP demonstrated a higher efficiency of ~76% despite its lower initial capacity. The presented results were only preliminary observation of conversion-based anodes in full LIB, there are still plenty of room to further improve their performance, such as mass ratio optimization, investigation on their reaction pathway.

Chapter 5 Discussions

This chapter is categorized into three sections. The influence of using nanostructured materials as LIB anodes is discussed in the first section and the optimum mass loading and particle size required to produce improved and reliable battery results are suggested. The performance between 1D nanofibers and 0D ball milled particles were intercompared. Advantages of having high aspect ratio fibrous morphology prepared by electrospinning are also emphasized.

Since the amorphization process experienced by TMOs during conversion reaction results in the formation of nanocrystalline products embedded in amorphous Li_2O matrix, it brings the difficulties in determining their reaction mechanisms. Hence, several spinel-based TMOs were examined by comprehensive characterization techniques in second section to reliable hypothesize their lithium activities.

The third section focuses on the impact of counter ion (either A or B-sites in AB_2O_4 spinels) substitution on the battery performance, revealing the competitive advantages of having mixed TMOs than binary oxides. Electrochemical performances of all previously presented spinels are evaluated; the results show that spinel-based anodes provide the feasibility to tune the battery performance by altering the counter ion.

5.1. Effect of Nanostructuring in Conversion Reaction

5.1.1. Effect of Particle Size

Nanoscaling of TMOs for anode application is very crucial,[14, 48] as some novel physical and chemical properties are observed only when materials are scaled down to nanodimensions, including conversion reaction. Despite their various advantages (Section 2.5), some concerns needed to be addressed before widely utilising the nanoscaled TMOs. Nanoscaling the engineered materials with no limits cannot be the perfect solution to answer all issues faced by LIB research community. Hence, an optimum particle size that favourable for battery performance is needed to be defined (discussed in this section). Furthermore, lower volume density of nanomaterials leads to lower mass loading on a

specific electrode with fixed coating thickness as compared to micro-sized materials. Hence, active mass loading per electrode is required to be standardized when comparing the electrochemical properties (discussed in next section, Section 5.1.2).

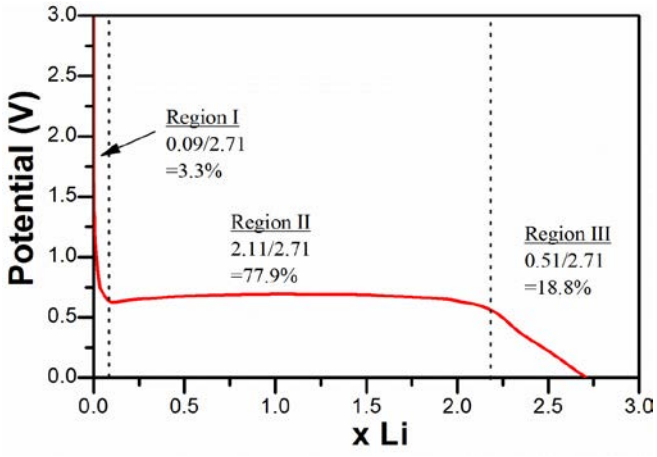

Figure 5-1 First discharge behaviour of TMOs can be categorized into three regions : (I) electrolyte decomposition, (II) amorphization, (III) interfacial storage. Commercial NiO cycled at 0.1C was taken as an example to illustrate the division of respective region.

Effect of particle size on battery performance was investigated using NiO samples prepared by different synthesis methods (refer to Section 4.1). In general, first discharge behavior of TMOs can be divided into three regions with different reaction principles with lithium ions, *i.e.* (I) decomposition of electrolyte, (II) amorphization and (III) interfacial storage by polymeric layer surrounded reduced metallic nanograins (refer to Section 2.2.3 for detailed illustration).[2, 20] The percentage of lithium activity in each region was calculated on all NiO samples cycled at both 0.05C and 0.1C as demonstrated in Figure 5-1. The galvanostatic cycling curves were shown in Figure 4-4 and the results were tabulated in Table 5-1.

When particle size was reduced (commercial NiO>NiO plates>NiO colloids), contribution from Region I and III significantly increased with gradual depletion of Region II at both 0.05C and 0.1C. This outcome implied that NiO electrodes with smaller size created more interfacial surface with electrolyte, thus electrolyte decomposition (Region I) and polymeric layer formation (Region III) were more severe. Although NiO colloids and NiO@C performed highest capacity at initial cycle, excessive side reactions may be detrimental to cause fast capacity decaying (Figure 4-5). Furthermore, NiO colloids of 10-20 nm exhibited worst coulombic efficiency, while NiO plates of ~100 nm demonstrated the optimum size range preferred in conversion reaction to increase battery efficiency (herein suggested for TMOs application in LIB), although it suffered from

agglomeration after extended cycling with the evidence of its depleting capacity. Hence, a self-assembled hierarchical structure prepared by electrospinning was suggested in this thesis (discussed in Section 5.1.3) to prepare a submicron secondary (~100 nm) structure comprising of nanocrystals which was beneficial in prohibiting agglomeration.

Table 5-1 Participation of lithium ions in each region of first discharge cycle on NiO samples cycled at current density of 0.05C or 0.1C, respectively.

Sample	Region I x Li (%)	Region II x Li (%)	Region III x Li (%)	1st Discharge x Li (mAh g^{-1})	1st Charge x Li (mAh g^{-1})	Coulombic Efficiency %
Current density = 0.05C						
Commercial NiO	0.09 (3.3%)	2.11 (77.9%)	0.51 (18.5%)	2.71 (972)	1.9 (682)	70.1
NiO Plates	0.37 (13.0%)	1.76 (61.8%)	0.72 (25.3%)	2.85 (1023)	2.32 (832)	81.4
NiO Colloids	0.47 (12.0%)	2.1 (53.4%)	1.36 (34.6%)	3.93 (1411)	2.37 (850)	60.3
NiO@C	0.78 (20.6%)	1.91 (50.3%)	1.11 (29.2%)	3.80 (1363)	2.77 (993)	72.9
Current density = 0.1C						
Commercial NiO	0.1 (3.8%)	2.05 (77.7%)	0.49 (18.6%)	2.63 (944)	1.69 (606)	64.3
NiO Plates	0.27 (10.6%)	1.53 (60.0%)	0.75 (29.4%)	2.55 (915)	2.02 (725)	79.2
NiO Colloids	0.44 (11.8%)	2.00 (53.6%)	1.29 (34.6%)	3.73 (1338)	1.97 (707)	52.8
NiO@C	0.84 (20.6%)	1.93 (47.3%)	1.31 (32.1%)	4.08 (1463)	2.55 (914)	62.5

5.1.2. Effect of mass loading on NiO performance

Lesser mass loading per electrode may affect the lithium ion participation, so this problem is tackled in this section by purposely comparing electrode with two distinctly different mass loadings.

On an electrode with 16 mm diameter, Chowdari *et al.*[3] suggested that active mass shall be 3-5 mg (equivalent to 1.5 – 2.5 mg cm^{-2}) to ensure reliable and fair battery data. Hence, commercial NiO electrodes were purposely prepared with different mass loadings of 1.65 mg cm^{-1} and 0.33 mg cm^{-1}. All comparison was shown in Figure 5-2 and Table 5-2. In the case of 1.65 mg cm^{-2}, participations of each region were similar regardless of C rate. On contrary, electrodes with 0.33 mg cm^{-2} experienced remarkably different coulombic efficiency at different C rate (97.2% at 0.05C, whereas 70.1% at 0.1C). Although NiO with mass loading of 0.33 mg cm^{-1} achieved higher capacities and efficiencies, side

reactions in Region I and Region III experienced a substantial increment. Hence, a mass loading of ~1.65 mg cm^{-2} was used throughout this thesis to minimize discrepancy and obtain good quality of battery data.

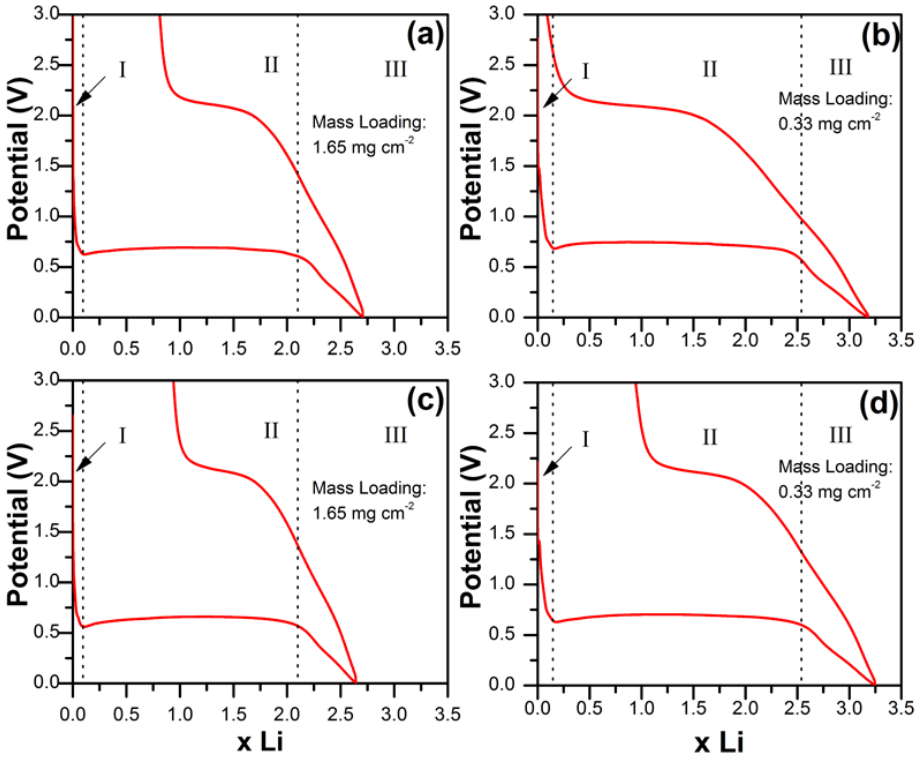

Figure 5-2 First cycling behavior of commercial NiO with different mass loadings of 1.65 mg cm^{-2} and 0.33 mg cm^{-2} tested at (a) and (b) 0.05C and (c) and (d) 0.1C, respectively.

Table 5-2 Lithium participation of NiO with different mass loadings in each region at current density (0.05C and 0.1C).

Mass Loading	Region I x Li (%)	Region II x Li (%)	Region III x Li (%)	1st Discharge x Li (mAh g^{-1})	1st Charge x Li (mAh g^{-1})	Coulombic Efficiency %
Current density = 0.05C						
1.65	0.09 (3.3%)	2.11 (77.9%)	0.51 (18.5%)	2.71 (972)	1.9 (682)	70.1
0.33	0.17 (5.4%)	2.11 (72.3%)	0.71 (22.3%)	3.18 (1141)	3.09 (1109)	97.2
Current density = 0.1C						
1.65	0.1 (3.8%)	2.05 (77.7%)	0.49 (18.6%)	2.63 (944)	1.69 (606)	64.3
0.33	0.15 (4.6%)	2.58 (79.6%)	0.51 (15.8%)	3.24 (1164)	2.29 (822)	70.1

5.1.3. Effect of 1D electronic wiring in electrospun $ZnMn_2O_4$

As discussed earlier, nano/micro hierarchical electrode materials combine competitive advantages of both micro and nanomaterials,[23, 109] which helps in to preventing the existence of inactive regions by agglomeration and retains extraordinary properties brought by nanomaterials. Electrospinning is one of the synthesis methods tailored to fabricate a self-assembled parent submicron fibers (diameter of ~100-200 nm and length of several micrometers) that made up of numerous building blocks at nanodimensions (~10 nm). Significant advantages of 1D nanofibers will be resolved in following sections using $ZnMn_2O_4$ (Section 5.1.3) and $ZnFe_2O_4$ (Section 5.1.4) as case studies.

Experimental data of ZMO-NR, ZMO-NF and ZMO-NW were analyzed in Section 4.2.3. Since three samples were formed by numerous nanocrystals of similar size (Table 4-1 and Figure 4-13), we initially assumed they posses same behavior as LIB anodes. Nevertheless, when nanocrystals were hierarchically constructed into a specific morphology, *i.e.* nanorods, nanofibers or nanowebs, significantly distinguishable battery performances were observed especially after prolonged cycling (Table 5-3). Capacity retention of ZMO-NR (Figure 4-17) faded severely probably due to the lack of electronic wiring for lithium ions diffusion during discharging/charging in nanorods. On the other hand, ZMO-NW outperformed ZMO-NF and ZMO-NR at initial 25 cycles, as its interconnected framework promoted a facile transportation channel for lithium ions. Its gradual capacity fading to 514 mAh g^{-1} at 50th cycle may possibly due to the closure of pores in nanowebs by volumetric expansion in conversion reaction, leading to the loss of its unique nanostructure. ZMO-NF with high aspect ratio has the most stable cyclability.

Table 5-3 Summary of the electrospun ZMO-NR, ZMO-NF and ZMO-NW presented in Section 4.2.3. (Reproduced by permission of The Royal Society of Chemistry)

Sample	Morphology	BET surface area (m^2 g^{-1})	Capacity (mAh g^{-1})			
			1st discharge	1st charge	50th discharge	50th charge
ZMO-NR	nanorods	40	1257	681	318	313
ZMO-NF	nanofibers	44	1469	716	706	690
ZMO-NW	nanowebs	47	1526	892	530	514

Supported by CV curves (Figure 4-15), ZMO-NR has shallowest area underneath the curves with irresolvable reduction/oxidation peaks, while ZMO-NF and ZMO-NW showed two distinct oxidation peaks. It suggested that diffusion of lithium ions is least efficient in ZMO-NR than ZMO-NF and ZMO-NW. Besides, 1D wiring offered ZMO-

NF promoted lithium intercalation process prior the conversion reaction, which is first time observed in $ZnMn_2O_4$ anodes, neither observed in ball milled ZMO-NP.

Table 5-4 Impedance values of electrospun $ZnMn_2O_4$ based on Nyquist plot in Figure 4-18 using the circuit in Figure 4-19. (Reproduced by permission of The Royal Society of Chemistry)

Cycle Number	$R_{(sf+ct)}$ (±5) Ω	$CPE_{(sf+dl)}$ (±5) μF	R_b (±5) Ω	CPE_b (±0.005) mF
ZMO-NR				
0 (Bare)	57	13	---	---
2	496	13	125	0.006
5	246	12	314	0.011
10	118	218	160	0.009
ZMO-NF				
0 (Bare)	80	17	---	---
2	46	38	10	0.012
5	29	37	49	0.013
10	19	58	39	0.019
ZMO-NW				
0 (Bare)	184	18	---	---
2	34	68	206	0.013
5	71	20	148	0.013
10	115	29	213	0.014

EIS was conducted to understand the kinetic of electrodes and the factors which were responsible for capacity degradation.[30, 42, 134, 135, 162] Electrolyte resistance (R_e) remained almost constant at 6(±0.5) Ω irrespective of cycle number and morphologies of $ZnMn_2O_4$, as presumed (Table 5-4). However, $R_{(sf+ct)}$ and R_b and the associated $CPE_{(sf+dl)}$ and CPE_b were sensitive to the morphology of active materials and varied upon cycling. Impedance values of bare electrodes were noticed to be highest in ZMO-NW due to its higher surface area than ZMO-NR and ZMO-NF (Table 5-3). Penetration of electrolyte through open pores embedded in interconnected nanowebs led to greater surface film formation, and thereby high surface resistance. These results were in tune with galvanostatic cycling, in which ZMO-NW demonstrated highest first discharge capacity (Table 5-3). Major constituent of surface film in bare electrodes is the salt in electrolyte, whereas chemical composition changes upon cycling. So, SEI formation and electrolyte decomposition are essentially to be taken into account for EIS fitting after first discharge, reflected by the fluctuations of $R_{(sf+ct)}$ values in subsequent cycles.[30]

Typically, formation and integration of electrodes took place in the first few cycles of conversion reaction,[106, 163] therefore the initial associated impedance values were unstable. Besides, volumetric contraction and expansion encountered by the electrode during cycling may cause the pulverization of electrode or the agglomeration of active

materials. This phenomenon was reflected as inconsistent impedance values and capacity degradation in galvonostatic cycling.[42, 162] Herein, largest variation of impedance were noticed in ZMO-NR, more precisely, the radii of its semicircle in Nyquist plot spread significantly (Figure 4-18(a)). As a result, there might be presence of inaccessible regions within bulk electrode since nanorods were weakly connected, thus ZMO-NR with poorer electrical contact with the current collector demonstrated poor cyclability.

Similar unstable impedance was also found in ZMO-NW, even though the fluctuation was smaller. The increment of charge transfer and bulk impedances upon cycling may be caused by the closure of open pores embedded in nanowebs by volumetric expansion/contraction. In this case, unique morphology of ZMO-NW diminished and steady capacity loss was observed. It is worth noting that the impedance values derived for ZMO-NF stayed relatively lower and stable than another two samples. So, 1D ZMO-NF with continuous electronic wiring and open pores provided facile conduction pathway for lithium ions and electrons, resulting in excellent capacity retention.

5.1.4. Effect of 1D electronic wiring in electrospun $ZnFe_2O_4$

Similarly, ZFO-NR and ZFO-NF were prepared (Section 4.2.4) to emphasize the importance of 1D electronic wiring and the summary was tabulated in Table 5-5. More lithium ions intercalated into the spinel framework prior conversion reaction was found in ZFO-NF than ZFO-NR (Figure 4-26), and this phenomenon was totally absent in ZFO-NP (Figure 4-43), therefore high aspect ratio fibrous morphology are beneficial in promoting the initial intercalation. Higher capacity retention was observed in ZFO-NF than ZFO-NR at 30th cycle, probably due to the presence of 1D electronic wiring. To have deeper understanding, EIS was again conducted to verify this hypothesis.

Table 5-5 Summary of the electrospun ZFO-NR and ZFO-NF presented in Section 4.2.4. (Reproduced by permission of The Royal Society of Chemistry)

Sample	Morphology	BET surface area (m^2 g^{-1})	Capacity (mAh g^{-1})			
			1st discharge	1st charge	50th discharge	50th charge
ZFO-NR	Nanorods	31	1317	900	221	214
ZFO-NF	Nanofibers	61	1292	925	709	682

Typically, high frequency semicircle was ascribed to the surface film formation or the charge transfer phenomenon (Figure 4-29). In addition, variation in the diameter of semicircle hinted that there might be another factor which governed the distinct

impedance behavior, so the inter-particle impedance was also considered. Long ZFO-NF depicted lower $R_{(sf+IP)}$ of ~120(5) Ω, than ZFO-NR with ~226(5) Ω (Table 5-6). Owing to it, thicker polymeric film formed by organic electrolyte decomposition on ZFO-NR may prevent efficient charge transfer and lithium ion diffusion between electrolyte/electrode interfaces. It explained the worse lithium cyclability behavior of ZFO-NR (Table 5-5).

Table 5-6 Impedance of electrospun $ZnFe_2O_4$ extracted from EIS data using circuit in Figure 4-30. (Reproduced by permission of The Royal Society of Chemistry)

Impedance Parameters	Electrode Materials	
	ZFO-NF	**ZFO-NR**
R_e (±1), Ω	5	5
$R_{(sf+IP)}$ (± 5), Ω	120	226
CPE (± 5), μF	17	20

In overall, EIS analysis proved the importance of maintaining interconnected and high aspect ratio nanofibers in battery cyclability. Interwoven ZMO-NF and ZFO-NF not only offer larger electrolyte/electrode contact, but also easier and facile lithium ion diffusion. Enhanced capacities released by ZMO-NF (Table 5-3) and ZFO-NF (Table 5-5) have explained the importance of having 1D electronic wiring during lithium insertion/extraction, especially during long term cycling.

5.1.5. Comparison of electrochemical performance between 0D ball milled particles and 1D electrospun nanofibers

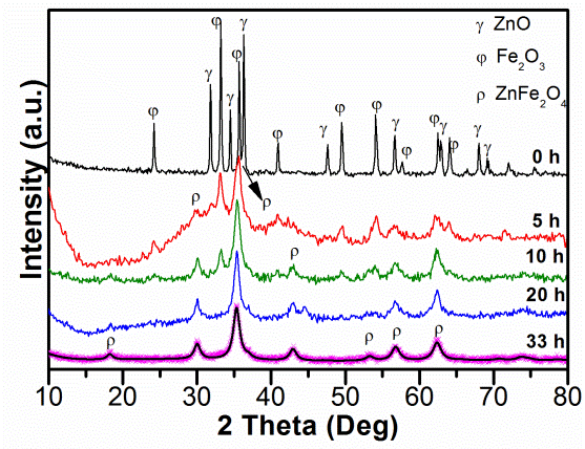

Figure 5-3 Phase transition from ZnO and Fe_2O_3 to $ZnFe_2O_4$ was observed by increasing the duration of HEBM.

Electrospun $ZnFe_2O_4$ (ZFO-NF in Section 4.2.5) presented a self-assembled hierarchical nanostructure by having nanocrystals being constructed into a secondary morphology of

~submicron sized nanofibers. Since excellent electrochemical performance was obtained, another $ZnFe_2O_4$ sample with similar nanocrystalline nature was purposely mimicked using HEBM, however the ball milled sample appeared as nanoparticles with no secondary morphology or hierarchical structure (experimental details in Section 3.1.1). Hence, the possible discrepancy in terms of battery performance between 1D nanofibers and 0D particles are addressed in this section.

Phase transition from ZnO and Fe_2O_3 composites to $ZnFe_2O_4$ particles as a function of ball milling duration was studied to obtain a single phase $ZnFe_2O_4$ spinel without undergoing any annealing post-treatment, while preserving their tiny crystallite size. In the course of ball milling, samples were retrieved intermittently for XRD analysis (Figure 5-3), ZnO and Fe_2O_3 phases gradually diminish and compensated by the appearance of $ZnFe_2O_4$ spinel phase. After 33 h, pure phase $ZnFe_2O_4$ was observed. Lattice parameter was refined by Rietveld method to be ~8.423(3) Å (space group: $Fd\bar{3}m$), which is in good agreement with 8.431(5) Å (ICSD code 91829). The peak broadening was due to continuous mechanical fragmentation and the crystallite size was found to be ~6.6(3) nm by Rietveld refinement, which is close to the value obtained in ZFO-NF (~8.3(1) nm).

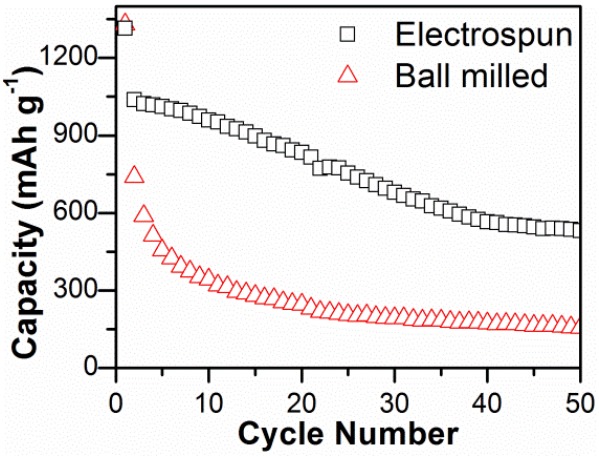

Figure 5-4 Cyclability of $ZnFe_2O_4$ prepared by electrospinning HEBM after 33 h (current density used: 60 mA g^{-1}).

Cycling performance of ball milled $ZnFe_2O_4$ after 33 h was compared with the ZFO-NF (Figure 5-4). It is obvious that electrospun ZFO-NF (previously presented in Figure 4-39) significantly outperformed ball milled sample, despite their comparable crystallite sizes. Briefly, first discharge capacities were comparable for both samples, however discharge capacity of ball milled powder depleted to ~155 mAh g^{-1} after 50 cycle and a reversible capacity of ~532 mAh g^{-1} was delivered by ZFO-NF. This result further suggests that

hierarchically formed 1D nanofibers offer facile and continuous electronic wiring which is beneficial for long term lithium ions transportation.

5.2. Conversion Reaction Mechanism in TMOs

Since mixed TMOs are rather new anodes in LIB application, it is important to understand their interaction towards lithium ions during cycling. In this section, *ex situ* studies using XRD, EELS, TEM were conducted and the reaction mechanisms were proposed accordingly. Besides, *in situ* XRD are also undertaken in $ZnFe_2O_4$ particles (ZFO-NP) to complement the *ex situ* studies.

5.2.1. Ball milled MgB_2O_4 (B: Mn, Fe or Cr)

There is no available report regarding the reaction mechanism of MgB_2O_4 spinels (B=Mn, Fe or Cr) anodes with lithium ions. To have a deeper understanding, *ex situ* XRD study on the discharged/charged electrodes at different cutoff voltages was conducted (refer to Section 4.3.4 for experimental data).

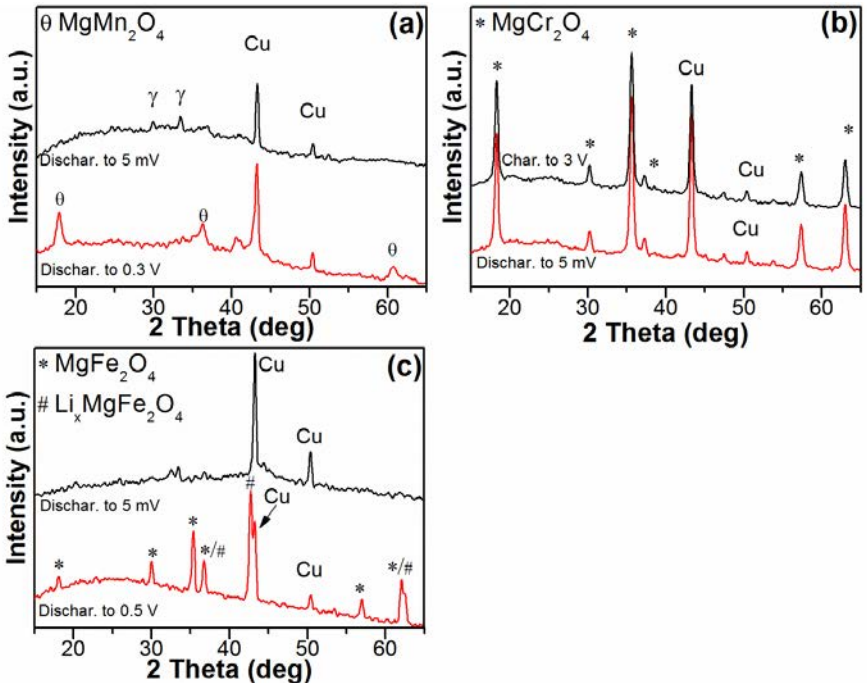

Figure 5-5 *Ex situ* study of reaction mechanisms of MgB_2O_4. (a) MMO-NP, (b) MCO-NP and (c) MFO-NP towards lithium ions by thin film XRD at different cutoff voltages. γ depicts the presence of $LiOH{\cdot}H_2O$.

Any obvious reduction/oxidation peak appeared in the CV curve can be indicative of the involvement of active materials in taking/releasing lithium ions.[3] According to CV curve of MMO-NP (Figure 4-49(a)), first and second reduction peaks were shown at ~0.7 V and ~0.2 V respectively. Hence, the electrodes were purposely discharged till cut off voltages of 0.3 V and 0.005 V to investigate the lithium reaction routes. *Ex situ* XRD pattern of discharged electrode till 0.3 V (Figure 5-5(a)) indicated the preservation of $MgMn_2O_4$ phase, so ~0.7 V can be assigned to the SEI formation or lithium intercalation into the spinel structure. The conversion reaction was completed when the electrode was fully discharged till 0.005 V, so no residual peak was observed (Figure 5-5(a)).

Spinel phase remained pristine after the electrodes were discharged to 5 mV or recharged to 3 V in MCO-NP (Figure 5-5(b)), implying it did not participate in lithium absorption/extraction. So, the only peak appeared in CV curve (~0.7 V, Figure 4-49(b)) can be correlated to electrolyte decomposition. More discussion about the chromite-based anodes will be done in Section 5.2.5.

Since MFO-NP demonstrated two reduction peaks at ~0.65 V and ~0.23 V (Figure 4-49(c)), the cut off voltages for *ex situ* study were decided to be 0.5 V and 0.005 V, respectively. Figure 5-5(c) displays the coexistence of $MgFe_2O_4$ phase and another isostructural $MgFe_2O_4$ phase with slightly smaller 2θ after being discharged to 0.5 V. It suggested that the intercalated lithium expanded the spinel framework and caused the left shift of XRD pattern to smaller 2θ. This was supported by its first discharge curve (Figure 4-50(c)) with a short plateau of ~1.7 moles lithium ion prior the conversion reaction. The intercalation behavior of Mg-based anodes is reported for the first time. When MFO-NP was deeply discharged to 0.005 V, no intense peak was observed as conversion reaction thoroughly transformed the TMOs into metallic nanograins (Mg and Fe) with crystallite size shorter than the XRD coherence length.[27] As a result, it may be postulated the amorphization process of MFO-NP started at ~0.23 V. As MgO is electrochemically inactive (Section 4.3.4) so the redox mechanism of MFO-NP can be proposed as:

Equation 5-1 $MgFe_2O_4 + 1.7Li^+ + 1.7e^- \rightarrow Li_{1.7}MgFe_2O_4$ (intercalation reaction only during first discharge)

Equation 5-2 $Li_{1.7}MgFe_2O_4 + 4.3Li^+ + 4.3e^- \rightarrow MgO + 2\,Fe + 3\,Li_2O$ (during first discharge)

Equation 5-3 $Fe_2O_3 + 6\,Li^+ + 6\,e^- \leftrightarrow 2\,Fe + 3Li_2O$ (first charge onwards)

Revising the case of MMO-NP, the reduction peak of ~0.7 V may also imply lithium intercalation into spinel, although the lattice expansion was less significant with shorter corresponding plateau (~0.7 moles of lithium ion, Figure 4-50(a)). According to Table 2-6, Mn_2O_3 has lower Gibbs free energy (ΔG_f = -881 kJ mol^{-1}) than Fe_2O_3 (ΔG_f = -742 kJ mol^{-1}),[49] so MMO-NP exhibited a lower characteristic discharge plateaus at ~0.21 V than MFO-NP (~0.38 V) in galvanostatic cycling (Figure 4-50). The first discharge and charge capacities were ~1021 mAh g^{-1} (~7.6 moles of lithium ions) and ~435 mAh g^{-1} (~3.2 moles of lithium ions), while theoretical capacity was presumed to involve 6 moles of lithium ions (811 mAh g^{-1}). It postulated that Mn may not be fully re-oxidized to Mn^{3+}, but a mixture of Mn^{2+} and Mn^{3+}. So, reaction of MMO-NP was suggested as following:

Equation 5-4 $MgMn_2O_4 + 0.7Li^+ + 0.7e^- \rightarrow Li_{0.7}MgMn_2O_4$ (intercalation reaction only during first discharge)

Equation 5-5 $Li_{0.7}MgMn_2O_4 + 5.3Li^+ + 5.3e^- \rightarrow MgO + 2\,Mn + 3\,Li_2O$ (during first discharge)

Equation 5-6 $\frac{x}{2}[Mn_2O_3 \text{ or } MnO] + x\,Li^+ + x\,e^- \leftrightarrow 2\,Mn + \frac{x}{2}Li_2O$ (x≈3.2, first charge onwards)

5.2.2. Ball milled $ZnFe_2O_4$

Currently, most of the reports on $ZnFe_2O_4$ reaction mechanisms were based on *ex situ* electrodes characterized by XRD. Therefore, an *in situ* experiment coupled with first discharge/charge cycle was conducted in this thesis to gain better insight.

The lithium participation during first lithiation process can be divided into three respective regions according to the proposed mechanisms in Figure 5-1, this was applied in Figure 5-6(a)). So, XRD patterns of Region I shifted slightly to lower 2θ range, *i.e.* d (lattice spacing) was expanded after lithium intercalation without destructing $ZnFe_2O_4$ host lattice (Figure 5-6(b) and (e)). In Region II, XRD patterns continuously matched to lower 2θ range accompanied by the gradual loss peak intensity at (311) and (440) Miller indices, implying the initiation of conversion reaction to amorphize $ZnFe_2O_4$ into their nanosized metals. This was well aligned with all previous report by *ex situ* XRD characterization.[9, 85] Interestingly, *in situ* characterization brought up a new observation, *i.e.* lithium ions first intercalated and enlarged the spinel structure before

fully converted it into amorphous phase. This phenomenon is originally investigated and reported for the first time in this thesis. Some residual $ZnFe_2O_4$ peaks were still noticed in Region III, because it is difficult to identify the end of conversion plateau in present work.

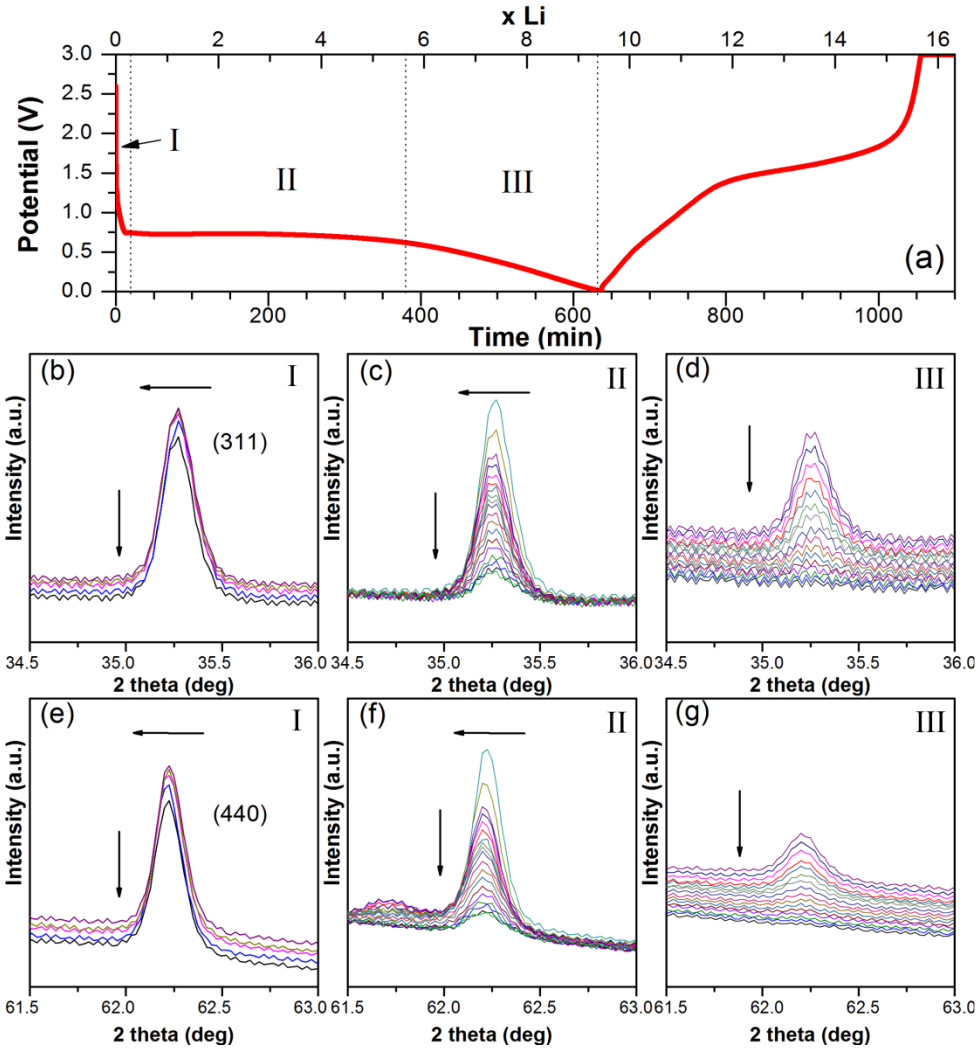

Figure 5-6 *In situ* characterization by XRD on ZFO-NP electrode. (a) First discharge/charge profiles categorized into three regions based Figure 5-1. (b), (c) and (d) represent the evolution of XRD pattern between 34.5° and 36.0° at Region I, II and III, respectively. (e), (f) and (g) ranges from 61.5° to 63°.

5.2.3. Electrospun $ZnFe_2O_4$

Electrochemical performance of electrospun ZFO-NF was presented in Section 4.2.4. The reaction mechanism of ZFO-NF was initially assumed to be similar as ZFO-NP discussed in the last section. Interesting, two plateaus of ~1.4 V and ~0.95 V were observed before conversion reaction during first discharge (Figure 4-26), which can be described as two-steps lithium intercalation into the spinel structure. This assumption was supported by *ex situ* XRD (Figure 5-7), as the patterns exhibited no obvious structural variation after

being discharged to 1.3 V and 0.9 V. Thus, ZFO-NF absorbed ~1.7 moles lithium ions (equivalent to ~192 mAh g^{-1}) *via* two-steps intercalation. This phenomenon was not discovered in ZFO-NR, so it may be promoted by the presence of 1D functional integrated nanofibers. The conversion reaction initiated at ~0.8 V and led to irreversible amorphization of spinel structure to Zn and Fe nanograins, so no XRD peak was found when the electrode experienced a deep discharge to 0.005 V.

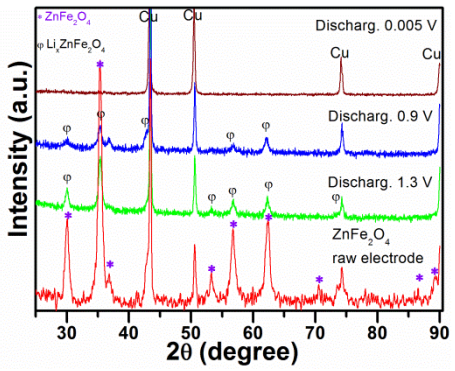

Figure 5-7 *Ex situ* characterization by XRD on $ZnFe_2O_4$ raw electrode (ZFO-NF), and electrodes discharged to 1.3 V, 0.9 V, 0.005 V respectively. (Reproduced by permission of The Royal Society of Chemistry)

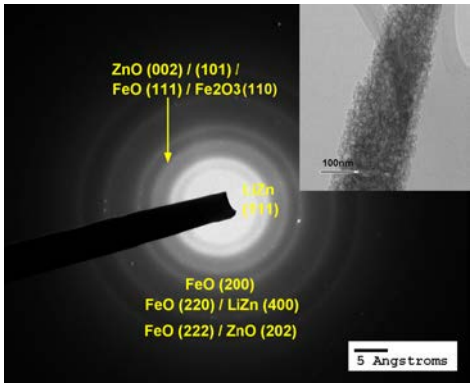

Figure 5-8 *Ex situ* SAED of charged ZFO-NF, (inset) corresponding *ex situ* HRTEM. (Reproduced by permission of The Royal Society of Chemistry)

During the re-oxidation of Fe metallic nanograins, it can be oxidised to either Fe^{2+} or Fe^{3+}, dependent on the reaction efficiency.[70] The first charge value of ZFO-NF was found to be ~925 mAh g^{-1} (Table 5-5), which was higher than 778 mAh g^{-1} (considered the reversible FeO formation upon charging), but lower than 1000 mAh g^{-1} (Fe_2O_3 formation), so it may suggest the formation of a mixed matrix containing FeO and Fe_2O_3. The detection of valence state is out of the scope of XRD analysis, so *ex situ* SAED was employed to verify the phase formation (Figure 5-8). The diffuse set of concentric rings

indicated the charged electrode consisting of nanocrystalline regions dispersed in amorphous matrix. Their d-spacings and respective Miller indices were retrieved (Table 5-7). It was found that mixture of ZnO, LiZn and FeO coexisted at charged state. HRTEM micrograph of ZFO-NF after 30 discharge/charge cycles (inset of Figure 5-8) revealed the preservation of nanofibrous morphology after prolonged cycling. So, ZFO-NF performed good reversibility in both conversion reaction and alloy-dealloy mechanism. Overall, ZFO-NF reacts with lithium ions by the following processes: (1) intercalation, (2) conversion reaction and (3) alloy reaction of Li and Zn, which can be proposed as below:

Equation 5-7: $ZnFe_2O_4 + 1.7Li^+ + 1.7e^- \rightarrow Li_{1.7}ZnFe_2O_4$ (during first discharge)

Equation 5-8: $Li_{1.7}ZnFe_2O_4 + 6.3Li^+ + 6.3e^- \rightarrow Zn + 2\,Fe + 4\,Li_2O$ (during first discharge)

Equation 5-9: $Zn + x\,Li^+ + x\,e^- \leftrightarrow Li_xZn\ (x \leq 1)$ (from first charge onwards)

Equation 5-10: $Zn + Li_2O \leftrightarrow ZnO + 2\,Li^+ + 2\,e^-$(from first charge onwards)

Equation 5-11: $Fe + Li_2O \leftrightarrow Fe^{(II)}O + 2\,Li^+ + 2\,e^-$(from first charge onwards)

Table 5-7 d-spacing and possible Miller indices observed in SAED pattern. (Reproduced by permission of The Royal Society of Chemistry)

d-spacing, Experimental Value (Å)	Phase	Miller Index	d-spacing, Reported Value (Å)	ICSD code number
3.59	LiZn	(111)	3.60	104791
2.57	ZnO	(002)	2.60	26170
2.10	FeO	(200)	2.16	633038
1.51	FeO	(220)	1.53	633038
	LiZn	(400)	1.56	104791
1.22	FeO	(222)	1.25	633038
	ZnO	(202)	1.24	26170

5.2.4. Electrospun $Zn_{1-x}Mn_xFe_2O_4$ nanofibers

Based on the interesting results shown by ZFO-NF, a solid solution of electrospun $Zn_{1-x}Mn_xFe_2O_4$ nanofibers ($0 \leq x \leq 0.7$) nanofibers were prepared (Section 4.2.9) and this section mainly discusses about the participation of Mn during cycling.

After substitution of Zn by Mn, Z5M5 and Z3M7 achieved a better cycling stability than ZF (Figure 4-39), so it is important to determine lithium activity of Mn in $Zn_{1-x}Mn_xFe_2O_4$ nanofibers. There were many reports using *ex situ* TEM and SAED to verify the phase

formation after prolonged cycling,[29-31] including work done in last section. So, similar *ex situ* TEM study was conducted on Z7M3 (Figure 5-9(a)). Diffuse set of concentric rings indicated the charged Z7M3 electrode consisted of nanocrystalline regions dispersed in amorphous matrix. The d-spacings and their respective Miller indices were retrieved from SAED data and summarized in Table 5-8, a mixed phase of LiZn, FeO, Fe_2O_3 and Mn_2O_3 coexisted in charged state, while ZnO was not found, possibly due to the poor cyclability of ZnO anodes which was widely reported.[101, 138] Surprisingly, the presence of Mn_2O_3 after reversible cycling was also ambiguously observed in *ex situ* SAED of Z3M7 electrode (Figure 5-9(b)). Notably, it is unusual to discover the formation of Mn_2O_3, instead of MnO after cycling in current study. So far, there is no report regarding the increment of oxidation state than its initial state after extended cycling. Hence, reaction mechanism of TMO is very difficult to be accurately characterized by TEM due to the fine-grained and heterogeneous nature of the electrode. Owing to it, ELNES spectrum was collected to determine the valence state of Mn 3d orbital to gain a more reliable analysis than *ex situ* TEM.

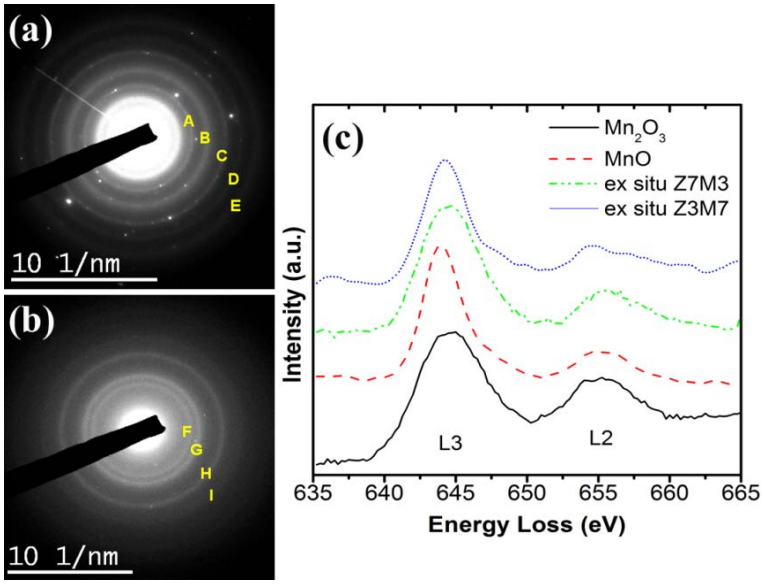

Figure 5-9 *Ex situ* characterization of cycled electrodes. SAED of (a) Z7M3 and (b) Z3M7 nanofibers. (c) Mn $L_{2,3}$ edges of *ex situ* Z7M3 and Z3M7, MnO and Mn_2O_3 were taken as references. (Reprinted with permission from [140], Copyright 2013 American Chemical Society.)

Representative EELS spectra Mn *L*-edge from commercial MnO and Mn_2O_3 were recorded in Figure 5-9(c) as references to quantitatively calibrate the peak energies. Two broad Mn L_2 and L_3 peak onsets were observed at ~640 eV and ~651 eV respectively, which was same as the interpretation by Garvie *et al*.[164] The *L*-edge of Mn^{2+} and Mn^{3+} was characterized by L_3/L_2 white-line ratio, resulting from the ratio of electronic transition

from spin-orbit levels $2p_{3/2}$ and $2p_{1/2}$ to unoccupied 3d states, respectively. So, this ratio has a strong relation with the spin state of a transition metal and it allows quantitatively calculate valence state of an element.[123, 165] Herein, L_3/L_2 white-line ratios were obtained by first removing the background using a power law fitting, while plural scattering was considered by Fourier ratio deconvolution with the zero loss regions. For a consistent calculation, energy width of 6 eV centered on *L* peak maxima was chosen as integral window for all samples to minimize the discrepancy. The results were summarized in Table 5-9. As expected, MnO formed at the charged state of Z7M3 and Z3M7, instead of Mn_2O_3 and hence the increment of valence state than its initial state is not physically possible in conversion reaction. This finding adhered to all reported reaction mechanism of Mn-based TMOs.[166] Therefore, EELS is a better characterization tool than TEM in *ex situ* study, especially when valence state of charged/discharged electrode is the main interest.

Table 5-8 d-spacings and possible Miller indices observed in *ex situ* SAED of Z7M3 and Z3M7 in Figure 5-9(a) and (b). (Reprinted with permission from [140], Copyright 2013 American Chemical Society.)

	d-spacing			**d-spacing**	
Label	**Experimental value (Å)**	**Phase**	**Miller index**	**Reported value (Å)**	**ICSD code number**
A	2.74	Fe_2O_3	(104)	2.70	173651
		Mn_2O_3	(222)	2.72	180891
B	2.18	FeO	(200)	2.16	633038
C	1.71	Fe_2O_3	(116)	1.70	173651
		Mn_2O_3	(440)	1.66	180891
D	1.44	LiZn	(331)	1.43	104792
E	1.25	FeO	(222)	1.24	633038
F	2.52	MnO	(111)	2.57	643195
		Mn_2O_3	(301)	2.55	180891
G	2.20	FeO	(200)	2.15	633038
H	1.55	FeO	(220)	1.52	633038
I	1.26	FeO	(222)	1.24	633038
		ZnO	(202)	1.24	26170

Based on the observation of *ex situ* TEM and EELS studies, reversible capacities given by Z7M3, Z5M5 and Z3M7 at 50th cycle, *i.e.* ~3.8, ~4.6 and ~5.3 moles of lithium ions per

formula unit, can be correlated to the reaction stated in Equation 5-12, and Y represents number of lithium ions transferred during the reaction. Greater reversibility and lower discharge were observed when increasing Mn, so it is possible to alter battery performance by selectively tuning the ratio of mixed TMOs (see Section 5.3).

Equation 5-12 $$xZn + \frac{Y-x}{2}[Fe_2O_3 \text{ or } FeO \ + \ MnO] + Y\,Li^+ + \ Y\,e^- \ \leftrightarrow$$

$$xLiZn + \frac{Y-x}{2}[Fe + Mn] + \frac{Y-x}{2}\,Li_2O$$

Table 5-9 Mn $L_{2,3}$ ELNES data measured by EELS analysis (Figure 5-9(c)). (Reprinted with permission from [140], Copyright 2013 American Chemical Society.)

Sample	Mn Intensity ratio (L_3/L_2)	Reported Mn Intensity ratio (L_3/L_2)	Reference
Mn_2O_3	2.62	2.50	[123]
		2.40	[165]
MnO	4.00	3.98	[123]
		3.90	[165]
Z7M3	3.91	-	
Z3M7	3.99	-	

5.2.5. Ball milled $ZnFe_{2-y}Cr_yO_4$

$ZnFe_2O_4$ consistently performed good capacity in this thesis, so $ZnCr_2O_4$ formed by a simple B-site substitution were assumed to react with lithium ions following the proposed reaction mechanisms of $ZnFe_2O_4$ in Equation 5-7-Equation 5-11. On the contrary, capacities achieved by mixed TMOs were gradually decreasing when increasing ratio of Cr in $ZnFe_{2-y}Cr_yO_4$ ($0 \leq y \leq 2$) solid solution (Section 4.3.6). Therefore, this section aims to investigate the electrochemically inactive behavior of chromite-based anodes.

To understand the reaction mechanism of $ZnFe_{2-y}Cr_yO_4$ anodes with lithium, thin film XRD patterns (Figure 5-10(a)) and SAED (Figure 5-11) were collected *ex situ* for cycled electrodes. SAED was also carried out for the pristine materials to establish comparisons. The set of concentric rings the pristine samples indicated the presence of polycrystalline spinels with d-spacings in agreement with the XRD results (Figure 4-53(a)). Figure 5-10(a) shows the XRD data for $ZnFe_2O_4$ (y=0) and $ZnFe_{1.5}Cr_{0.5}O_4$ (y=0.5) after undergoing a deep discharge to 0.005 V, revealing the absence of peaks related to the initial spinel structure or any other new phase. A set of highly diffuse SAED rings were obtained for fully reduced $ZnFe_2O_4$ (Figure 5-11(d)), the possible phases present were

very difficult to identify unambiguously due to their nanocrystalline nature, but they were proposed to be LiZn and Fe metallic nanograins uniformly dispersed in an amorphous Li_2O matrix.[9, 26, 27]

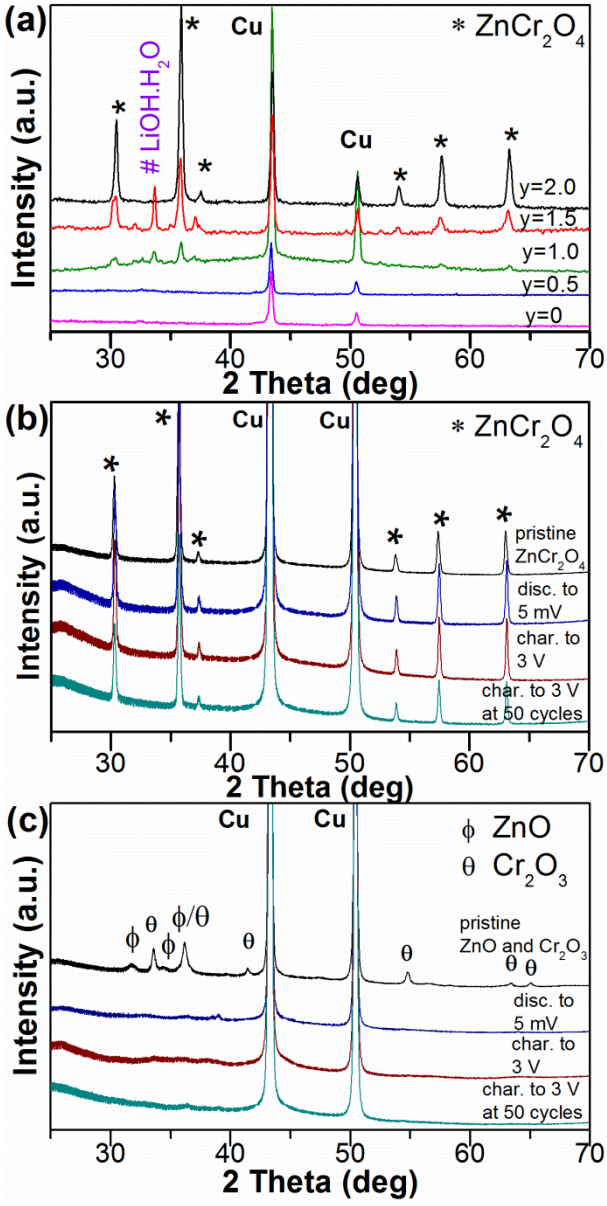

Figure 5-10 *Ex situ* XRD pattern of (a) $ZnFe_{2-y}Cr_yO_4$ particles after first discharge to 0.005 V. (b) $ZnCr_2O_4$ and (c) ZnO and Cr_2O_3 composites were discharged or charged to specific cutoff potential at 60 mA g^{-1} and the electrodes were recovered for *ex situ* characterization by XRD. (Reprinted with permission from [151], Copyright 2013 American Chemical Society.)

When y≥1.0, residual spinel peaks started to emerge in XRD patterns (Figure 5-10(a)), their intensity being higher with Cr substitution, indicating they belong to unreacted material. Discharged $ZnFe_{1.0}Cr_{1.0}O_4$ and $ZnCr_2O_4$ electrodes showed clear SAED patterns with distinct polycrystalline nature (Figure 5-11(e) and (f), respectively), implying the crystalline spinel phases were preserved after the battery cycling, especially for $ZnCr_2O_4$.

$ZnFe_{1.0}Cr_{1.0}O_4$ showed a reversible capacity close to $ZnFe_2O_4$ (Table 4-4) and its corresponding *ex situ* SAED presented a more diffuse pattern than $ZnCr_2O_4$, indicating a portion of the spinel experienced conversion to the nanocrystalline metallic phase. It is possible that ohmic losses prevented full utilization of the oxide in the presence of a working voltage that is very close to the cutoff, resulting in domains that were converted and others that preserved the pristine structure (Figure 5-11(e)). The diffuse nature of the diffraction rings in the reduced sample compared to the spotty patterns in the pristine material probably reflects the pulverization of the electrode driven by the formation of multiple converted domains during the amorphization process.[167]

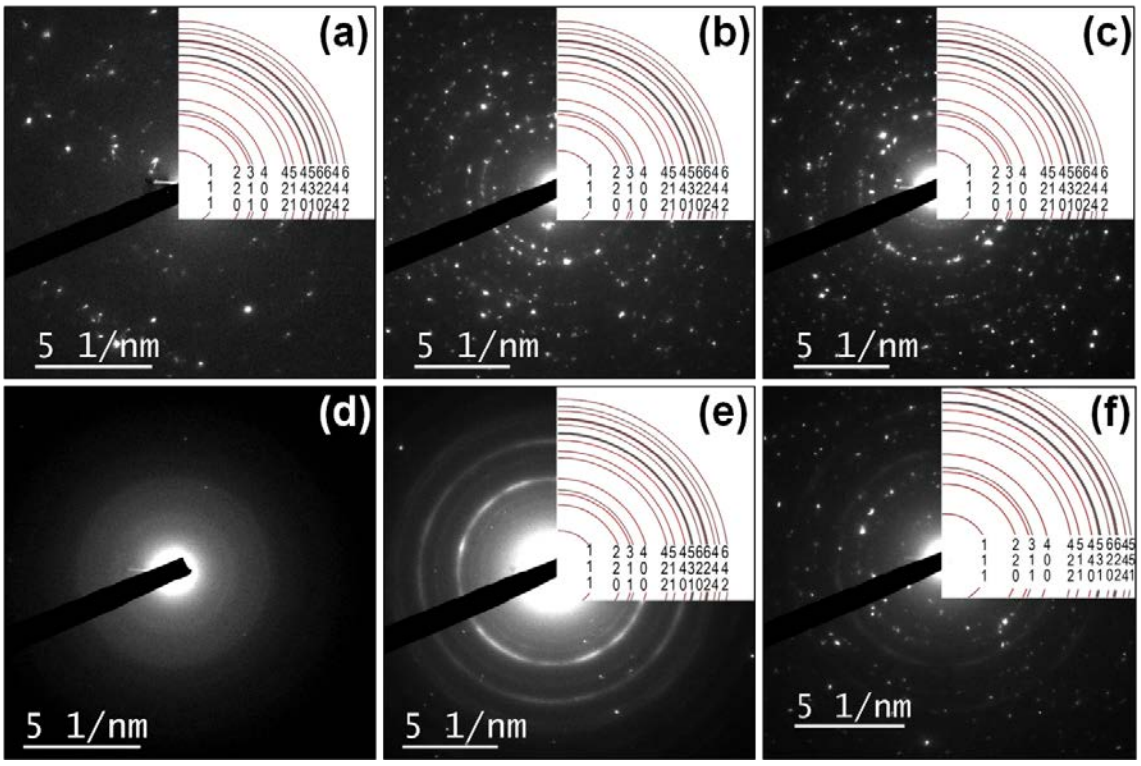

Figure 5-11 SAED and simulated diffraction rings of (top) pristine $ZnFe_{2-y}Cr_yO_4$ powders and (bottom) *ex situ* electrodes after 1st discharge. (a) and (d) y=0; (b) and (e) y=1.0; (c) and (f) y=2.0. (Reprinted with permission from [151], Copyright 2013 American Chemical Society.)

Extended *ex situ* XRD studies were carried out for $ZnCr_2O_4$ at different discharge/charge cutoff potentials (Figure 5-10(b)). No evidence of reaction was found at any voltage or after 50th cycle, confirming that capacity values observed in $ZnCr_2O_4$ electrodes are mainly ascribed to the carbon additive and/or other undesirable side reactions. Hence, $ZnCr_2O_4$ is inactive toward electrochemical reaction with lithium, and thus not a viable electrode material. In the case of ZnO and Cr_2O_3 composites electrode, Figure 5-10(c) clearly shows that both hexagonal ZnO and rhombohedral Cr_2O_3 disappeared after first discharge to 0.005 V, and there was no presence of any crystalline product throughout the

cycling. Thus, ZnO and Cr_2O_3 undergo conversion reactions with amorphization when physically mixed. It is aligned to aforementioned discussion regarding their reaction mechanism with lithium (Table 2-6).

All these results confirm the inherent electrochemical inactivity of Zn and Cr when together in a spinel structure. This inactivity must be related to electronic structure changes in the mixed ternary metal oxides versus the individual binary phases. It is worth mentioning that there is no related publication on any inactive spinel anodes yet. In general, all chromites, including $ZnCr_2O_4$, are essentially normal spinels (inversion degree less than 0.05),[168] with the tetrahedral site preference of Zn^{2+} and a very strong octahedral site preference of Cr^{3+} to form $[Zn^{2+}]^T[Cr^{3+}Cr^{3+}]^OO_4$.[73, 74, 152, 169, 170] Müller *et al.* found that $ZnCr_2O_4$ has the most exothermic enthalpy of formation from their component oxides when compared with other chromites such as Cr_2O_3, $CoCr_2O_4$, $FeCr_2O_4$, $MgCr_2O_4$ and $NiCr_2O_4$,[170] indicating it is an extremely stable compound once formed. Levy *et al.* has also investigated the stability of $ZnCr_2O_4$ as a function of pressure and temperature.[152] It was proposed that a very high pressure of 18 GPa is required to decompose $ZnCr_2O_4$ spinel into ZnO and Cr_2O_3 at room temperature, in agreement with the *ab initio* computational simulations of Catti *et al.*[169] Since Cr^{3+} has a prominent octahedral crystal field stabilization energy (CFSE) of ~224.5 kJ mol^{-1},[131] it results in strong orbital hybridization and a wide band gap between the top of the filled O 2p band and bottom of the transition metal 4s and 4p conduction bands,[171] as discussed in the context of the XAS data above (Figure 4-57(b) and (d)). The increase in covalence could explain both the inactivity of $ZnCr_2O_4$ and, more broadly, the trends in reduction potentials in $ZnFe_{2-y}Cr_yO_4$. The electrochemical potential (E^0) of reduction of a given solid phase is related to the position of the bottom of the conduction band with respect to a reference level (Li metal in current study), as electron injection occurs at these states.[161] Since their position shifts upward, closer to the Li metal level with greater covalence, the macroscopic observation is a decrease in E^0. This phenomenon could lead to values of E^0 that are very close to the Li metal electrode. In the presence of severe energy penalties imposed by the conversion from crystalline oxide to metallic nanograins embedded in a Li_2O matrix,[172] it is feasible that the actual value of reduction potential may fall below 0 V *versus* Li^+/Li^0, so that no activity is observed in a typical electrochemical experiment such as those performed here. We believe this hypothesis applies to the voltage trends when substituting Fe by Cr in $ZnFe_{2-y}Cr_yO_4$, which are consistent with the lower reduction potential of Cr_2O_3 compared to Fe_2O_3.[20] The

inactivity of $ZnCr_2O_4$ compared to ZnO/Cr_2O_3 is consistent with the picture painted by the O *K* edge XAS data (Figure 4-57(a)), *i.e.* the O 2p-Cr t_{2g} peak appeared at higher energies for $ZnCr_2O_4$ than Cr_2O_3. As discussed above, this shift is a reflection of the upward move of the Fermi level, closer to the continuum and, by extension, to the Fermi level of Li metal.[161]

It is worth noting that the existence of single reduction plateaus of $ZnFe_{2-y}Cr_yO_4$, especially in the first discharge, could be considered unexpected based on the significant difference in reduction potential of the respective binary oxides (Figure 4-59(b) and (c)). According to the XAS results, electronic level mixing between the metals occurs and leads to overall shifts of the corresponding transitions. In the presence of such mixing, electron injection destabilizes both Cr and Fe states and causes their concurrent reduction to metal. This process would occur at a single potential, consistent with the presence of a single plateau in the first discharge of $ZnFe_{2-y}Cr_yO_4$. The difference in potential between the binary oxides ZnO[173] and Fe_2O_3[50] does not lead to a mechanism in which one of the two metals is preferentially extruded from the spinel structure first, followed by complete amorphization to metal particles and Li_2O. As a result, all metals in $ZnFe_{2-y}Cr_yO_4$ always get reduced simultaneously.

5.3. Effect of A site Substitution

This section aims to understand the impact of A-site substitution on electrochemical performance of AB_2O_4 spinel. The comparison was based on the solid solution of electrospun $Zn_{1-x}Mn_xFe_2O_4$ nanofibers (Section 4.2.10), ball milled AMn_2O_4 and AFe_2O_4 (A: Mg and Zn) (Section 4.3.2 and 4.3.4).

5.3.1. Electrospun $Zn_{1-x}Mn_xFe_2O_4$ nanofibers

With referring to the electrochemical data of electrospun $Zn_{1-x}Mn_xFe_2O_4$ nanofibers in Section 4.2.10, the impact of counter ion on electrochemical performance was summarized in Figure 5-12. The discharge voltages at 1st and 50th cycle were detected by CV, the voltages were substantially brought down by Mn substitution. This is analogue to the speculatation by Nernst equation (Table 2-6 and Equation 2-13). Since MnO has lower Gibbs free energy of formation ($\Delta G^0 = -363\ kJ\ mol^{-1}$) than ZnO ($\Delta G^0 =$

$-320\ kJ\ mol^{-1}$), so it explains why the working voltage slightly decreases when the Mn ratio is higher.

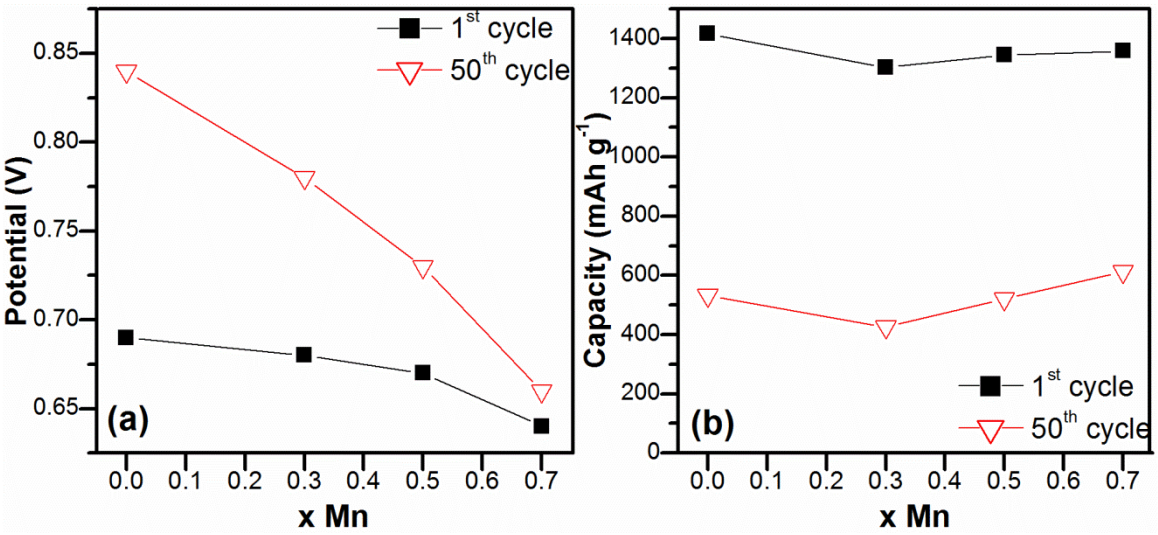

Figure 5-12 Impact of A-site substitution on battery performance in electrospun $Zn_{1-x}Mn_xFe_2O_4$ nanofibers (a) Discharge voltages recorded by CV and (b) capacities measured by galvanostatic cycling at 1st and 50th cycle.

Reversible capacity is one of the key factors for selecting anodic material in LIBs. Therefore, cycling performance shown in Figure 5-12 helps to understand the impact of replacing Zn by Mn. At first cycle, comparable capacities were observed, whereas better capacity retention was achieved by substituting the Zn with Mn in spinel anodes. Hence, Mn is a better counter ion than Zn in AFe_2O_4 by providing higher capacity and lower working voltage.

5.3.2. Ball milled AMn_2O_4 and AFe_2O_4 (A: Zn and Mg)

Discussion in this section was based on the experimental results in Section 4.3.2 and 4.3.4. ACr_2O_4 was excluded from the comparison since this series was proven to be electrochemically inactive in lithium ion absorption/extraction (Section 5.2.5).

Table 5-10 tabulates the electrochemical performance of ball milled AMn_2O_4 and AFe_2O_4 particles with A-site substitution by either Zn or Mg, as well as the electrospun nanofibers discussed in the last section. In terms of the impact of counter ion on working voltages, Zn and Mn at A-sites consistently exhibited better advantage than Mg, as it provided a smaller voltage polarization between reduction (discharge) and oxidation (charge) reactions (~0.9 V), whereas the hysteresis was found to be ~1.1 V in MgB_2O_4 series. In

generally, it is beneficial to have a lower working voltage towards lithium metal when selecting an anode, in order to maximize the total output voltage with respect to $LiCoO_2$ as cathode material.[9, 26, 85, 139] Nevertheless, if discharge voltage is proximate to 0 V, it leads to the possibility of lithium plating and eventually causing a short circuit. Therefore, $MgMn_2O_4$ is not a safe candidate as LIB anode with its discharge voltage of <0.1 V.

By comparing the capacities among ball milled particles (AMn_2O_4 and AFe_2O_4, A: Mg, Zn), there was no consistent trend available in predicting the influence of counter ion on their cyclability. In summary, all spinel in Table 5-10 possessed better cyclability than their respective binary oxides (refer to Table 2-6), while $ZnMn_2O_4$, $ZnFe_2O_4$ and $MgFe_2O_4$ were more promising. Since A-site substitution does not give a governing rule in flexibly altering the battery performance, B-site substitution was conducted and discussed in next section.

Table 5-10 Comparison of electrochemical performance between some manganites and ferrites after A-site substitution.

Sample	Morphology	Voltage (discharge/charge) (V)		Capacity (discharge/charge) (mAh g^{-1})			% of theoretical capacity
		1st cycle	5th cycle	1st cycle	50th cycle	Theoretical	
$ZnMn_2O_4$	Particles	0.14/1.22	0.44/1.30	1132/676	731/724	1008	71.8
$MgMn_2O_4$	Particles	0.02/1.09	0.09/1.15	1021/435	425/418	811	51.5
$ZnFe_2O_4$	Particles	0.54/1.64	0.85/1.75	1111/752	612/611	1001	61.0
$MgFe_2O_4$	Particles	0.23/1.70	0.64/1.72	1096/765	614/606	804	75.4
ZF	Nanofibers	0.69/1.59	0.84/1.64	1314/988	532/522	1001	52.1
Z7M3	Nanofibers	0.68/1.60	0.78/1.68	1217/891	426/418	1013	41.3
Z5M5	Nanofibers	0.67/1.66	0.73/1.67	1321/934	521/517	1022	50.6
Z3M7	Nanofibers	0.64/1.63	0.66/1.67	1358/1015	612/598	1031	59.0

5.4. Effect of B Site Substitution

As presented in Section 5.3, A-site substitution in electrospun $Zn_{1-x}Mn_xFe_2O_4$ nanofibers displayed a slight possibility in tuning battery performance, however the trend in ball milled samples remains uncertain. Hence, this section aims to systematically study the impact of B-site substitution by taking ZnB_2O_4 and MgB_2O_4 (B: Mn, Fe, Cr) as examples. The experimental results were shown in Section 4.2 and Section 4.3.

5.4.1. ZnB_2O_4 (B: Mn, Fe, Cr) and $ZnFe_{2-y}Cr_yO_4$

Table 5-11 Summary of electrochemical performance of ZnB_2O_4 with different morphologies prepared by electrospinning or HEBM.

Sample	Morphology	Voltage (discharge/charge) (V)		Capacity (discharge/charge) (mAh g^{-1})			% of theoretical capacity
		1st cycle	5th cycle	1st cycle	50th cycle	Theoretical	
$ZnMn_2O_4$	nanofibers	0.24/1.24	0.55/1.31	1469/716	706/690	1008	68.5
$ZnMn_2O_4$	particles	0.14/1.22	0.44/1.30	1132/676	731/724	1008	71.8
$ZnFe_2O_4$	nanofibers	0.69/1.59	0.84/1.64	1314/988	532/522	1001	52.1
$ZnFe_2O_4$	particles	0.54/1.64	0.86/1.75	1111/752	612/611	1001	61.0
$ZnCr_2O_4$	nanofibers	n.a.	n.a.	513/145	176/172	1033	16.7
$ZnCr_2O_4$	particles	n.a.	n.a.	142/71	91/90	1033	8.7
$ZnFe_{1.5}Cr_{0.5}O_4$	particles	0.30/1.55	0.72/1.60	1181/862	637/627	1008	62.2
$ZnFe_{1.0}Cr_{1.0}O_4$	particles	0.15/1.52	0.70/1.54	996/740	553/544	1016	53.5
$ZnFe_{0.5}Cr_{1.5}O_4$	particles	n.a./1.45	0.67/1.47	609/402	505/495	1026	48.2

'n.a.': not available as chromite-based spinels do not exhibit any reaction with lithium ions.

The results of B-site substitution in ZnB_2O_4 spinel were summarized in Table 5-11 and Figure 5-13. In terms of working voltage variation, $ZnMn_2O_4$ consistently demonstrated lower working voltage than $ZnFe_2O_4$ in two different morphologies. Looking at the theoretical voltage of Mn_2O_3 (1.431 V), working voltages of $ZnMn_2O_4$ were obviously lower than the assumption after combining with ZnO. It may be due to the voltage polarization experienced by the electrode during cycling, so it is more practical by referring to their experimental values (~1.2 V, also included in Table 2-6). $ZnFe_2O_4$ constantly exhibited lower working voltage and highly retained capacity than its simple binary oxides (ZnO or Fe_2O_3, Table 2-6), implying the advantages of constructing spinel structure. On the other hand, working voltages of $ZnCr_2O_4$ could not be verified since it was proven to be inactive in Section 5.2.5, although its binary oxides reacted with lithium ions reversibly. This circumstance obviously implied that cation substitution successfully alters the state mixing at Fermi levels in AB_2O_4.[20] This hypothesis is well supported by the gradual working voltage decrement in $ZnFe_{2-y}Cr_yO_4$ ($y \leq 1.5$) at both 1st and 50th cycle

when Cr is higher (Figure 5-13(a)), since Cr_2O_3 has a lower working voltages than Fe_2O_3 (Table 2-6). The voltage variation is more pronounced by B-site substitution than A-site.

From the perspectives of storage ability, electrospun nanofibers demonstrated much higher capacity than ball milled particles at initial cycling, undoubtedly nanofibers offer facile transportation pathway for lithium ions and increase the efficiency of battery. However, ball milled particles surpassed nanofibers at 50th cycle, probably due to the gradual lost of distinct fibrous morphology after prolonged cycling or excessive side reactions due to their higher surface area density. Hence, mechanical integrity of electrospun nanofibers is required to be improved to preserve the competitive advantages of fibrous nanostructured architecture throughout the battery life.

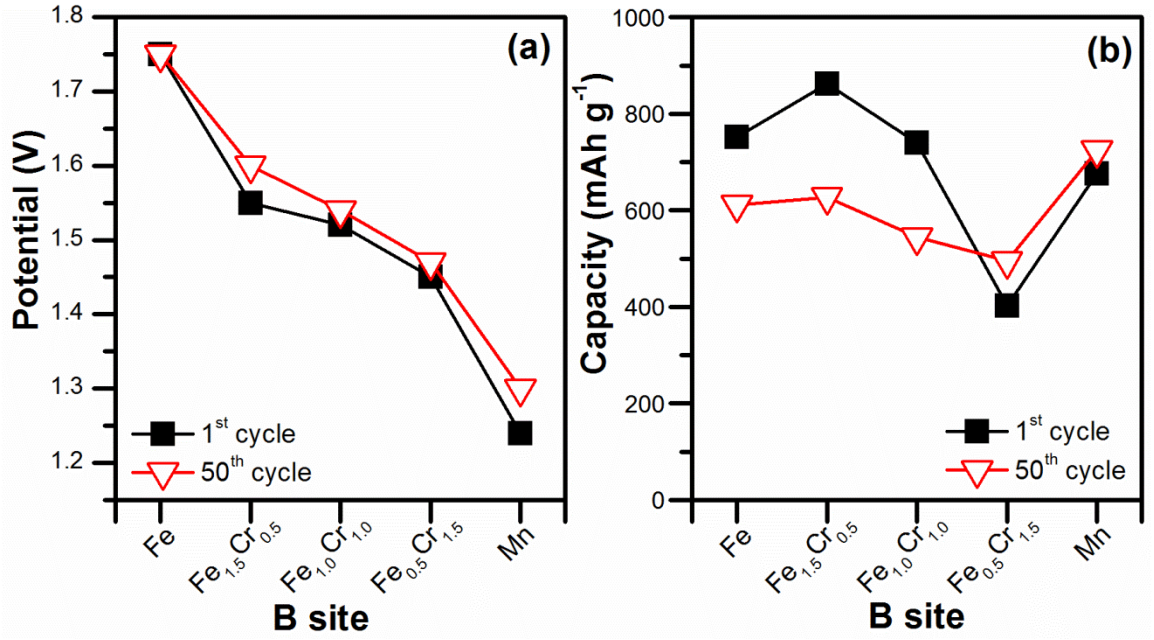

Figure 5-13 Impact of B-site substitution on battery performance. in ball milled ZnB_2O_4 particles (a) Charge voltages and (b) charge capacities at 1st and 50th cycle.

When Mn replaced A-site in $Zn_{1-x}Mn_xFe_2O_4$ nanofibers, lower voltages and better capacity retention were observed. Similar but greater influence was noticed when Mn substituted B-site in ZnB_2O_4 series (Table 5-11), despite Mn_2O_3, Fe_2O_3 and Cr_2O_3 were reported to have comparable theoretical capacities (Table 2-6). $ZnMn_2O_4$ particles and nanofibers achieved as high as 71.8% and 68.5% of their theoretical capacities after 50th cycle. On the other hand, a gradual decrement of capacity was observed in the solid solution of $ZnFe_{2-y}Cr_yO_4$ with increasing y content. Eventually, the combination of ZnO and Cr_2O_3 to form $ZnCr_2O_4$ resulted in an electrochemically inactive spinel, even though ZnO and Cr_2O_3 have theoretical capacities of 659 mAh g^{-1} and 1058 mAh g^{-1}. Hence, it is

interesting that chromites-based spinels do not obey the expectation presumed by thermodynamics parameter, so d level mixing is also required to be considered when choosing a counter ion in AB_2O_4 anodes.

In summary, the amorphization process successfully destructed TMOs into tiny metallic nanograins embedded in Li_2O matrix with extremely large interfacial layer with different bondings (ionic *versus* covalent). The incompatibility at interface may be the driving force to cause reversible conversion reaction. Generally, we may also consider the working voltage and capacity of an amorphized spinel as the average performance of their individual component oxides. However, *in situ* amorphized spinel is presumed to have larger tendency to be re-oxidized than physically mixed binary oxides. This provides the convenience of tuning the final working voltage by selecting a favorable combination of transition metals to be crystallized in the spinel structure. After the systematic studies in this thesis, B-site substitution is more effective than A-site. This observation intuitively fulfilled one of the main objectives of this thesis, *i.e.* tuning the battery performance by choosing the best counter ion in spinel-based anodes. Apparently, Mn and Fe are better candidates than Cr.

Due to the promising battery performance exhibited by $ZnMn_2O_4$ and $ZnFe_2O_4$, these two materials were assembled with $LiFePO_4$ cathode to build a full LIB (Section 4.4).

5.4.2. Ball milled MgB_2O_4 (B: Mn, Fe, Cr)

The performance of MgB_2O_4 was compared in Table 5-12. Similar to the observation in ZnB_2O_4 anodes, B-site substitution is more effectively in changing the capacity and working voltages of spinel. Mn brought down the working voltages of MMO-NP as a desired property as LIB anode in spite of its less impressive capacity, whereas MFO-NP achieved comparably good storage behavior as ZFO-NP.

As discussed earlier, MgO is inactive in lithium absorption/extraction. Instead, it serves as a buffer matrix to suppress the volumetric expansion/contraction and prevent the agglomeration of metallic nanograins, so initially it was assumed to be irrelevant in tuning the capacity or working voltages. Surprisingly, the working voltages listed in Table 5-10 demonstrated a remarkable decrement after combing MgO with Fe_2O_3 or Mn_2O_3 as compared to their binary oxides (Table 2-6). Hence, the formation of spinel

structure substantially altered the state mixing at the Fermi level, and thus spinel-based anodes offer competitive advantages than their binary oxides.

Table 5-12 Performance of MgB_2O_4 anodes , B-site was varied among Mn, Fe or Cr.

Samples	Morphology	Voltage (V)		Capacity (discharge/charge) (mAh g^{-1})			% of theoretical capacity
		1st cycle	5th cycle	1st discharge	50th discharge	Theoretical	
MMO-NP ($MgMn_2O_4$)	Particles	0.02/1.09	0.09/1.15	1021/435	425/418	811	51.5
MFO-NP ($MgFe_2O_4$)	Particles	0.23/1.70	0.64/1.72	1096/765	614/606	804	75.4
MCO-NP ($MgCr_2O_4$)	Particles	n.a.	n.a.	175/82	87/85	836	10.2

'n.a.': not available as chromites based spinel does not exhibit any reaction with lithium ions.

Chapter 6 Conclusions

This thesis presents in depth investigation on the conversion reaction of spinel TMOs (AB_2O_4) and their discharge/charge reaction mechanisms in LIB application. The applicability of nanostructured materials and spinel-based anode in full LIB cell are also studied.

Synthesis methodologies such as electrospinning, HEBM, hydrothermal and colloidal syntheses were studied to prepare TMOs with distinctly different surface morphologies. An optimum range of particle size (~100 nm) and mass loading per electrode (~3-5 mg per electrode with 16 mm diameter) were identified to be beneficial and appropriate to maximize the potential of nanostructured materials as LIB anodes. Particularly, simple and cost effective electrospinning methodology was explored to produce different architectures (nanorods, nanofibers and nanowebs) by altering the sintering condition or viscosity of precursor solution. This is the first original contribution generated from this thesis. Basically, 1D $ZnMn_2O_4$ and $ZnFe_2O_4$ nanofibers achieved high capacities of ~706 mAh $g^{-1}$and 709 mAh g^{-1} at 50^{th} and 30^{th} cycle, respectively, which were much higher than their corresponding nanorods with capacities of ~318 mAh g^{-1} and ~214 mAh g^{-1}. The excellent performance of 1D $ZnFe_2O_4$ nanofibers was compared with ball milled 0D $ZnFe_2O_4$ with similar structural information (similar crystallite size without hierarchically nanostructured). The ball milled powder rapidly depleted to ~194 mAh g^{-1} at 30^{th} cycle, so 1D $ZnFe_2O_4$ nanofibers outperformed the 0D nanoparticles. After characterized by EIS study, excellent storage properties of $ZnMn_2O_4$ and $ZnFe_2O_4$ were contributed by the continuous 1D electronic wiring offered by high aspect ratio nanofibers, resulting in facile electronic and ionic conduction pathway for lithium ions and electrons, especially during long term cycling. Therefore, the stacking of nanofibers into a connective and interwoven mat with open pores remarkably enhances the uniform penetration of electrolyte into the TMOs and offers a larger electrolyte/electrode effective contact surface, eventually achieving a higher capacity than currently used commercial graphite. Moreover, *ex situ* characterization by TEM witnessed the preservation of fibrous morphology after 30 discharge/charge cycles.

As spinel-based anodes are still an emerging aspect in research community, so several unreported spinel-based anodes were testified in this thesis and their reaction mechanisms

with lithium were proposed based on *ex situ* electrode characterization. It is well known that, TMOs are reduced to their metallic states of 2-5 nm and embedded in the Li_2O amorphous matrix after experiencing the conversion reaction at first discharge. Hence, nature of nanocrystalline phases of reduced species posted great challenges for research community to accurately postulate the phase transition upon cycling. Hence, comprehensive characterization was conducted using laboratory XRD, *in situ* synchrotron XRD, EELS and SAED systematically in this thesis. Besides, reaction mechanism of MgB_2O_4 (B: Mn, Fe, Cr) were originally proposed and lithium intercalation prior the conversion reaction was also clarified by XRD study. Similar intercalation phenomenon was also observed in electrospun $ZnFe_2O_4$ and electrospun $Zn_{1-x}Mn_xFe_2O_4$ nanofibers, however this phenomena was less obvious in ball milled $ZnFe_2O_4$. It suggested the degree of intercalation into the spinel structure is highly contingent upon the surface morphology of host materials, nanostructured architecture is favorable. On the basis of *in situ* XRD characterization, we proposed for the first time that lithium ions intercalate into the spinel framework and substantially expands the lattice spacing before being amorphized/destructed in conversion reaction. Although XRD studies have conveyed important information regarding the materials participation in lithium absorption/extraction, a better characterization tool is required to reliably inspect the change of valence states during redox reaction. Hence, EELS was employed on electrospun $Zn_{1-x}Mn_xFe_2O_4$ nanofibers and the formation of MnO after cycling was precisely pointed out, instead of Mn_2O_3 as suspected by SAED analysis. So, complementary study using EELS, SAED, XRD and HRTEM provides a better insight on the reaction mechanism of TMOs as LIB anodes. Interestingly, the systematic *ex situ* studies on the solid solution series of $ZnFe_{2-y}Cr_yO_4$ revealed the electrochemically inactive behavior of $ZnCr_2O_4$.

The obtained results implied that the combination of more than one TMO and crystallized in spinel (AB_2O_4) structure realized the flexibility in tuning the working voltages and capacities by changing the counter ion. Besides, battery performance of spinel-based anodes surpassed their respective binary oxides with higher capacity reversibility and lower discharge/charge voltages. A-site substitution was performed by electrospun $Zn_{1-x}Mn_xFe_2O_4$ nanofibers and ball milled AMn_2O_4 and AFe_2O_4 (A: Mg, Zn). On the other hand, the investigation of B-site substitution was conducted on ball milled MgB_2O_4 and ZnB_2O_4 (B: Mn, Fe, Cr) particles, in which B-site substitution exhibited greater and more consistent impact on the battery performance and no steady trend was observed by A-site

substitution. Basically, the variation of battery performance can be indirectly postulated by their thermodynamics parameters and Nernst equation, or decided by the degree of valence states changes upon discharge/charge in simplicity. After the cation substitution in spinel, the mixing of energy states at Fermi level was substantially affected, thus the working voltages (both discharge and charge) were intuitively altered based on the selection of counter ion. Hence, B-site substitution in AB_2O_4 spinel offers greater influence in altering the battery performance (working voltage/capacity) by replacing the counter ion in the lattice metrics.

To address the inactive $ZnCr_2O_4$, a solid solution of $ZnFe_{2-y}Cr_yO_4$ was prepared. With the substitution of Fe^{3+} by Cr^{3+}, a gradual decrement in terms of working voltages and capacities was noticed. The end member, $ZnCr_2O_4$ demonstrated extremely poor storage behaviour (~93 mAh g^{-1} at 5^{th} cycle), whereas their component oxides ZnO and Cr_2O_3 reversibly absorb/release lithium ions (~618 mAh g^{-1} at 5^{th} cycle). A prudent and systematic study was conducted by *ex situ* characterization by XRD and HRTEM, the results showed that $ZnCr_2O_4$ stayed pristine even after 50 cycles, so it confirmed that $ZnCr_2O_4$ is electrochemically inactive after crystallizing in spinel phase. This is the first reported inactive TMO. A possible explanation regarding the excessively stable $ZnCr_2O_4$ was proposed to be related to the strong tendency of Cr^{3+} at octahedral sites based on their crystal field stabilization energy, which resulted in higher covalence in $ZnCr_2O_4$, or more broadly speaking, it reacts with lithium ions at lower voltage than the lithium metal reference. So, d level mixing is also one of the important factors when chooing counter ion, which is not mentioned in any other publication. In summary, Cr is not a good counter ion, as compared to the excellent properties demonstrated by Mn and Fe.

6.1. Novel Contributions

Based on the studies carried out in this thesis, several scientific and technological contributions have been made and are summarized in the sections below.

6.1.1. Scientific contributions

- Synthesis of ZnB_2O_4 (B: Mn, Fe, Cr) spinels using electrospinning technique to produce samples with different nanostructured morphologies (nanofibers, nanorods and nanowebs) by simply tuning the sintering conditions or viscosity of

precursor solution. High aspect ratio nanofibers demonstrate improved electrochemical performance due to the presence of 1D electronic wiring to facilitate lithium transportation.

- Modification on high energy ball milling synthesis by incorporating citric acid as reagent to prohibit agglomeration and facilitate grinding, in order to produce MgB_2O_4 (B: Mn, Fe, Cr) spinels with excellent cycling properties as new anode candidates.
- Investigation on the effect of 0D particles and 1D nanofibers on lithium absorption/extraction behavior.
- Comprehensive characterization on cycled electrode to propose reaction mechanisms of several new spinel-based anodes in lithium activity
- Fundamental studies on A-site and B-site substitution in AB_2O_4 spinel and the impact on electrochemical properties

6.1.2. Technological significances

- Scalable high energy ball milling technique to produce high capacity materials ($ZnMn_2O_4$ and $ZnFe_2O_4$).
- Lithium ion battery full-cell studies of $ZnMn_2O_4$ and $ZnFe_2O_4$ as anode materials, by using lithium iron phosphate ($LiFePO_4$) as cathode.

Chapter 7 Recommendations for Future Works

Based on the work done in this theis, the following possibilities for future work are recommended to further develop a better commercial anode to replace currently available graphite in LIB application.

7.1. Fundamental Studies on Crystal Chemistry of AB_2O_4 and their Lithium Activity

Since the practical working voltage of a TMO is decided not only by the theoretical postulation based on Nernst equation and thermodynamics parameter, but also the orbital state mixing at Fermi level. Hence, it will be interesting to conduct a simulation to understand band energies *versus* density of states of spinel. It may provide better guidelines in selecting the best combination of counter ion in spinel-based anodes. While neutron diffraction is more appropriate to analyze the cation distribution and the bond length variation upon lithium insertion, as the scattering factors of Zn, Fe, Mn and Cr are almost indistinguishable in XRD.

In present work, we have demonstrated *in situ* study of spinel lithium activity using synchrotron XRD and interesting results were obtained, however other *in situ* characterization techniques are required to gain a further insight. Firstly, we would suggest conducting *in situ* imaging technique with the purpose to capture the real time situation upon the destructive amorphization process takes place, such as full-field x-ray microscopy (TXM) with high spatial resolution of less than 40 nm which requires exposure time of several seconds.[167]

During subsequent charging, a new interfacial layer is formed between the covalent-bonded metallic nanograins and ionic-bonded Li_2O region in amorphized electrode. We propose that the reversible conversion reaction may be driven by the existence of surface incompatibility at the interfacial layer. Simply speaking, if the contact sites are “clean”

with no new daggling bonds created, there is a great tendency for the electrode to undergo re-conversion to minimize the surface energy. However, the interfacial components have not been investigated so far in any report, so it will be interesting to utilize XAS in identifying the coordination environment of metallic nanograins and O *K* edge of discharged elements. If a clean surface is observed, then it explains the great reversibility of conversion reaction.

7.2. Investigation of the Voltage Hysteresis

It is commonly observed that a flat plateau is generally absent in reversible conversion reaction due to the remarkable variation of the structural environment after first discharge, contrarily, a sloping curve is presented. It may be due to the nature of nanocrystalline TMOs after conversion reaction, which creates excessive surface sites to react with lithium at slightly different working voltages or the possibility of multiple steps re-oxidation/reduction process.[20] From the application perspective, this phenomenon penalized the battery efficiency. As of yet, there is no viable explanation to address this major drawback of conversion reaction. Although the suitable selection of counter ion has resulted in narrower voltage polarization, more efforts are required to further understand the origins of the voltage hysteresis before realizing conversion-based anodes in commercial market. As the first attempt in tackling this issue, we would suggest preparing a TMOs series with different level of initial crystallinity to correlate the relationship between amorphous character and inherent reaction routes with lithium. It helps to reinforce our previous assumptions about the presence of increasing surface sites with different equilibrium working voltages.

7.3. Enhancement of Full Cell Performance

The voltage hysteresis of spinel-based anode mentioned above has caused negative impact on the round trip efficiency of full cell performance. Besides, we are unable to unambiguously identify the working potential of $LiFePO_4$/ZMO-NP and $LiFePO_4$/ZFO-NP, despite their good capacity reversibility. Their performance are lagging behind $LiCoO_2$/CoO and $LiCoO_2$/Co_3O_4 demonstrated by Badway *et al*,[57] although Co is highly toxic and expensive less our combinations. So, a few measures shall be taken to

improve the applicability of ZMO-NP and ZFO-NP in full LIB cell, for instance to select another cathode with higher working voltage, optimize the mass ratio between cathode and anodes, characterize the reaction pathway of lithium.

References

[1]. Brilmeyer, G.H., *The 23rd International Battery Seminar & Exhibit*. 2006.
[2]. Winter, M. and R.J. Brodd, *What are batteries, fuel cells, and supercapacitors?* Chemical Reviews, 2004. **104**(10): p. 4245-4269.
[3]. Reddy, M.V., G.V. Subba Rao, and B.V.R. Chowdari, *Metal Oxides and Oxysalts as Anode Materials for Li Ion Batteries.* Chemical Reviews, 2013.
[4]. Takeuchi, E.S. and R.A. Leising, *Lithium batteries for biomedical applications.* MRS Bulletin, 2002. **27**(8): p. 624-627+596.
[5]. Albertus, P., J. Christensen, and J. Newman, *Modeling side reactions and nonisothermal effects in nickel metal-hydride batteries.* Journal of the Electrochemical Society, 2008. **155**(1): p. A48-A60.
[6]. Garrett, J. *Toyota and Tesla Trot Out the RAV4 EV*. The New York Times 2012 [cited 2013 05 May].
[7]. Lowe, M., *et al.*, *Lithium-ion Batteries for Electric Vehicles*. 2010, October.
[8]. Tarascon, J.M. and M. Armand, *Issues and challenges facing rechargeable lithium batteries.* Nature, 2001. **414**(6861): p. 359-367.
[9]. Sharma, Y., *et al.*, *Li-storage and cyclability of urea combustion derived $ZnFe_2O_4$ as anode for Li-ion batteries.* Electrochimica Acta, 2008. **53**(5): p. 2380-2385.
[10]. Buqa, H., *et al.*, *High rate capability of graphite negative electrodes for lithium-ion batteries.* Journal of the Electrochemical Society, 2005. **152**(2).
[11]. Tran, T.D., *et al.*, *Rate effect on lithium-ion graphite electrode performance.* Journal of Applied Electrochemistry, 1996. **26**(11): p. 1161-1167.
[12]. Thomas, F., *et al.*, *Lithium battery fires: Implications for air medical transport.* Air Medical Journal, 2012. **31**(5): p. 242-248.
[13]. Liu, C., *et al.*, *Advanced materials for energy storage.* Advanced Materials, 2010. **22**(8).
[14]. Bruce, P.G., B. Scrosati, and J.M. Tarascon, *Nanomaterials for rechargeable lithium batteries.* Angewandte Chemie, International Edition in English, 2008. **47**(16): p. 2930-2946.
[15]. Li, H., *et al.*, *Research on advanced materials for Li-ion batteries.* Advanced Materials, 2009. **21**(45): p. 4593-4607.
[16]. Chen, Z., *et al.*, *Preparation and electrochemical performance of Sn–Co–C composite as anode material for Li-ion batteries.* Journal of Power Sources, 2009. **189**(1): p. 730-732.
[17]. Hassoun, J., *et al.*, *An electrochemical investigation of a Sn-Co-C ternary alloy as a negative electrode in Li-ion batteries.* Journal of Power Sources, 2007. **171**(2): p. 928-931.
[18]. Yazami, R. and P. Touzain, *A reversible graphite-lithium negative electrode for electrochemical generators.* Journal of Power Sources, 1983. **9**(3): p. 365-371.
[19]. Poizot, P., *et al.*, *Nano-sized transition-metal oxides as negative-electrode materials for lithium-ion batteries.* Nature, 2000. **407**(6803): p. 496-499.
[20]. Cabana, J., *et al.*, *Beyond intercalation-based Li-ion batteries: The state of the art and challenges of electrode materials reacting through conversion reactions.* Advanced Materials, 2010. **22**(35): p. E170-E192

[21]. Manthiram, A., *et al.*, *Nanostructured electrode materials for electrochemical energy storage and conversion.* Energy and Environmental Science, 2008. **1**(6): p. 621-638.

[22]. Aricò, A.S., *et al.*, *Nanostructured materials for advanced energy conversion and storage devices.* Nature Materials, 2005. **4**(5): p. 366-377.

[23]. Guo, Y.G., J.S. Hu, and L.J. Wan, *Nanostructured materials for electrochemical energy conversion and storage devices.* Advanced Materials, 2008. **20**(15): p. 2877-2887.

[24]. Centi, G. and S. Perathoner, *The role of nanostructure in improving the performance of electrodes for energy storage and conversion.* European Journal of Inorganic Chemistry, 2009(26): p. 3851-3878.

[25]. Sharma, Y., *et al.*, *Nanophase $ZnCo_2O_4$ as a high performance anode material for Li-ion batteries.* Advanced Functional Materials, 2007. **17**(15): p. 2855-2861.

[26]. NuLi, Y.N., Y.Q. Chu, and Q.Z. Qin, *Nanocrystalline $ZnFe_2O_4$ and Ag-doped $ZnFe_2O_4$ films used as new anode materials for Li-ion batteries.* Journal of the Electrochemical Society, 2004. **151**(7): p. A1077-A1083

[27]. Teh, P.F., *et al.*, *Nanoweb anodes composed of one-dimensional, high aspect ratio, size tunable electrospun $ZnFe_2O_4$ nanofibers for lithium ion batteries.* Journal of Materials Chemistry, 2011. **21**(38): p. 14999-15008.

[28]. Hu, Y.S., *et al.*, *High lithium electroactivity of nanometer-sized rutile TiO_2.* Advanced Materials, 2006. **18**(11): p. 1421-1426.

[29]. Kim, H., *et al.*, *Multicomponent effects on the crystal structures and electrochemical properties of spinel-structured M_3O_4 (M = Fe, Mn, Co) anodes in lithium rechargeable batteries.* Chemistry of Materials, 2012. **24**(4): p. 720-725.

[30]. Sharma, Y., *et al.*, *Studies on spinel cobaltites, $FeCo_2O_4$ and $MgCo_2O_4$ as anodes for Li-ion batteries.* Solid State Ionics, 2008. **179**(15-16): p. 587-597.

[31]. Sharma, Y., *et al.*, *Studies on nano-$CaO{\cdot}SnO_2$ and nano-$CaSnO_3$ as anodes for Li-ion batteries.* Chemistry of Materials, 2008. **20**(21): p. 6829-6839.

[32]. NuLi, Y.-N. and Q.-Z. Qin, *Nanocrystalline transition metal ferrite thin films prepared by an electrochemical route for Li-ion batteries.* Journal of Power Sources, 2005. **142**(1-2): p. 292-297.

[33]. Patil, A., *et al.*, *Issue and challenges facing rechargeable thin film lithium batteries.* Materials research bulletin, 2008. **43**(8): p. 1913-1942.

[34]. Smith, M., R.E. García, and Q.C. Horn, *The effect of microstructure on the galvanostatic discharge of graphite anode electrodes in $LiCoO_2$-based rocking-chair rechargeable batteries.* Journal of the Electrochemical Society, 2009. **156**(11): p. A896-A904.

[35]. Kita, C., *Events and Sightings.* Annals of the History of Computing, IEEE. **34**(2): p. 60-69.

[36]. Brain, M. *Lithium-ion battery discharge mechanism.* 2006 [cited 2013 06-16]; Available from: http://electronics.howstuffworks.com/everyday-tech/lithium-ion-battery1.htm.

[37]. Winter, M., *et al.*, *Insertion electrode materials for rechargeable lithium batteries.* Advanced Materials, 1998. **10**(10): p. 725-763.

[38]. Park, C.M., *et al.*, *Li-alloy based anode materials for Li secondary batteries.* Chemical Society Reviews, 2010. **39**(8): p. 3115-3141.

[39]. Dey, A.N., *Electrochemical Alloying of Lithium in Organic Electrolytes.* Journal of the Electrochemical Society, 1971. **118**(10): p. 1547-1549.

[40]. Ji, L., *et al., Recent developments in nanostructured anode materials for rechargeable lithium-ion batteries.* Energy and Environmental Science, 2011. **4**(8): p. 2682-2689.

[41]. Kasavajjula, U., C. Wang, and A.J. Appleby, *Nano- and bulk-silicon-based insertion anodes for lithium-ion secondary cells.* Journal of Power Sources, 2007. **163**(2): p. 1003-1039.

[42]. Chan, C.K., *et al., Surface chemistry and morphology of the solid electrolyte interphase on silicon nanowire lithium-ion battery anodes.* Journal of Power Sources, 2009. **189**(2): p. 1132-1140.

[43]. Chen, H., *et al., Silicon nanowires with and without carbon coating as anode materials for lithium-ion batteries.* Journal of Solid State Electrochemistry, 2010. **14**(10): p. 1829-1834.

[44]. Vaughey, J., *et al., Studies of $LaSn_3$ as a negative electrode for lithium-ion batteries.* Journal of The Electrochemical Society, 2009. **156**(7): p. A536-A540.

[45]. Christensen, J.M., *Human exposure to toxic metals: Factors influencing interpretation of biomonitoring results.* Science of the Total Environment, 1995. **166**: p. 89-135.

[46]. Malini, R., *et al., Conversion reactions: a new pathway to realise energy in lithium-ion battery—review.* Ionics, 2009. **15**(3): p. 301-307.

[47]. Zhang, W.J., *Lithium insertion/extraction mechanism in alloy anodes for lithium-ion batteries.* Journal of Power Sources, 2011. **196**(3): p. 877-885.

[48]. Scrosati, B., *Nanomaterials: Paper powers battery breakthrough.* Nature Nanotechnology, 2007. **2**(10): p. 598-599.

[49]. Li, H., P. Balaya, and J. Maier, *Li-storage via heterogeneous reaction in selected binary metal fluorides and oxides.* Journal of the Electrochemical Society, 2004. **151**(11): p. A1878-A1885.

[50]. Reddy, M.V., *et al., α-Fe_2O_3 nanoflakes as an anode material for li-ion batteries.* Advanced Functional Materials, 2007. **17**(15): p. 2792-2799.

[51]. Tarascon, J.M., *et al., New concepts for the search of better electrode materials for rechargeable lithium batteries.* Comptes Rendus Chimie, 2005. **8**(1): p. 9-15.

[52]. Ehl, R.G. and A.J. Ihde, *Faraday's electrochemical laws and the determination of equivalent weights.* Journal of Chemical Education, 1954. **31**(5): p. 226-232.

[53]. Yang, Y., *et al., Nanocrystalline $ZnMn_2O_4$ as a novel lithium-storage material.* Electrochemistry Communications, 2008. **10**(8): p. 1117-1120.

[54]. Xiao, L., *et al., Low temperature synthesis of flower-like $ZnMn_2O_4$ superstructures with enhanced electrochemical lithium storage.* Journal of Power Sources, 2009. **194**(2): p. 1089-1093.

[55]. Ponrouch, A., *et al., On the origin of the extra capacity at low potential in materials for Li batteries reacting through conversion reaction.* Electrochimica Acta, 2012. **61**: p. 13-18.

[56]. Wu, Z.S., *et al., Graphene anchored with Co_3O_4 nanoparticles as anode of lithium ion batteries with enhanced reversible capacity and cyclic performance.* ACS Nano, 2010. **4**(6): p. 3187-3194.

[57]. Badway, F., *et al., Metal oxides as negative electrode materials in Li-ion cells.* Electrochemical and Solid-State Letters, 2002. **5**(6): p. A115-A118.

[58]. Do, J.S. and C.H. Weng, *Electrochemical and charge/discharge properties of the synthesized cobalt oxide as anode material in Li-ion batteries.* Journal of Power Sources, 2006. **159**(1 SPEC. ISS.): p. 323-327.

[59]. Kang, Y.-M., *et al.*, *A study on the charge-discharge mechanism of Co_3O_4 as an anode for the Li ion secondary battery.* Electrochimica Acta, 2005. **50**(18): p. 3667-3673.

[60]. Lou, X.W., *et al.*, *Self-supported formation of needlelike Co_3O_4 nanotubes and their application as lithium-ion battery electrodes.* Advanced Materials, 2008. **20**(2): p. 258-262.

[61]. Guo, B., C. Li, and Z.Y. Yuan, *Nanostructured Co_3O_4 Materials: Synthesis, Characterization, and Electrochemical Behaviors as Anode Reactants in Rechargeable Lithium Ion Batteries.* Journal of Physical Chemistry C, 2010. **114**(29): p. 12805-12817.

[62]. Lipparoni, F.R., *et al.*, *Electrochemical properties of metal oxides as anode materials for lithium ion batteries.* Ionics, 2002. **8**(3-4): p. 177-182.

[63]. Wu, X.L., *et al.*, *α-Fe_2O_3 nanostructures: Inorganic salt-controlled synthesis and their electrochemical performance toward lithium storage.* Journal of Physical Chemistry C, 2008. **112**(43): p. 16824-16829.

[64]. Liu, H., *et al.*, *Electrochemical performance of α-Fe_2O_3 nanorods as anode material for lithium-ion cells.* Electrochimica Acta, 2009. **54**(6): p. 1733-1736.

[65]. Liu, J., *et al.*, *Iron oxide-based nanotube arrays derived from sacrificial template-accelerated hydrolysis: Large-area design and reversible lithium storage.* Chemistry of Materials, 2010. **22**(1): p. 212-217.

[66]. NuLi, Y., *et al.*, *Preparation of α-Fe_2O_3 submicro-flowers by a hydrothermal approach and their electrochemical performance in lithium-ion batteries.* Electrochimica Acta, 2008. **53**(12): p. 4213-4218.

[67]. NuLi, Y., *et al.*, *Controlled synthesis of α-Fe_2O_3 nanostructures and their size-dependent electrochemical properties for lithium-ion batteries.* Journal of Power Sources, 2008. **184**(2): p. 456-461.

[68]. Zeng, S., *et al.*, *Facile route for the fabrication of porous hematite nanoflowers: Its synthesis, growth mechanism, application in the lithium ion battery, and magnetic and photocatalytic properties.* Journal of Physical Chemistry C, 2008. **112**(13): p. 4836-4843.

[69]. Liu, H., *et al.*, *Magnetite/carbon core-shell nanorods as anode materials for lithium-ion batteries.* Electrochemistry Communications, 2008. **10**(12): p. 1879-1882.

[70]. Morales, J., *et al.*, *Synthesis and characterization of nanometric iron and iron-titanium oxides by mechanical milling: Electrochemical properties as anodic materials in lithium cells.* Journal of the Electrochemical Society, 2005. **152**(9): p. A1748-A1754.

[71]. Zhou, G., *et al.*, *Graphene-wrapped Fe_3O_4 anode material with improved reversible capacity and cyclic stability for lithium ion batteries.* Chemistry of Materials, 2010. **22**(18): p. 5306-5313.

[72]. Waerenborgh, J.C., *et al.*, *Temperature and Composition Dependence of the Cation Distribution in Synthetic ZnFeyAl2-yO4 ($0 \leqslant y \leqslant 1$) Spinels.* Journal of Solid State Chemistry, 1994. **111**(2): p. 300-309.

[73]. Yoon, S.J., *et al.*, *Electrical and magnetic properties of spinel $ZnCr_{2-x}Fe_xO4$ ($0 \leqslant x \leqslant 1.0$).* Materials Chemistry and Physics, 2002. **73**(2-3): p. 330-334.

[74]. Lenaz, D., *et al.*, *Structural changes and valence states in the $MgCr_2O_4$-$FeCr_2O_4$ solid solution series.* Physics and Chemistry of Minerals, 2004. **31**(9): p. 633-642.

[75]. O'Neill, H.S.C. and W.A. Dollase, *Crystal structures and cation distributions in simple spinels from powder XRD structural refinements: $MgCr_2O_4$,*

$ZnCr_2O_4$, Fe_3O_4 and the temperature dependence of the cation distribution in $ZnAl_2O_4$. Physics and Chemistry of Minerals, 1994. **20**(8): p. 541-555.

[76]. Coutts, T.J., *et al., Search for improved transparent conducting oxides: A fundamental investigation of CdO, Cd_2SnO_4, and Zn_2SnO_4.* Journal of Vacuum Science and Technology A: Vacuum, Surfaces and Films, 2000. **18**(6): p. 2646-2660.

[77]. Zhong, Q., *et al., Synthesis and electrochemistry of $LiNi_xMn_{2-x}O_4$.* Journal of the Electrochemical Society, 1997. **144**(1): p. 205-213.

[78]. Levy, D., A. Pavese, and M. Hanfland, *Phase transition of synthetic zinc ferrite spinel ($ZnFe_2O_4$) at high pressure, from synchrotron X-ray powder diffraction.* Physics and Chemistry of Minerals, 2000. **27**(9): p. 638-644.

[79]. Lee, Y.S., N. Kumada, and M. Yoshio, *Synthesis and characterization of lithium aluminum-doped spinel ($LiAl_xMn_{2-x}O_4$) for lithium secondary battery.* Journal of Power Sources, 2001. **96**(2): p. 376-384.

[80]. NuLi, Y., *et al., $NiCo_2O_4$/C Nanocomposite as a highly reversible anode material for lithium-ion batteries.* Electrochemical and Solid-State Letters, 2008. **11**(5): p. A64-A67.

[81]. Ai, C., *et al., Synthesis and characterization of spinel type $ZnCo_2O_4$ as a novel anode material for lithium ion batteries.* Journal of Materials Science, 2004. **39**(3): p. 1077-1079.

[82]. Sharma, Y., *et al., Lithium recycling behaviour of nano-phase-$CuCo_2O_4$ as anode for lithium-ion batteries.* Journal of Power Sources, 2007. **173**(1): p. 495-501.

[83]. Li, J., *et al., A facile route to synthesize multiporous $MnCo_2O_4$ and $CoMn_2O_4$ spinel quasi-hollow spheres with improved lithium storage properties.* Nanoscale, 2013. **5**(5): p. 2045-2054.

[84]. Zhang, D., *et al., Low-temperature fabrication of $MnFe_2O_4$ octahedrons: Magnetic and electrochemical properties.* Chemical Physics Letters, 2006. **426**(1-3): p. 120-123.

[85]. Guo, X., *et al., Lithium storage in hollow spherical $ZnFe_2O_4$ as anode materials for lithium ion batteries.* Electrochemistry Communications, 2010. **12**(6): p. 847-850.

[86]. Ding, Y., Y. Yang, and H. Shao, *High capacity $ZnFe_2O_4$ anode material for lithium ion batteries.* Electrochimica Acta, 2011. **56**(25): p. 9433-9438.

[87]. Deng, Y., *et al., One-pot synthesis of $ZnFe_2O_4$/C hollow spheres as superior anode materials for lithium ion batteries.* Chemical Communications, 2011. **47**(24): p. 6828-6830.

[88]. Mueller, F., *et al., Influence of the carbonaceous conductive network on the electrochemical performance of $ZnFe_2O_4$ nanoparticles.* Journal of Power Sources, 2013. **236**: p. 87-94.

[89]. Chu, Y.Q., Z.W. Fu, and Q.Z. Qin, *Cobalt ferrite thin films as anode material for lithium ion batteries.* Electrochimica Acta, 2004. **49**(27): p. 4915-4921.

[90]. Zhao, H., *et al., Fabrication and electrochemical performance of nickel ferrite nanoparticles as anode material in lithium ion batteries.* Electrochemistry Communications, 2007. **9**(10): p. 2606-2610.

[91]. Sivakumar, N., *et al., Nanostructured $MgFe_2O_4$ as anode materials for lithium-ion batteries.* Journal of alloys and compounds, 2011. **509**(25): p. 7038-7041.

[92]. Wang, J., P. King, and R.A. Huggins, *Investigations of binary lithium-zinc, lithium-cadmium and lithium-lead alloys as negative electrodes in organic solvent-based electrolyte.* Solid State Ionics, 1986. **20**(3): p. 185-189.

[93]. Chen, C., M. Greenblatt, and J. Waszczak, *Lithium insertion reactions of spinels: Effect of the distribution and reducibility of cations in selected manganite and zinc spinels.* Materials research bulletin, 1986. **21**(5): p. 609-619.

[94]. Courtel, F.M., *et al.*, *High capacity anode materials for Li-ion batteries based on spinel metal oxides AMn_2O_4 (A = Co, Ni, and Zn).* Journal of Materials Chemistry, 2011. **21**(27): p. 10206-10218.

[95]. Courtel, F.M., Y. Abu-Lebdeh, and I.J. Davidson, *$ZnMn_2O_4$ nanoparticles synthesized by a hydrothermal method as an anode material for Li-ion batteries.* Electrochimica Acta, 2012. **71**: p. 123-127.

[96]. Deng, Y., *et al.*, *Controllable synthesis of spinel nano-$ZnMn_2O_4$ via a single source precursor route and its high capacity retention as anode material for lithium ion batteries.* Journal of Materials Chemistry, 2011. **21**(32): p. 11987-11995.

[97]. Kim, S.W., *et al.*, *Electrochemical performance and ex situ analysis of $ZnMn_2O_4$ nanowires as anode materials for lithium rechargeable batteries.* Nano Research, 2011. **4**(5): p. 505-510.

[98]. Zhou, L., *et al.*, *Facile preparation of $ZnMn_2O_4$ hollow microspheres as high-capacity anodes for lithium-ion batteries.* Journal of Materials Chemistry, 2012. **22**(3): p. 827-829.

[99]. Chen, X.F., *et al.*, *Self-templated synthesis of hollow porous submicron $ZnMn_2O_4$ sphere as anode for lithium-ion batteries.* Journal of Alloys and Compounds, 2013. **559**: p. 5-10.

[100]. Cai, Y., *et al.*, *Facile preparation of porous one-dimensional Mn_2O_3 nanostructures and their application as anode materials for lithium-ion batteries.* Physica E: Low-Dimensional Systems and Nanostructures, 2010. **43**(1): p. 70-75.

[101]. Wang, H., *et al.*, *Evaluation of ZnO nanorod arrays with dandelion-like morphology as negative electrodes for lithium-ion batteries.* Electrochimica Acta, 2009. **54**(10): p. 2851-2855.

[102]. Zu, C.X. and H. Li, *Thermodynamic analysis on energy densities of batteries.* Energy and Environmental Science, 2011. **4**(8): p. 2614-2624.

[103]. Yu, X.Q., *et al.*, *Nanocrystalline MnO thin film anode for lithium ion batteries with low overpotential.* Electrochemistry Communications, 2009. **11**(4): p. 791-794.

[104]. Chang, L., *et al.*, *Pore-controlled synthesis of Mn_2O_3 microspheres for ultralong-life lithium storage electrode.* RSC Advances, 2013. **3**(6): p. 1947-1952.

[105]. Hu, J., H. Li, and X. Huang, *Cr_2O_3-based anode materials for Li-ion batteries.* Electrochemical and Solid-State Letters, 2005. **8**(1): p. A66-A69.

[106]. Dupont, L., *et al.*, *Mesoporous Cr_2O_3 as negative electrode in lithium batteries: TEM study of the texture effect on the polymeric layer formation.* Journal of Power Sources, 2008. **175**(1): p. 502-509.

[107]. Wu, M.S. and H.W. Chang, *Self-assembly of NiO-coated ZnO nanorod electrodes with core-shell nanostructures as anode materials for rechargeable lithium-ion batteries.* Journal of Physical Chemistry C, 2013. **117**(6): p. 2590-2599.

[108]. Lavela, P., N. Kyerematen, and J. Tirado, *$NiMn_{2-x}Fe_xO_4$ prepared by a reverse micelles method as conversion anode materials for Li-ion batteries.* Materials Chemistry and Physics, 2010. **124**(1): p. 102-108.

[109]. Magasinski, A., *et al., High-performance lithium-ion anodes using a hierarchical bottom-up approach.* Nature Materials, 2010. **9**(4): p. 353-358.
[110]. Yu, Y., *et al., Encapsulation of Sn@carbon nanoparticles in bamboo-like hollow carbon nanofibers as an anode material in lithium-based batteries.* Angewandte Chemie - International Edition, 2009. **48**(35): p. 6485-6489.
[111]. Yu, Y., *et al., Tin nanoparticles encapsulated in porous multichannel carbon microtubes: Preparation by single-nozzle electrospinning and application as anode material for high-performance Li-based batteries.* Journal of the American Chemical Society, 2009. **131**(44): p. 15984-15985.
[112]. Liu, R., J. Duay, and S.B. Lee, *Heterogeneous nanostructured electrode materials for electrochemical energy storage.* Chemical Communications, 2011. **47**(5): p. 1384-1404.
[113]. Bid, S. and S.K. Pradhan, *Preparation of zinc ferrite by high-energy ball-milling and microstructure characterization by Rietveld's analysis.* Materials Chemistry and Physics, 2003. **82**(1): p. 27-37.
[114]. Li, D. and Y. Xia, *Electrospinning of nanofibers: Reinventing the wheel?* Advanced Materials, 2004. **16**(14): p. 1151-1170.
[115]. Tonejc, A., *High-resolution transmission electron microscopy (HRTEM): image processing analysis of defects and grain boundaries in nanocrystalline materials.* Acta chimica slovenica, 1999. **46**(3): p. 435-461.
[116]. Cheary, R.W. and A. Coelho, *A fundamental parameters approach to X-ray line-profile fitting.* Journal of Applied Crystallography, 1992. **25**(2): p. 109-121.
[117]. Bruker, *Bruker AXS Inc.* SAINT. Version 6.0, 2005.
[118]. Watt, I.M., *The principles and practice of electron microscopy*. 1997: Cambridge University Press.
[119]. Stadelmann, P., *EMS-a software package for electron diffraction analysis and HREM image simulation in materials science.* Ultramicroscopy, 1987. **21**(2): p. 131-145.
[120]. Socrates, G., *Infrared and Raman characteristic group frequencies: Tables and charts*. John Wiley & Sons. 2004, Chichester, New York John Wiley & Sons.
[121]. Brodowski, S., *et al., Morphological and chemical properties of black carbon in physical soil fractions as revealed by scanning electron microscopy and energy-dispersive X-ray spectroscopy.* Geoderma, 2005. **128**(1-2): p. 116-129.
[122]. Battistoni, C., *et al., An XPS and Mössbauer study of the electronic properties of* $ZnCr_xGa_{2-x}O_4$ *spinel solid solutions.* Solid State Communications, 1981. **39**(4): p. 581-585.
[123]. Tan, H., *et al., Oxidation state and chemical shift investigation in transition metal oxides by EELS.* Ultramicroscopy, 2012. **116**: p. 24-33.
[124]. Dong, C., *et al., Electronic structure of nanostructured ZnO from x-ray absorption and emission spectroscopy and the local density approximation.* Physical Review B, 2004. **70**(19): p. 195325.
[125]. De Groot, F., *et al., Oxygen 1s x-ray-absorption edges of transition-metal oxides.* Physical Review B, 1989. **40**(8): p. 5715.
[126]. Crocombette, J., *et al., X-ray-absorption spectroscopy at the Fe* $L_{2,3}$ *threshold in iron oxides.* Physical Review B, 1995. **52**(5): p. 3143.
[127]. Bard, A.J. and L.R. Faulkner, *Electrochemical methods: fundamentals and applications*. Vol. 2. 1980: Wiley New York.

[128]. Zheng, W., *et al.*, *Electrospinning route for α-Fe_2O_3 ceramic nanofibers and their gas sensing properties.* Materials Research Bulletin, 2009. **44**(6): p. 1432-1436.
[129]. Wee, G., *et al.*, *Synthesis and electrochemical properties of electrospun V_2O_5 nanofibers as supercapacitor electrodes.* Journal of Materials Chemistry, 2010. **20**(32): p. 6720-6725.
[130]. Borodko, Y., *et al.*, *Probing the interaction of poly(vinylpyrrolidone) with platinum nanocrystals by UV - Raman and FTIR.* Journal of Physical Chemistry B, 2006. **110**(46): p. 23052-23059.
[131]. Dunitz, J.D. and L.E. Orgel, *Stereochemistry of Ionic Solids*, in *Advances in Inorganic Chemistry and Radiochemistry*. 1960. p. 1-60.
[132]. Ramgir, N.S., *et al.*, *ZnO Multipods, Submicron Wires, and Spherical Structures and Their Unique Field Emission Behavior.* The Journal of Physical Chemistry B, 2006. **110**(37): p. 18236-18242.
[133]. Han, Y.-F., *et al.*, *Coral-like nanostructured α-Mn_2O_3 nanaocrystals for catalytic combustion of methane: Part I. Preparation and characterization.* Catalysis Today, 2008. **131**(1–4): p. 35-41.
[134]. Kang, Y.-M., *et al.*, *A study on the charge–discharge mechanism of Co_3O_4 as an anode for the Li ion secondary battery.* Electrochimica Acta, 2005. **50**(18): p. 3667-3673.
[135]. Sharma, N., *et al.*, *Mixed oxides $Ca_2Fe_2O_5$ and $Ca_2Co_2O_5$ as anode materials for Li-ion batteries.* Electrochimica Acta, 2004. **49**(7): p. 1035-1043.
[136]. MacÍas, M., *et al.*, *Electrospun mesoporous metal oxide fibers.* Microporous and Mesoporous Materials, 2005. **86**(1-3): p. 1-13.
[137]. López, F.A., *et al.*, *Synthesis of nanocrystalline zinc ferrite powders from sulphuric pickling waste water.* Journal of alloys and compounds, 1998. **265**(1-2): p. 291-296.
[138]. Liu, J., *et al.*, *Carbon/ZnO nanorod array electrode with significantly improved lithium storage capability.* Journal of Physical Chemistry C, 2009. **113**(13): p. 5336-5339.
[139]. Kalai Selvan, R., *et al.*, *$CuFe_2O_4/SnO_2$ nanocomposites as anodes for Li-ion batteries.* Journal of Power Sources, 2006. **157**(1): p. 522-527.
[140]. Teh, P.F., *et al.*, *Electrospun $Zn_{1-x}Mn_xFe_2O_4$ Nanofibers as Anodes for Lithium-Ion Batteries and the Impact of Mixed Transition Metallic Oxides on Battery Performance.* ACS Applied Materials & Interfaces, 2013. **5**(12): p. 5461-5467.
[141]. Shannon, R.D., *Revised effective ionic radii and systematic studies of interatomic distances in halides and chalcogenides.* Acta Crystallographica, 1976. **A32**: p. 751-767.
[142]. Teh, P.F., *et al.*, *Tuning the morphology of $ZnMn_2O_4$ lithium ion battery anodes by electrospinning and its effect on electrochemical performance.* RSC Advances, 2013. **3**(8): p. 2812-2821.
[143]. Gibot, P. and L. Vidal, *Original synthesis of chromium (III) oxide nanoparticles.* Journal of the European Ceramic Society, 2010. **30**(4): p. 911-915.
[144]. Wang, Y., A. Muramatsu, and T. Sugimoto, *FTIR analysis of well-defined α-Fe_2O_3 particles.* Colloids and Surfaces A: Physicochemical and Engineering Aspects, 1998. **134**(3): p. 281-297.
[145]. Fu, L.J., *et al.*, *Surface modifications of electrode materials for lithium ion batteries.* Solid State Sciences, 2006. **8**(2): p. 113-128.

[146]. Wang, Y., *et al.*, *Nanocrystalline NiO thin film anode with MgO coating for Li-ion batteries.* Electrochimica Acta, 2003. **48**(28): p. 4253-4259.
[147]. Gong, C., *et al.*, *Preparation of carbon-coated $MgFe_2O_4$ with excellent cycling and rate performance.* Electrochimica Acta, 2013. **90**: p. 119-127.
[148]. Reda, S.Y., *Evaluation of antioxidants stability by thermal analysis and its protective effect in heated edible vegetable oil.* Avaliação da estabilidade de antioxidantes por análise térmica e seu efeito protetor em óleo vegetal aquecido, 2011. **31**(2): p. 475-480.
[149]. Connor, P.A. and J.T.S. Irvine, *Novel tin oxide spinel-based anodes for Li-ion batteries.* Journal of Power Sources, 2001. **97–98**(0): p. 223-225.
[150]. Zhou, W., S. Upreti, and M.S. Whittingham, *High performance Si/MgO/graphite composite as the anode for lithium-ion batteries.* Electrochemistry Communications, 2011. **13**(10): p. 1102-1104.
[151]. Teh, P.F., *et al.*, *Electrochemical Reactivity with Lithium of Spinel-type $ZnFe_{2-y}Cr_yO_4$ ($0 \leqslant y \leqslant 2$).* The Journal of Physical Chemistry C. **117**(46): p. 24213-24223.
[152]. Levy, D., *et al.*, *P-V equation of state, thermal expansion, and P-T stability of synthetic zincochromite ($ZnCr_2O_4$ spinel).* American Mineralogist, 2005. **90**(7): p. 1157-1162.
[153]. Vegard, L., *Die Konstitution der Mischkristalle und die Raumfüllung der Atome.* Zeitschrift für Physik, 1921. **5**(1): p. 17-26.
[154]. Hawn, D.D. and B.M. DeKoven, *Deconvolution as a correction for photoelectron inelastic energy losses in the core level xps spectra of iron oxides.* Surface and Interface Analysis, 1986. **10**(2-3): p. 63-74.
[155]. Reddy, K.M., *et al.*, *On the room-temperature ferromagnetism of $Zn_{1-x}Cr_xO$ thin films deposited by reactive co-sputtering.* Solar Energy Materials and Solar Cells, 2007. **91**(15-16): p. 1496-1502.
[156]. Lepot, N., *et al.*, *Synthesis of ZnO nanorods from aqueous solution.* Materials Letters, 2007. **61**(13): p. 2624-2627.
[157]. Carta, G., *et al.*, *A comparative study of Cr_2O_3 thin films obtained by MOCVD using three different precursors.* Chemical Vapor Deposition, 2005. **11**(8-9): p. 375-380.
[158]. Waldron, R.D., *Infrared spectra of ferrites.* Physical Review, 1955. **99**(6): p. 1727-1735.
[159]. Hu, Y., *et al.*, *Structural and morphological evolution in magnetron co-sputtered (Zn, Cr) O films.* Journal of Physics D: Applied Physics, 2008. **41**(20): p. 205301.
[160]. Pool, V., *et al.*, *Site determination of Zn doping in protein encapsulated $Zn_xFe_{3-x}O_4$ nanoparticles.* Journal of Applied Physics, 2009. **105**(7): p. 07B515-07B515-3.
[161]. Goodenough, J.B. and Y. Kim, *Challenges for rechargeable Li batteries.* Chemistry of Materials, 2010. **22**(3): p. 587-603.
[162]. Ruffo, R., *et al.*, *Impedance analysis of silicon nanowire lithium ion battery anodes.* Journal of Physical Chemistry C, 2009. **113**(26): p. 11390-11398.
[163]. Shaju, K.M., *et al.*, *Mesoporous and nanowire Co_3O_4 as negative electrodes for rechargeable lithium batteries.* Physical Chemistry Chemical Physics, 2007. **9**(15): p. 1837-1842.
[164]. Garvie, L.A.J., A.J. Craven, and R. Brydson, *Use of electron-energy loss near-edge fine structure in the study of minerals.* American Mineralogist, 1994. **79**(5-6): p. 411-425.

[165]. Schmid, H.K. and W. Mader, *Oxidation states of Mn and Fe in various compound oxide systems.* Micron, 2006. **37**(5): p. 426-432.
[166]. Lin, Z., *et al.*, *Electrodeposited MnO_x/carbon nanofiber composites for use as anode materials in rechargeable lithium-ion batteries.* Journal of Power Sources, 2010. **195**(15): p. 5025-5031.
[167]. Meirer, F., *et al.*, *Three-dimensional imaging of chemical phase transformations at the nanoscale with full-field transmission X-ray microscopy.* Journal of Synchrotron Radiation, 2011. **18**(5): p. 773-781.
[168]. Dunitz, J.D. and L.E. Orgel, *Electronic properties of transition-metal oxides-II. Cation distribution amongst octahedral and tetrahedral sites.* Journal of Physics and Chemistry of Solids, 1957. **3**(3-4): p. 318-323.
[169]. Catti, M., *et al.*, *High-pressure decomposition of MCr_2O_4 spinels (M=Mg, Mn, Zn) by ab initio methods.* Physics and Chemistry of Minerals, 1999. **26**(5): p. 389-395.
[170]. Müller, F. and O.J. Kleppa, *Thermodynamics of formation of chromite spinels.* Journal of Inorganic and Nuclear Chemistry, 1973. **35**(8): p. 2673-2678.
[171]. Gabr, R.M., *et al.*, *Effect of spinel ($ZnCr_2O_4$) formation on the texture, electrical conduction and catalytic behaviour of the ZnO-Cr_2O_3 system.* Materials Chemistry and Physics, 1994. **39**(1): p. 53-62.
[172]. Doe, R.E., *et al.*, *First-principles investigation of the Li-Fe-F phase diagram and equilibrium and nonequilibrium conversion reactions of iron fluorides with lithium.* Chemistry of Materials, 2008. **20**(16): p. 5274-5283.
[173]. Pan, Q., *Flower-like ZnO-NiO-C films with high reversible capacity and rate capability for lithium-ion batteries.* Electrochimica Acta. **55**(20): p. 5780-5785.

Appendix

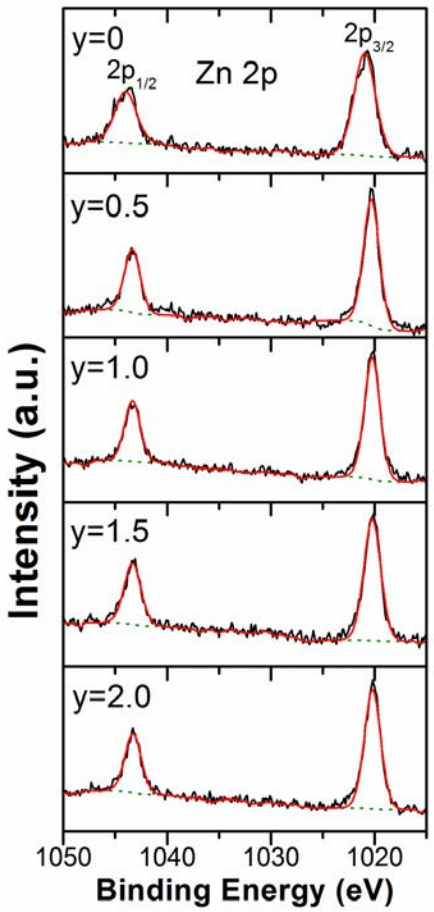

Figure S1 XPS Zn 2p collected from $ZnFe_{2-y}Cr_yO_4$ samples.

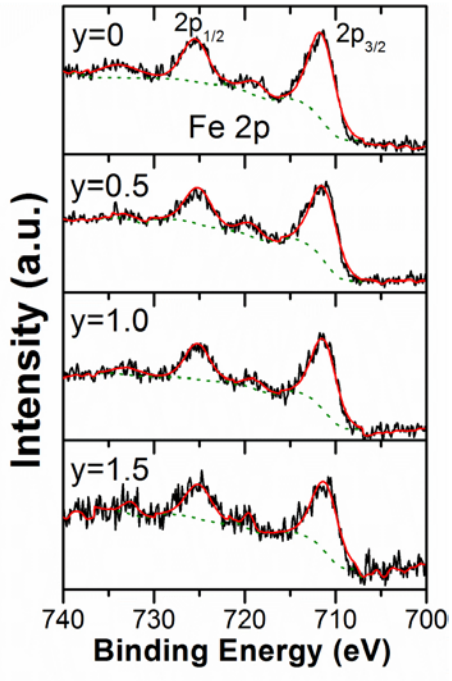

Figure S2 XPS Fe 2p collected from $ZnFe_{2-y}Cr_yO_4$ samples.

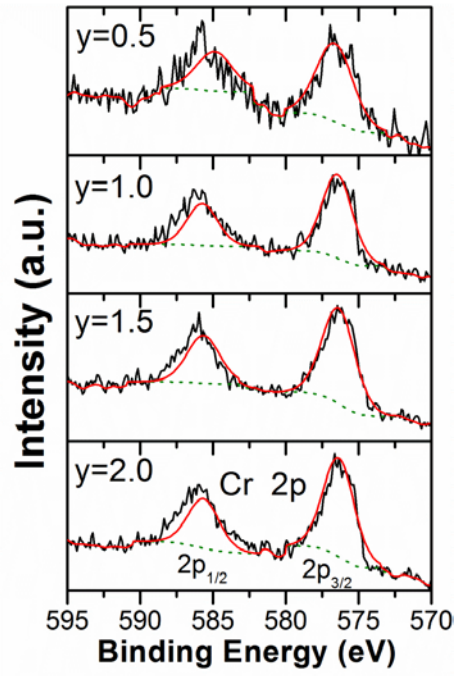

Figure S3 XPS Cr 2p collected from $ZnFe_{2-y}Cr_yO_4$ samples.

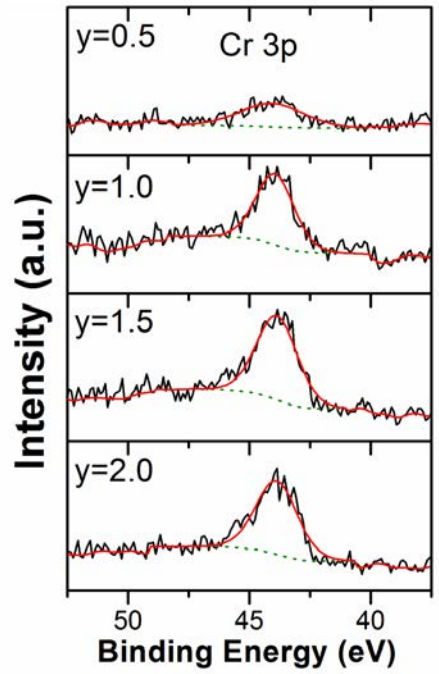

Figure S4 XPS Cr 3p collected from $ZnFe_{2-y}Cr_yO_4$ samples.